Spectroscopie magnéto-optique de nanostructures semiconductrices magnétiques

Petr Stepanov

▶ **To cite this version:**

Petr Stepanov. Spectroscopie magnéto-optique de nanostructures semiconductrices magnétiques. Autre [cond-mat.other]. Université de Grenoble, 2013. Français. NNT : 2013GRENY042 . tel-00994939

HAL Id: tel-00994939
https://theses.hal.science/tel-00994939

Submitted on 22 May 2014

UNIVERSITÉ DE GRENOBLE

THÈSE

Pour obtenir le grade de

DOCTEUR DE L'UNIVERSITÉ DE GRENOBLE

Spécialité : **Physique**

Arrêté ministériel : 7 aout 2006

Présentée par

Petr Stepanov

Thèse dirigée par **David Ferrand**
et codirigée par **Joël Cibert**

préparée au sein **de l'Institut Néel**
et de l'**Université de Grenoble**

Magneto-optical spectroscopy of semiconductor magnetic quantum dots

Thèse soutenue publiquement le **11/12/2013**,
devant le jury composé de :

Denis Scalbert
Directeur de Recherche, CNRS Montpellier , Rapporteur
Jean-Pierre Hermier
Professeur, Université de Versailles Saint Quentin , Rapporteur
Val Zwiller
Professeur, Kavli Institute of Nanoscience, Delft, Examinateur
Dmitry Yakovlev
Professeur, Technische Universität, Dortmund , Examinateur
Etienne Gheeraert
Professeur, Université Joseph Fourier, Grenoble, Président
David Ferrand
Maitre de Conference, Unversité de Grenoble , Directeur de thèse
Joël Cibert
Directeur de Recherche, CNRS Grenoble , Co-Directeur de thèse

Abstract

The first part of the present work is devoted to a study of the diluted magnetic semiconductor (DMS) self-assembled quantum dots optical properties. The unique feature of DMS is a magnetic polaron: a local ferromagnetic order of spins of magnetic atoms induced by the strong exchange interaction with a spin of the exciton optically injected in the quantum dot. Providing time-resolved and cw magneto-optical spectroscopy, we demonstrate the formation of the magnetic polaron with a negatively charged exciton along with a neutral exciton. We show that the MP formed with a negatively charged exciton is characterized by a stronger exchange field and higher polaron energy than the ones of a neutral exciton magnetic polaron. The observed result seems unexpected since one considers the spins of the two electrons in a negatively charged exciton to be compensated by each other and to be expelled from the magnetic polaron formation process. A theoretical description is provided in terms of the newly developed model, which, in contrast to the widely used "exchange box" model, takes into account the Coulomb interaction between an electron and a hole. The numerical calculation based on this theory allowed us to demonstrate its efficiency and to obtain parameters of the magnetic polaron being in a good agreement with the experiment.

The second part of the present work is devoted to a study of quasi-one-dimensional semiconductor heterostructures. Such geometry provides the better access to a single object studies, better control on the size and position of the quantum dot which may be inserted in a nanowire. The unique anisotropic properties and the possibility of doping with magnetic impurities make nanowires a promising candidate for future studies of DMS heterostructures. As the first step, the study of non-magnetic single nanowire optical properties with and without the quantum dot have been performed in the present work. Polarization resolved photoluminescence experiments combined with the cathodoluminescence allowed us to demonstrate the spatial localization of the emitted light. The influence of the strain arising in the nanowire with the core-shell structure on the photoluminescence energy is discussed. The single-photon emitter properties are characterized by the photon correlation measurements. The exciton confinement in the quantum dot inserted in the nanowire is investigated by means of the photoluminescence temperature dependence.

Contents

Introduction

Since the creation of p-n junction and a transistor in 1947, the increasing processing rate of microelectronic devices was followed by the miniaturization of the integrated circuit components. Modern technologies demand fast transfer and processing of information, at the limit of capabilities of the integrated-circuit technology. The possibility of using electrons' spins in addition to their charge in information technology has created much enthusiasm for a new field of electronics popularly known as "spintronics." A prominent example of utilizing both properties is the giant magneto-resistance effect resulting from spin-dependent scattering of electrons propagating through thin metallic films [1]. A challenging candidate for a device based on the electron spin as an information carrier is the spin field-transistor which has been proposed by S. Datta and B. Das in 1984 [2].

An intensely studied approach to obtain spin-polarized carriers for data-storage devices is the use of diluted magnetic semiconductors (DMS) created by inserting magnetic ions like Mn, Fe, or Co into a semiconducting host such as II-VI or III-V semiconductors. The interaction among these spins can lead to ferromagnetic order at low temperatures, which is necessary to create spin-polarized carriers in the absence of an applied magnetic field. Soon after the discovery of carrier-controlled ferromagnetism in Mn-doped III-V [3] and II-VI semiconductor compounds [4], it has become clear that these systems offer unprecedented opportunities to control the magnetic properties by tuning the carrier densities using gate voltage. The highest critical temperature of the carrier induced ferromagnetism, which has been achieved with GaAs is T_C=200 K [5]. Among the DMS materials studied during the past decades, $Cd_{1-x}Mn_xTe$ compound, in spite of a much lower T_C, attracts much interest due to the facilitated fabrication of low-dimensional structures by means of Molecular Beam Epitaxy (MBE).

Single CdTe quantum dots (QDs) doped with a single Mn atom can be probed by means of single exciton spectroscopy in photoluminescence experiments. This has been done both in II-VI [6, 7], and III-V [8] materials. In the case of single Mn doped CdTe dots, information about the quantum spin state of a single Mn atom is extracted from the single exciton quantum dot photoluminescence due to the one to one relation between photon energy and polarization on one hand, and the spin state of the Mn atom on the other hand. This has made it possible to measure the spin relaxation time of a single Mn atom in a quantum dot, using photon autocorrelation measurements [9], and to realize the optical initialization and readout of the spin of the single Mn atom [7, 10, 11].

An increasing amount of magnetic atoms inside semiconductor offers a possibility of manipulating the Mn magnetization with charges (electrons and hole introduced by doping, excitons). In bulk CdMnTe, the continuous transition from diamagnetic behavior of CdTe, to paramagnetism (for $x < 0.05$), spin-glass and finally antiferromagnetic ordering (for $x > 0.6$) has been observed [12]. Turning to nanostructures, the clearest demonstrations of confined carrier induced ferromagnetism have been provided in the CdMnTe quantum structures. In a quantum well of CdMnTe a ferromagnetic phase can be obtained and manipulated by photon illumination or bias application due to the strong exchange coupling of Mn spins to charge carriers [13].

In a quantum dot, the relevant concept of the carrier induced magnetization is the formation of Magnetic Polarons (MP). The magnetic polaron is a local ferromagnetic order induced by exchange interaction between the spin of a charge carrier and spins of magnetic atoms located in the vicinity of the charge carrier. The spin ordering decreases the carrier energy. If the Mn concentration is large enough, the Bohr radius even shrinks, increasing further the stability. The exchange field (field "seen" by the Mn spins) is usually of the order of a few Tesla, or less. The optical properties of MPs have been widely investigated in 3D and 2D DMS. In a DMS quantum dot the MP formation is much more pronounced due to the strong, three-dimensional confinement of the charge carriers [14]. So far, only the formation of the Exciton Magnetic Polaron (EMP or XMP) had been studied in different low-dimensional systems including single quantum dots. But no attention had been paid to the more complex charge combinations such as trions or biexcitons.

The first goal of the present work is to study the formation of magnetic polarons in

a single self-assembled DMS quantum dot, the photoluminescence spectrum of which contains either an exciton or a charged exciton. This provides us a unique opportunity to put in direct comparison the properties of magnetic polarons formed with these two complexes. A set of QD samples with Mn concentration ranged between 2% and 10% will allow us to trace the dependence of MP parameters on the concentration of magnetic atoms inside the dot and define the optimal Mn content where one can follow the (partial) formation of the magnetic polaron while identifying both exciton and charged exciton at the same time in the spectra.

The composition and spatial distribution of the magnetic ions greatly influence the magnetic polaron stability and dynamical properties. The morphology and the chemical composition influence the optical properties of magnetic semiconductor nanostructure. If we want to adjust specific properties, quantum dots inserted in nanowires (NWs) offer numerous advantages over self-assembled QDs:

The vapor-liquid-solid (VLS) synthesis method, which consists in using a metal catalyst (usually gold) to nucleate the nanowire growth, offers a possibility to control the diameter of the nanowire and its location on the substrates. The size and density of the QDs are not imposed by the respective material parameters (the lattice mismatch) but are determined simply molecular fluxes during growth and by the initial density of catalyst nanoparticles. This offers a possibility of a single object studies and an easier access to the geometrical and structural properties compared to the MBE-grown self-assembled QDs studied in the first part.

The formation of QD in a NW is not a strain-driven process in contrast to Stranski Krastanow growth, therefore a much larger choice of materials can be used. The absence of a wetting layer offers also a better confinement.

Furthermore, the NW growth mechanism offers the possibility to grow core-shell heterostructures where the nanowires are surrounded by a radial shell (usually made of a higher band gap material). This shell enables passivation of interfaces, allowing to enhance the emission efficiency [15]. One can vary the thickness of the shell and control the energy of the emission of the nanowire. The catalyzed growth mode of nanowire allows also the insertion of several dots in the same nanowire. The coupling between the dots is then controlled by their separation. The control of the quantum dot geometry provides a possibility of controlling the shape of the confinement potential. As a result we can control the spin anisotropy of the hole and, therefore, the magnetic anisotropy.

All these advantages make DMS quantum dots inserted in nanowires very promising candidates for future studies on magnetic polarons.

The second goal of the present work is to make the first several steps towards these future studies and to characterize the optical properties of non-magnetic nanowires either containing a quantum dot or not.

The present work is organized in the following way: Chapter 1 is devoted to the basic properties of low-dimensional semiconductor structures and diluted magnetic semiconductors. The description of the experimental set-ups is also presented in this chapter.

Chapter 2 describes the observation of the magnetic polaron formation process in single CdMnTe quantum dots using magneto-optical spectroscopy and time-resolved spectroscopy. A review on existing theory is provided, outlining the difficulties to describe the magnetic properties of charged QD, and a new theoretical approach is proposed in order to overcome these difficulties. A numerical calculation based on this new theory is provided in order to estimate the parameters of MP formed in lens-shaped quantum dots.

In the Chapter 3, we will describe the first steps towards the studies of the MP in nanostructures with well controlled anisotropy. We will study the optical properties of non-magnetic ZnTe nanowires with and without CdTe insertion by means of micro-photoluminescence and cathodoluminescence. The influence of the strain on the photoluminescence energy is discussed for nanowires having a core-shell structure. The exciton confinement in a quantum dot inserted in a nanowire is investigated by analyzing the temperature variation of the photoluminescence. The single-photon source properties will be characterized by photon correlation measurements.

Chapter 1

Basic properties of DMS and experimental set-ups

1.1 CdTe/ZnTe semiconductor heterostructures

In this introduction chapter, we will recall the basic ideas which are necessary for a good understanding of this manuscript. First, we'll briefly describe the crystalline and electron band structure of the II-VI semiconductors and the influence of strain on the bands offsets. Then, we will give a few theoretical and experimental elements on diluted magnetic semiconductors.

1.1.1 Crystalline structure
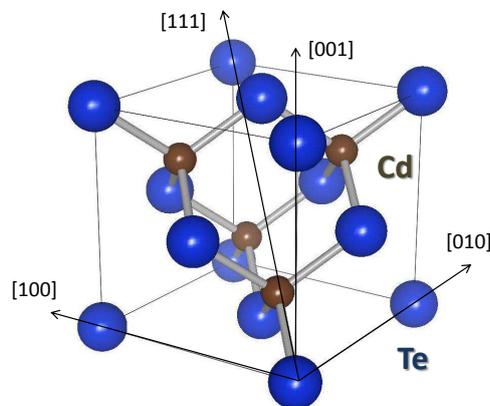
FIGURE 1.1: Zinc blende crystalline structure

The crystalline structure of cadmium telluride (CdTe) and zinc telluride (ZnTe) as well as the alloys of $Cd_{1-x}Zn_xTe$, $Cd_{1-x}Mg_xTe$ and $Cd_{1-x}Mn_xTe$ is a zinc blende structure (F-43m) (Fig.1.1). This structure consists of two interpenetrating face centered cubic sublattices with one shifted from the other by $1/4$ of the distance along the $\langle 111 \rangle$ direction. The first sublattice is filled with the element of the group II, whereas the second sublattice is filled with group VI elements (tellurium in our case). Lattice parameters of these materials are [16]:

$$
\begin{aligned}
a_{CdTe} &= 6.481 \text{ Å} \\
a_{ZnTe} &= 6.104 \text{ Å} \\
a_{MgTe} &= 6.42 \text{ Å} \\
a_{MnTe} &= 6.337 \text{ Å}.
\end{aligned}
\tag{1.1}
$$

The lattice parameter of ternary alloy depends on its composition x and can be estimated by a linear interpolation of the two binary alloys which it consists of. This is the Vegard's law [16].

1.1.2 Band structure

In solid-state physics, the electronic band structure (or simply band structure) of a solid describes those ranges of energy that an electron within the solid may have (called energy bands, allowed bands, or simply bands), and ranges of energy that it may not have (called band gaps or forbidden bands). II VI semiconductor materials are composed by two elements, each of them characterized by their 4 external levels (1 type s and 3 type p). Hybridization of these atomic orbitals result in 4 bounding states (1 s orbital and 3 p orbitals) and 4 antibonding states (1 s and 3 p orbitals). The type II element (Cd,Zn) has two electrons on its external layer and the type VI (Te) has 4 electrons. The 4 bonding orbitals are populated by the 6 electrons and form the valence band. The 4 antibonding orbitals are initially empty. The lowest empty state is the antibonding s orbital. This is the conduction band. More precisely, we call respectively the valence band and the conduction band the 3 bonding p orbitals and 1 antibonding s orbital. The description of exact calculation of the band structure in $\vec{k} \cdot \vec{p}$ approximation can be found in [17] and the result of such a calculation is presented in Fig.1.2. The semiconductors studied in present work have direct band gap. It means that the conduction and the valence band have a minimum and a maximum respectively in the center of the Brillouin zone

at $\vec{k} = 0$ (point Γ in Fig.1.2). The optical properties of the material are controlled by the bands symmetry at this point. Electrons, belonging to the the conduction band (Γ_6 symmetry), formed by the s antibonding orbital, have no angular momentum and their total angular momentum is $J = 1/2$. The valence band of Γ_8 symmetry is separated from the valence band of Γ_7 symmetry by the spin-orbit coupling Δ_{SO}. In CdTe $\Delta_{SO} = 0.9$ eV. Fourfold degenerate valence band Γ_8 is decomposed in two level groups: one of a $J = 3/2$ (heavy hole) and another of a $J = 1/2$ (light hole).

The parabolic approximation, also known as an effective mass approximation, consist
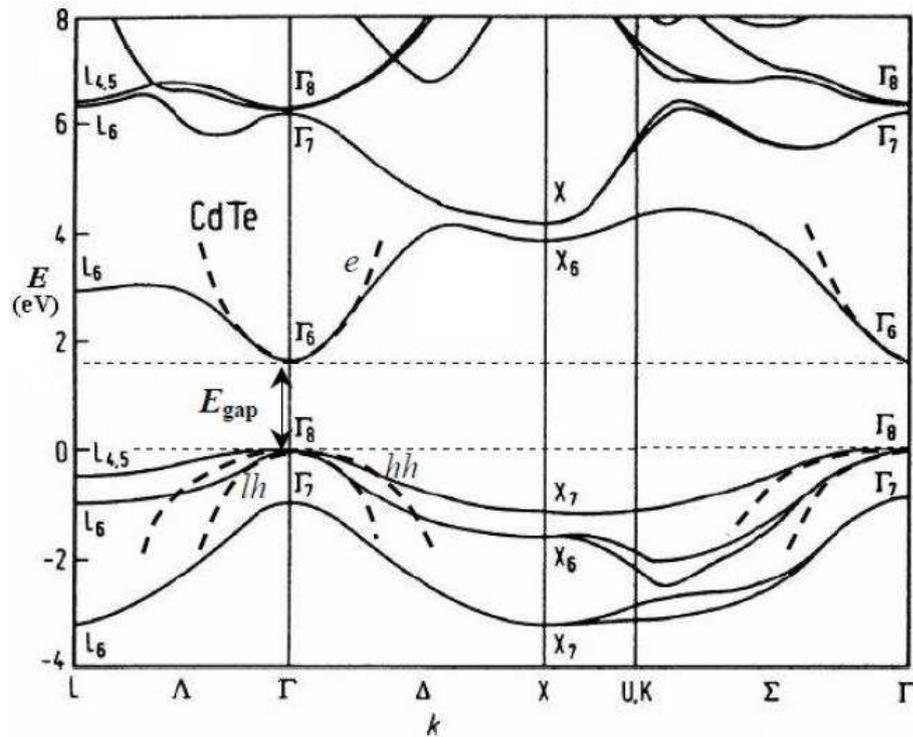
FIGURE 1.2: Electron bands structure of CdTe

of a development of the order 2 in k which allows the vicinity of Brillouin zone center to be taken into account. Hence, the dispersion of the bands is described by the relation:

$$E(\vec{k}) = E(\vec{k} = 0) + \frac{\hbar^2 k^2}{2m^*},\qquad(1.2)$$

where m^* is the effective mass. For the conduction band the effective mass of the electron is isotropic and is equal to

$$m^* = 0.1m_0,\qquad(1.3)$$

where m_0 is the free electron mass. It is more difficult to describe the valence band. With the effective mass approximation one obtains, on one hand, the different effective masses for the heavy hole and the light hole and, on the other hand, the mass which is not anymore isotropic and depends on the direction of $\vec{k}$. In $\langle 001 \rangle$ direction the effective masses of the heavy hole and the light hole are[18]:

$$m_{hh}^* = 0.6m_0, \ m_{lh}^* = 0.12m_0. \tag{1.4}$$

In the present work we will be interested as well in effective mass of the heavy hole in $\langle 111 \rangle$ direction[18]:

$$m_{hh}^* = 0.69m_0 \ m_{lh}^* = 0.11m_0. \tag{1.5}$$

The energy between the conduction and valence band is defined as the energy band gap
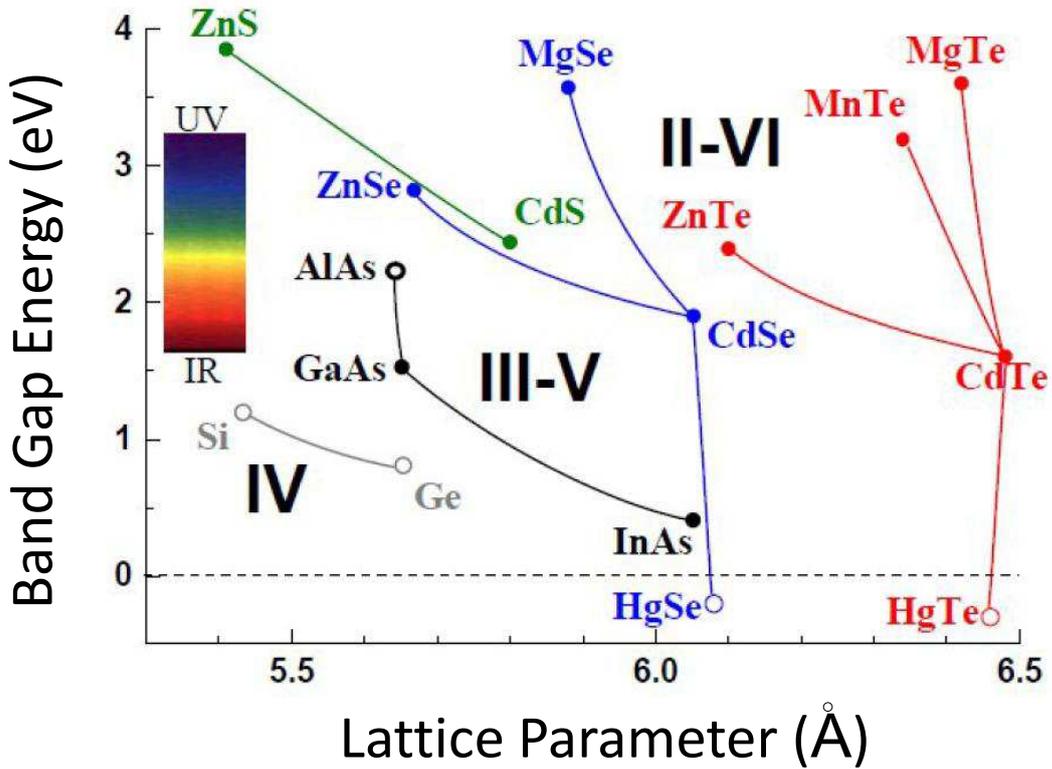
FIGURE 1.3: Band gap energy at $T = 4$ K as a function of the lattice parameter for different semiconductors. Filled and empty symbols correspond to the semiconductors with the direct and indirect band gap, respectively.

E_G. The values of E_G for some Te-based semiconductors at $T = 2$ K are [16]:

$$E_{G_{CdTe}} = 1606 \text{ meV}$$

$$E_{G_{ZnTe}} = 2391 \text{ meV}$$

$$\text{(1.6)}$$

$$E_{G_{MnTe}} = 3198 \text{ meV}$$

$$E_{G_{MgTe}} = 3600 \text{ meV}.$$

For the ternary alloys of the type $A_{1-x}B_x$Te, the band gap varies continuously by varying the composition x from 0 to 1 (see Fig.1.3).

The expressions, describing the variation of the band gap of Te-based semiconductors
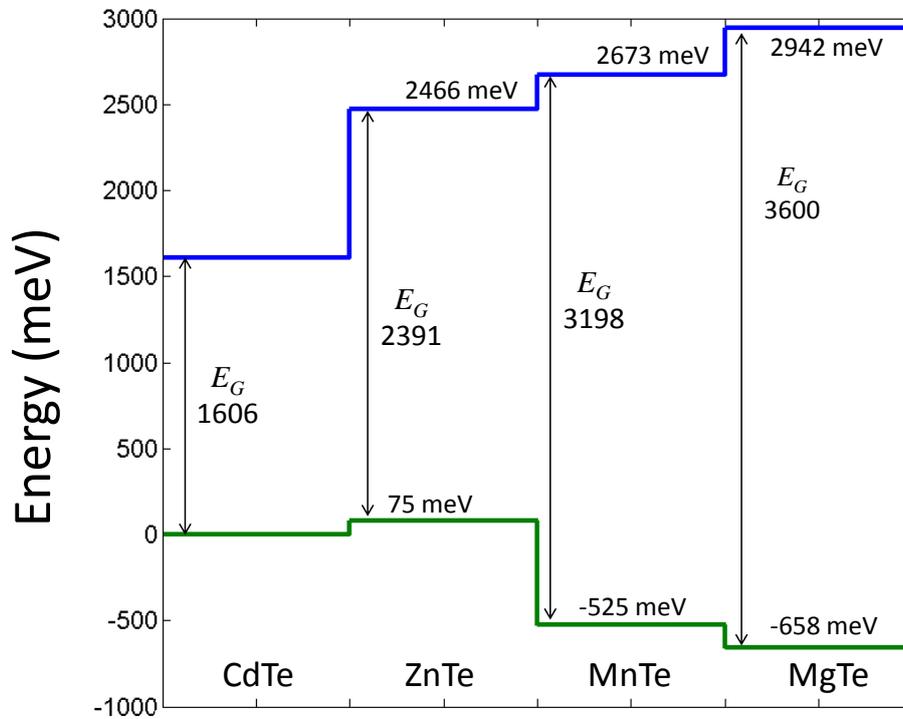
FIGURE 1.4: Relative offsets of some Te-based semiconductor compounds

at $T = 2$ K are following (in meV) [16]:

$$E_{G_{Cd_{1-x}Zn_xTe}} = 1606 + 525x + 260x^2$$

$$E_{G_{Cd_{1-x}Mg_xTe}} = 1606 + 1700x + 300x^2$$

$$E_{G_{Cd_{1-x}Mn_xTe}} = 1606 + 1592x \qquad (1.7)$$

$$E_{G_{Zn_{1-x}Mg_xTe}} = 2391 + 959x + 250x^2$$

$$E_{G_{Zn_{1-x}Mn_xTe}} = 2391 + 537x + 270x^2.$$

For the comprehensive studies of Te-based semiconductor heterostructures optical properties, one should know the relative offsets of conduction and valence bands. In Fig.1.4 offsets values of the valence bands and conduction bands of some unstrained Te-based semiconductor compounds are compared to CdTe. In this work we are interested in CdTe/ZnTe heterostructures. It can be seen from the figure that bands offsets between these two materials have a type-II alignment in the absence of strain.

1.2 Optical properties of semiconductor heterostructures of reduced dimensionality

1.2.1 Different types of semiconductor heterostructures

There are several possible ways of limiting the motion of charge carriers along the spatial directions. By creating small particles of semiconductor materials (as for the colloidal quantum dots), or by inserting a small gap semiconductor in a larger gap semiconductor, one can realize different types of carrier confinement: quantum wells, quantum wires or quantum dots. Thus, by reducing the confinement dimensions from bulk to the order of the exciton Bohr radius, one confines the exciton and make its energy discrete. The full calculation of the exciton energy in a quantum dot requires to take into account the confinement energy of the hole and the electron, to consider the effective mass anisotropy of the hole, strain contributions, and an evaluation of the exciton binding energy. This calculation is relatively challenging and is most commonly done by a variational calculation. The result is highly influenced by the confinement potential considered. The most simple and efficient are the finite or harmonic confinement, but as the real confinement potentials of the quantum dots are rarely well known they only provide approximated values.

One can experimentally probe the confinement properties by spectrally analyzing the photons coming from the recombination of the exciton. As in a quantum dot it has a discrete density of states, one expect a very sharp band emission energy. As electrons and holes are fermions of total angular momentum projection $\pm 1/2$ or $\pm 3/2$, one can put at maximum 2 carriers on the same confined level. The resulting combinations
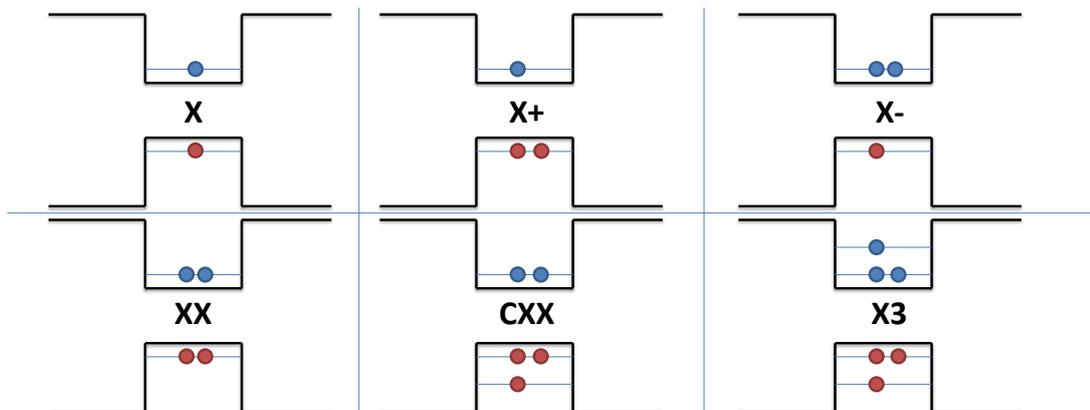
FIGURE 1.5: Different types of exciton complexes

of charges in the quantum dots are compiled in Fig.1.5 The exciton can coexist with an extra carrier: it is the charged exciton. When the exciton recombination happens in the presence of an extra carrier, the emission energy is shifted because of Coulomb interaction between the exciton and the charge. Thus one can separate spectrally the emission of the different possible combinations of charges in the quantum dot. The same way, the biexciton is the presence of two excitons at the same time in the quantum dot and the charged biexciton is composed by two excitons and an extra carrier in the P shell.

1.2.2 CdTe/ZnTe nanostructures bands offsets: influence of strain and Mn incorporation

The dramatic changes in the structure of energy bands happen during the formation of low-dimensional CdTe/ZnTe heterostructures. Lattice parameters mismatch ($\Delta a/a = -0.06$) induces the compressive strain in CdTe layer during the growth on a fully relaxed ZnTe substrate. The deformation of the CdTe crystalline structure results in the shift of the conduction and valence band energies:

$$\Delta E_C = a_c(2 - R_{001})\varepsilon_{||}$$
$$\Delta E_V^{hh} = a_v(2 - R_{001})\varepsilon_{||} + b(1 + R_{001})\varepsilon_{||}, \tag{1.8}$$

where $\varepsilon_{||} = \Delta a/a$ - lattice mismatch, a_c, a_v and b are the deformation potentials [19] defined by

$$a_c = \frac{\partial E_c}{\partial(\ln V)} \ ; \ a_v = \frac{\partial E_v}{\partial(\ln V)}, \tag{1.9}$$

and $R_{001} = 2c_{12}/c_{11}$ is the relaxation coefficient for $\langle 001 \rangle$ growth direction.

The values of deformation potentials for CdTe and ZnTe are given in the table together with stiffness constants:

	c_{11}(GPa)	c_{12}(GPa)	c_{44}(GPa)	a_c(eV)	a_v(eV)	a_g(eV)	b(eV)	R_{001}
CdTe	53.51[20]	36.81[20]	19.94[20]	-2.687[19]	0.756[19]	-3.44[19]	-0.99[21]	1.38
ZnTe	73.7[22]	42.3[22]	32.1[22]	-3.64[19]	0.83[19]	-5.3[19]	-1.3[19]	1.14

Hence, by the shift of the energy of the conduction and valence band induced by strain, we can recalculate the relative band offsets . This is illustrated in Fig.1.6. From initially type-II bands offsets between unstrained CdTe and ZnTe (Fig.1.6(a)), the strain leads

to the transformation into a type-I alignment (Fig.1.6(b)).

Replacing cations such as Cd with a paramagnetic ion such as Mn in the same crystallographic structure does not markedly disturb the semiconductor properties of the material [12]. The energy gap increases but the conduction and valence bands conserve their symmetry and character as in nonmagnetic semiconductor alloy crystals. Insertion of Mn inside CdTe changes the band offsets: on the one hand it increases the band gap of (Cd,Mn)Te, which depends on the Mn concentration x according to Eq.1.7. On the other hand insertion of Mn in CdTe partially relaxes the strain, which induces further decrease of bands offsets. Hence, with an increasing Mn concentration the bands alignment tends to return to the type-II.

The calculation of the bands offsets for the ternary alloy is performed in the same way
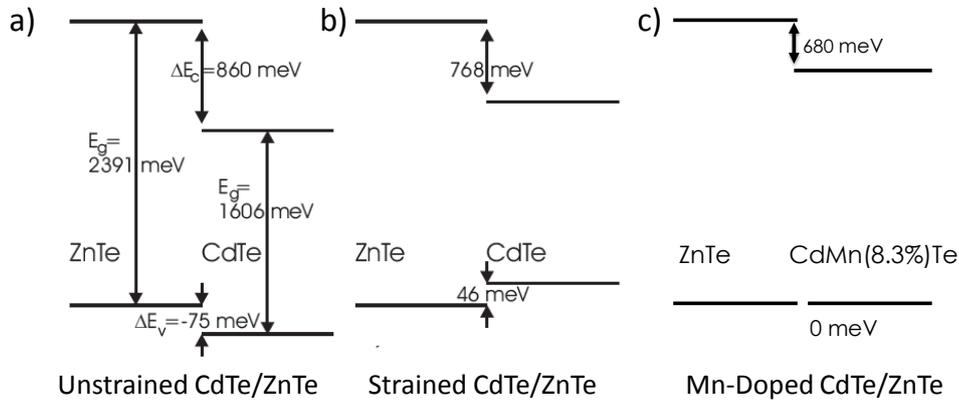
FIGURE 1.6: a) CB and VB offsets of the unstrained CdTe/ZnTe. b) CB and VB offsets of the strained CdTe/ZnTe. c) CB and VB offsets of the strained Mn-doped CdTe/ZnTe (8.3% Mn).

as for the binary alloy with the only difference of the lattice mismatch determination. It is defined by

$$\Delta a = a_{ZnTe} - a(x)a_{CdMnTe}(x). \tag{1.10}$$

Performing the calculation of conduction band and valence band energies for different Mn concentrations, we show that at 8.3% Mn concentration the valence bands offset between CdMnTe and ZnTe is equal to zero (Fig.1.6(c)). Hence, there is no confinement potential for the hole induced by the crystalline structure and the hole is confined only due to the Coulomb interaction with an electron.

1.3 Diluted magnetic semiconductors

Diluted Magnetic Semiconductors (DMS) form a new class of magnetic materials, which fill the gap between ferromagnets and semiconductors. In the early literature these DMS were often named semimagnetic semiconductors, because they are midway between non-magnetic and magnetic materials. DMS are semiconductor compounds ($A_{1-x}Mn_xB$) in which a fraction x of the cations is substituted by magnetic impurities, thereby introducing magnetic properties into the host semiconductor AB. This makes a great difference with semiconducting ferromagnets, i.e., ferromagnetic materials exhibiting semiconductor-like transport properties, which have been known for some time. A DMS is expected to retain most of its classical semiconducting properties, and to offer the opportunity of a full integration into heterostructures, including heterostructures with the host material. The great challenge and ultimate goal of the research in this field is to obtain DMS ferromagnetic at room temperature, which can be integrated in semiconductor heterostructures for electronic or optoelectronic applications. This is one of the key issues for the advent of spintronics devices.

1.3.1 Semiconductor in an applied field: Zeeman effect

The ground state of the quantum dot has a two-fold degeneracy by spin. Hence, the application of the magnetic field allows one to increase this degeneracy. The Hamiltonians, which describe the interaction of the magnetic field with an electron and a hole are:

$$\mathcal{H}_e = g_e \mu_B \vec{B} \cdot \vec{\sigma_e},$$
$$\mathcal{H}_{hh} = g_{hh} \mu_B \vec{B} \cdot \vec{\sigma_h} \tag{1.11}$$

where $\vec{\sigma_e}$ and $\vec{\sigma_h}$ are the spin operators of an electron and a hole, respectively. We consider only the heavy holes with kinetic moment $J_{hh} = \pm\frac{3}{2}$ and with spin projection $\sigma_{h_z} = \pm\frac{1}{2}$. g_e and g_{hh} denote the Landé factors of electrons and holes, respectively. $\mu_B = \frac{e\hbar}{2m_0}$ is the Bohr's magneton. Experimentally measured values of Lande factors in CdTe QW are $g_e = -1.4$ (compare to the value of the bulk CdTe $g_e = -1.6$ [23]) and $g_{hh} = -0.3$[24]. The observed values of Lande factors in CdTe self-assembled quantum dots are $g_e \approx -0.4$ and $g_{hh} \approx +0.4$ [25], but these values can vary from dot to dot.

One obtains, hence, the splitting of the conduction band by electron spin projection $\sigma_e = \pm 1/2$ and of the valence band by the heavy hole kinetic moment J_{hh} (see Fig.1.7).
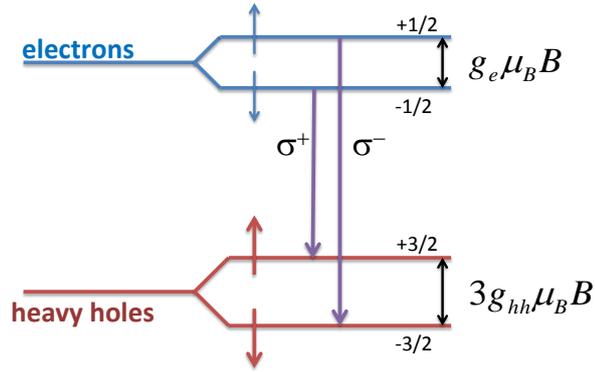
FIGURE 1.7: Zeeman effect in a semiconductor

This is the Zeeman effect. The two allowed transitions of bright excitons are circularly polarized and have different energy. The separation between two degenerated levels increases with an increasing field not more than by 0.1 meV/T. We will see that this effect is very weak comparing to the Giant Zeeman effect and we can, therefore, neglect its contribution in this work.

1.3.2   Introducing Mn in II-VI semiconductor

The Diluted Magnetic Semiconductors (DMS) are the semiconductors in which we introduce a certain number of magnetic atoms [16] (see Fig.1.8). In particular, we can substitute the ions of manganese at the places of cations in the II-VI semiconductor compound without simultaneous doping of the material (contrary to the case of III-V semiconductors). The electronic structure of a Mn atom is $[Ar]3d^54s^2$: the two valence electrons (similarly to the case of Cd) are brought together with the local spin $S = 5/2$ provided by $d-$shell electrons.

The interaction between Mn atom and an applied external magnetic field is described by the Hamiltonian:

$$\mathcal{H}_{Mn} = -\vec{\mu}\vec{B} = g_{Mn}\mu_B\vec{B}\vec{S} = g_{Mn}\mu_B B S_z, \qquad (1.12)$$

where $\vec{S}$ is the spin operator of Mn (and $\vec{\mu}$ is associated magnetic moment). g_{Mn} is the Lande factor given by the Lande equation:

$$g = 1 + \frac{J(J+1) + S(S+1) - L(L-1)}{2J(J+1)}, \qquad (1.13)$$
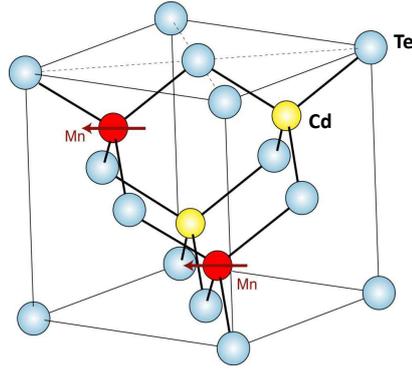
FIGURE 1.8: Crystalline structure of the diluted magnetic semiconductor (Cd,Mn)Te

where $J = 5/2$ is the kinetic moment of Mn atom, $L = 0$ orbital moment and $S = 5/2$ its spin. These give $g_{Mn} = 2$ and is confirmed experimentally. The average magnetization of Mn $\langle S_z \rangle$ is calculated as an average value of the spin projection on the axis (z) corresponding to the direction of the applied field. Assuming the paramagnetic behavior of Mn in an applied field, the calculation of statistical partition functions gives:

$$\langle S_z \rangle = -\frac{5}{2} B_{\frac{5}{2}} \left(\frac{\frac{5}{2} g_{Mn} \mu_B B}{k_B T} \right), \tag{1.14}$$

where $B_S(x)$ denotes the Brillouin function defined by:

$$B_S(x) = \frac{2S+1}{2S} \coth \left(\frac{2S+1}{2S} x \right) - \frac{1}{2S} \coth \left(\frac{1}{2S} x \right). \tag{1.15}$$

Assuming that each cation site of the lattice, defined by $\vec{R}$, is occupied whether by one Mn ($x_i = 1$) whether by on Cd ($x_i = 0$), the projection on the axis z of the total magnetization of the system is given by:

$$M_z(\vec{r}) = -\sum_i x_i \delta(\vec{r} - \vec{R}) g_{Mn} \mu_B S_{zi}. \tag{1.16}$$

We use then the mean field treatment and the virtual crystal approximation to replace S_{zi} by $\langle S_z \rangle$ and x_i by x which denotes the average number of cation sites occupied by Mn and the sum of Dirac functions is replaced by the volume density of cation sites N_0. We obtain:

$$\langle M_z \rangle = g_{Mn} \mu_B x N_0 \frac{5}{2} B_{\frac{5}{2}} \left(\frac{\frac{5}{2} g_{Mn} \mu_B B}{k_B T} \right) \tag{1.17}$$

With an increasing Mn concentration, deviations from the Brillouin function arise due to anti-ferromagnetic interaction of nearest-neighbor Mn atoms. In thermal equilibrium, the magnetization can be expressed through an empirical modified Brillouin function introduced by J.Gaj, R.Planel, and G.Fishman[26]:

$$\langle M_z \rangle = N_0 x_{eff} g_{Mn} \mu_B \frac{5}{2} B_{\frac{5}{2}} \left(\frac{\frac{5}{2} g_{Mn} \mu_B B}{k_B (T + T_{AF})} \right),$$ (1.18)

where x_{eff} is the effective Mn concentration and T_{AF} is the effective temperature introduced in the Brillouin function in order to take into account the anti-ferromagnetic interaction between nearest-neighbor Mn atoms. The susceptibility may be written as

$$\chi_V = \frac{N_0 x_{eff} (g_{Mn} \mu_B)^2 S(S+1)}{3 k_B (T + T_{AF})}.$$ (1.19)
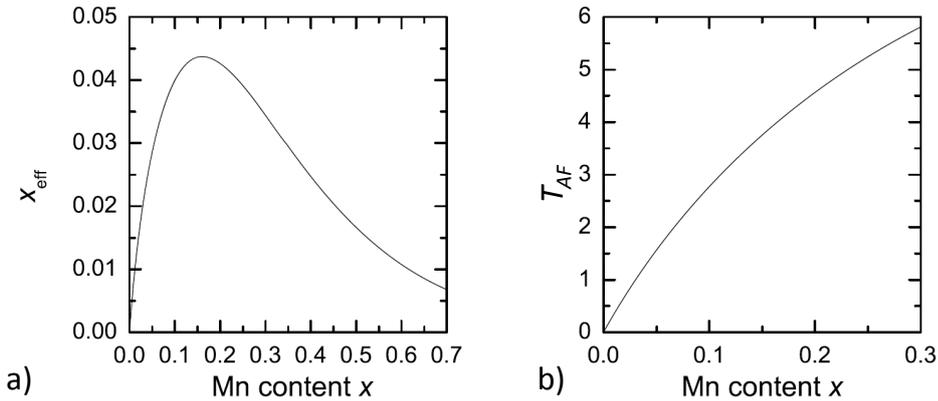
FIGURE 1.9: Variation of the effective concentration x_{eff} and of the antiferromagnetic interaction effective temperature T_{AF} as a function of Mn concentration x

1.3.3   DMS in magnetic field: Giant Zeeman effect

In DMS the carriers are not only exposed to the direct interaction with an applied magnetic field, but as well to the interaction with magnetic ions which in turn interact with an applied field. This exchange interaction between carriers and Mn ions is called an $sp - d$ interaction. The sd exchange interaction is a simple example of direct exchange interaction. Due to Pauli exclusion principle, two electrons with the same spin avoid each other, thus their (repulsive) Coulomb interaction energy is reduced, while electrons

with opposite spins can approach each other. The sd exchange interaction is thus ferromagnetic. When the d levels fall within the valence band, as is the case in IIVI based DMS, pd hybridization leads to an additional exchange interaction mechanism called kinetic exchange, with an antiferromagnetic sign.

The Hamiltonian of an exchange interaction between an electron with spin $\vec{\sigma}$ and variable position $\vec{r}$ and a Mn atom with spin $\vec{S_i}$ located at the cation site $\vec{R_i}$ is:

$$\mathcal{H}_{e-Mn} = -J_{s-d}\delta(\vec{r} - \vec{R_i})\vec{\sigma}\vec{S_i}, \tag{1.20}$$

where J_{s-d} is the exchange integral between the states $3d$ of Mn and $s-$electrons of the conduction band. Taking the average value $|s\rangle$ in the orbital part of the $s-$electrons wave function, one obtains the Hamiltonian of the Heisenberg type. We denote

$$\alpha = \left\langle s \left| J_{s-d}\delta(\vec{r} - \vec{R_i}) \right| s \right\rangle, \tag{1.21}$$

where α is the statistical average of the $s - d$ interaction. Its value is defined for each material. One, therefore, obtains:

$$\mathcal{H}_{e-Mn} = -\alpha\vec{\sigma_e}\vec{S_i}\delta(\vec{r} - \vec{R_i}), \tag{1.22}$$

Calculating the sum over the ensemble of Mn ions and using the two approximations of the mean field and a virtual crystal one obtains for the field applied along z-axis:

$$\mathcal{H}_{e-Mn} = -\alpha\sigma_{e_z}x_{eff}N_0\left\langle S_z\right\rangle = \alpha\sigma_{e_z}\frac{\left\langle M_z\right\rangle}{g_{Mn}\mu_B} \tag{1.23}$$

For the holes the exchange integral between the states $3d$ of Mn and holes p of the valence and is denoted as β. Its value is defined as well for each material [16]. β is defined using the spin operator of the heavy hole with projection $\sigma_{h_z} = \pm 1/2$ and not its full kinetic moment. It gives:

$$\mathcal{H}_{hh-Mn} = -\beta\sigma_{h_z}x_{eff}N_0\left\langle S_z\right\rangle = \beta\sigma_{h_z}\frac{\left\langle M_z\right\rangle}{g_{Mn}\mu_B} \tag{1.24}$$

The values of $N_0\alpha = 220$ meV and $N_0\beta = -880$ meV are known from literature [16, 26]. Their signs mean that an exchange interaction electron-Mn is ferromagnetic and hole-Mn is antiferromagnetic. The splittings of the conduction and the valence bands are

given by:

$$\Delta_e = \alpha \frac{\langle M_z \rangle}{g_{Mn}\mu_B}$$
$$\Delta_{hh} = \beta \frac{\langle M_z \rangle}{g_{Mn}\mu_B}$$

(1.25)

Hence, the transition energies evolve with an increasing magnetic field according to the Brillouin function 1.18. *The splitting of bands is proportional to the Mn magnetization.* This is the key feature of diluted magnetic semiconductors. Conduction and valence
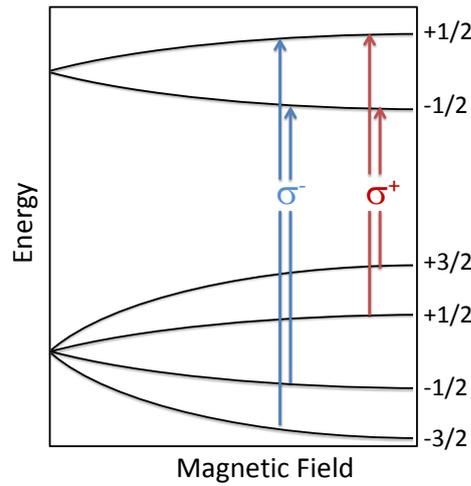
FIGURE 1.10: Scheme of band to band transitions close to band gap energy, and their polarization, in the Faraday configuration. The spin states of the electron in the conduction band, and hole in the valence band, are indicated.

band splittings induced by the Giant Zeeman effect scale with Mn concentration. The typical values of such splitting observed in the present work are about 50 meV which allows us to neglect the influence of the usual Zeeman effect.

1.4 Experimental set-up

There are several types of experiments which have been done in present work: magneto-optical studies, time-resolved measurements, photon correlation measurements and cathodo-luminescence studies. In this section we will describe in details the set-ups which have been used.

1.4.1 Micro-photoluminescence set-up

DMS quantum dots have been studied in confocal micro-photoluminescence set-up under applied magnetic field. The samples are placed on the top of the column of piezo-positioners which allow a controlled displacement in plane (x,y) and focal (z) directions with the step of 10 nm. The column of positioners together with the microscope lens (20X magnification, 0.4 numerical aperture, 3 mm working distance) makes part of the insert depicted in Fig.1.11. The insert is placed in the helium-flow cryostat (Oxford Spectromag). This cryostat allows us to control the temperature between 300 K and 4.2 K. The superconducting coil allows us to apply an external magnetic field to our samples up t 11 T. Only the Faraday geometry is possible in this type of the cryostat.

Several cw lasers have been used for the photoluminescence excitation: Nb:YAG 532 nm laser used for excitation below the ZnTe barrier energy (2391 meV or 518 nm), 405 nm and 488 nm diode lasers for excitations above the barrier. Spatial filtering have been performed in order to obtain the homogeneous laser spot which is then focused on the sample surface. Photoluminescence is collected by the same microscope as used for the excitation and focused on the entrance slits of the spectrometer. The laser light reflected from the sample surface is filtered by the low-pass filter. In order to perform the fine adjustment of the focal distance and laser spot position on the sample surface, the imaging system has been used. The image of the sample surface is obtained by focusing the white light on it and projecting the reflected light on the video camera which is movable and can be placed behind the entrance slits.

The analysis of the circular polarization degree of emitted light is performed by a combination of quarter-wave plate with a Wollaston prism placed in front of the entrance slits of the monochromator. This prism separates the incoming beam in two spatially separated linearly polarized beams with different orientation of the polarization horizontal and vertical. Projecting these two beams on the nitrogen-cooled CCD camera allows
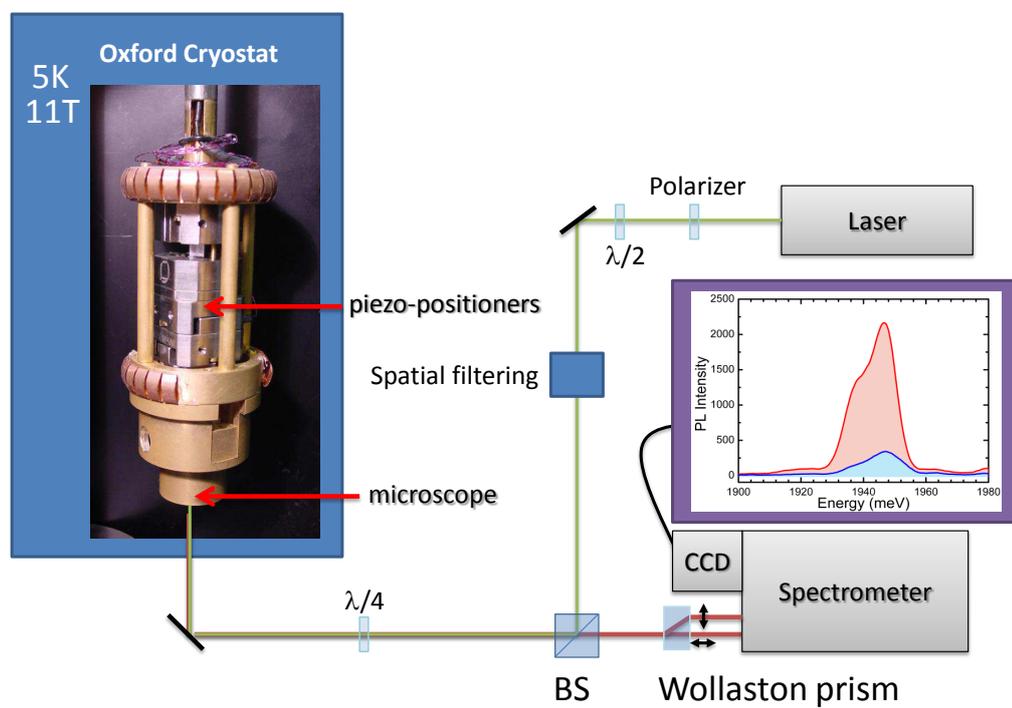
FIGURE 1.11: Scheme of the set-up for magneto-optics
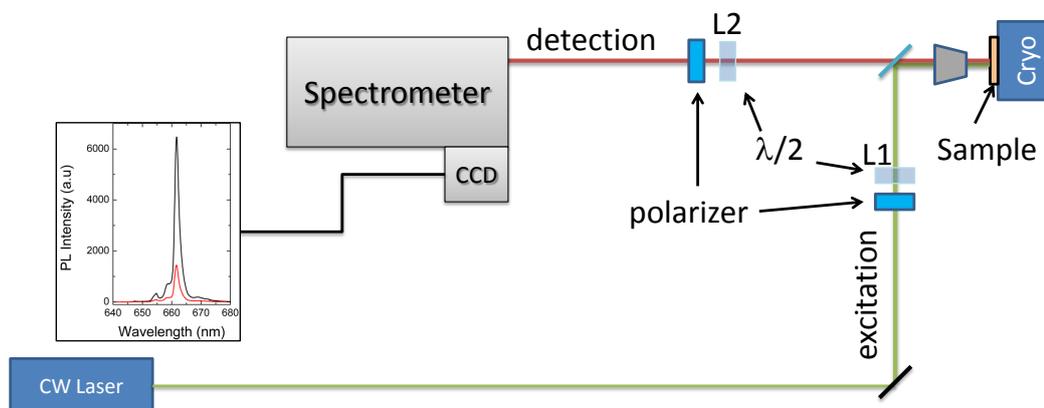
FIGURE 1.12: Scheme of nanowire photoluminescence polarization measurement set-up

us to record spectra in both polarizations simultaneously. The spectral composition of the photoluminescence is resolved by the Jobin-Yvon HR460 spectrometer with gratings 600 gr/mm or 1800 gr/mm. The spectral resolution of the set-up is 30 µeV.

For the applied electric field studies, samples are placed in the helium-cooled cold-finger cryostat (Janis-ST500). It provides a control on temperature between 300 K and 5 K. This cryostat has been used as well for nanowires micro-photoluminescence and polarization studies described in Sec.3.2.4 and Sec.3.3.3. In this case the photoluminescence is collected by the microscope with 100X magnification, 0.55 numerical aperture and 1 cm working distance.

Excitation laser polarization orientation is rotated by the half-wave plate L1 in Fig.1.12 and linear polarization of the nanowire photoluminescence is analyzed by L2 half-wave plate placed in front of the polarizer.

1.4.2   Cathodo-luminescence set-up

CL images of the NWs, studied in Chapter 3, deposited on the silicon substrate were recorded using an FEI Quanta 200 SEM equipped with a CL accessory and a low temperature Gatan stage able to cool down the sample to 5 K [27].

The single NW was excited by an electron beam of 30 keV and a current of typically
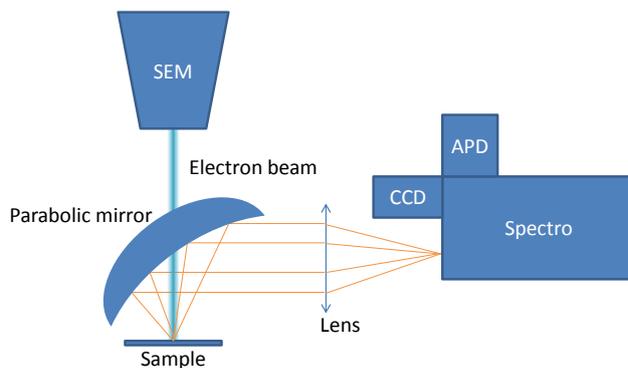
FIGURE 1.13: Scheme of the cathodo-luminescence set-up

250 pA. In comparison with high resolution field-effect SEM images, the spatial resolution of the CL images is limited by the low spatial resolution of the thermionic SEM. The CL light was collected by a parabolic mirror and sent to an avalanche photo diode synchronized with the electron beam scan.

For small objects such as NWs, the CL excitation efficiency is more than three orders of magnitude lower than the μPL one. The ratio between the electron-hole excitation density in CL experiments and in μPL is given by $\frac{P_e/3}{P_{ph}} \times \frac{\eta_e}{\eta_{ph}}$. Here $P_e \simeq 2\ \mu\text{W}/\mu\text{m}^2$ is the mean value of the electrical power density of the CL electron beam when recording a typical image, from which is it generally considered that about one third gives rise to luminescence. $P_{ph} \simeq 25\ \mu\text{W}/\mu\text{m}^2$ is the laser power density used in the μPL experiment. The excitation in μPL is non-resonant so that we consider that a good order of magnitude of the absorption by an object of thickness D (the NW diameter) is given by $\eta_{ph} = \alpha_{ph}D$, where α_{ph} is an absorption coefficient specific for each material. For the case of a ZnTe NW, $\alpha_{ph} = 4 \times 10^4\ \text{cm}^{-1}$ [28]. An incident electron has a very small probability to be scattered and create an electron-hole pair in the NW; most of its energy is deposited in the substrate where it is scattered many times and propagates randomly. As a result, the creation probability of electron-hole pairs in the NW is also proportional to D, and much smaller, with an $\alpha_e = 4 \times 10^2\ \text{cm}^{-1}$. This low excitation density prevents any spectral analysis of the CL images for the small NWs studied in Sec.3.2.5.

Chapter 2

Magneto-optical properties of CdMnTe self-organized quantum dots

In this Chapter we will present the results on Exciton Magnetic Polaron (EMP) formation in (Cd,Mn)Te quantum dots, grown by molecular beam epitaxy on a non magnetic ZnTe buffer layer, with different concentration of Mn (from 2 to 10%). First, we will demonstrate that a negatively charged exciton can be observed in the single dot photoluminescence spectrum and that the formation of the magnetic polaron results in a larger energy shift compared to the one observed for the magnetic polaron formed with the neutral exciton. Second, it will be demonstrated that the widely used theoretical "exchange box" model can't explain the observed difference in energies due to its oversimplified nature. The explanation will be provided in terms of the new theoretical approach based on the realistic envelope functions of electrons and holes, interactions between them and with magnetic medium. This approach will be used as the basis of the numerical model with which the characteristic parameters of the magnetic polaron will be retrieved and compared to the experimentally observed values. The dependence of EMP parameters on Mn concentration will be demonstrated. The magnetic polaron formation dynamics will be discussed.

2.1   Introduction

A magnetic polaron is a complex, consisting of the carrier spin coupled with localized spins of surrounding magnetic atoms by strong exchange interactions [16]. These interactions result in a ferromagnetic alignment of the localized spins in the vicinity of the carrier. Usually, the total magnetic moment of such a system of correlated spins may be as great as hundreds of Bohr magnetons at low temperatures[29]. Such a large value is explained by a comparatively large field created by a localized carrier on the neighboring magnetic ions (~ 1T) and by a large number of these ions. The first theoretical studies of the magnetic polarons were performed by De Gennes in 1960 [30].

Experimentally the existence of magnetic polarons was established via transport and magnetization measurements in magnetic semiconductors like EuO [31]. But a detailed information about the polaron energy spectrum and its spin structure was not available from these experiments. Diluted magnetic semiconductors provided a possibility of the magnetic polarons study by optical methods. II-VI DMS with magnetic Mn^{2+} ions, like (Cd,Mn)Te, (Cd,Mn)Se and (Zn,Mn)Se, were widely used for these studies.

There are several types of magnetic polarons depending on the way of initial charge carrier localization. The free magnetic polaron (FMP) consists of a carrier trapped, via the exchange interaction, in a magnetic potential well created by local alignment of spins of magnetic atoms. The problem of the stability of free magnetic polarons was first analyzed by Kasuya et al. for 3D systems [32] and by Ryabchenko and Semenov for low-dimensional systems [33]. Their analysis shows that the polaron energy is determined by a balance of two terms of opposite sign: a positive kinetic energy due to carrier localization, and a negative energy due to the exchange well. The experimental demonstration of the free magnetic polaron formation has been first performed in [34] for CdTe/(Cd,Mn)Te quantum wells.

Bound magnetic polaron (BMP), i.e. a MP formed by carriers localized on impurities, have attracted the most experimental and theoretical efforts before 1988. The carrier lifetime on the impurity center is usually much longer than the characteristic times of spin relaxation in the magnetic polaron allowing polarons to reach their equilibrium states. Optical experiments have given the most convincing evidence for the existence of BMP in DMS. Two techniques are used: spin flip Raman scattering (SFRS) [35] and luminescence [36].

When observable, SFRS gives detailed information concerning the BMP whose interpretation is relatively straightforward since the center under study involves a single carrier plus associated Mn^{2+} spin cloud. SFRS has only been seen in donor-BMP (i.e., electrons, bound to donors) where polaron effects are weak. The observation of SFRS from the more strongly coupled acceptors may be precluded, in cubic crystals, by the complexity of the valence band [37].

Luminescence lines that exhibit BMP effects are, in contrast, the result of recombination by complexes, such as excitons bound to impurities (a three body problem): an acceptor-bound exciton (A^0X) and a donor-bound exciton (D^0X). The identifications are made by comparing alloy luminescence spectra to that of the non-magnetic binary compound. The energy, shape, temperature variation, and magnetic field variation of these lines give microscopic information concerning these centers. For example, in contrast to the pure CdTe case, the A^0X binding energy is a rapidly varying function of temperature in the magnetic alloys; furthermore, at low temperatures it exceeds that in pure CdTe by a sizable factor in the more concentrated alloys. Such large temperature variations of impurity energies have been assigned to BMP formation around the bound exciton complex by Golnik et.al. in work [29]. The main features of bound magnetic polarons are fairly well understood (for review see [38]).

Experimental findings on exciton magnetic polarons (EMPs) [34, 36, 40, 41], whose formation is schematically displayed in Fig.2.1, rose new questions related to localization conditions of excitons and dynamics of spin organization in the polaron formation process. These specific features distinguish the exciton magnetic polarons from the bound magnetic polarons:

(i) The localization area and the energy of EMP ground state are not determined by the Coulomb potential of the impurity center, but depend on the exciton localization or self-localization conditions. In DMS, the exciton localization is determined by both magnetic and nonmagnetic fluctuating potentials. In turn the EMP formation, which is accompanied by a decrease of the exciton energy, can be considered as an additional localization process and, hence, can affect the exciton mobility in the crystal.

(ii) The radiative and non-radiative recombination limits the exciton lifetime. In II-VI semiconductors the EMP formation time strongly depends on Mn concentration: from the order of nanoseconds at low Mn concentration, it rapidly decreases with an increasing concentration and becomes comparable with the exciton lifetime at high concentrations
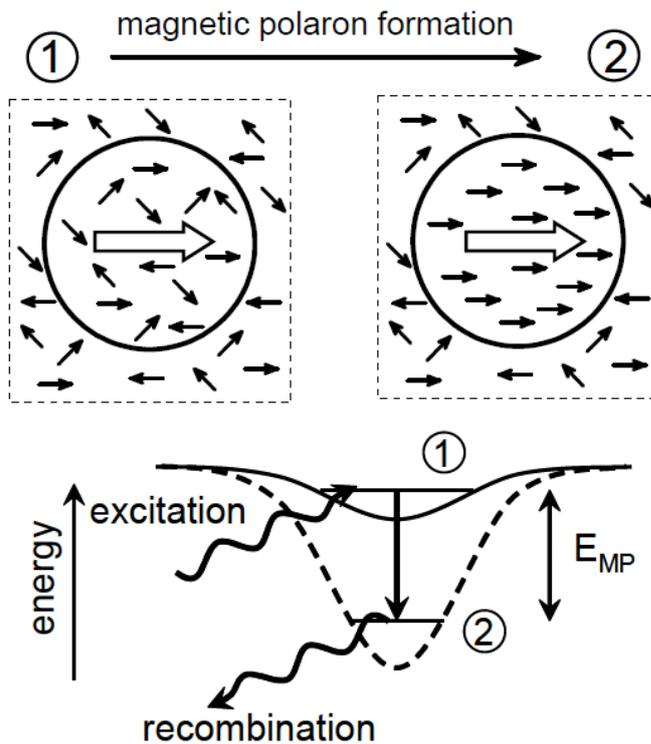
FIGURE 2.1: Schematic presentation of the exciton magnetic polaron formation in diluted magnetic semiconductors[39]. After localization of the photogenerated exciton in the confining potential of the quantum dot (state 1, fluctuation regime) the exciton, during the characteristic time τ_f aligns ferromagnetically the Mn spins inside its orbit and decreases its energy by forming a magnetic polaron in the collective regime (state 2). E_P is the energy of magnetic polaron. Exciton lifetime is limited by recombination.

($x > 20\%$ in bulk). Hence, the process of the magnetic polaron formation can be interrupted by exciton recombination before the polaron reaches its equilibrium energy. Exciton localization conditions, temperature and external magnetic fields influence the dynamics of magnetic polaron formation. The exchange energy gained in the process of the polaron formation depends on the Mn concentration (this dependence is nonlinear and nonmonotonic because of antiferromagnetic coupling of nearest-neighbor Mn-spins [16]).

Modern semiconductor technologies, such as molecular-beam epitaxy and colloidal synthesis, allow one to fabricate different types of DMS heterostructures. For instance, quantum wells (QW) and superlattices (SL) containing thin layers of diluted magnetic semiconductors; self-assembled quantum dots (QDs) which are formed by a small amount of DMS material surrounded by nonmagnetic barriers, and colloidal quantum dots which may have a DMS core and a nonmagnetic shell. The formation of the exciton magnetic

polaron has been, therefore, extended from the bulk II-VI DMS [42, 43] to 2D quantum wells and super-lattices[44–50]. Most of the recent results on EMP formation studies have been obtained for DMS self-assembled [14, 51–53] and colloidal quantum dots [54]. In the latter work the largest effective field of the exchange interaction between Mn atoms and injected exciton has been reported (75 Tesla). For comparison, the typical values obtained for self-assembled quantum dots do not exceed 4 Tesla [14, 51]. The influence of the Mn concentration in QDs on the parameters and the dynamical properties of magnetic polaron is only reported in work [53].

These works considered only the magnetic polaron associated with a neutral exciton, i.e. one electron and one hole confined in the quantum dot. It is very interesting, therefore, to study the possible modification of the magnetic polaron formation process by increasing the number of charges. Negatively and positively charged excitons (two electrons and one hole ore two holes and one electron, respectively), biexcitons and, sometimes, triexcitons are observed in different non-magnetic semiconductor heterostructures. But for the case of the DMS heterostructures such an observation has never been reported. In this work, new results on magnetic polaron formation associated with a negatively charged exciton in a single DMS quantum dot will be presented, demonstrating a larger polaron energy compared to the one of the neutral exciton magnetic polaron. This may seem unexpected as the spin of two electrons forming the negatively charged exciton are anti-parallel and, therefore, compensate each other, leaving only the spin of a hole to interact with spins of magnetic atoms. The widely used theoretical "exchange box" model is not able to explain these results due to its oversimplified approach. The goal of this chapter is to present these experimental results and to find an explanation of the observed experimental results by applying a more general theoretical approach which accounts the real form of the envelope function of the charge carriers. The efficiency of this new theoretical model will be confirmed by a numerical calculation of the magnetic polaron energy based on the charge carriers envelope functions calculated from the geometrical parameters of the quantum dot. The estimation of the minimal Mn concentration needed in order to observe the formation of the magnetic polaron will be discussed.

2.2   Exciton Magnetic Polaron formation

2.2.1   Exciton Magnetic Polaron formation dynamics

The formation of the exciton magnetic polaron passes through two principal stages: initial correlation and ferromagnetic alignment which can be interrupted by the exciton recombination. In Fig.2.2 these stages are depicted schematically.

Let's consider a CdMnTe quantum dot with a finite number of Mn atoms. An exciton
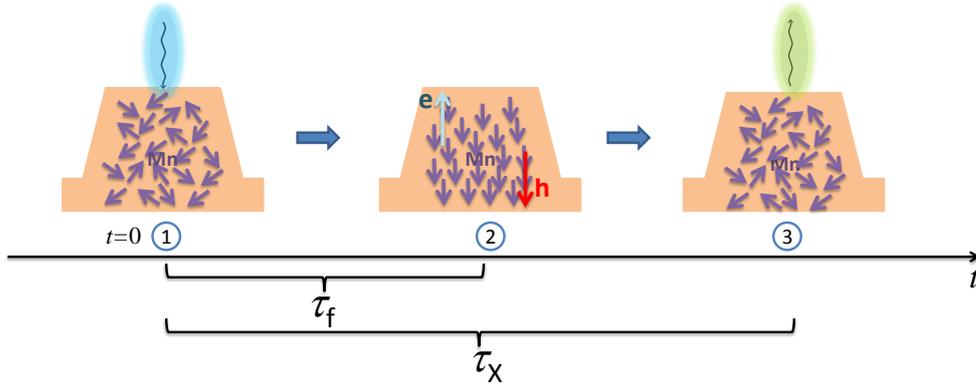
FIGURE 2.2

consisting of a heavy hole and an electron with envelope functions $|\psi_h|^2(\vec{r})$ and $|\psi_e|^2(\vec{r})$, respectively, is optically injected into the quantum dot (Fig.2.2, stage 1). At the moment of time $t = 0$, the instantaneous magnetic moment of Mn atoms is not equal to 0. At this stage the initial correlation between the moment of the exciton and the instantaneous moment of Mn atoms is established by the exchange interactions. This stage is usually called the fluctuation regime, because the average magnetic moment of Mn atoms is controlled by the fluctuations of magnetization [44].

At the second stage of the MP formation process, the exciton exchange field B_P causes the ferromagnetic alignment of N_P localized spins and an increase of polaron energy E_P and polaron magnetic moment M_P. The collective regime is developed. The time τ_f during which the magnetic polaron reaches its equilibrium state should be compared to the exciton lifetime τ_X. If the MP formation time is longer than the the exciton lifetime, which, as we will see further, is the case for our system, the MP formation is interrupted and the whole system returns to the fluctuation regime before the injection of the next exciton.

We can see, therefore, that the photons emitted after the exciton recombination contain the information about the polaron formation process. By injecting a heavy hole exciton (+1) into the quantum dot and recording the photoluminescence spectra, we can probe the development of the local magnetic moment. Applying an external magnetic field we create a magnetic moment in the quantum dot and reduce the effect of the MP formation. We can increase the magnetic field up to the value at which the MP formation will be completely suppressed. As it was shown in Sect.1.3.3, DMS in an applied field exhibit Giant Zeeman effect and a shift of the exciton emission line which is proportional to the Mn magnetization (see Fig.2.3(a)). It is defined according to Eq.1.18 by expression

$$E_Z(B,T) = E_{sat}B_{5/2}\left[\frac{5g_{Mn}\mu_B B}{2k_B(T+T_{AF})}\right].$$
(2.1)

For the homogeneous distribution of Mn atoms ($S=5/2$) inside the quantum dot, the energy at saturation is expressed in the form:

$$E_{sat} = \frac{N_0(\alpha - \beta)x_{eff}}{2}S.$$
(2.2)

This is one of the experimentally measured parameters, which plays an important role in the characterization of the EMP formation process and we will use it in our studies.
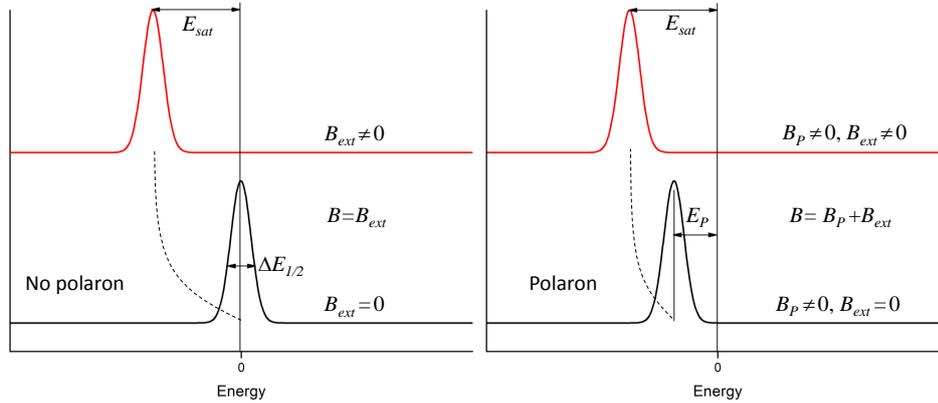
FIGURE 2.3: Parameters of the MP

The exchange interaction between the exciton moment and moments of Mn atoms is characterized by an effective field B_P. So, even in the absence of the real external magnetic field, the exciton line is shifted due to the polaron formation by this effective field (see Fig.2.3). Hence, we should take this into account and consider the field B in Eq.2.1 as a sum of the external field B_{ext} and the exchange field B_P (see Fig.2.3(b)).

Time-resolved photoluminescence spectroscopy allows one to measure the characteristic times of MP formation dynamics: τ_f and τ_X. It also gives an estimation of the MP energy E_P by measuring the shift of the PL line during the lifetime of the exciton. The distribution of the magnetization, formed by the fluctuating magnetic moments of the finite number of Mn atoms N_P, is usually described by a Gaussian function:

$$\Phi(M_z) = \frac{1}{(2\pi \langle M^2 \rangle)^{1/2}} \exp\left(\frac{|M_z - \langle M_z \rangle|^2}{2 \langle M_z^2 \rangle}\right) \tag{2.3}$$

We will show further that the width of this distribution determines the width of the exciton photoluminescence emission line $\Delta E_{\frac{1}{2}}$. This is another important parameter, which is measured experimentally.

We list here the main parameters of interest of the magnetic polaron:

(i) polaron energy E_P - the energy gained by the exciton due to the EMP formation,

(ii) effective field of exchange interaction between the moment of the exciton and moments of magnetic atoms B_P,

(iii) the number of magnetic atoms involved in EMP formation N_P,

This set of parameters allows a complete description of the magnetic polaron formation process. The experimentally measured values are:

(i) Zeeman shift E_Z of the heavy-hole excitonic states in applied external magnetic field,

(ii) Exciton emission linewidth $\Delta E_{\frac{1}{2}}$.

Hence, we have only two experimental parameters with which one should determine the three parameters of the exciton magnetic polaron at thermal equilibrium. Another two parameters which can be obtained from an experiment are exciton lifetime τ_X and MP formation time τ_f. The ratio of these two parameters will determine whether MP will reach its thermal equilibrium or not. It will determine as well the value of the photoluminescence energy red shift ΔE_T, which is observed in the spectra of PL temperature variation. By developing a theoretical model, a relation between experimentally measured parameters and parameters of interest will be found.

2.2.2   Exchange box model

A general difficulty in the calculation of magnetic polaron parameters in self-assembled QDs is that the structural and geometrical parameters are not precisely known and that these parameters even fluctuate across the ensemble. TEM and AFM studies may help to determine the characteristic shape of the quantum dot, but they don't provide any information about the distribution of magnetic ions inside the quantum dot. Hence, one should consider a model with approximations describing how the Mn is distributed inside the quantum dot and how the exciton interacts with the magnetic environment. Based on the chosen model, one should then consistently deduce all the characteristic parameters of the excitonic magnetic polaron at thermal equilibrium from the values measured experimentally.
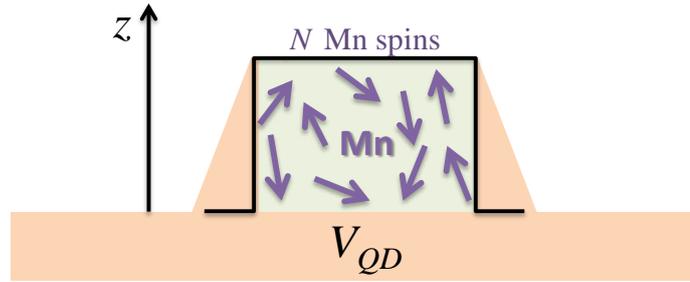
FIGURE 2.4: Exchange box model

a. The case of a neutral exciton

Exchange interactions between magnetic moments of Mn atoms and carriers are usually formulated in terms of exchange interaction of a non localized carrier with a magnetic ion, using Kondo-like Hamiltonian:

$$\mathcal{H}_{exc} = -\alpha \sum_{\vec{R}_i} \mathbf{S}_i \mathbf{s}_e \delta(\vec{r}_e - \vec{R}_i) - \frac{\beta}{3} \sum_{\vec{R}_i} \mathbf{S}_i \mathbf{J}_h \delta(\vec{r}_h - \vec{R}_i), \qquad (2.4)$$

where $\mathbf{S}_i$ and $\mathbf{s}_e$ are the spin operators for a magnetic ion and an electron, respectively, $\mathbf{J}_h$ is a kinetic moment of the heavy hole, $\alpha > 0$ and $\beta < 0$ are the exchange constants of an electron and a hole, $\vec{r}_{e,h}$ is the position (= argument of the wave function) of the carrier and the sum is calculated over the fixed positions $\vec{R}_i$ of magnetic ions.

For an exciton localized in a quantum dot the exchange interaction Hamiltonian should

be written in form:

$$\mathcal{H}_{exc} = -\alpha \sum_{\vec{R}_i} S_{z_i} s_{e_z} |\psi_e|^2(\vec{R}_i) - \frac{\beta}{3} \sum_{\vec{R}_i} S_{z_i} J_{h_z} |\psi_h|^2(\vec{R}_i), \tag{2.5}$$

where $s_{e_z} = \mp 1/2$ and $J_{h_z} = \pm 3/2$. The simplest assumption used in order to facilitate the calculation of magnetic polaron parameters is to consider the exciton localization volume as a box with Mn moments distributed homogeneously inside the box. The envelope functions of electron and hole $|\psi|^2(\vec{r})$ is assumed to be equal to $1/V_{QD}$ inside the dot and zero outside. The parameter V_{QD} is the volume of the quantum dot (see Fig.2.4). This is the main assumption of the so-called "exchange box" model first introduced in [33, 36] which was commonly used previously for the description of magnetic polarons in bulk crystals and then in heterostructures of reduced dimensionality [14, 49, 51, 55, 56]. Because of the $sp - d$ exchange interaction between the three dimensionally confined carriers and the spins of the Mn ions, the magnetic moment M_z is formed by the sum of spins of Mn atoms within the exciton localization volume and is defined as follows:

$$M_z = -g_{Mn}\mu_B \left(\sum_i S_{z_i} \right). \tag{2.6}$$

Taking all these considerations into account, the exchange Hamiltonian can be written in the following form:

$$\mathcal{H}_{exc}^X = M_z \left[\frac{\beta J_{h_z}}{3g_{Mn}\mu_B V_{QD}} + \frac{\alpha s_{e_z}}{g_{Mn}\mu_B V_{QD}} \right] = -M_z B_P^X, \tag{2.7}$$

where B_P^X is the effective field of the exchange interaction between the spins of an electron and a hole forming a neutral exciton and Mn spins:

$$B_P^X = \frac{\sigma_z(\alpha - \beta)}{2g_{Mn}\mu_B V_{QD}}. \tag{2.8}$$

Here, $\sigma_z = \pm 1$ represent the two projections of the exciton kinetic momentum. The value of the magnetic moment itself at thermal equilibrium is a function of this exchange field:

$$\langle M_z \rangle = M_{sat} B_{\frac{5}{2}} \left[\frac{5g_{Mn}\mu_B B_P^X}{2k_B(T + T_{AF})} \right], \tag{2.9}$$

and it defines the shift of the exciton energy due to the Giant Zeeman effect:

$$\Delta E_{PL}^X = - \langle M_z \rangle B_P^X. \tag{2.10}$$

In Fig.2.5(a) the schematic representation of the exciton emission energy shift is shown for both projections of the exciton angular momentum. Linearizing Eq.2.9 and using Eq.2.10 one concludes, that the exciton emission energy shift is proportional to the $(B_P^X)^2$:

$$\Delta E_{PL}^X \propto (\alpha - \beta)^2. \tag{2.11}$$
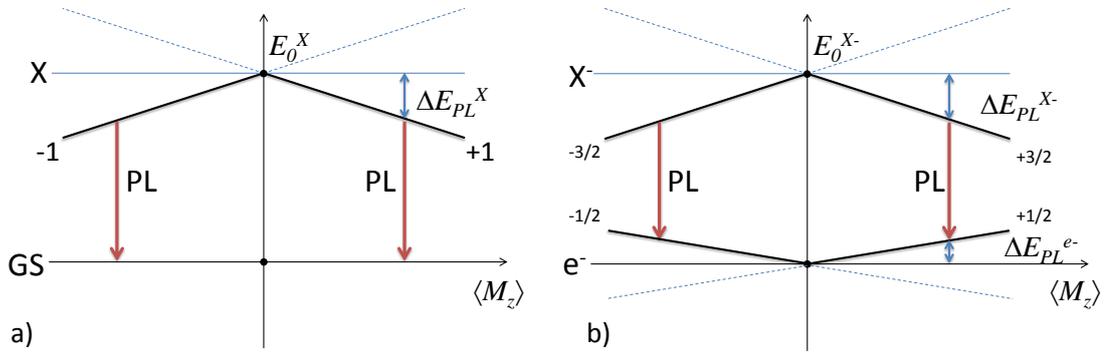
FIGURE 2.5: Schematic representation of the emission energy shift due to the Giant Zeeman effect for a) a neutral exciton and b) for a negatively charged exciton

b. The case of a negatively charged exciton

In the case of a negatively charged exciton, there are two electrons and one hole confined in the quantum dot. The two electrons have the anti-parallel spins and, therefore, they do not interact with the spins of magnetic atoms. Hence, the exchange Hamiltonian 2.4 has only a term, related to the hole:

$$\mathcal{H}_{exc}^{X-} = -\frac{\beta}{3} \sum_{\vec{R}_i} S_{z_i} J_{h_z} |\psi_h|^2 (\vec{R}_i). \tag{2.12}$$

Similarly to Eq.2.7, we can write this Hamiltonian using the total magnetic moment and the exchange field:

$$\mathcal{H}_{exc}^{X-} = M_z \left[\frac{\beta J_{h_z}}{3 g_{Mn} \mu_B V_{QD}} \right] = -M_z B_P^{X-}, \tag{2.13}$$

where

$$B_P^{X-} = \frac{\beta}{2 g_{Mn} \mu_B V_{QD}}. \tag{2.14}$$

The shift induced by the Giant Zeeman effect is defined using

$$\Delta E_{PL}^{X-} = -\langle M_z \rangle B_P^{X-}.$$ (2.15)

After the recombination of the electron-hole pair, there is one remaining electron which is still confined in the quantum dot. The exchange interaction between its spin and the spins of magnetic atoms is described by the exchange Hamiltonian with the only term related to an electron:

$$\mathcal{H}_{exc}^e = -\alpha \sum_{\vec{R}_i} S_{z_i} s_{e_z} \delta(\vec{r}_e - \vec{R}_i).$$ (2.16)

The shift is then defined using

$$\Delta E_{PL}^{e-} = -\langle M_z \rangle B_P^{e-},$$ (2.17)

where the exchange field

$$B_P^{e-} = \frac{\alpha}{2g_{Mn}\mu_B V_{QD}}.$$ (2.18)

In Fig.2.5(b) the diagram related to this case is given. One can see, that the total magnetic moment of Mn atoms is defined only by the exchange interaction with a hole in the negatively charged exciton, while the emission energy is defined both by exchange interactions with the hole and, after the exciton recombination, by the remaining electron. We can conclude, therefore, that the energy shift is proportional to the following expression:

$$\Delta E_{PL}^{X-} \propto (-\beta)(\alpha - \beta).$$ (2.19)

The ratio between Eq.2.19 and Eq.2.11:

$$\frac{\Delta E_{PL}^{X-}}{\Delta E_{PL}^X} = \frac{(-\beta)(\alpha - \beta)}{(\alpha - \beta)^2} < 1.$$ (2.20)

It means that we should expect weaker polaron associated with a negatively charged exciton, than with a neutral exciton. In other words, the characteristic parameters of the magnetic polaron at thermal equilibrium, such as polaron energy E_P and exchange field B_P, should have smaller values for a negatively charged exciton. In the optical spectroscopy studies we measure the saturation energy of the Zeeman shift E_{sat} and the FWHM ($\Delta E_{\frac{1}{2}}$) of the emission line. We should now correlate these values with the theoretical ones.

c. Correlation with experimentally measured values

The exchange energy for a MP associated with an exciton is expressed in the form:

$$E_P^X = \langle M_z \rangle B_P^X = \approx -N_P g_{Mn} \mu_B \langle S_z \rangle B_P^X, \qquad (2.21)$$

or, using the magnetic susceptibility $\chi_V = \frac{1}{V_{QD}} \mathrm{d} \langle M_z \rangle / \mathrm{d}B$, the polaron energy can be expressed by

$$E_P = V_{QD} \chi_V B_P^{X2}. \qquad (2.22)$$

As we have mentioned in the previous Section, the distribution $\Phi(M)$ of the magnetic moment M_z of a finite number of Mn spins can be written in Gaussian form (Eq.2.3). The characteristic width (FWHM) ΔM_z of this distribution is directly related to the SQD emission linewidth (FWHM) $\Delta E_{\frac{1}{2}}$ via the $sp - d$ exchange interaction. Using the well-known fluctuation-dissipation theorem $\langle M_z^2 \rangle = (\mathrm{d} \langle M_z \rangle / \mathrm{d}B) k_B T$, one obtains

$$\Delta E_{\frac{1}{2}} = \sqrt{8 \ln(2) \Delta E^2} = \sqrt{8 \ln(2) k_B T B_P^2 \chi_V V_{QD}}, \qquad (2.23)$$

where $\Delta E^2 = \langle M_z^2 \rangle B_P^2$ is the variance of photoluminescence energy. Next, using Eq.2.22

$$\Delta E_{\frac{1}{2}} = \sqrt{8 \ln(2) k_B T E_P}, \qquad (2.24)$$

or, conversely

$$E_P = \frac{\Delta E_{\frac{1}{2}}^2}{8 \ln(2) k_B T}, \qquad (2.25)$$

Hence, from the experimental width of the exciton emission line we obtain the magnetic polaron energy. Using the combination of experimental parameters E_{sat} and $\Delta E_{\frac{1}{2}}$ we deduce all other parameters of magnetic polaron. Deducing the expression for V_{QD} from Eq.2.8 and substituting it together with Eq.1.19 and Eq.2.22 in Eq.2.23 one obtains:

$$\Delta E^2 = \frac{N_0 x_{eff} (g_{Mn} \mu_B)^2 S(S+1)}{3 k_B T} \frac{(\alpha - \beta)}{2(g_{Mn} \mu_B)} B_P^X k_B T, \qquad (2.26)$$

which after transformation and using Eq.2.2 becomes

$$\Delta E^2 = E_{sat} \frac{(S+1)}{3} (g_{Mn} \mu_B) B_P^X. \qquad (2.27)$$

Thus, the exchange field B_P^X is expressed in the form:

$$B_P^X = \frac{3\Delta E^2}{E_{sat}(S+1)(g_{Mn}\mu_B)}, \tag{2.28}$$

and localization volume V_{QD} is immediately defined as:

$$V_{QD} = \frac{(\alpha-\beta)}{2}\frac{E_{sat}(S+1)}{3\Delta E^2}, \tag{2.29}$$

or, using

$$E_{sat} = N_0 x_{eff}\frac{(\alpha-\beta)}{2}S, \tag{2.30}$$

the number of Mn atoms, participating in magnetic polaron formation is defined as:

$$N_P = V_{QD}N_0 x_{eff} = \frac{E_{sat}^2(S+1)}{3S\Delta E^2}. \tag{2.31}$$

For the case of a negatively charged exciton, the magnetic polaron energy is defined in the linear approximation in the form:

$$E_P = V_{QD}\chi_V B_P^X B_P^{X-}, \tag{2.32}$$

where B_P^{X-} is defined by Eq.2.14. Using Eq.2.14 and Eq.2.8, we obtain the relation between B_P^X and B_P^{X-}:

$$B_P^{X-} = B_P^X\left(\frac{\beta}{\alpha-\beta}\right). \tag{2.33}$$

We can determine B_P^{X-} using Eq.2.28:

$$B_P^{X-} = \frac{3\Delta E^2}{E_{sat}(S+1)(g_{Mn}\mu_B)}\left(\frac{\beta}{\alpha-\beta}\right) \tag{2.34}$$

The use of an "exchange box" model provides a successful description of experimentally observed data for magnetic polaron in quantum dots [14, 51, 56], despite the fact it is based on rather crude simplifications. The main result obtained using this model is Eq.2.24, which is very simple and allows one to determine the polaron energy at thermal equilibrium from the emission linewidth. It is interesting to understand, does this equation appear as a result of the "exchange box" model? We will show in Section 2.6.1 that this result can be obtained without strong assumptions on the Mn distribution and the strength of exchange interaction.

2.3   Sample preparation and characterization

2.3.1   Samples growth

In this section the description of the studied DMS quantum dots is provided. The samples have been fabricated and processed by H.Boukari at Neel Institute, CNRS, Grenoble, France. A set of (Cd,Mn)Te quantum dots samples with different Mn concentration is grown in a standard molecular-beam epitaxy (MBE) chamber on ⟨001⟩ ZnTe substrates. After the growth of a ZnTe buffer layer, CdTe and MnTe layers were grown by successive atomic layer epitaxy (ALE) cycles with a substrate temperature of 280°C. The ALE consists in sending alternatively cations (Cd, Zn or Mn), and anions (Te), coming from elemental sources onto the surface, leaving growth interruptions (GI) between each vapor pulse in order to re-evaporate the possible excess material. During a cycle of evaporation, excess Cd and Te atoms re-evaporate while Mn sticks to the surface. The sequence of these stages (exposure to cations, GI, exposure to Te, GI) corresponds to one ALE cycle (see Fig.2.6). Compared to conventional MBE, in which the two constituent elements are brought simultaneously onto the surface, the mobility of adsorbed species on the growing surface is expected to be greatly enhanced, as it was demonstrated for III-V semiconductor compounds such as GaAs [57].

The film thickness in the ALE growth is determined by the total number of cycles
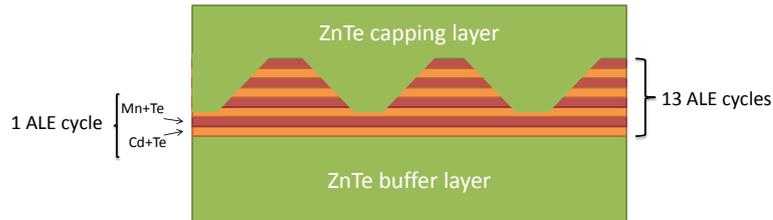
FIGURE 2.6: Schematic representation of the CdMnTe QDs ALE growth process.

of pulses rather than by the beam intensity or source temperature. The advantage of the ALE technique is the high precision of the structure thickness. But this precision is achieved at the price of a slower growth rate, which imposes the possibility of impurity inclusion. The quantity of CdTe and MnTe deposited, corresponds to a number of monolayers (MLs) just below the thickness required for the onset of plastic relaxation [58]. In our case this number equals 6.5 MLs. The repetition of ALE cycles is observed

by the intensity of a reflection high-energy electron diffraction (RHEED) pattern. The needed concentration of Mn in $Cd_{1-x}Mn_x Te$ is achieved by calibrating the Mn source cell temperature and the time during which the sample is exposed to the Mn flux. The intended concentration of Mn in $Cd_{1-x}Mn_x Te$ is varied from sample to sample between 2% and 10%. As we have seen in Sect.2.2, the magnitude if the Giant Zeeman effect scales with Mn concentration. This will provide us more precise estimation of the Mn content in the single quantum dot. The formation of the quantum dots is activated by exposing the sample to the Te source. A 100 nm ZnTe capping layer is then deposited on the top of the sample in order to protect the quantum dots from oxidation.
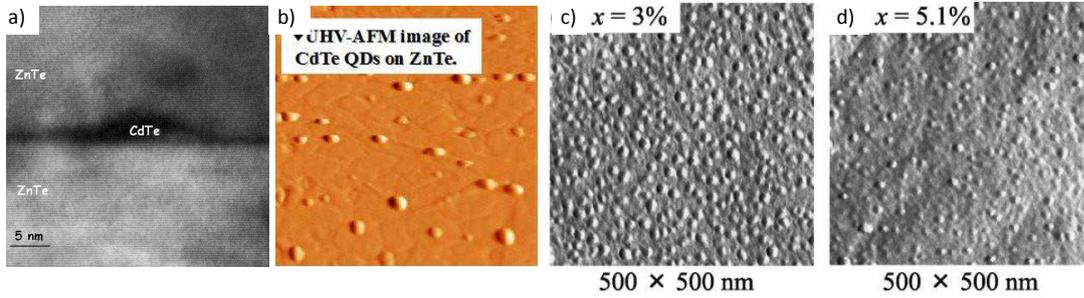
FIGURE 2.7: a) and b): TEM and AFM images of the CdTe/ZnTe QDs from work [59]. c) and d): AFM top view of the surface on which 3.5-ML-thick CdTe was deposited by ALE. The Mn composition was c) 3% , d) 5.1% [60]

Though the studies of the QD sizes distribution had not been performed for our set of samples, we can get an approximate estimation from the results on the quantum dots grown in similar conditions from literature. In work [59] TEM and AFM studies have been performed for MBE-grown CdTe/ZnTe quantum dots (Fig.2.7(a) and (b), respectively). The average diameter of the QD was estimated to be ≈ 10 nm and the average height to be ≈ 3 nm. In work [60] the AFM studies had been performed for the set of the CdMnTe quantum dot samples with different Mn concentration grown by ALE. In Fig.2.7(c) and (d) the AFM top views of the $Cd_{1-x}Mn_x Te$ surface layer with $x = 3\%$ and $x = 5.1\%$, respectively, are shown. The average dot size of a) x=3% [b) 5.1%] was given by $D = 23 \pm 1.3$ nm [20 ± 1.8 nm] in diameter and $h = 2.0 \pm 0.2$ nm [1.4 ± 0.2 nm] in height, and the density was 1×10^{11} cm^{-2} [4×10^{10}] cm^{-2}]. These

studies provide us an idea of the quantum dot density and their average size which will be used in Sect.2.6.3 as a range of possible dot sizes.

2.3.2 Macro-photoluminescence of the quantum dots ensemble

The set of quantum dots samples with different values of the Mn concentration has been characterized by optical spectroscopy. For each sample, low-temperature photoluminescence spectra of quantum dots ensembles have been recorded. A CW 405 nm laser beam of 50 μW has been focused by an optical lens, providing a spot size of ∼100 μm in diameter.
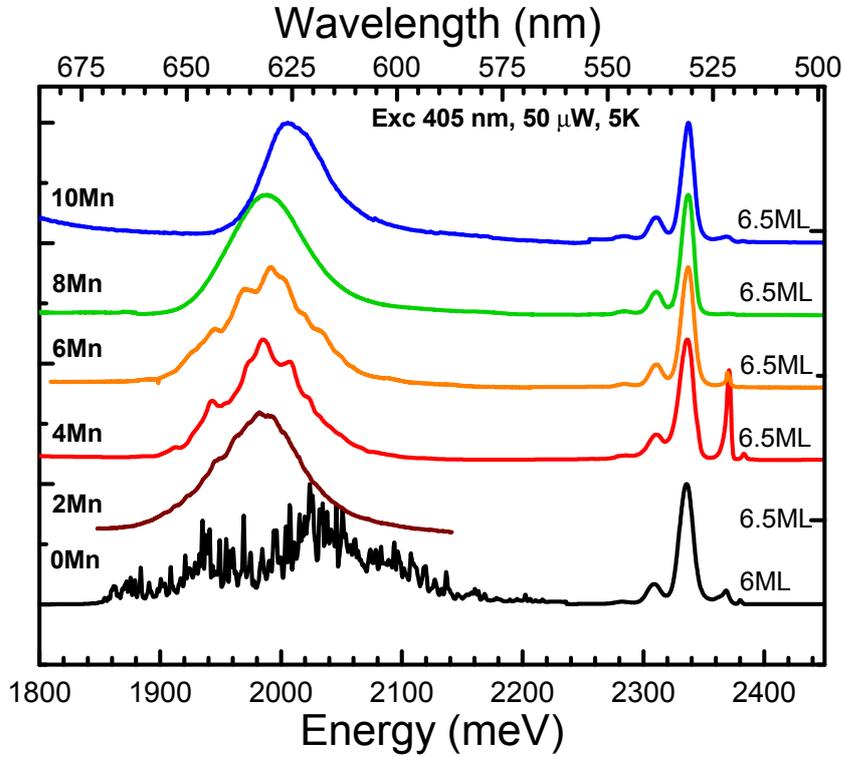
FIGURE 2.8: Macro-photoluminescence spectra of quantum dots ensembles containing different intended Mn concentration recorded with 405 nm CW laser excitation of 50 μW at 6 K.

In Fig.2.8, the comparison between the photoluminescence spectra of different CdMnTe quantum dots is shown. One can observe emission lines with wavelength around 530 nm corresponding to the emission of different energy states localized in the ZnTe barriers. A broad emission band with an average wavelength ranging between 600 nm and 650 nm is attributed to the emission of CdMnTe quantum dots. The distribution of the exciton energy is due to the size and the shape distributions of the QDs. The shape of this

emission band changes by increasing the Mn concentration: from a broad distribution of sharp peaks for the non magnetic sample, to a smoothed line originating from the overlapping broadened exciton PL lines of the individual QDs. It can be seen that the width of the PL band of the non-magnetic quantum dots emission is at least 2 times larger than for magnetic dots.

In order to characterize the exciton dynamics in quantum dots with different concentration of magnetic atoms, time-resolved photoluminescence studies on quantum dots ensembles can be performed. The idea here is to estimate an average exciton lifetime and trace its possible variation with increasing Mn concentration.

Time-resolved photoluminescence (TRPL) measurements were performed in the group of M. Bayer, D. Yakovlev and I. Akimov in Dortmund Technische Universitaet. The excitation was performed using second-harmonic generation of light emitted from a mode-locked Ti:Sa laser with the pulse duration of about 2 ps and a repetition rate of about 76 MHz (Mira 900 D). The excitation wavelength was tuned to 405 nm and the excitation power of 100 μW was used. The samples were mounted in a He-bath cryostat with a variable temperature insert. The excitation light was focused at the sample using the microscope objective with 10x magnification (excitation spot ≈10 μm, NA=0.26). The PL was collected in reflection geometry using the same microscope objective. The signal was dispersed by a single 0.5 m spectrometer with 6 nm/mm linear dispersion and detected with a streak camera synchronized with the repetition rate of the laser (Hamamatsu was equipped with synchroscan unit). The overall temporal and spectral resolution of the experimental set-up for time-resolved measurements was about 20 ps and 1 nm, respectively.

Recorded TRPL images were analyzed by extracting the PL decay curves and by fit-
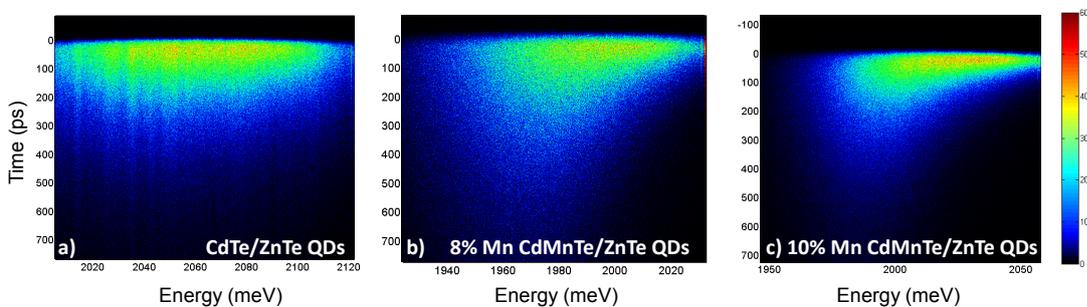
FIGURE 2.9: Time resolved macro-photoluminescence spectra of quantum dots ensembles containing different Mn concentration recorded with 405 nm pulsed laser excitation of 100 μW at 5 K

ting them with a simple exponential decay law $I(t) = I_0 \exp(-t/\tau)$ with the parameter τ which defines the decay time (see Fig.2.10(b)).

For samples containing Mn, the observed decay time τ of the PL is found to critically depend on the emission energy of the QDs. A systematic increase of τ from 40 to 400 ps can be observed in CdMnTe (10% Mn) QDs with for emission energy varying from 2050 meV down to 1950 meV. This variation of τ can be attributed to interdot exciton transfer from the dots with higher exciton energies to the ones with lower energies.
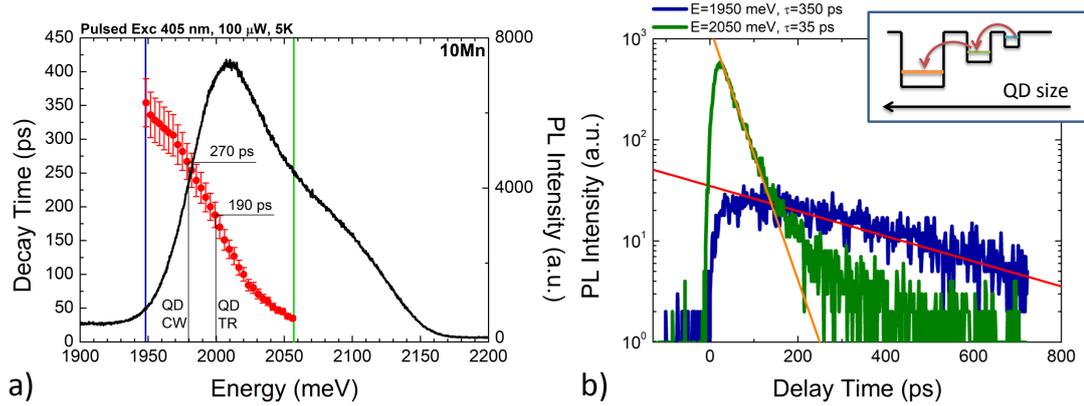
FIGURE 2.10: a) Excitonic PL spectrum (black solid line) and the PL decay times (closed circles) as a function of photon energy at 5 K. b) Typical PL decay curves at higher and lower detection energies (green and blue solid lines, respectively), from which the PL decay times were obtained. Inset shows the scheme of exciton energy transfer from smaller size dots to bigger ones.

The effect of exciton energy transfer has been observed in CdSe/ZnSe SK quantum dots[61], in CdSe quantum dots coupled with a DMS ZnMnSe quantum well[62] and many other semiconductor structures. It was shown that this effect strongly depends on temperature: a red shift of several meV of PL band maximum at low temperature is attributed to exciton tunneling processes. Thermally activated hopping becomes the dominant transfer process with rising temperatures[61].

In our case, the behavior of QD ensemble photoluminescence in time has been studied at 5 K. It means that another mechanism is responsible for the exciton transfer. As it can be seen from the Fig.2.9, by increasing the Mn concentration, the effect of exciton transfer becomes stronger, with very short decay times in the high energy side of emission band. In the non magnetic quantum dots ensemble, where there is almost no variation of PL decay time, such effect is seems to be negligible.

An increasing Mn concentration in the QD causes the change in bands offsets between CdMnTe and ZnTe significantly decreasing the confinement potential of quantum dots. The difference in bands offsets between non-magnetic CdTe/ZnTe QDs and 8.3% Mn

CdMnTe/ZnTe QDs is demonstrated in Fig.1.6(b) and (c) of Chapter 1. It can be seen that for a concentration of Mn approaching 8% the confinement potential for the holes becomes very small. For a given Mn concentration and assuming a homogeneous distribution of Mn in each QD, the confinement potential of each QD will be determined by its size. For small quantum dots the exciton energy level is situated very close to the barrier energy level, whereas the localization of excitons is still possible in bigger ones. This may be a reason why the exciton transfer becomes important even at low temperature (see inset in Fig.2.10(b)). Another possible reason could be the magnetic polaron formation: it may bring in resonance the energy levels of the neighboring quantum dots of different size.

As we have just seen, time-resolved photoluminescence studies of DMS QDs ensembles do not allow us to estimate the average lifetime of the exciton because of the exciton transfer effect. To proceed, we need to isolate a single quantum dot from an ensemble.
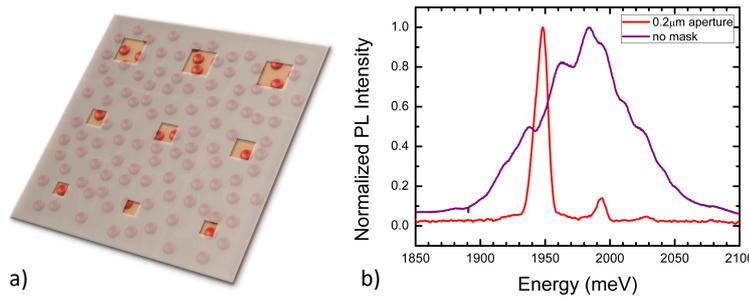
FIGURE 2.11: a) Scheme of a sample containing quantum dots and an aluminium mask with apertures of different size, which allow to isolate single dot from an ensemble. b) Comparison between PL spectra of QD ensemble and single QD.

For this purpose, apertures of size varying from 0.2 μm to 2 μm have been fabricated in an opaque aluminium mask using electron-beam lithography and wet etching (see Fig.2.11(a)). This mask deposited on the surface of a sample containing quantum dots allows us to isolate a small number of quantum dots in a single aperture, decreasing the number of emission lines in the observed spectra (see Fig.2.11(b)).

2.4   Single quantum dot micro-photoluminescence

This Section is devoted to single QD micro-photoluminescence studies. The photoluminescence spectrum of a single CdMnTe QD is presented and its structure is characterized by power dependence studies and by the applied voltage studies. The formation of the exciton magnetic polaron is evidenced by CW magneto-optical studies and time-resolved studies.

2.4.1   Micro-photoluminescence

Using the smallest apertures of 0.2 μm, we can select a spectrum where the emission lines of single quantum dots are spectrally isolated from the others. An example of such a spectrum is presented in Fig.2.12(a) for a single CdMnTe (10% Mn) quantum dot. It is recorded at 6 K with a 405 nm excitation wavelength of 100 μW and with 2 μm spot size. It consists of a single emission line with full width at half maximum of ∼8.6 meV
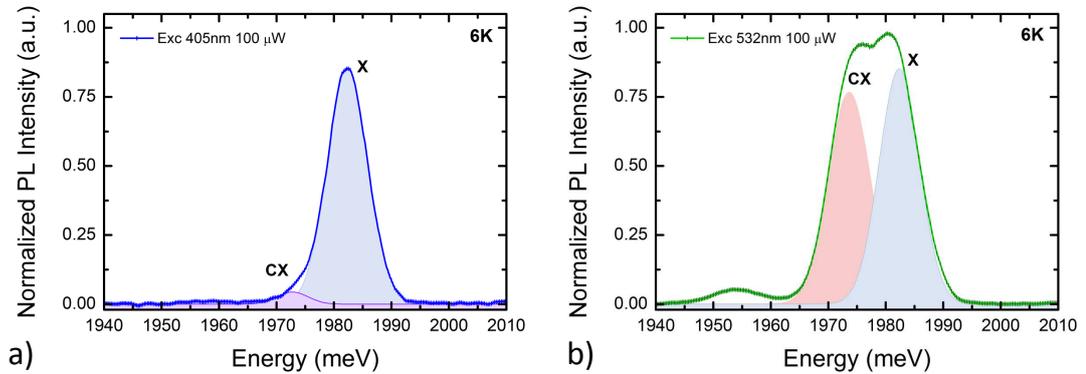
FIGURE 2.12: Micro-photoluminescence spectra of single CdMnTe (10% Mn) quantum dot recorded with a) 405 nm of 30 μW at 6 K and b) 532 nm CW laser excitation of 30 μW at 6 K

which is at least an order of magnitude larger than the emission line of non magnetic quantum dots (Fig.2.13(a)). The linewidth is measured by fitting the main line with a Gaussian (Fig.2.13(a)). The values of linewidth and line area extracted from photoluminescence spectrum fit will be used later to determine the exciton magnetic polaron parameters. The increase in linewidth observed in a set of samples, follows the increase of the magnetic ions concentration (see Fig.2.13(c)).

Photoluminescence spectra recorded for the same aperture with the same excitation
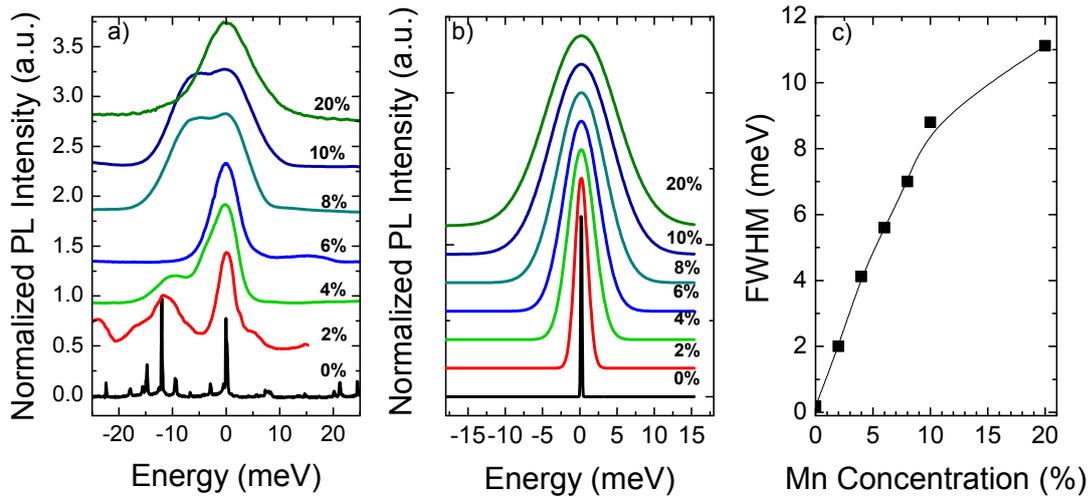
FIGURE 2.13: a) Experimental spectra of (Cd,Mn)Te QDs with different Mn concentration recorded at 6 K. b) Fitted exciton emission lines of samples with different Mn concentration. c) Full width at half maximum of emission line as a function of Mn concentration

power but with the excitation wavelength changed to 532 nm, demonstrates the appearance of a second emission line having a FWHM of ∼9.5 meV and 7 to 9 meV red shifted from the main emission line (see Fig.2.12(b)). The observed energy difference corresponds to the charged exciton binding energy usually measured in the CdTe QD[63], whereas the biexciton binding energy in CdTe/ZnTe ranges between 12 and 14 meV[64]. In order to study the nature of this emission line, additional experiments should be performed. The observed broadening of the emission lines hinders the access to the fine structure of the quantum dot emission spectrum. The fitting of experimental spectrum may induce considerable errors if one makes a mistake in the number of lines which should be used in the fit. Hence, one should change the experimental conditions in order to observe the response of the system under study and determine its fine structure. For the single quantum dot spectrum shown in Fig.2.12, measurements of the laser power dependence has been performed (see Fig.2.14(a)). One can see in this figure, that the two emission lines are better resolved at low excitation power than at high power. In order to obtain the intensities of both lines at each power, the recorded spectra have been fitted with two Gaussian lines. After the fitting of the low-power spectrum, the energy positions of lines are fixed and further fitting is performed only by the intensity variation. In Fig.2.14(b) the results of the fitting are shown. With an increasing excitation density, the peak labeled as X gains intensity linearly at first, reaches a maximum, and then falls sharply for higher excitation. The intensity of CX peak increases slightly

faster than linearly at low-excitation density with the slope of the logarithmic plot of 1.2, indicating that this line does not correspond to a biexciton complex. Power dependence studies of this sample do not reveal any emission line, characteristic to biexciton, with quadratic behavior of photoluminescence intensity with power, as observed in non magnetic quantum dots[64].
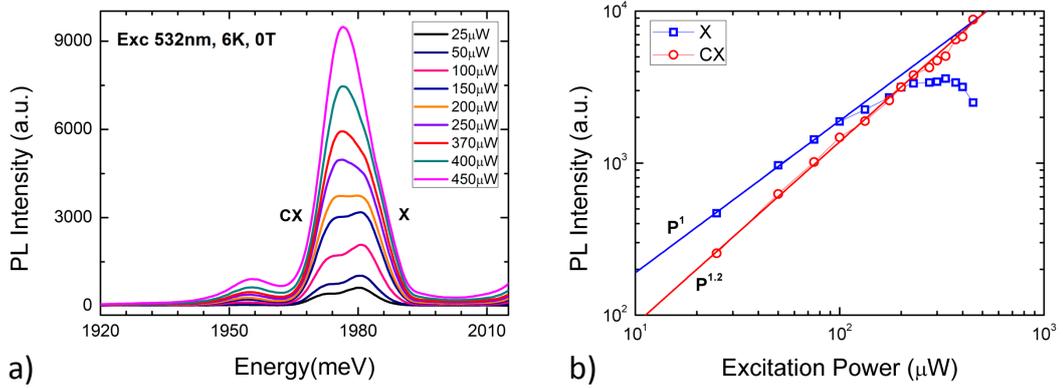
FIGURE 2.14: a) Evolution of micro-photoluminescence spectra of single CdMnTe (10% Mn) quantum dot as a function of excitation power. b) Photoluminescence intensity as a function of laser excitation power plotted for exciton and charged exciton emission lines.

The absence of biexciton in photoluminescence spectrum can tentatively be explained by a weak confinement potential for holes, weaker than the Coulomb repulsion between them, preventing the two holes to be confined in the quantum dot simultaneously. Hence, only the trion consisting of two electrons and one hole is possible, providing the negatively charged exciton.

2.4.2   Applied voltage studies

In order to determine the sign of the charged exciton, the evolution of photoluminescence spectra under applied voltage has been studied. By placing contacts on top surface (where the aluminium mask is deposited), and on bottom surface (connected to the sample holder) of the sample, we can use our sample as a Schottky diode[65]. The ZnTe substrate at the bottom of the sample has a residual p-doping and the surface states of a capping layer under the aluminium mask behave like acceptors, blocking the Fermi level close to the edge of the valence band[66, 67] (Fig.2.15(a)). Hence, by applying a positive voltage sufficient to make Fermi level to pass below the holes energy level, one can expect the quantum dot to be positively charged, and to observe the positively charged exciton
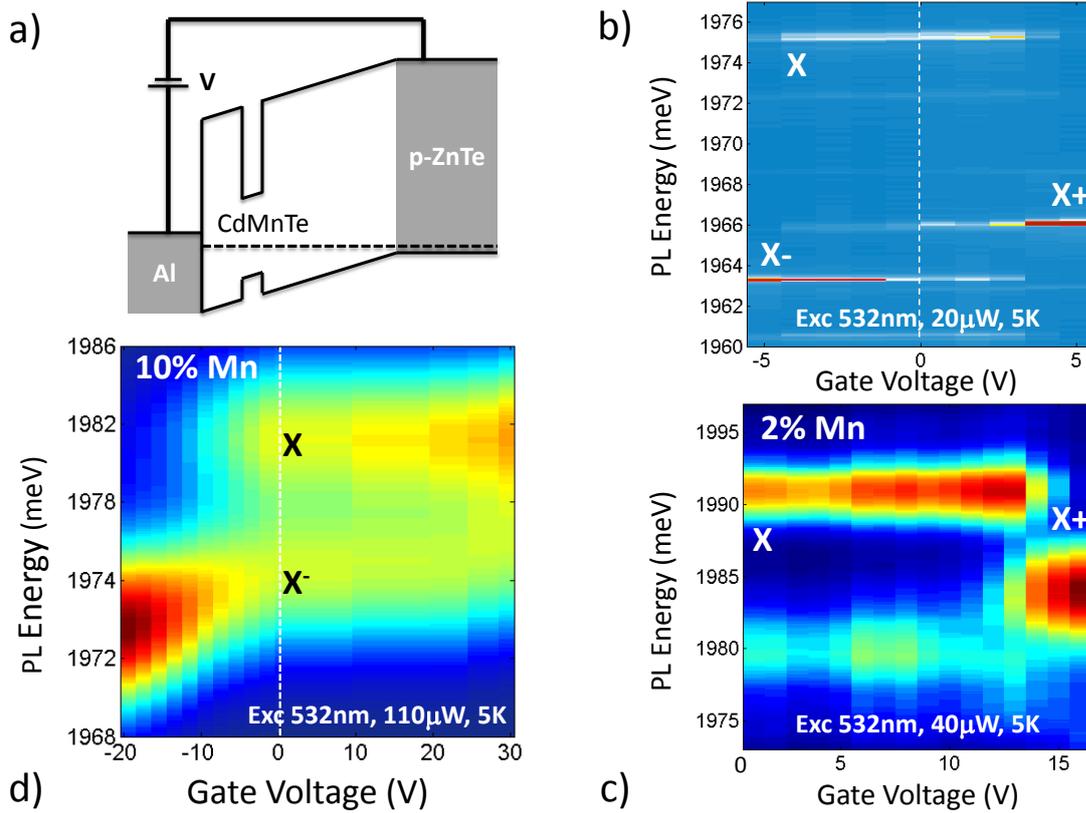
FIGURE 2.15: a) Scheme of sample wiring. Voltage is applied between the aluminium mask on top of the sample and a sample holder. b) Micro-photoluminescence spectra of single CdTe quantum dot under applied voltage recorded with 532 nm CW laser excitation of 20 µW at 5 K. c) Micro-photoluminescence spectra of single CdMnTe (2% Mn) quantum dot under applied voltage recorded with 532 nm CW laser excitation of 40 µW at 5 K. d) Micro-photoluminescence spectra of single CdMnTe (10% Mn) quantum dot under applied voltage recorded with 532 nm CW laser excitation of 110 µW at 5 K.

complex. On the other hand, by applying a negative voltage, the negatively charged exciton can be observed.

Charge control studies have been performed in [63] for non magnetic quantum dots of CdTe/ZnTe and quantum dots containing a single Mn atom. It was confirmed, that the application of a positive (negative) voltage gives rise to the positively (negatively) charged exciton, respectively.

For our set of samples with different concentration of Mn, original charge control measurements have been performed in order to investigate the possibility of magnetic polaron formation with charged excitons. We have observed a similar behavior with non magnetic quantum dot (see Fig.2.15(b)) and QDs containing 2% of Mn (Fig.2.15(c)).

However, for quantum dot with a Mn concentration of 10% (Fig.2.15(d)), the application of a positive voltage does not induce any significant changes in spectra, whereas

application of negative voltage results in enhancing the charged exciton line emission intensity and disappearance of the exciton line. This is another hint that the presence of the negatively charged exciton and not the positively charged one in the quantum dot with 10% of Mn, may be explained by a weak hole confinement potential, formed by the bands offset and by Coulomb interaction.

We can conclude, therefore, that without applying any bias to the sample, by simply exciting the quantum dot with 532 nm laser, we have a negatively charged exciton together with a neutral exciton. This fact provides us a unique opportunity to compare the magnetic polaron formation phenomena for two excitonic complexes located in the same quantum dot.

2.4.3   EMP formation evidenced by cw measurements

So far we have evidenced the presence of magnetic ions inside the quantum dot by the broadened photoluminescence emission lines, almost 2 orders of magnitude broader than in non-magnetic quantum dots. Exchange interactions between Mn spins and the moment of the electron-hole pair manifests itself in the photoluminescence spectra through Giant Zeeman effect, described in section 1.3.3, which is a unique feature of diluted magnetic semiconductors. Another manifestation of strong exchange interaction is the Exciton Magnetic Polaron (EMP) formation, i.e., of a ferromagnetically aligned spin complex consisting of one exciton and several hundred of Mn^{2+} ions with strongly correlated spins in the absence of external magnetic field, which results in red shifted exciton emission energy at low temperature. Performing micro-photoluminescence experiments with external magnetic field applied to the DMS sample will allow us to characterize the exchange interaction between the exciton and the magnetic ions spins. Spectroscopy studies at different temperature and time-resolved micro-photoluminescence experiments will help us to observe and characterize the exciton magnetic polaron formation process.

 Micro-photoluminescence spectra have been recorded for a chosen aperture of each sample. The spectra were recorded for various temperatures and external magnetic fields applied in Faraday geometry using the set-up described in Sec.1.4.1. In Fig.2.16(a) the evolution of spectra at 6 K in an applied external magnetic field up to 7 T, measured on the sample with 10% of nominal Mn concentration, is shown for σ^+ polarization. There is a very strong circular polarization of the photoluminescence, so that the σ^- line could only be observed in rather weak (≤ 1 T) fields.
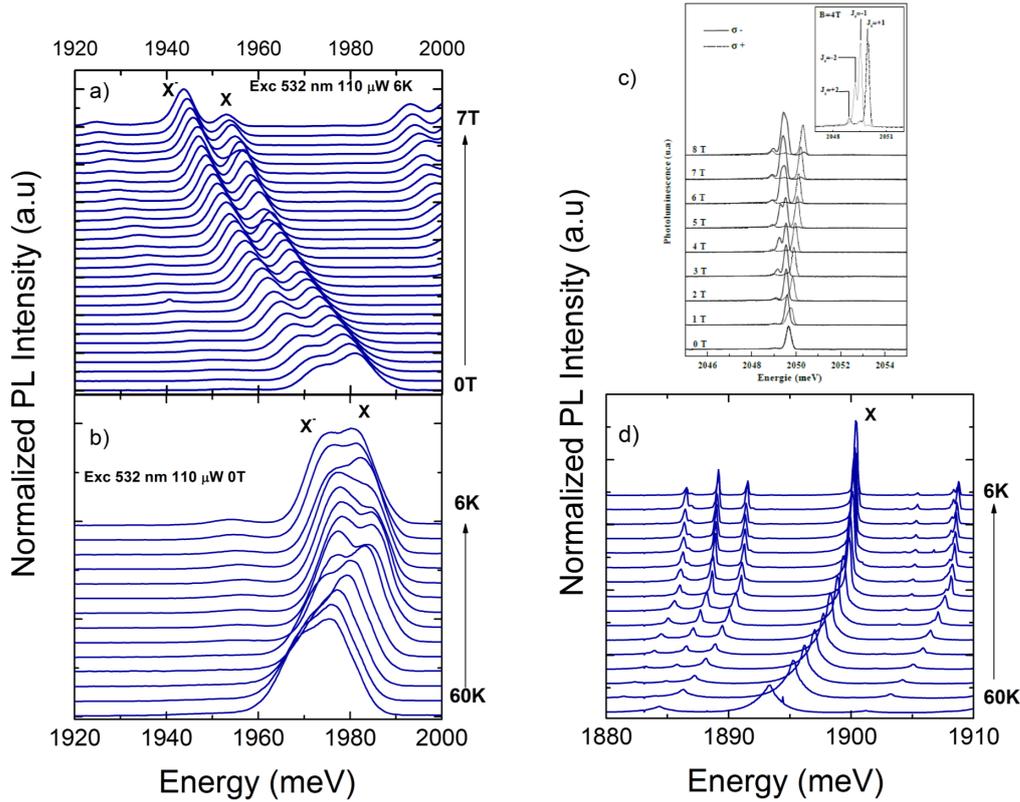
FIGURE 2.16: μPL spectra of a single CdMnTe quantum dot: a)(10% Mn) in external magnetic field. b) (10% Mn) as a function of the cryostat temperature. c) CdTe/ZnTe in external magnetic field [68] , d) CdTe/ZnTe as a function of the cryostat temperature.

One can observe from figure 2.16(a) that the emission energy of two lines, originated from the same quantum dot and previously identified as exciton and negatively charged exciton, is decreasing with an increasing external magnetic field. The value of this decrease ($\sim$ 30 meV) is two orders of magnitude larger than the one ($\sim$ 0.5 meV) observed for non-magnetic quantum dots (Fig.2.16(c)[68]). One can mention as well, that with an increasing magnetic field the overlap between the two emission lines becomes smaller and they become spectrally separated at high field due to the decrease of the linewidth. This decrease is well known and it is a consequence of statistical magnetic fluctuations suppression due to the alignment of Mn spins along the direction of the external magnetic field.

In Fig.2.16(b) the temperature evolution of photoluminescence spectra recorded in the absence of any external magnetic field is shown for the same quantum dot studied in Fig.2.16(a). We observe a blue shift of the emission energy by decreasing temperature from 60 K down to 20 K, followed by a red shift between 20 K and 5 K. This non-monotonic behavior is especially remarkable when one compare it to the temperature
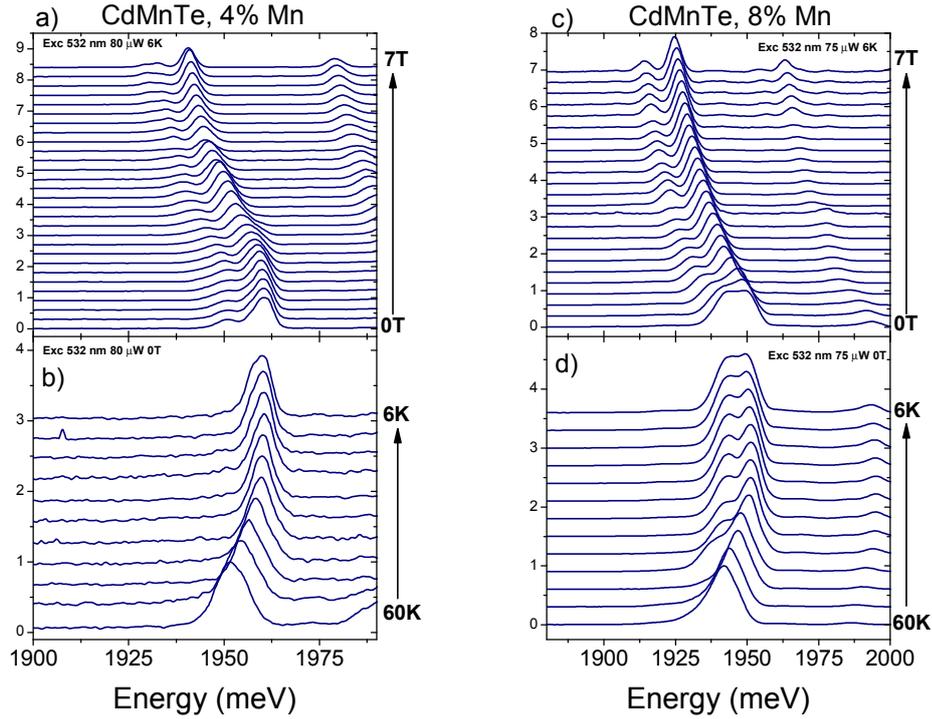
FIGURE 2.17: μPL spectra of a single CdMnTe quantum dot: a)(4% Mn) in external magnetic field. b) (4% Mn) as a function of the cryostat temperature. c) (8% Mn) in external magnetic field. , d) (8% Mn) as a function of the cryostat temperature.

dependence of CdTe quantum dot emission energy, which shows a monotonic blue shift related to the band gap opening (see Fig.2.16(c)). Hence, the red shift of DMS QD emission energy between 5 and 20 K is ascribed to the presence of Mn, and is interpreted as resulting from magnetic polaron formation.

In Fig.2.17 the evolution of the photoluminescence spectrum as function of an applied magnetic field and of the cryostat temperature is shown for two samples with nominal Mn concentration of 4% (Fig.2.17(a,c)) and 8% (Fig.2.17(b,d)). One can mention from these figures, that the value of the exciton emission energy red shift in applied field decreases when the Mn concentration decreases (~ 25 meV for 8% and ~ 20 meV for 4%).

In order to provide a quantitative comparison of energy redshift observed for samples with different Mn concentration, on should retrieve the exact energy positions of emission lines and trace their dependences as function of temperature and external magnetic field. In Fig.2.18 the energy of the exciton emission is plotted as a function of temperature and applied magnetic field for CdMnTe QD with 10% of Mn. These values are obtained from a fit of PL spectra, depicted in Fig.2.16(a) and (b), with Gaussian lines.
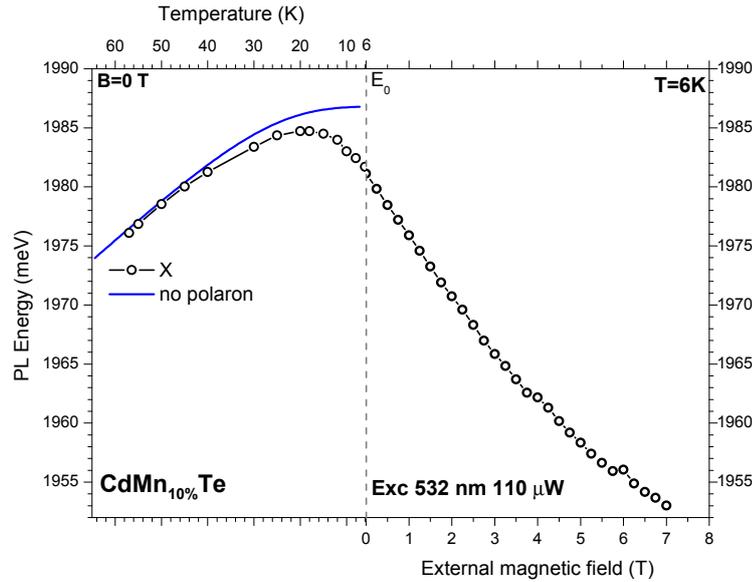
FIGURE 2.18: Energy of the exciton emission as a function of temperature and external field. Blue lines correspond to the non formed polaron.

The high-temperature part of corresponding dependence describes the thermal variation of the band gap. It is fitted using Eq.2.38 (blue line in Fig.2.18). The procedure and parameters of this fit will be given later in Sect.2.5. The fitting is done in order to determine the energy E_0, which is the energy of the exciton with not formed polaron. Having determined this value for each sample, we have the possibility to compare the corresponding energy shifts.
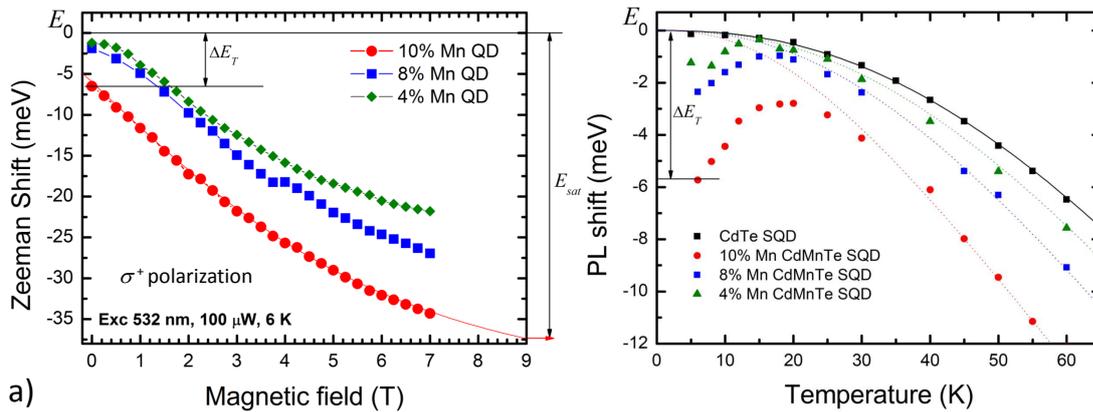
FIGURE 2.19: a) Zeeman shift energy as a function of external magnetic field. b) Energy shift of PL line of a single CdMnTe and CdTe/ZnTe quantum dot emission energy as a function of temperature

The energy shift scales with the Mn concentration inside the quantum dot, as it can be seen from Fig.2.19(a). The higher the Mn concentration, the larger is the energy shift induced by the external magnetic field. This finding points unambiguously that

the $sp - d$ exchange interaction and the resulting giant Zeeman splitting are the origin of the observed energy shifts. The energy E_{sat} at which the saturation of Zeeman shift is reached is an important parameter, characterizing the maximum exchange interaction energy between the exciton and Mn spins. For a proper determination of this energy the influence of the exciton magnetic polaron formation should be taken into account. The value of the PL red shift $\Delta E_T(T)$ observed below 20 K in the absence of any external magnetic field also scales with Mn concentration, as it can be seen in Fig.2.19(b), where the temperature dependence of exciton emission energy is plotted for three different samples and is compared to the temperature dependence of the non-magnetic CdTe QD. The variation of the energy shift $\Delta E_T(T)$ in the temperature range between 6 K and 20 K directly reflects the temperature variation of the magnetic moment of the magnetic polaron [51]. However, we will see that the polaron is not completely formed, so that the value of $\Delta E_T(T)$ at a given temperature is determined by dynamic parameters of the magnetic polaron formation, which can not be determined from this experiment.
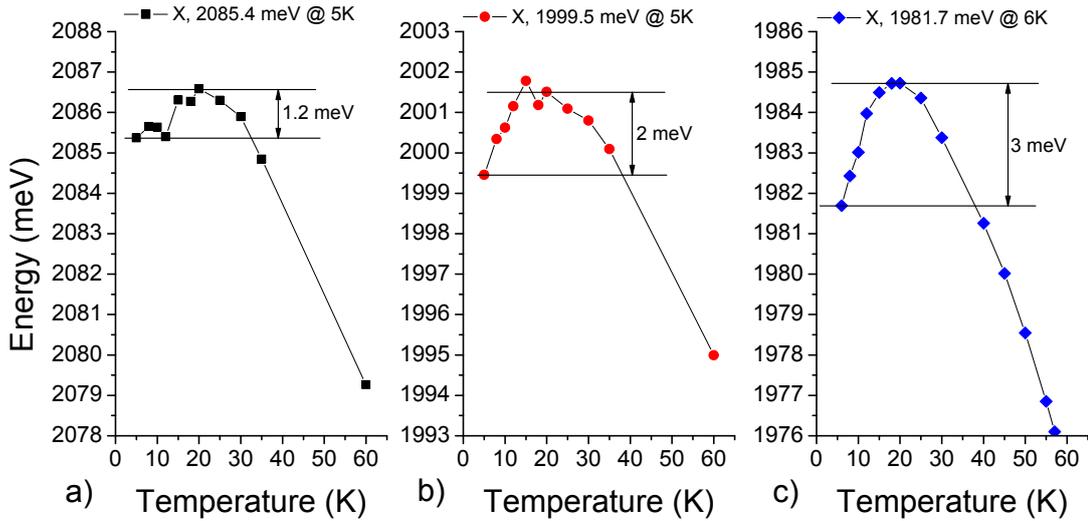
FIGURE 2.20: CdMnTe (10% Mn) QD: PL energy temperature dependence for 3 different single quantum dots.

In Fig.2.20 temperature dependences of the photoluminescence of 3 different single quantum dots of the CdMnTe with 10% Mn are shown. These quantum dots have different energy of the exciton at $T = 5$ K. One can see, that with a decreasing exciton energy the red shift of the PL $\Delta E_T(T)$ increases. From the time-resolved measurements of the ensemble of quantum dots (Fig.2.10) we can see that the average lifetime of the exciton is smaller in the dots with higher exciton energy. This indicates, that the magnetic polaron is more formed in quantum dots with smaller exciton energy. In order to confirm

this, single dot time-resolved measurements should be provided. It will be done in the next section.
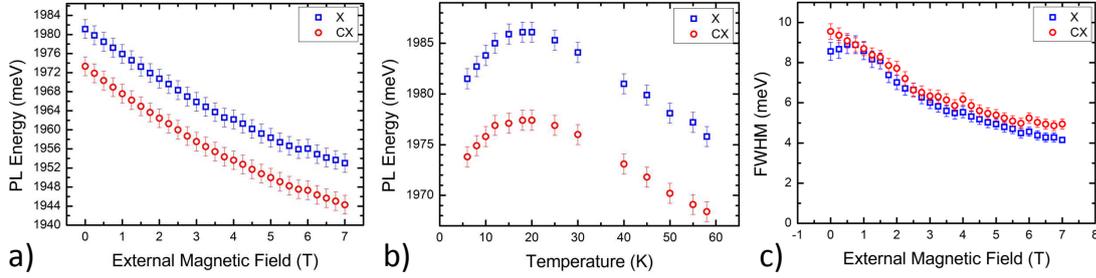
FIGURE 2.21: CdMnTe (10% Mn) QD: a) Emission energies of the exciton and the charged exciton as a function of an external magnetic field. b) Emission energies of the exciton and the charged exciton as a function of the cryostat temperature. c) Exciton and charge exciton emission lines FWHM as a function of an external magnetic field.

In Fig.2.21 the neutral exciton and negatively charged exciton emission energy is plotted as a function of an applied external magnetic field (a) and of the cryostat temperature (b) for a single (Cd,Mn)Te quantum dot with 10% of Mn concentration. We observe similar behavior for both excitonic complexes, which means that the magnetic polaron forms with each of them. However, as we will see further, the parameters of these magnetic polarons are different.

2.4.4 EMP formation evidenced by time-resolved measurements

The development of the magnetization can be monitored in a time-resolved photoluminescence experiment, in which a transient shift of the exciton energy is observed after the injection of an electron-hole pair in the dot at $t = 0$. It allows us to evaluate the magnetic polaron formation time, τ_f, which will be compared to the exciton lifetime, τ_X. The ratio of these two times will determine how much the red shift of the PL line recorded under steady state conditions reflects the polaron energy E_P. Performing time-resolved photoluminescence measurements on single quantum dot one can characterize the dynamics of EMP formation.

Time-resolved photoluminescence investigations were performed using the same set-up as the one used for QD ensemble studies described in Section 2.3.2.

Fig.2.22 shows the streak camera images of PL signals for two isolated QDs with 8 and
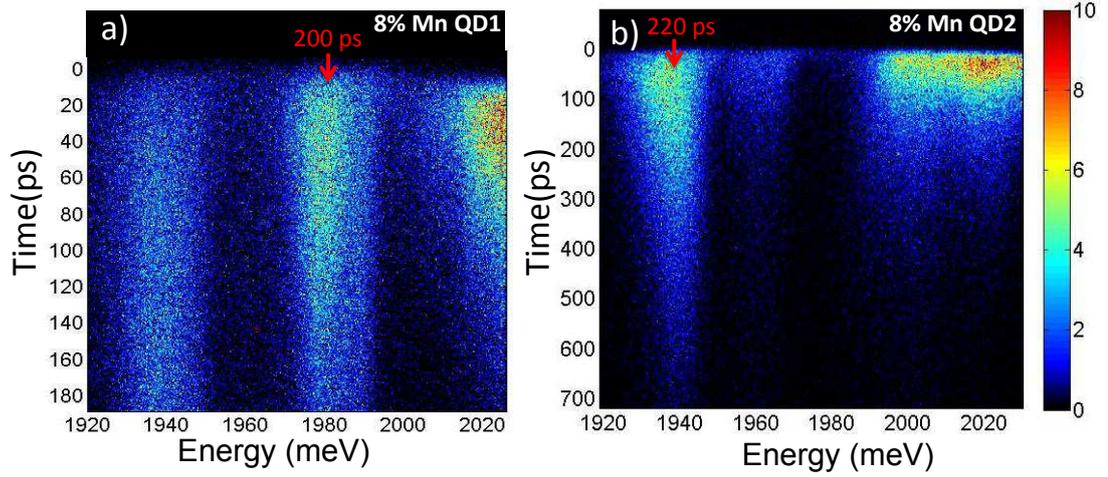
FIGURE 2.22: Streak camera images of PL signals for two CdMnTe QDs with 8% of intended Mn concentration.

10% of nominal Mn concentration.

For the emission lines indicated by red arrows in Fig.2.22(a) and (b) a small transient shift of the PL maximum can be observed indicating a very weak exchange interaction between exciton and Mn spins in the QD. By measuring the decay time of the photoluminescence we obtain the exciton lifetime of 200 ps and 220 ps, respectively.

In Fig.2.23(a) the streak camera image of the single CdMnTe quantum dot with 10% of Mn concentration is shown. One can see a distinct redshift of the emission line saturating about 300 ps after excitation. Another interesting feature which is seen in this image is the luminescence peak at higher energy with a very short decay time (~ 40 ps). Its origin is not known, but its decay time may indicate that this is an emission from the p-shell states of the quantum dot [69]. A set of transient photoluminescence spectra extracted from the image at different times reveal a spectral separation between two emission lines (see Fig.2.24). This finding allows us to fit the transient spectra with two Gaussian lines and use the parameters of these lines for fitting. As suggested by the CW experiment, the emission lines are attributed to the emission of the exciton and the negatively charged exciton. For the fit of the transient spectra we use the FWHM of the Gaussian lines obtained from CW measurements (~ 8.6 meV and ~ 9.5 meV) (see Fig.2.23(b)).

The parameters extracted by fitting the transient photoluminescence spectra are the energy position of the maximum of each line and the photoluminescence intensity. With these data we determine the exciton and trion lifetime (τ_X and τ_{CX}) by fitting the PL intensity decays with an exponential decay curve $I_{PL} = I_0 \exp(-t/\tau)$ (see
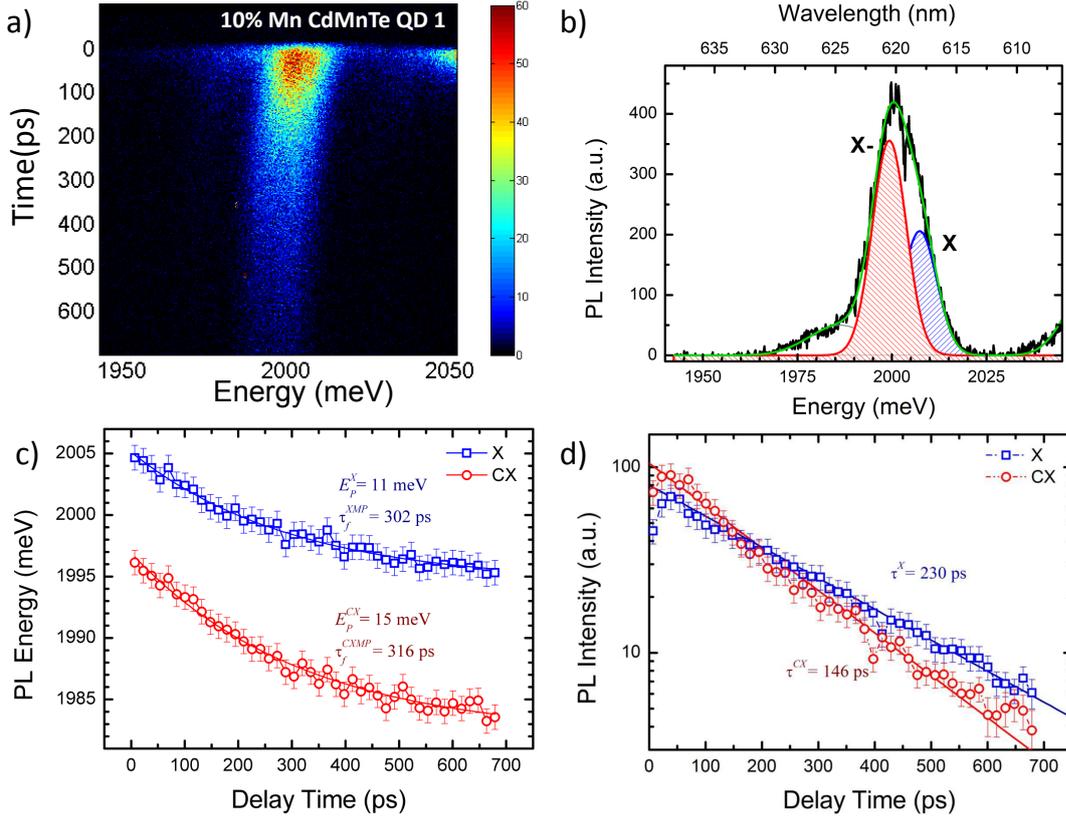
FIGURE 2.23: a)Streak camera image of PL signal of a single CdMnTe QDs with 10% of intended Mn concentration. b) Fit of the transient spectrum taken at $t = 0ps$. c) Evolution of the PL line maximum energy in time for exciton and charged exciton emission lines. d) Decay of the photoluminescence intensity of exciton and charged exciton emission lines.

	QD1		QD2		QD3	
	X	X-	X	X-	X	X-
E_0, meV	2007.8	2001	2015.2	2007.5	2006.5	1998
E_P, meV	11	15	5.6	6	8.2	10
τ, ps	200	150	180	135	260	170
τ_f, ps	320	300	300	250	290	310
m	0.38	0.33	0.37	0.35	0.47	0.36

TABLE 2.1: Comparison of EMP and CEMP dynamic parameters.

Fig.2.23(d)). Magnetic polaron formation times for both exciton complexes (τ_f^X and τ_f^{CX}) are determined by fitting the emission energy shift in time with an expression $\Delta E_{PL} = E_P(1 - \exp(-t/\tau_f))$ (see Fig.2.23(c)). The energy of fully formed magnetic polaron (E_P^X and E_P^{CX}) is directly evaluated from this fit.

The parameters of the fit are listed in the Table.2.1. One can see that the magnetic polaron formation time with an exciton is almost equal to the one with a trion and exceeds the lifetime of both excitonic complexes. The polaron energy of the trion is found to be larger than the one gained by the exciton. This is an interesting finding
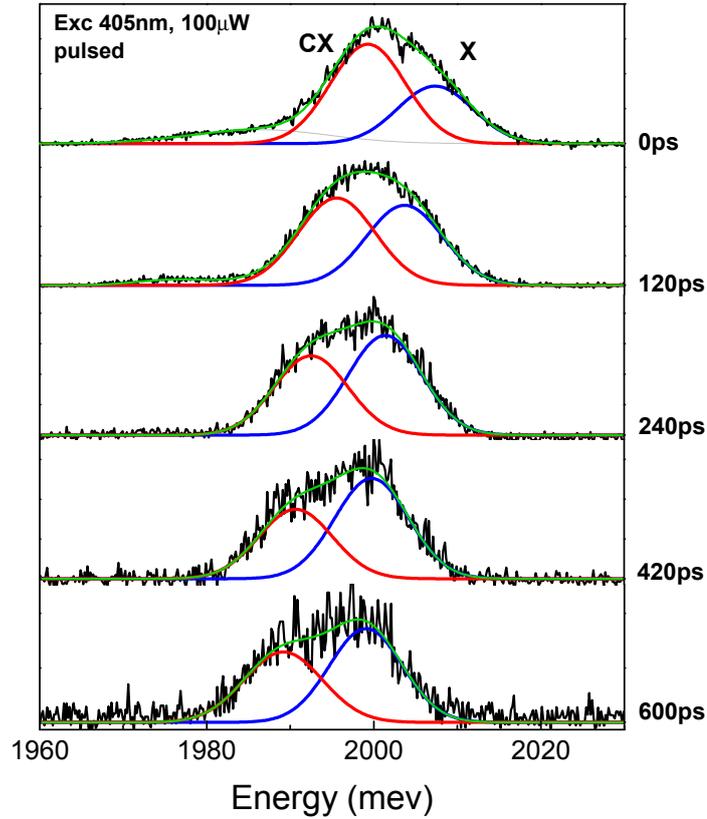
FIGURE 2.24: Cross-section spectra extracted from the streak camera image (Fig.2.23(a)) at different moments of time.

because one would expect the polaron energy of the trion to be smaller the one of the exciton because the two electrons in the trion compensate each other's spin and do not participate in the MP formation. As it will be shown in Sec.2.6.3, the reason for this is the increased overlap of the hole wave function with surrounding Mn moments due to the stronger hole confinement induced by the Coulomb interaction with two electrons.

In Fig.2.25 the exciton and the trion lifetimes of the three quantum dots (see Appendix A) are plotted and compared to the PL decay times obtained from a QD ensemble measurements (see Sect.2.3.2). One can see that the exciton emission decay time of an individual quantum dot is higher than the average decay time of an ensemble at the same energy. The effect of the exciton transfer, the emission of charged exciton and of p-shell states mentioned above, decrease the average decay time obtained from the ensemble measurements. Hence, the real exciton lifetime can only be obtained from the single-dot time-resolved measurements.

One can see as well, that with the decreasing energy of the exciton emission, the exciton lifetime increases while the magnetic polaron formation time stays approximately
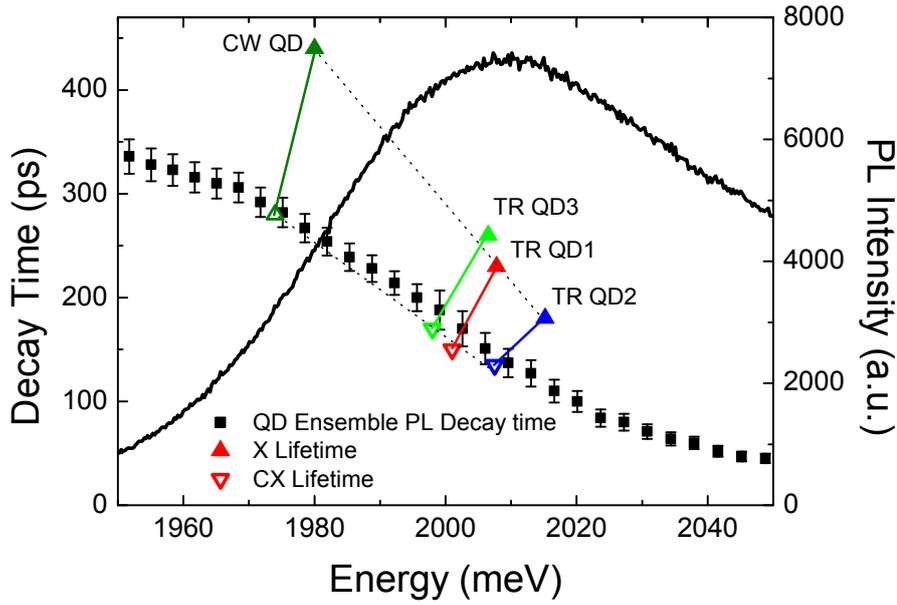
FIGURE 2.25: Comparison of the single dot PL decay constants measured for an exciton and a trion with a QD ensemble PL decay time measurements.

constant (see Table.2.1). It means that the larger fraction of magnetic polaron energy at thermal equilibrium is reached in quantum dots with lower exciton emission energy. This fraction is determined by the parameter $m = \tau/(\tau + \tau_f)$ (see Table.2.1). The CW experiment data is collected for the quantum dot with an exciton energy of 1980 meV, with which we did not succeed to perform TR experiment. In order to estimate the exciton lifetime in this quantum dot we perform a linear extrapolation of the exciton lifetimes measured in TR experiment and find the value $\tau = 440$ ps (see Fig.2.25). Assuming, that the polaron formation time is constant, we find the parameter $m \approx 0.6$ for this dot. Similarly for the charged exciton we find $\tau = 280$ ps and $m \approx 0.5$, respectively. We will use these values for the fitting of the CW experiment results in Sect.2.5.

The time-resolved photoluminescence measurements is a powerful technique which allows one to directly observe the magnetic polaron formation and to determine its dynamic parameters. These parameters together with parameters obtained from CW measurements will be used in order to complete the description of the magnetic polaron formation process.

2.5   Polaron parameters

In this Section we will demonstrate the procedure to determine the exciton magnetic polaron parameters from the experimental data presented in Section 2.4 using the "exchange box" model described in Section 2.2.2. The magnetic polaron parameters obtained from the experimental data will be discussed and compared to the ones retrieved from numerical calculation described in Section 2.6.3, which accounts for the shape of the quantum dot and confinement potential formed by bands offsets and Coulomb interaction between an electron and a hole, forming an exciton. The same calculation will be applied to the trion case.

2.5.1   Experimental determination

As it was shown in Section 2.2, exciton magnetic polaron parameters at thermal equilibrium are determined from the saturation energy E_{sat} of Zeeman shift and from the emission linewidth $\Delta E_{\frac{1}{2}}$ in zero field. Time-resolved measurements provide a direct measurement of the magnetic polaron energy E_P and show, whether the magnetic polaron is formed or not. Hence, having obtained these 3 experimental values one can obtain all the parameters of magnetic polaron.

In this section we will demonstrate the way we determine the polaron parameters for the (Cd,Mn)Te quantum dot with 10% of the nominal Mn concentration, as for this sample all the relevant data had been obtained. For other samples, time resolved measurements do not reveal any signs of the magnetic polaron formation. Hence, only the parameters of magnetic polaron in thermal equilibrium will be determined.

Unfortunately, the data collected in time-resolved and CW measurements does not belong to the same quantum dot. Therefore, we will have to commit some additional assumptions and operate with larger number of free parameters in order to correctly fit the data.

The quantum dot studied in CW measurements has an exciton emission energy of 1980 meV and the ones studied in time-resolved have the exciton energy in the range between 2000 meV and 2020 meV. As discussed in Sect.2.4.4, the exciton lifetime increases with the decreasing exciton energy. It means, that the quantum dot studied in CW experiment has a longer exciton lifetime and, as a consequence a more formed magnetic

polaron. The parameter which defines the completeness of the magnetic polaron forma-
tion is the ratio $m = \tau/(\tau + \tau_f)$, where τ is the exciton lifetime and τ_f is the magnetic
polaron formation time. For quantum dots studied in time-resolved experiment this pa-
rameter was roughly $m = 0.4$. Using the linear extrapolation of TR lifetimes value and
assuming the constant MP formation time, we found the value $m \approx 0.6$ (see Fig.2.25).
The parameter m also affects the value of the PL energy red-shift ΔE_T observed in
temperature dependence measurements. And we have seen in Fig.2.20 that the value of
ΔE_T is larger for a quantum dot with smaller exciton energy.

The first important parameter, which should be determined, is the Mn temperature
T_{Mn}, which differs from the cryostat temperature and comprises the heating induced by
the laser excitation: $T_{Mn} = T_{cryo} + T_{las}$. It can be evaluated using equation 2.25:

$$T_{Mn} = \frac{\Delta E_{\frac{1}{2}}^2}{8\ln(2)k_B E_P}. \tag{2.35}$$

With the value of $E_P = 11 \pm 1$ meV obtained for the exciton from time-resolved measure-
ments (Fig.2.23) and the value of $\Delta E_{\frac{1}{2}} = 8.6 \pm 0.5$ meV used for the fit of the transient
photoluminescence spectrum, we obtain $T_{Mn} = 12 \pm 1$ K.
Experimental determination of E_{sat} is hindered by the fact that the Zeeman shift of
emission line in applied field does not reach the saturation even at 7 T (see Fig.2.19(a)).
The energy of the exciton emission in the absence of an applied field is determined by
dynamic parameters of the MP formation process. From time-resolved measurements
we know, that MP is formed only partially. It means, that EMP formation process is
interrupted by the exciton recombination and that during this process exciton's emission
energy is reduced by mE_P, where m is the parameter defined above. We should take
these into account in order to fit correctly the experimentally measured dependence of
the exciton emission energy with the applied field.
The saturation energy of Zeeman shift is determined from the fit of emission energy
dependence on applied magnetic field using the modified Brillouin function (Eq.2.1).
We assume, that the resulting function, used for magnetic field dependence data fitting,
consists of two contributions:

$$E_X(B + B_P, T) = E_0 - E_{sat}\left[(1-m)\cdot B_{\frac{5}{2}}(B, T_{Mn}) + m \cdot B_{\frac{5}{2}}(B + B_P, T_{Mn})\right], \tag{2.36}$$

where the first contribution describes the dependence of Mn magnetization on an applied

external magnetic field and the second contribution describes the Mn magnetization dependence on an external field in presence of an exchange field B_P, created by the exciton. As it was shown in Sect.2.2.2, the parameters B_P and E_{sat} in case of a neutral exciton are linked by Eq.2.28 and, therefore, we have only one free parameter in Eq.2.36. E_0 is the energy of exciton emission in the absence of the exchange interaction with Mn atoms. It is determined as $E_0 = E_X + m \cdot E_P$, where E_X is the observed emission energy at $T = 6$ K and $B = 0$ T.

The exciton emission energy temperature dependence is fitted using the following expression:

$$E_X(B_P, T) = E_G(T) - m \cdot E_{sat} \cdot B_{\frac{5}{2}}(B + B_P, T_{Mn}), \tag{2.37}$$

where $E_G(T)$ is written in form[70]:

$$E_G(T) = E_0 - \frac{a\Theta_p}{2}\left[\sqrt[p]{1 + \left(\frac{2T}{\Theta_p}\right)^p} - 1\right]. \tag{2.38}$$

The parameters $a = 0.36$ and $p = 2.415$ are determined from the fit of the non magnetic CdTe/ZnTe quantum dot exciton energy temperature dependence and are fixed. The only parameter which is adjusted in order to fit the experimental data of the magnetic quantum dot is $\Theta_p = 57$ K. Its value is different from the bulk CdTe value ($\Theta_p = 135$ K). This may be attributed to the presence of Mn and of Zn inside the CdTe quantum dots, which contribute in the temperature dependence of a complex alloy $Cd_xMn_yZn_{1-x-y}Te$.
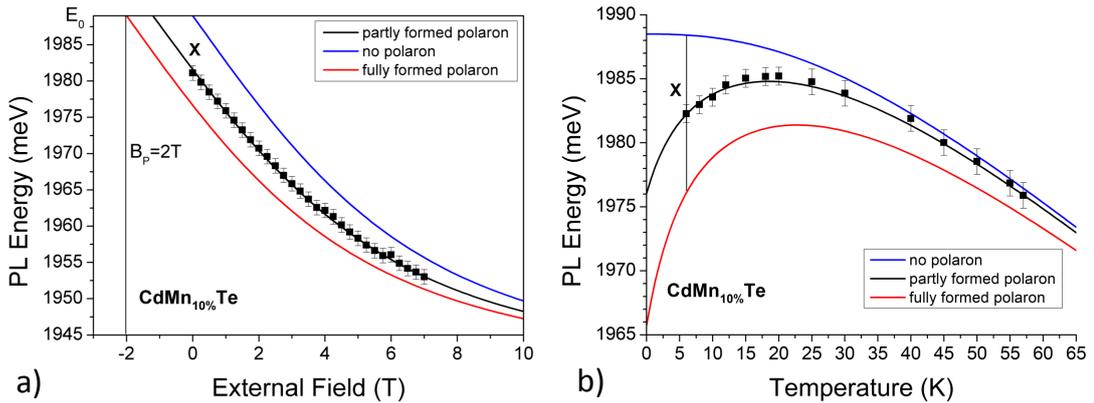
FIGURE 2.26: Single CdMnTe (10% Mn) quantum dot exciton emission energy dependence on a) applied magnetic field; b)sample temperature. Experimental data is fitted using equations 2.36 and 2.37, respectively.

In Fig.2.26 the result of the fitting procedure for a single CdMnTe (10% Mn) quantum

dot is shown, demonstrating a good agreement between experimental data and theoretical approach.

The average number of spins N_P involved in EMP formation process is evaluated by Eq.2.31 and one obtains $N_P = 74$. Assuming a homogeneous distribution of Mn ion inside the quantum dot volume V_{QD} (an "exchange box approximation"), we determine this volume as:

$$V_{QD} = \frac{N_P}{N_0 x_{eff}}, \tag{2.39}$$

where the number of cation cites in cubic centimeter $N_0 = 14.7$ nm^{-3}, and x_{eff} is an effective Mn concentration. It is determined using the Zeeman saturation energy:

$$E_{sat} = S x_{eff} \frac{N_0 (\alpha - \beta)}{2}, \tag{2.40}$$

where $N_0 \alpha = 0.22$, $N_0 \beta = -0.88$ and $S = \frac{5}{2}$. Hence, $x_{eff} = 3.52\%$ and the quantum dot volume $V_{QD} = 137$ nm^3.
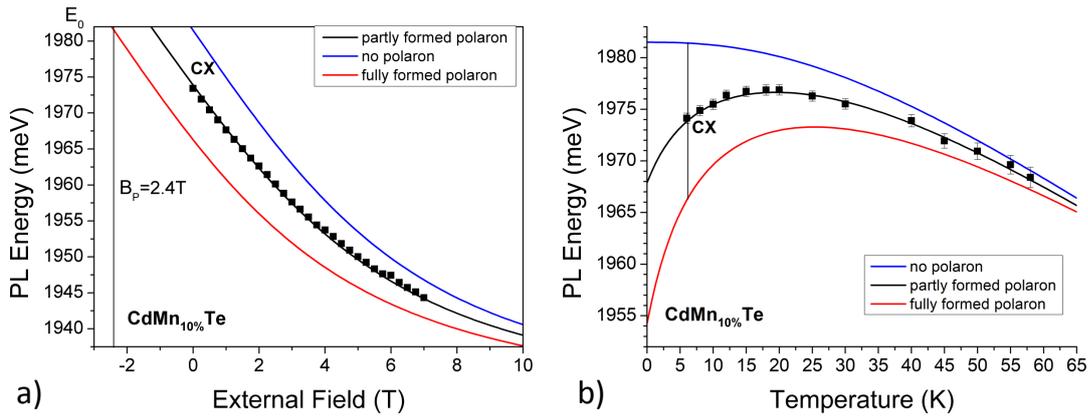
FIGURE 2.27: Single CdMnTe (10% Mn) quantum dot negatively charged exciton emission energy dependence on a) applied magnetic field; b)sample temperature. Experimental data is fitted using equations 2.36 and 2.37, respectively.

We will now try to fit the experimental results obtained for the negatively charged exciton. Similarly to the case of a neutral exciton, we estimate the trion lifetime as a linear extrapolation of results obtained for trions in TR experiment (see Fig.2.25). The value of $m \approx 0.5$ is used during the fit. As it was shown in Sect.2.2.2, the exchange field B_P^{X-} of the negatively charged exciton is linked to the Zeeman shift saturation energy E_{sat} by Eq.2.34. Equation 2.33, which relates the exchange field of a neutral exciton with the one of a trion, shows us, that the value of B_P^{X-} should be smaller than B_P^X by the factor $\left(\frac{\beta}{\alpha-\beta}\right) = 0.8$. However, it is impossible to fit experimental results with such conditions. In Fig.2.27 the result of the fitting procedure for negatively charged exciton having

	EMP	CEMP
FWHM	8.6 meV	9.5 meV
E_P	11 meV	15 meV
E_{sat}	49 meV	50.5 meV
B_P	2 T	2.4 T
N_P	83	74
V_P	160 nm^3	135 nm^3
τ	440 ps	270 ps
τ_f	320 ps	300 ps
m	0.6	0.5

TABLE 2.2: Comparison of EMP and CEMP parameters.

$B_P^{X^-}$ larger than B_P^X is shown. It is important to emphasize here, that the fit parameters should be <u>consistent</u> for PL magnetic field dependence and temperature dependence <u>at the same time</u>. This reduces significantly the error in the values of resulting parameters. The comparison of magnetic polaron parameters is given in Table.2.2.

As one can see from this table, the energy of the negatively charged exciton magnetic polaron is higher than the one of the exciton magnetic polaron. CEMP is also characterized by a slightly higher saturation energy and higher exchange field. At the first glance it looks surprising because one should expect a decrease of the polaron energy and of the exchange field created by a negatively charged exciton due to the reciprocal compensation of electrons spins forming the trion. One can see, therefore, that the "exchange box" model do not describe properly the experimental results. This model due to its oversimplified assumptions does not account for the true nature of the exciton and neglects the interaction between an electron and a hole. Moreover, in most cases the exchange interaction between the electron spin and Mn spins is neglected [49, 51]. In order to describe theoretically the observed values, one should go beyond the simplifications of the "exchange box" model and consider the realistic shape of the carrier wave function and take into account the Coulomb interaction between electron and hole. This will be done in the next Section.

2.6   Beyond the exchange box model

2.6.1   Beyond the exchange box model: envelope function model

The assumptions made in the "exchange box" model do not correspond to the actual situation. The distribution of Mn atoms is not uniform and the effective field of the exchange interaction is not homogeneous. As it can be seen from the TEM-image of a single CdTe/ZnTe quantum dot [59], the shape of the quantum dot is far from being a simple "box". Hence, it is initially wrong to assume the exchange interaction of an exciton with the magnetic atom located in the center of the quantum dot or at its border, to be homogeneous. We will show below that these assumptions are not needed. The only assumption made is the linear response of the magnetic moments of Mn atoms to the presence of an external (or exchange) field.
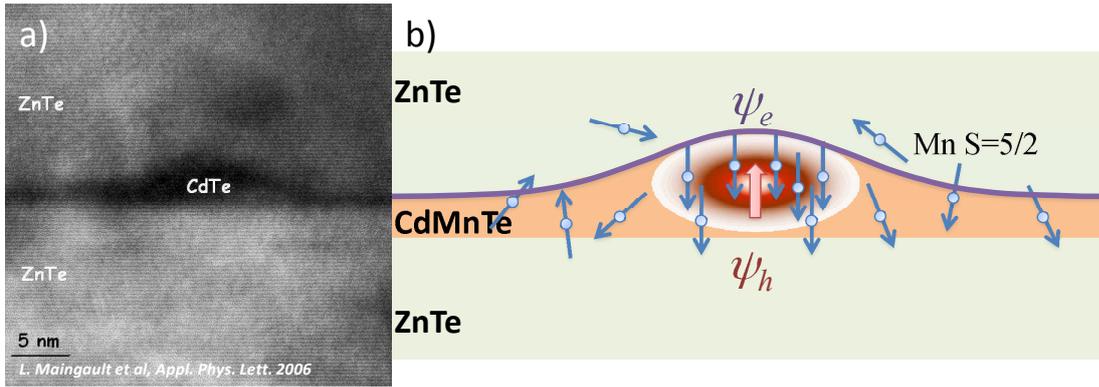
FIGURE 2.28: Scheme of the model

We consider that the Mn density is characterized by a volume density $\rho(\vec{r})$, which is not uniform (see Fig.2.28(b)). The exciton consisting of a heavy hole and an electron is characterized by envelope functions $\psi_h(\vec{r})$ and $\psi_e(\vec{r})$. Exchange interactions between the magnetic moments and carriers are usually formulated in terms of exchange interaction of a non localized carrier with a magnetic ion, using Kondo-like Hamiltonians:

$$\mathcal{H}_{ex} = -\alpha \sum_{\vec{R}_i} \mathbf{S}_i \mathbf{s}_e \delta(\vec{r}_e - \vec{R}_i) - \frac{\beta}{3} \sum_{\vec{R}_i} S_{i_z} J_{h_z} \delta(\vec{r}_h - \vec{R}_i), \qquad (2.41)$$

where $\mathbf{S}_i$ and $\mathbf{s}_e$ are the spin operators for a magnetic ion and an electron, respectively, J_{h_z} is the kinetic moment of the heavy hole, $\alpha > 0$ and $\beta < 0$ are the exchange constants of an electron and a hole, $\vec{r}_{e,h}$ is the position (= argument of the wave function) of the carrier and sum is calculated over the fixed positions $\vec{R}_i$ of magnetic ions.

For an electron and a hole localized in a quantum dot the exchange interaction Hamiltonian should be written in form:

$$\mathcal{H}_{ex} = -\alpha \sum_{\vec{R}_i} S_{i_z} s_{e_z} |\psi_e|^2(\vec{R}_i) - \beta \sum_{\vec{R}_i} S_{i_z} s_{h_z} |\psi_h|^2(\vec{R}_i), \tag{2.42}$$

where $s_{e_z} = s_{h_z} = \pm 1/2$. To simplify the notation we make a definition:

$$(\alpha - \beta)|\Psi_X|^2 = \alpha|\psi_e|^2 - \beta|\psi_h|^2 \tag{2.43}$$

We assume that a bright exciton is present in the dot. The total kinetic momentum projection of the electron-hole pair is noted $\sigma_z^X = \pm 1$. The influence of the exciton on Mn moments is described by:

$$\mathcal{H}_{ex}^{Mn} = \frac{(\alpha - \beta)}{2} \sum_{\vec{R}_i} S_{i_z} \sigma_z^X |\Psi_X|^2(\vec{R}_i). \tag{2.44}$$

Assuming that the Mn moments are at thermal equilibrium, the Mn magnetization is given by:

$$m_z(\vec{r}, T) = -\rho(\vec{r}) g_{Mn} \mu_B \langle s_z(\vec{r}) \rangle_T, \tag{2.45}$$

where $g_{Mn}\mu_B$ is the magnetic moment of one Mn^{2+} ion with $g_{Mn} \approx 2$ g-factor and Bohr's magneton μ_B; $\langle s_z(\vec{r}) \rangle$ is the average spin projection of the one Mn moment located at the point $\vec{r}$. Assuming the density $\rho(\vec{r})$ to be high, the discrete sum in equation 2.44 is replaced by an integral over volume, defining the exchange energy at equilibrium:

$$\mathcal{E}_{ex}(T) = -\frac{(\alpha - \beta)}{2g_{Mn}\mu_B} \int_V \sigma_z^X m_z(\vec{r}) |\Psi_X|^2(\vec{r}) \mathrm{d}^3\vec{r}. \tag{2.46}$$

The coupling of the Mn moments to an external magnetic field $\vec{B} \parallel Oz$ is described in terms of Zeeman Hamiltonian:

$$\mathcal{H}_Z = \sum_{\vec{R}_i} g_{Mn}\mu_B S_{i_z} B_z(\vec{r_i}) \tag{2.47}$$

and the Zeeman energy at thermal equilibrium is given by

$$\mathcal{E}_Z = -\int_V m_z(\vec{r}) B_z(\vec{r}) \mathrm{d}^3\vec{r}. \tag{2.48}$$

Equation 2.47 describes the Giant Zeeman effect which, in the low-field limit, can be approximated by the linear response of the Mn spin system on external magnetic field:

$$m_z(\vec{r}, T) = \chi_V(\vec{r}, T) B_z$$
$$\chi_V(\vec{r}, T) = \frac{\rho(\vec{r})(g_{Mn}\mu_B)^2 S(S+1)}{3k_B(T + T_{AF})(\vec{r})}, \tag{2.49}$$

where $\chi_V(T)$ is the magnetic susceptibility, $\rho(\vec{r})$ and T_{AF} are the effective density of magnetic ions and effective temperature, respectively, which take into account the anti-ferromagnetic interaction of next nearest-neighbor pairs. One can mention that the expression 2.49 for χ_V is similar to the Eq.1.19 with substitution of $\rho(\vec{r})$ instead of $N_0 x_{eff}$.

Using equation 2.46 the energy of the exciton in a DMS quantum dot in a uniform external magnetic field B_z is expressed in the form:

$$E_X^{\sigma_z^X = \pm 1} = -\frac{(\alpha - \beta)}{2g_{Mn}\mu_B} \sigma_z^X \int \chi_V(\vec{r}, T) |\Psi_X|^2(\vec{r}) B_z \mathrm{d}^3\vec{r}, \tag{2.50}$$

or, substituting 2.49:

$$E_X^{\sigma_z^X = \pm 1} = -\frac{(\alpha - \beta)S(S+1)g_{Mn}\mu_B}{6k_B(T + T_{AF})} \sigma_z^X B_z \int_V \rho(\vec{r}) |\Psi_X|^2(\vec{r}) \mathrm{d}^3\vec{r}. \tag{2.51}$$

Hence, equation 2.51 defines the slope of the PL energy shift at low field in $\sigma_\pm$ polarization:

$$E_X^{\sigma = \pm 1} = -\chi_E(T) B_z$$
$$\chi_E(T) = \sigma_z^X \frac{(\alpha - \beta)S(S+1)g_{Mn}\mu_B}{6k_B(T + T_{AF})} \int_V \rho(\vec{r}) |\Psi_X|^2(\vec{r}) \mathrm{d}^3\vec{r} \tag{2.52}$$

At high external magnetic field ($B_Z > 3$ T) or low-temperature ($T < 3$ K) the linear approximation fails, as the energy of Zeeman shift saturates. At saturation the magnetization should be expressed in the form:

$$m_z(\vec{r}) = -(g_{Mn}\mu_B)S\rho(\vec{r}), \tag{2.53}$$

providing the expression for saturation energy:

$$E_{sat}^{\sigma^+} = \frac{(\alpha - \beta)S}{2} \int_V \rho(\vec{r}) |\Psi_X|^2(\vec{r}) \mathrm{d}^3\vec{r}. \tag{2.54}$$

The saturation energy is obtained from the experiment and it provides us a value of the integral in expression 2.54.

Comparing equations 2.47 and 2.46 one can make a conclusion, that in the case of an exciton localized in the quantum dot and in the absence of an external magnetic field, Mn spins are coupled to the spin of an exciton through the local exchange field $B_P(\vec{r})$, which is expressed in the form:

$$B_P(\vec{r}) = \frac{(\alpha - \beta)}{2g_{Mn}\mu_B}\sigma_{z_X}|\Psi_X|^2(\vec{r}), \tag{2.55}$$

which leads to the exchange energy given by

$$E_P = -\int_V \langle m_z(\vec{r})\rangle B_P(\vec{r})\mathrm{d}^3\vec{r}. \tag{2.56}$$

The average magnetization $\langle m_z(\vec{r})\rangle$ can be expressed in the form

$$\langle m_z(\vec{r})\rangle = \chi_V(\vec{r}, T)B_P(\vec{r}) \tag{2.57}$$

using the linear approximation. Substituting 2.57 in 2.56 and using expressions 2.55 one obtains the energy of the exciton magnetic polaron:

$$\begin{aligned} E_P &= \int_V \chi_V(\vec{r}, T)B_P^2(\vec{r})\mathrm{d}^3\vec{r} \\ E_P(T) &= \frac{(\alpha - \beta)^2 S(S+1)}{12k_B(T + T_{AF})}\int_V \rho(\vec{r})|\Psi_X|^4(\vec{r})\mathrm{d}^3\vec{r} \end{aligned} \tag{2.58}$$

Here, using definition 2.43, we obtain the expressions for polaron energy of neutral exciton:

$$E_P^X(T) = \frac{S(S+1)}{12k_B(T + T_{AF})}\int_V \rho(\vec{r})\left[\alpha^2|\psi_e|^4 + \beta^2|\psi_h|^4 + 2\alpha|\beta||\psi_e|^2|\psi_h|^2\right]\mathrm{d}^3\vec{r} \tag{2.59}$$

Each term in the expression 2.59 has the physical interpretation:

- $\alpha^2|\psi_e|^4$ characterizes a conduction band splitting induced by Mn spins polarization and probed by electrons;

- $\beta^2|\psi_h|^4$ characterizes a valence band splitting induced by Mn spins polarization and probed by holes;

- $2\alpha|\beta||\psi_e|^2|\psi_h|^2$ is the cross-term describing the probing of conduction band splitting by holes and vice-versa.

In the case of the negatively charged exciton, the terms describing the conduction band splitting are not present because of the opposite direction of two electrons spins, compensating each other:

$$E_P^h(T) = \frac{S(S+1)}{12k_B(T+T_{AF})} \int_V \rho(\vec{r}) \left[\beta^2|\psi_h|^4\right] \mathrm{d}^3\vec{r} \qquad (2.60)$$

However, as one can see in Fig.2.5, the emission energy differs from the polaron energy by the value of Zeeman shift caused by a single electron remaining in the QD after the exciton recombination:

$$E_{PL}^{CX}(T) = \frac{S(S+1)}{12k_B(T+T_{AF})} \int_V \rho(\vec{r}) \left[\beta^2|\psi_h|^4 + \alpha|\beta||\psi_e|^2|\psi_h|^2\right] \mathrm{d}^3\vec{r} \qquad (2.61)$$

In order to obtain a theoretical magnetic polaron energy one needs to calculate the value of the integral proportional to $|\Psi_X|^4$ in expression 2.58. We will show next, that using the exciton photoluminescence emission linewidth in the absence of an applied magnetic field, the value can be determined experimentally.

Let's consider two magnetic ions at points $\vec{R}_i$ and $\vec{R}_j$ with a value of spin projection on z-axis S_{i_z} and S_{j_z}, respectively: in this case, the energy of the exchange interaction, which defines the red shift of exciton energy is given by definition 2.44 in the form of discrete sum as:

$$E_X = \frac{(\alpha-\beta)}{2} \sum_{\vec{R}_i} S_{i_z}\sigma_{z_X}|\Psi_X|^2(\vec{R}_i). \qquad (2.62)$$

The variance of the exciton energy is defined by:

$$\langle E_X^2 \rangle = \frac{(\alpha-\beta)^2}{4} \sum_{\vec{R}_i}\sum_{\vec{R}_j} \langle S_{i_z}S_{j_z}\rangle |\Psi_X|^2(\vec{R}_i)|\Psi_X|^2(\vec{R}_j). \qquad (2.63)$$

In the absence of an external magnetic field and of a magnetic polaron, the mean value of spin fluctuations $\langle S_{i_z}\rangle$ and $\langle S_{j_z}\rangle$ is equal to zero and the spins are assumed to be not correlated:

$$\langle S_{i_z}S_{j_z}\rangle = \langle S_{i_z}^2\rangle \delta_{ij}. \qquad (2.64)$$

Using the fluctuation dissipation theorem, for each spin we write:

$$\left\langle S_{i_z}^2 \right\rangle = -\frac{k_B T}{g_{Mn}\mu_B}\frac{\mathrm{d}\left\langle S_{i_z}\right\rangle}{\mathrm{d}B} \tag{2.65}$$

Substituting expressions 2.65 and 2.64 in 2.63 one obtains:

$$\left\langle E_X^2 \right\rangle = \frac{(\alpha-\beta)^2}{4}\sum_{\vec{R}_i} -\frac{k_B T}{g_{Mn}\mu_B}\frac{\mathrm{d}\left\langle S_{i_z}\right\rangle}{\mathrm{d}B}|\Psi_X|^4(\vec{R}_i). \tag{2.66}$$

The number of Mn spins is assumed to be large, allowing to transform the discrete sum in the integral over volume of spin density:

$$\left\langle E_X^2 \right\rangle = \frac{(\alpha-\beta)^2}{4}\int_V -\frac{\rho(\vec{r})k_B T}{(g_{Mn}\mu_B)^2}(g_{Mn}\mu_B)\frac{\mathrm{d}\left\langle S_{i_z}\right\rangle(\vec{r})}{\mathrm{d}B}|\Psi_X|^4(\vec{R}_i)\mathrm{d}^3\vec{r}. \tag{2.67}$$

One can find in the equation 2.67 the volume magnetization density $\langle m_z \rangle = -\rho(\vec{r})(g_{Mn}\mu_B)\langle S_{i_z}\rangle(\vec{r})$ and the derivative of magnetization density with respect to the magnetic field, which is nothing else than magnetic susceptibility $\chi_V = \frac{\mathrm{d}\langle m_z\rangle(\vec{r})}{\mathrm{d}B}$. Hence, using the definition of B_P given by Eq.2.55, one can rewrite the equation 2.67 in the following way:

$$\left\langle E_X^2 \right\rangle = \int_V k_B T \chi_V B_P^2(\vec{r})\mathrm{d}^3\vec{r}, \tag{2.68}$$

which coincides with definition of E_P (Eq.2.58), multiplied by $k_B T$:

$$\left\langle E_X^2 \right\rangle = k_B T E_P. \tag{2.69}$$

The full width at half-maximum $\Delta E_{\frac{1}{2}}$ of the exciton photoluminescence line, having a Gaussian distribution shape, is related to the energy variance as:

$$\boxed{\Delta E_{\frac{1}{2}} = \sqrt{8\ln 2 \left\langle E_X^2 \right\rangle} = \sqrt{8\ln 2 k_B T E_P}}. \tag{2.70}$$

The combination of the expression 2.68 with the one for saturation energy (2.54) allows us to determine all the parameters of the exciton magnetic polaron from the quantities ΔE and E_{sat} obtained from the experiment.

Among parameters which characterize the DMS system, the most interesting are the average exchange field $\bar{B}_P$ and the number of spins N_P involved in the formation of the exciton magnetic polaron.

An average exchange field is obtained from expression

$$\bar{B}_P = \frac{E_P(T)}{\bar{M}_P(T)}, \tag{2.71}$$

where $\bar{M}_P(T)$ is the magnetic moment induced in the quantum dot:

$$\bar{M}_P = \int_V \langle m_z(\vec{r}) \rangle \, \mathrm{d}^3\vec{r}. \tag{2.72}$$

Substituting expression for the average magnetization 2.57, one obtains:

$$\bar{M}_P(T) = \frac{S(S+1)g_{Mn}\mu_B(\alpha-\beta)}{6k_B(T+T_{AF})} \int_V \rho(\vec{r})|\Psi_X|^2(\vec{r})\mathrm{d}^3\vec{r} \tag{2.73}$$

Using expressions for magnetic polaron energy, we obtain the value of an average exchange field independent on temperature:

$$\bar{B}_P = \left[\frac{(\alpha-\beta)}{2g_{Mn}\mu_B}\right] \frac{\int_V \rho(\vec{r})|\Psi_X|^4(\vec{r})\mathrm{d}^3\vec{r}}{\int_V \rho(\vec{r})|\Psi_X|^2(\vec{r})\mathrm{d}^3\vec{r}}, \tag{2.74}$$

where the ratio of integrals can be expressed using 2.66 and 2.54 as

$$\frac{\int_V \rho(\vec{r})|\Psi_X|^4(\vec{r})\mathrm{d}^3\vec{r}}{\int_V \rho(\vec{r})|\Psi_X|^2(\vec{r})\mathrm{d}^3\vec{r}} = \frac{\langle E_X^2 \rangle}{E_{sat}} \frac{6}{(\alpha-\beta)(S+1)} \tag{2.75}$$

which determines $\bar{B}_P$ as

$$\bar{B}_P = \frac{3\langle E_X^2 \rangle}{(g_{Mn}\mu_B)E_{sat}(S+1)} \tag{2.76}$$

Finally, the average number of spins N_P is determined from the relation $\bar{M}_P = N_P\chi_{Mn}\bar{B}_P$, which gives

$$N_P = \frac{\left[\int_V \rho(\vec{r})|\Psi_X|^2(\vec{r})\mathrm{d}^3\vec{r}\right]^2}{\int_V \rho(\vec{r})|\Psi_X|^4(\vec{r})\mathrm{d}^3\vec{r}} = \frac{\langle E_X^2 \rangle}{E_{sat}} \frac{3}{(\alpha+|\beta|)(S+1)}, \tag{2.77}$$

or, using 2.75:

$$N_P = \frac{E_{sat}^2}{\langle E_X^2 \rangle} \left[\frac{(S+1)}{3S}\right]. \tag{2.78}$$

The comparison between the "exchange box" model and a model based on exciton wave function is given in the table:

	Exchange box model	Envelope function model
E_P	$E_P = \frac{(\alpha-\beta)^2 S(S+1)}{12K_B T} \frac{N_0 x_{eff}}{V_{QD}}$	$E_P(T) = \frac{(\alpha-\beta)^2 S(S+1)}{12K_B T} \int_V \rho(\vec{r})\|\psi\|^4(\vec{r})\mathrm{d}^3\vec{r}$
B_P	$B_P = \frac{(\alpha-\beta)}{2g_{Mn}\mu_B} \frac{1}{V_{QD}}$	$\bar{B}_P = \frac{(\alpha-\beta)}{2g_{Mn}\mu_B} \frac{\int_V \rho(\vec{r})\|\Psi_X\|^4(\vec{r})\mathrm{d}^3\vec{r}}{\int_V \rho(\vec{r})\|\Psi_X\|^2(\vec{r})\mathrm{d}^3\vec{r}}$
N_P	$N_P = N_0 x_{eff} V_{QD}$	$N_P = \frac{\left[\int_V \rho(\vec{r})\|\Psi_X\|^2(\vec{r})\mathrm{d}^3\vec{r}\right]^2}{\int_V \rho(\vec{r})\|\Psi_X\|^4(\vec{r})\mathrm{d}^3\vec{r}}$

The envelope function model developed above is free from assumptions introduced in the "exchange box" model. All the formulas of the "exchange box" can be derived from this model assuming a uniform density of Mn atoms $\rho = N_0 x_{eff}$ and a homogeneous exchange field B_P. Nevertheless, having obtained the equation 2.70 which is equal to Eq.2.24 we have demonstrated, that these non realistic assumptions of "exchange box" model do not introduce considerable errors in the determination of magnetic polaron parameters.

In order to verify both models it is worth to try to describe the magnetic polaron formation process basing on an even more general approach.

2.6.2   Beyond the exchange box model: free energy approach

In this section we will show that the magnetic polaron formation process can be described in terms of the free energy of the system. It will allow us to describe the absorption of a photon, the magnetic polaron formation and the recombination processes, using the expression for the free energy at each stage.

a. Basic theory

For the system of N paramagnetic spins ($S = -5/2... + 5/2$) forming discrete non degenerate quantum states with energies $E_s = S g_{Mn}\mu_B$, the free energy is expressed in the form:

$$F = -Nk_B T \ln(Z), \tag{2.79}$$

where Z is the partition function:

$$Z = \sum_s \mathrm{e}^{-\beta_T E_s} \tag{2.80}$$

with $\beta_T \equiv \frac{1}{k_B T}$. The exponential factor $\mathbf{e}^{-\beta_T E s}$ is known as the Boltzmann factor. The development of the sum 2.80 allows one to write the free energy in form:

$$F(T, B) = -Nk_B T \ln \left[\frac{\sinh\left(\frac{6\mu_B B}{k_B T}\right)}{\sinh\left(\frac{\mu_B B}{k_B T}\right)} \right] \tag{2.81}$$

The magnetization is nothing else than the first derivative of this function with respect to external magnetic field B:

$$M = -\frac{\partial F}{\partial B} = N(g_{Mn}\mu_B S) B_{5/2}\left(\frac{g_{Mn}\mu_B B}{k_B T}\right), \tag{2.82}$$

where $B_{5/2}$ is the Brillouin function for spin $S = 5/2$ (Eq.1.15). In the low-field limit, magnetization increases linearly with field $M \approx \chi_V B$ with χ_V - magnetic susceptibility defined as:

$$\chi_V = \frac{N(g_{Mn}\mu_B)^2 S(S+1)}{3k_B T}. \tag{2.83}$$

Using the Legendre transformation, the free energy can be expressed as a function of M and T in the form:

$$F^\star(M, T) = -Nk_B T \ln \left[\frac{\sinh\left(\frac{6}{5}B_{5/2}^{-1}\left(\frac{M}{M_{sat}}\right)\right)}{\sinh\left(\frac{1}{5}B_{5/2}^{-1}\left(\frac{M}{M_{sat}}\right)\right)} \right] + Nk_B T \left(\frac{M}{M_{sat}}\right) B_{5/2}^{-1}\left(\frac{M}{M_{sat}}\right), \tag{2.84}$$

with M_{sat} defined as $M_{sat} = N(g_{Mn}\mu_B)S$. Here, $B_{5/2}^{-1}$ is the function reciprocal to the Brillouin function. The magnetization at thermal equilibrium is obtained by the equation

$$\frac{\partial \widetilde{F}^\star}{\partial M} = 0, \tag{2.85}$$

where the free energy is written in the form:

$$\widetilde{F}^\star(M, T) = (F^\star(M, T) - MB). \tag{2.86}$$

This choice allows the free energy function to be minimized by the magnetization. In the low-field limit, the free energy can be written as a function of magnetization M in the form:

$$\widetilde{F}^\star(M) = \frac{M^2}{2\chi} - MB \tag{2.87}$$

with magnetic susceptibility χ given by

$$\chi = \left(\frac{\partial M}{\partial B}\right)_T. \tag{2.88}$$

b. Application to the DMS quantum dot

Consider a quantum dot, which contains localized Mn spins, non interacting with each other. Their distribution is not necessarily uniform. Here, we limit the approach to the case of hole confined, or not, in the quantum dot. The envelope function of the hole is defined in form:

$$\psi_h = a\psi_{QD}(\vec{r}) + b\psi_B(\vec{r}), \tag{2.89}$$

where $\psi_{QD}(\vec{r})$ and $\psi_B(\vec{r})$ are the parts of the hole wave function situated inside the quantum dot and inside the barriers, respectively; a and b obey the relation $|a|^2+|b|^2 = 1$. $\psi_{QD}(\vec{r})$ and $\psi_B(\vec{r})$ are normalized:

$$\iiint \mathrm{d}^3\vec{r}|\psi_{QD}|^2(\vec{r}) = \iiint \mathrm{d}^3\vec{r}|\psi_B|^2(\vec{r}) = 1. \tag{2.90}$$

This assumption allows us to consider a tunable probability p of the hole presence inside the quantum dot, which can be adjusted whether continuously (for instance, by applying a bias to the system), or abruptly (in an optical transition, $p = a^2$, p increases rapidly from 0 to 1 (absorption) or decreases rapidly from 1 to 0 (recombination)).

The spin-hole coupling is described by the usual Kondo Hamiltonian assuming pure heavy holes:

$$\mathcal{H}_K = -\beta \sum_i \delta(\vec{r} - \vec{R}_i)s_z S_{z_i} \tag{2.91}$$

Magnetic ions assumed to be distributed only inside the dot: $\psi_B(\vec{R}_i) = 0$, and $\psi_{QD}(\vec{r})$ is fixed, i.e., in particular, it is not influenced by the spin-carrier interaction. The spin system experiences an interaction with the hole system, described by the Kondo Hamiltonian

$$\mathcal{H}_K = -p\beta s \sum_i \delta(\vec{r} - \vec{R}_i)S_{z_i}, \tag{2.92}$$

with $s = \pm\frac{1}{2}$ depending on the spin state of the hole. For $s = \frac{1}{2}$, the restriction to the spin system is

$$\mathcal{H}_K = -p \sum_i \frac{1}{2}\beta|\psi_{QD}|^2(\vec{R}_i)s_z S_{z_i} = -pM. \tag{2.93}$$

M is an operator acting on the spins, with the dimension of an energy. Its mean value $\langle M \rangle = Tr(\rho M)$, where ρ is a density matrix, is the conjugate variable of the external parameter p. For given values of the temperature T and hole presence probability p, $\langle M \rangle$ takes the value which minimizes the free energy (Eq.2.87) of the spin system

$$\widetilde{F}^{\star}(M) = \frac{M^2}{2\chi} - pM \tag{2.94}$$

Hence, $\langle M \rangle = \chi p$ where χ in linear response regime is given by the fluctuation-dissipation theorem

$$\chi = (\langle M^2 \rangle - \langle M \rangle^2)/k_B T. \tag{2.95}$$

At zero field and $p = 0$, we have $\langle S_{z_i} \rangle = 0$, $\langle \mathcal{H}_K \rangle = 0$ and $\langle S_{z_i} S_{z_j} \rangle = \delta_{ij} \frac{S(S+1)}{3}$. The free energy F_0 in this state is then

$$F_0^{\star}(\langle M \rangle) = \frac{\langle M \rangle^2}{2\chi} \tag{2.96}$$

and it is minimum for $\langle M \rangle = 0$. The magnetic fluctuations are described by the second moment (summations run over the sites occupied by Mn):

$$\langle M^2 \rangle = \sum_i \frac{1}{2} \beta |\psi_{QD}|^2(\vec{R}_i) \times \sum_j \frac{1}{2} \beta |\psi_{QD}|^2(\vec{R}_j) \langle S_{z_i} S_{z_j} \rangle =$$
$$= \beta^2 \sum_i |\psi_{QD}|^4(\vec{R}_i) \frac{S(S+1)}{12} \tag{2.97}$$

c. Absorption-recombination cycle

Now consider an optical cycle, absorption-recombination. Initially (in the absence of an applied field), the spin system is in the state, characterized by the free energy $F_0^{\star}(\langle M \rangle)$ (see Fig.2.29). The creation of an electron-hole pair in the dot increases rapidly p from 0 to 1. In this fast process, $\langle M \rangle$ keeps it initial value $\langle M \rangle_0 = 0$. The magnetic free energy stays at 0: there is no polaron effect in the absorption process and the transition energy is the bare exciton energy.

Once hole is in the dot ($p = 1$), the magnetic free energy of the spin system is

$$F_1^{\star}(\langle M \rangle) = \frac{M^2}{2\chi} - M \tag{2.98}$$
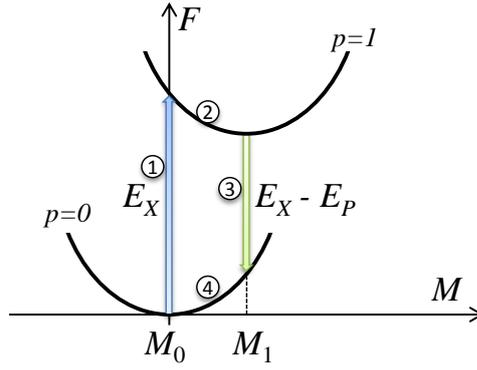
FIGURE 2.29: Free energy approach scheme

and $\mathrm{d}F_1^\star/\mathrm{d}M = -1$. Hence, a fluctuation of $\langle M \rangle$ induces a fluctuation of the magnetic energy, and this broadens the line by the same amount: the second moment of the line (proportional to the square of the linewidth) is given by $\langle E^2 \rangle - \langle E \rangle^2 = |\mathrm{d}F_1^\star/\mathrm{d}M| \left[\langle M^2 \rangle - \langle M \rangle^2 \right]$. Hence,

$$\langle E^2 \rangle = \beta^2 \sum_i |\psi_{QD}|^4(\vec{R}_i) S(S+1)/12 \qquad (2.99)$$

If the exciton lifetime is long enough, the spin system relaxes to the value which minimizes the free energy $F_1^\star(\langle M \rangle)$. Hence, $\langle M \rangle_1 = \chi = \left[\langle M^2 \rangle - \langle M \rangle^2 \right] /k_B T$, or

$$\langle M \rangle_1 = \beta^2 \sum_i |\psi_{QD}|^4(\vec{R}_i) S(S+1)/12 k_B T \qquad (2.100)$$

The minimum of the free energy is at $F = -\chi/2 = -\langle M \rangle_1 /2$.

In the recombination of the electron-hole pair, p decreases rapidly back to 0, $\langle M \rangle$ again keeps its initial value which is now $\langle M \rangle_1$. The free energy in the final state is $F_0^\star(\langle M \rangle_1) = \langle M \rangle_1 /2$. The transition energy is decreased by $\langle M \rangle_1$: this is the so-called polaron energy E_P. Hence,

$$\boxed{E_P = \frac{(\langle E^2 \rangle - \langle E \rangle^2)}{k_B T} = \beta^2 \sum_i |\psi_{QD}|^4(\vec{R}_i) S(S+1)/12 k_B T} \qquad (2.101)$$

Using Eq.2.101 one connects the polaron energy with the emission linewidth, similarly to the previous models. The only conditions used to obtain this equation are the linear response of magnetization on the presence of external field and rigid hole envelope function. Combination of Eq.2.101 with an expression for saturation energy E_{sat} defined

as

$$E_{sat} = \frac{1}{2}\beta \sum_i |\psi_{QD}|^2(\vec{R}_i)S \tag{2.102}$$

allows us to determine all the characteristic parameters of magnetic polaron.

Hence, we have shown that using the theoretical approach based on the free energy determination, we can independently obtain the same relation between the emission linewidth and the energy of magnetic polaron as the ones, obtained using the envelope function model (Eq.2.70) and an "exchange box" model (Eq.2.24). We prove therefore, that this relation is not just a consequence of assumptions of the simplified model, but it has a real physical meaning.

2.6.3   Numerical calculation of MP parameters

The more general theoretical model developed in Sect.2.6.1 allows us to calculate the magnetic polaron energy associated with an exciton and with a negatively charged exciton. In this section we will try to understand the differences we observe in the magnetic polaron parameters associated with an exciton and with a charge exciton. In order to estimate these parameters, we perform a numerical calculation of electron and hole confinement potential and of the electron and hole envelope functions. Knowing the geometrical parameters of the quantum dot, values of band gap energies together with the relative offsets, one can calculate the confinement energy of the charge carrier and its envelope function. The Coulomb attraction between an electron and a hole creates an additional potential which helps to confine the carrier in the QD. The problem is expressed in terms of a particle in a finite-walled box of height $h(\rho)$, which can be evaluated from the TEM-image. We will use the TEM image from work [59] obtained for CdTe/ZnTe quantum dot (see Fig.2.31), assuming that the presence of Mn atoms does not change significantly the shape of the quantum dot. As it was shown in Sec.1.2.2, at
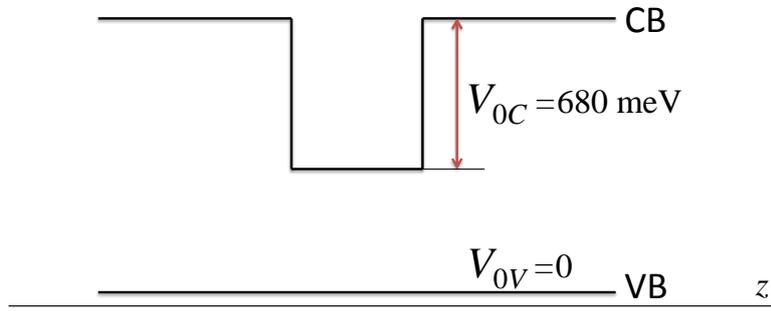

FIGURE 2.30: Scematic illustration of the conduction and valence band offsets used in the calculation

Mn concentration of 8.3%, with a contribution of strain taken into account, the valence band offset between CdMnTe and ZnTe is equal to zero. Hence, the hole is confined by the Coulomb attraction of an electron in case of the neutral exciton or of two electrons in case of the negatively charged exciton (see Fig.2.30).

  The height profile in cylindrical coordinates $h(\rho)$ of the quantum dot is modeled by a Gaussian function with a width σ and maximum height $h_{QD} = h_{WL} + h(0)$, where h_{WL} is the wetting layer height ($h_{WL} = 1.7$ nm is estimated from TEM image) and $h(0)$ is a free parameter corresponding to the Gaussian amplitude. The lateral FWHM of the
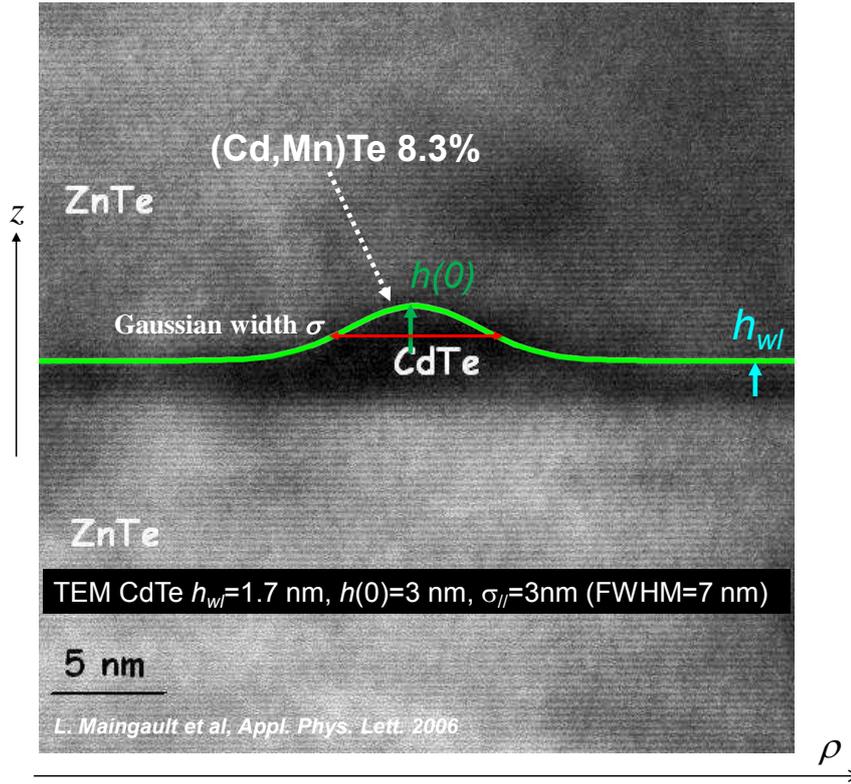
FIGURE 2.31: TEM image of a single CdTe/ZnTe QD obtained in work [59]

quantum dot is determined by the Gaussian width σ as $L = \sqrt{8\ln(2)}\sigma$.

We use the method of probe functions in order to solve the Schroedinger equation of a charge carrier confined in a potential well with defined parameters [71]. The calculation is performed in several steps. At the first step, we calculate the electron energy in a quantum well having a variable width $h(\rho)$. Far from the quantum dot, the confinement potential is determined by the wetting layer of thickness h_{WL} (see Fig.2.31) and in the center of the quantum dot - by h_{QD}. Following the CdMnTe layer thickness $h(\rho)$, we can calculate the electron energy profile $\mathbf{E}_e(\rho)$ at each point ρ by solving the Schroedinger equation

$$\mathcal{H}_{QW} = \frac{p_z^2}{2m_e^*} + \mathbf{V}[z, h(\rho)], \tag{2.103}$$

where the potential $\mathbf{V}[z, h(\rho)]$ is defined in the form:

$$\begin{cases} \mathbf{V}[z, h(\rho)] = 0, |z| \leq \dfrac{h(\rho)}{2} \\ \qquad\quad = V_{0C}, |z| > \dfrac{h(\rho)}{2} \end{cases} \tag{2.104}$$

the effective mass of the electron has the value $m_e^* = 0.1 m_0$. A probe Gaussian function

$$|\phi_{\perp e}(z)|^2 = \frac{1}{\sigma_{\perp e}\sqrt{2\pi}} \; \mathrm{e}^{-\frac{z^2}{2\sigma_{\perp e}^2}} \tag{2.105}$$

with a width $\sigma_{\perp e}$ taken as a free parameter, is used in order to determine the energy level and the wave function of the electron in the dot along the z-axis. The value of the energy of the electron obtained for the QD depicted in Fig.2.31 is 320 meV.

At the second step, we calculate the total confinement of an electron in the QD by solving the Schroedinger equation

$$\mathcal{H}_{\parallel} = \frac{p_{\parallel}^2}{2m_e^*} + \mathbf{E}_e(\rho), \tag{2.106}$$

where $\mathbf{E}_e(\rho)$ is the electron energy profile calculated at the step 1. Using a probe Gaussian function

$$\left|\phi_{\parallel e}(\rho)\right|^2 = \frac{1}{\bar{\sigma}_{\parallel e}\sqrt{2\pi}} \; \mathrm{e}^{-\frac{\rho^2}{2\bar{\sigma}_{\parallel e}^2}}, \tag{2.107}$$

we obtain the the energy level and the wave function of the electron in the dot in the plane. The final envelope function of an electron is determined as

$$\phi_e(z,\rho) = \bar{\phi}_{\perp e}(z)\phi_{\parallel e}(\rho), \tag{2.108}$$

where

$$\left|\bar{\phi}_{\perp e}(z)\right|^2 = \frac{1}{\sigma_{\perp e}\sqrt{2\pi}} \; \mathrm{e}^{-\frac{z^2}{2\bar{\sigma}_{\perp e}^2}} \tag{2.109}$$

and

$$\bar{\sigma}_{\perp e} = \int |\phi_{\parallel e}(\rho)|^2 \sigma_{\perp e}(\rho) 2\pi\rho \mathrm{d}\rho. \tag{2.110}$$

We can now calculate the envelope function of the hole. For this, we solve the Schroedinger equation

$$\mathcal{H}_{\parallel} = \frac{p_{\parallel}^2 + p_z^2}{2m_h^*} + \mathbf{V}_{Coul}(z,\rho), \tag{2.111}$$

where $\mathbf{V}_{Coul}(z,\rho)$ is the Coulomb potential created by the electrons and seen by the hole. It is defined by

$$\mathbf{V}_{Coul}(z,\rho) = - \iiint \frac{\mathbf{Q}|e||\phi_e|^2(\vec{r'})\mathrm{d}^3 r'}{4\pi\varepsilon_0\varepsilon_r|\vec{r}-\vec{r'}|}, \tag{2.112}$$

where $|e|$ is the electron charge and **Q** is the number of electrons. In the case of a neutral exciton, this number is equal to 1 and for the negatively charged exciton - to 2. Using a probe function defined by

$$|\phi_h(z,\rho)|^2 = \frac{1}{\sigma_{\perp h}\sqrt{2\pi}}\,\mathbf{e}^{-\frac{z^2}{2\sigma_{\perp h}^2}} \times \frac{1}{\sigma_{\parallel h}\sqrt{2\pi}}\,\mathbf{e}^{-\frac{\rho^2}{2\sigma_{\parallel h}^2}}, \qquad (2.113)$$

we obtain the envelope function of the hole and its energy level.
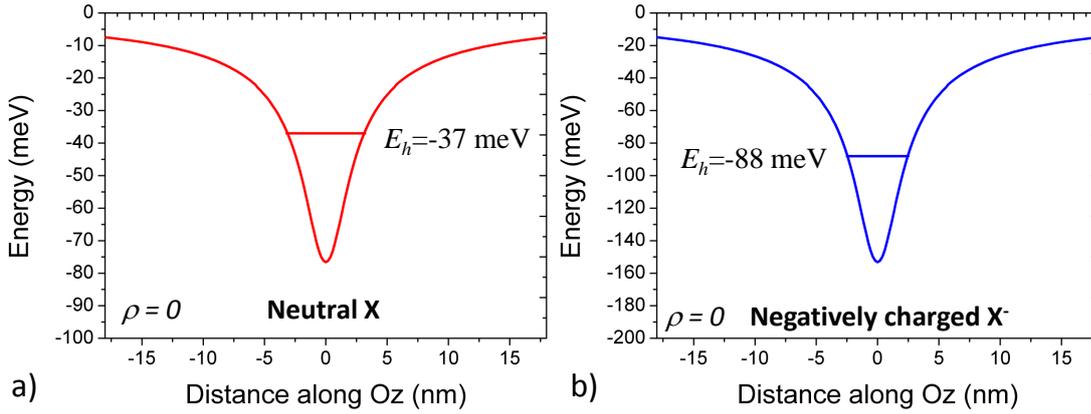
FIGURE 2.32: Confinement potential seen by the hole and created in CdMn(8.3%)Te/ZnTe QD by: a) one electron (neutral exciton), b) two electrons (negatively charged exciton)

In Fig.2.32 the results of calculation of the confinement potential created by the electron and seen by the hole, are shown for the case of neutral exciton (a) and negatively charged exciton (b). From this figure we can conclude that the magnetic polaron created by the negatively charged exciton must be characterized by a larger polaron energy and a larger exchange field, because the two electrons create a deeper confinement potential for the hole which results in stronger localization of the hole envelope function in the quantum dot and, as a result, stronger exchange interaction with the Mn magnetic moments.

Having calculated the confinement energy for an electron and a hole in a DMS quantum dot with a given height and width, we can now vary these parameters and calculate the emission energy of the exciton confined in the quantum dots of different sizes. The result is shown in Fig.2.33(a): for each value of quantum dot height we calculate the confinement potentials for electron and a hole and determine the emission energy for different widths of the quantum dot. The resulting map of exciton emission energies allows us to determine the range of quantum dots sizes, corresponding to the emission energy
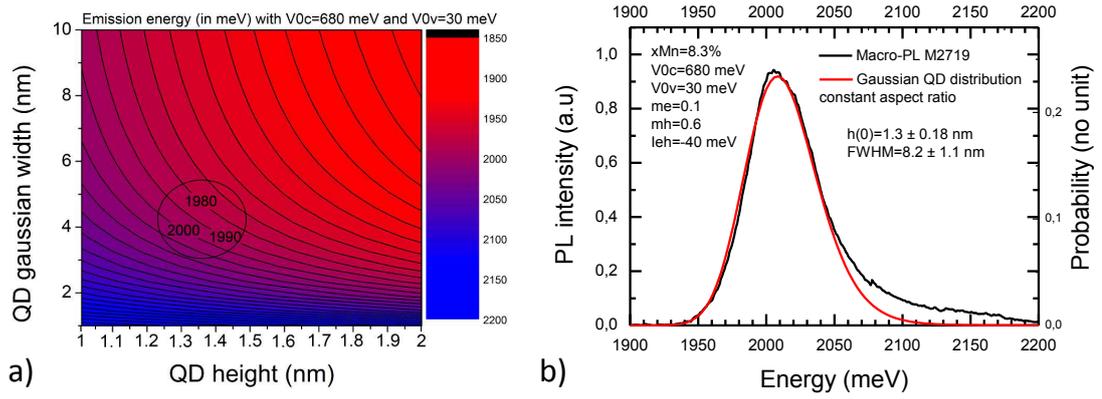
FIGURE 2.33: a) Exciton emission energy plotted as a function of lateral size and height of the quantum dot. b) Comparison between the macro-PL spectrum of CdMn(10%)Te quantum dots and calculated distribution of emission energies.

distribution, observed experimentally. In Fig.2.33(b) the comparison between the experimental macro-photoluminescence spectrum of the CdMn(10%)Te/ZnTe quantum dots and the calculated distribution of the exciton emission energies for quantum dots with size parameters having a constant aspect ratio, is demonstrated. The good agreement between experiment and calculation allows us to assess the size parameters of quantum dots in this sample. Excitons confined in quantum dots with heights $h(0) = 1.3 \pm 0.2$ nm, and widths $L = 8.2 \pm 1.1$ nm emit in the experimentally observed energy range.
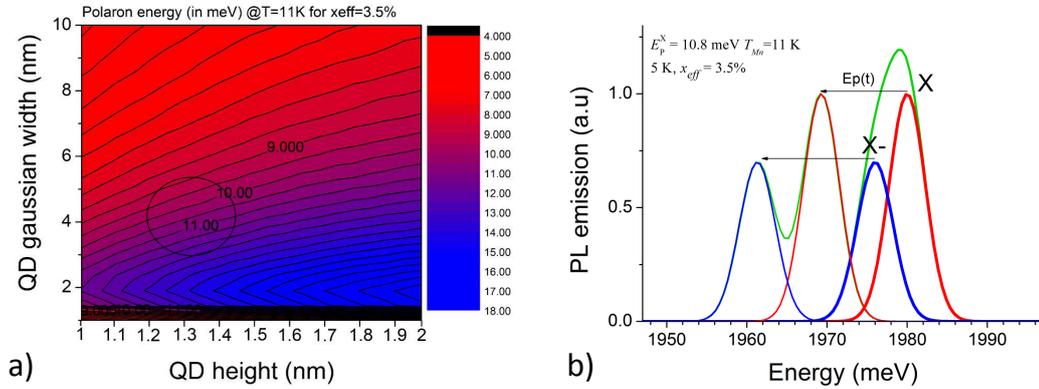

FIGURE 2.34: a) Exciton magnetic polaron energy plotted as a function of lateral size and height of the quantum dot. b) Calculated spectrum of a single CdMn(8.3%)Te quantum dot before (bold solid lines) and after (thin lines) the MP formation

The exciton magnetic polaron energy can be determined by this calculation for a given width and height of the quantum dot. Following the procedure described above, we obtain the parameters of the charge carriers envelope functions $|\psi_e|$ and $|\psi_h|$. Then, using equation 2.59, we calculate the MP energy formed with exciton. In order to calculate the energy of a MP formed with a negatively charged exciton, we calculate the Coulomb

confinement potential created for a hole by two electrons and determine the parameters of the hole envelope function. Then, using Eq.2.60, we calculate the polaron energy of such system. Combining the two previous calculations, we obtain the photoluminescence spectrum of a quantum dot with a given size before and after the MP formation. An example is plotted in Fig.2.34(a): calculation provides the emission energy of an exciton (or a trion), and the emission linewidth is determined by the energy of magnetic polaron (Eq.2.25). The result of these calculations corresponds to experimental observations: the energy of the MP formed with a negatively charged exciton is larger than the one of a neutral exciton MP ($E_P^C X = 1.4 E_P^X$). We have confirmed by this calculation that the observed difference in MP energies is a direct consequence of the Coulomb interaction of electrons and a hole.

Repeating the calculation of the exciton MP energy for the distribution of quantum dot sizes determined previously, we obtain the map shown in Fig.2.34(a). One can see from this figure that exciton magnetic polaron energies are comprised between 9 and 14 meV, which is in agreement with experimental observations.

Hence, the calculation based on the confinement potential determination allows one to assess the parameters of the exciton magnetic polaron and determine the characteristic size of the quantum dots. This calculation shows that even in the absence of the potential well for the hole formed by the valence band offset, the formation of magnetic polaron is still possible due to the confining potential created by an electron. This method can be used in order to determine the magnetic polaron parameters in other types of DMS heterostructures, i.e. DMS nanowires the structural parameters of which can be retrieved by TEM and EDX studies.

2.7   Influence of Mn concentration

In Section 2.5, the exciton magnetic polaron parameters have been obtained for the most concentrated sample of the set: CdMn(10%)Te/ZnTe. In this Section we will present parameters of magnetic polaron at thermal equilibrium for other samples of the set, obtained using single dot magneto-optical spectroscopy.

2.7.1   Thermal equilibrium parameters

For each sample, exciton emission linewidth and Zeeman shift saturation energy have been determined. Following the same procedure as used in Section 2.5, all the characteristic parameters have been determined. However, time-resolved measurements have not been performed for all the samples of the set. As it will be demonstrated below, the polaron formation process is detectable only when the polaron energy exceeds the emission linewidth. Hence, the procedure of Zeeman shift saturation energy determination is divided in several steps: the first step is to assume that the polaron is not formed and fit the magnetic field dependence using Eq.2.36 fixing $B_P = 0$ and $m = 0$. At second step we calculate the exchange field, using Eq.2.28 and substitute it in Eq.2.36 to fit the experimental data adjusting parameter m. In Table.2.35 obtained parameters of magnetic polaron for all samples of the set are listed.

x_{Mn}(%)	FWHM (meV)	γ(meV)	T_{Mn}(K)	E_P(meV)	E_{sat} (meV)	x_{eff} (%)	x_{tot} (%)	B_P (T)	N_P	V_{QD}(nm³)
0	0.2	0.08	-	-	-	-	-	-	-	-
2	2	0.85	20	0.42	20	1.5	1.7	0.3	257	1200
4	4	1.70	18	1.98	32	2.3	3.5	0.7	155	455
6	5.6	2.38	13	5.10	40	2.9	5.5	1.0	131	310
8	7	2.97	13	7.91	45	3.3	7	1.4	107	220
10	8.6	3.65	13	11	49	3.6	8.5	2.1	80	160

FIGURE 2.35: Parameters of the exciton magnetic polaron formed in CdMnTe quantum dot with different Mn concentration.

In Fig.2.36 the effective Mn concentration is plotted as a function of total Mn concentration introduced in the quantum dot sample during the growth. Experimental points are obtained using the Eq.2.2 and a green line shows the calibration in work [72] for

(Cd,Mn)Te:

$$x_{eff} = x[0.265 \exp(-43.34x) + 0.735 \exp(-6.19x)]. \tag{2.114}$$

This phenomenological model is interpreted in terms of a formation of antiferromagnetically coupled nearest-neighbor Mn pairs. In the relevant field and temperature ranges,(0 to 5 T and 1.5 to 20K) in (Cd, Mn)Te, x_{eff} matches the number of Mn atoms which remain free when the nearest-neighbor pairs have been deducted.
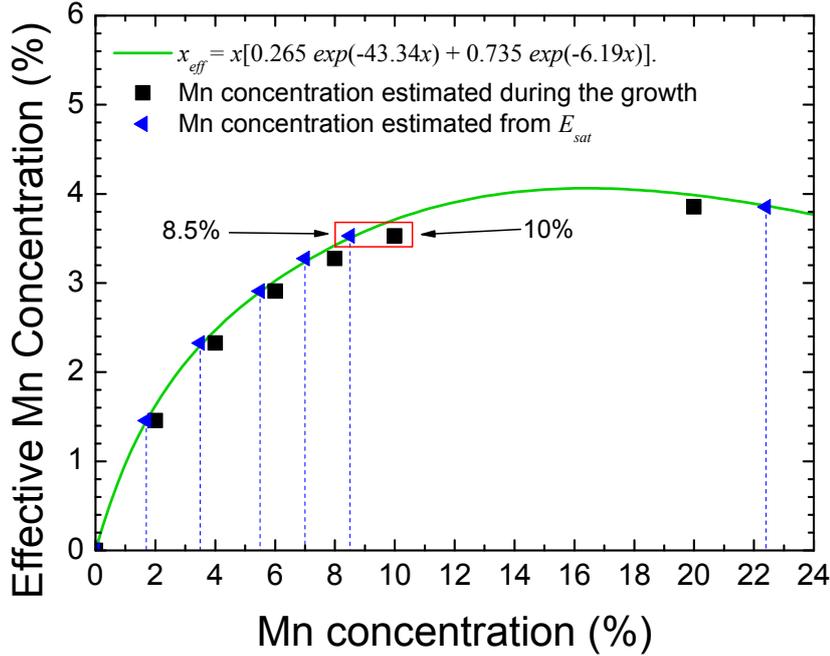

FIGURE 2.36: Effective Mn concentration as a function of nominal concentration introduced in the dot during the growth. The solid line represents the Eq.2.114.

Using this model the total Mn concentration in the quantum dot is corrected by reading the value of the fit function at the x_{eff} ordinate value. For example the corrected value of total Mn concentration for nominally 10% Mn sample is 8.5%. These corrected values has been used in numerical calculations described in Section 2.6.3.

In Fig.2.37 the comparison between the exciton emission linewidth $\Delta E_{\frac{1}{2}}$ and the magnetic polaron energy is shown. The X axis is the effective Mn concentration. The values of the polaron energy are calculated using Eq.2.25 for the fixed temperature $T_{Mn} = 12$ K.

At low Mn concentration ($x_{eff} < 3\%$) the effect of Mn heating plays an important role [73] and provokes the decrease of the polaron energy. The formation of magnetic polaron
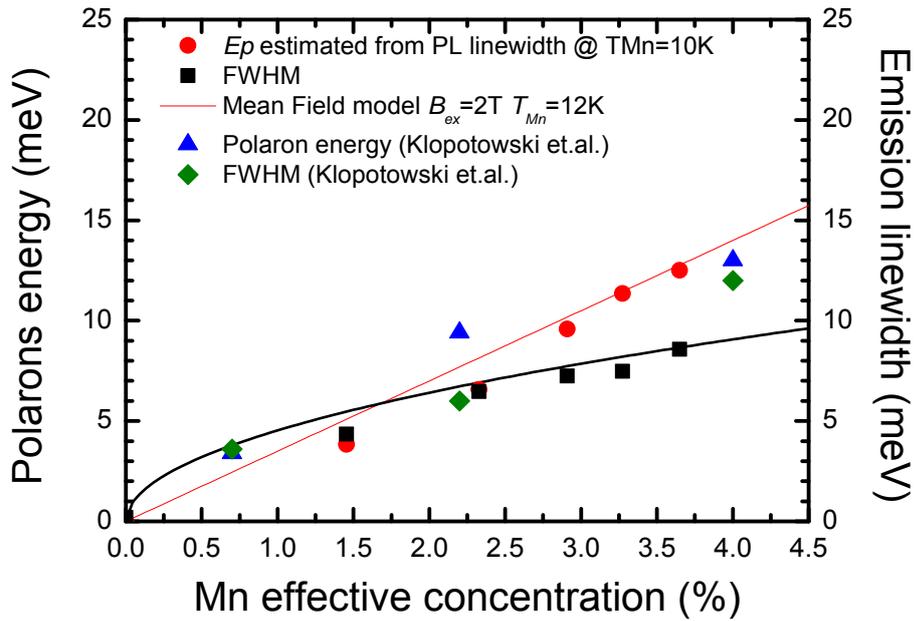
FIGURE 2.37: Comparison between magnetic polaron energy (circles) and exciton emission linewidth (squares) plotted as a function of Mn concentration for CdMnTe quantum dots studied in this work. Green and magenta triangles correspond to the data of the work [53].

can not be detected neither by CW experiments nor by time-resolved experiments. For the Mn concentration $x_{eff} > 3\%$ the effect of Mn heating is not anymore important and the MP formation is detectable. Blue triangles and green diamonds in Fig.2.36 show the values of the polaron energy and emission FWHM of CdMnTe/ZnMnTe QDs, studied in work [53]. The shift of the exciton line was observed in time-resolved measurements for sample with Mn concentration as low as 3.5%. The fact, that for this type of structures the magnetic polaron formation can be observed at lower Mn concentrations than for the structures studied in this work, is possibly due to the increased amount of magnetic ions overlapped by the exciton wave function.

2.8   Conclusion

In this Chapter the formation of the Exciton Magnetic Polaron in a single CdMnTe QD has been demonstrated. We have shown that the negatively charged exciton can be observed in the photoluminescence spectrum of a single QD by simply exciting it with a 532 nm laser wavelength. It was shown that MP forms with a neutral exciton and with a negatively charged exciton, and that the latter demonstrates a stronger effective exchange field. Simple "exchange box" model is not capable to explain this fact due to its oversimplified nature. In order to give an explanation, a new theoretical model based on a realistic form of the exciton wave function had been developed. It was demonstrated, that the same results obtained with "exchange box" can be obtained with a more general model and that this model allows one to describe the MP formation process with the charged exciton. A numerical calculation based on this model allows one to estimate the MP parameters and compare them to the observed experimental values. It was demonstrated that the results of this calculation are in a good agreement with experiments. Another result which is confirmed by this calculation is that the hole is confined in the quantum dot by the Coulomb potential created by one or two electrons. In the latter case, the exchange interaction between the spin of the hole and spins of magnetic atoms becomes stronger which results in higher polaron energy.

These results show that an information about the geometry and the structure of the quantum dot plays a crucial role. It is not very simple, however, to obtain this information for self-assembled quantum dots. The presence of a capping layer prevents Atom Force Microscopy studies and Transmission Electron Microscopy is hindered by the requirement of the fabrication of a very thin slice of the sample. That is why the 1D semiconductor structures attract more and more attention in present days. The structural analysis is much more easily accessible, the chemical composition of the single nanowire can be studied by analyzed by non-destructive methods and a better control on the growth process allows one to obtain different types and sizes of 1D structures.

Chapter 3

Optical properties of ZnTe and CdTe/ZnTe nanowires

3.1 Introduction: Nanowires for magneto-optics

In Chapter 2 we have studied the exciton magnetic polaron formation in CdMnTe/ZnTe self-assembled quantum dots. It was shown that the overlap of the exciton wave function with surrounding Mn ions plays an essential role in the EMP formation process. The lack of structural analysis data hinders the theoretical description of the EMP formation process forcing one to apply oversimplified models. Better properties can be achieved in specifically prepared structures with stronger exciton confinement and which offer a possibility of single object studies. Therefore, 1D DMS heterostructures are the promising candidates for the further investigations of EMP formation process. Semiconductor nanowires (NWs) can be grown by molecular beam epitaxy (MBE), using gold particles as catalyst. MBE technique provides a good control on growth conditions. The structure of nanowires can be investigated using well-known techniques, such as Transmission Electron Microscopy (TEM) and Energy Dispersive X-Ray analysis (EDX). Single nanowire optical studies and characterization can be easily done with the help of photoluminescence and cathodo luminescence measurements. The combination of all these techniques provides the necessary data, with which the formation of exciton magnetic polaron can be characterized.

There is currently a wide-spread interest for semiconductor nanowires, driven by their potential to constitute suitable building blocks for future nanoelectronic and nanophotonic devices [74]. During the past decade, selenides and tellurides II-VI NWs have been extensively investigated for various applications such as nano-pillar solar cells [75], photodetectors [76] or single photon sources [77]. Among II-VI's, ZnTe based nanowires are particularly promising by offering a large range of potentialities. They can be efficiently doped electrically [78] and magnetically [79, 80] due to the absence of the difference in temperature between growth and Mn incorporation processes, contrary to the case of magnetic III-V semiconductors [81]. As (Zn,Mn)Te can be doped strongly p-type so that ferromagnetism appears and transport studies are feasible in 2D[82], ZnTe based NWs are attractive for a basic study of spintronics mechanisms in 1D. CdTe quantum dots can be incorporated [83] and used as a single photon source or as a very sensitive optical probe of the spin properties [6]. A good control and the optimization of the growth conditions are still prerequisites to improve the electronic and optical properties of the nanowires.

ZnTe is an interesting material for spintronic and optoelectronic future devices as well as for fundamental research. It is a direct band gap semiconductor ($E_g = 2.26$ eV at room temperature) and it can be easily p-type doped. In the form of nanowire, it could be used as a 1D building block for prospective nanodevices, as already shown for other p-type nanowires [74, 84]. Among others, prospective applications for ZnTe nanowires(NWs) are high performance visible/ultraviolet photodetectors, field-effect transistors and green-light emitting diodes [78, 85]. Moreover, ZnTe nanowires can be grown with CdTe insertions facilitating the control of quantum dot size and positioning [83]. The possibility of incorporating Mn impurities in ZnTe NWs with CdTe quantum dot insertions is specially promising to investigate the properties of diluted magnetic semiconductors incorporated in NWs. The main advantage of these material system is the feasibility of the low-temperature growth compatible with the Mn incorporation.

In this Chapter we present first results on non magnetic nanowires of pure ZnTe and ZnTe nanowires with a CdTe insertion. The optical properties of single nanowires will be studied by micro-photoluminescence. Excitation and emission polarization studies will be provided in order to demonstrate the peculiar properties of 1D nanostructures. Diffusion of electron-hole pairs will be characterized by cathodo-luminescence studies. It will be shown that emission energy is influenced by strain and quantitative analysis of such an effect will be provided. Emission lines identification will be performed for

the spectrum of ZnTe nanowire with CdTe insertion. 0D confinement and single-photon emitter properties will be studied by photon correlation measurements. The influence of temperature on exciton confinement will be studied.

These results are obtained in collaboration with CEA-INAC laboratory, which provided us the samples and their characterization by TEM, EDX and SEM, in course of the ANR "MagWires" project. The optical properties studies have been performed in Institut Neel, CNRS.

3.2 Optical properties of ZnTe nanowires

3.2.1 Sample description

This section is devoted to the ZnTe nanowires sample growth performed by P.Rueda-Fonseca (INAC), E.Bellet-Amalric (INAC) and S.Tatarenko (NEEL). TEM characterization performed by M. Den Hertog (NEEL) and C. Bougerol (NEEL). ZnTe nanowires are grown by MBE using gold-catalyst particles. Nanowire growth starts from a 500 nm-thick ZnTe⟨111⟩ buffer layer grown over a GaAs⟨111⟩B substrate. A thin layer of gold is deposited over the ZnTe layer. The sample is subsequently annealed at 350 °C to form gold droplets. The nanowires are then grown at the same temperature. As we observed that Te-rich conditions result in a larger diffusion length on the ⟨111⟩ ZnTe surface the present NWs were grown with a Zn:Te flux ratio 1:2.3, for 30 or 60 min. More details on the growth of these ZnTe nanowires (and of the ZnTe buffer layer) are published in [86].

Typical ZnTe nanowires are shown in Fig. 3.1. This sample presents an ultra-low-
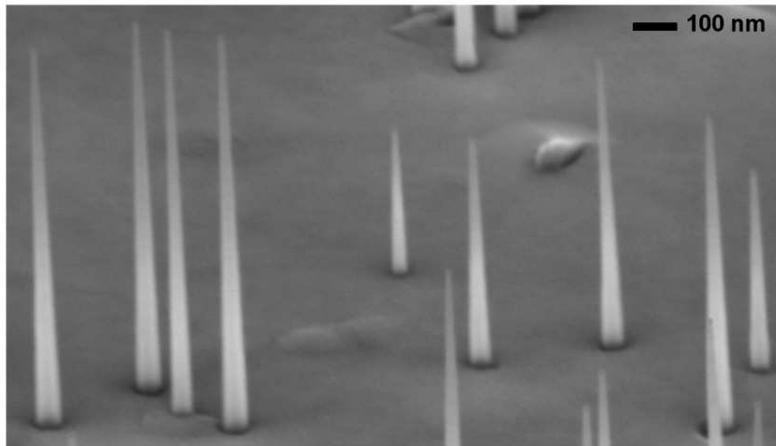
FIGURE 3.1: SEM image of ZnTe nanowires on as-grown sample

density of nanowires (2 NW per μm^2). Nanowires are tapered: they have a thick base and a very thin tip. In average nanowire diameter decreases from 60 nm at the base to 15 nm at the level of the catalyst particle. The resulting conic shape is due to lateral growth induced by the low growth temperature. Nanowire height distribution is very large. The nanowire height variation ranges from 300 nm to 1.5 μm whereas the NWs base-diameters are in the 50-70 nm range.

Two thirds of nanowires are ⟨111⟩ oriented and from the rest many are ⟨112⟩ oriented.
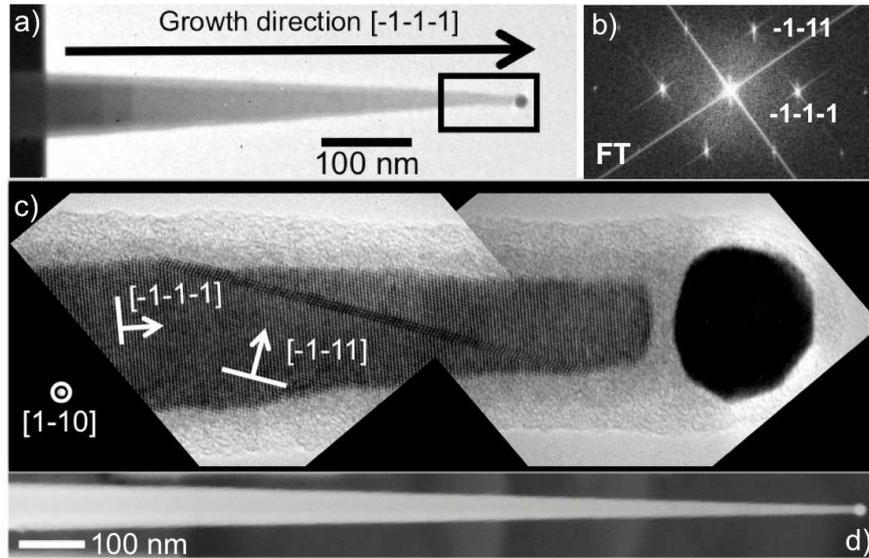
FIGURE 3.2: (a) Low Resolution TEM image of a ZnTe NW grown for 30 min. (b) Fourier transform. (c) High Resolution TEM image. (d) A ZnTe NW grown for 60 min.

Transmission Electron Microscopy (TEM) performed on a Philips CM300 microscope equipped with a CCD camera and operated at 300 kV, reveal a zinc blende crystal structure Fig.3.2. The gold particle has a diameter of 16 nm and presents clear facets on the surface that could be assigned to the $\langle 110 \rangle$, $\langle 100 \rangle$ and $\langle 112 \rangle$ planes. Some nanowires do not present any defects but most of them show twins, these are frequently observed in $\langle 111 \rangle$ zinc blende nanowires. Twins can be either perpendicular to the nanowire growth direction or along a diagonal to the nanowire growth axis, as shown in Fig.3.2(c). We systematically observe an amorphous layer (5 nm thick) all around the NW which we attribute to oxidation. ZnTe$\langle 111 \rangle$ surfaces tend to rapidly oxidized either by forming TeO_2 or/and ZnO [87]. A partially crystallized ZnO shell has already been observed for ZnTe NWs which were thermally oxidized under oxygen flux [88], although the presence of Te-oxide in the outermost part was also suggested by electron energy loss spectroscopy analysis. For the samples presented here, the oxidation process is not under a controlled atmosphere, simply the nanowires are taken outside the MBE chamber, thus put in direct contact with air. Energy dispersive X-Ray analysis performed with these nanowires reveals an amorphous ZnO shell. In addition, we note that an amorphous layer is also seen all around the the gold particle.

3.2.2 Isolation of the single quantum object: Substrate preparation

The observed density of nanowires on as grown sample does not allow us to study a single nanowire. Moreover, the luminescence of the buffer layer or of a 2D regrowth layer may dominate the luminescence of the nanowires. Therefore we need to isolate a single object from the ensemble by putting them on a substrate.

The study of optical properties requires a sufficient amount of photons emitted by the nanoscale objects to be detected by CCD camera. Photoluminescence emitted by the object is distributed in all possible spatial directions, and only a part of it is collected by the microscope objective. In order to enhance the efficiency of light collection, the object can be deposited on a dielectric mirror.

A dielectric mirror, also known as a Bragg mirror, is a type of a mirror composed of one or multiple thin layers of dielectric material, typically deposited on a substrate of glass or some other optical material. By careful choice of the type and thickness of the dielectric layers, one can design an optical coating with specified reflectivity at different wavelengths of light. Dielectric mirrors function based on the interference of light reflected from the different layers of dielectric stack. The thicknesses of the layers are chosen such that the path-length differences for reflections from different high-index layers are integer multiples of the wavelength for which the mirror is designed. The reflections from the low-index layers have exactly half a wavelength in path length difference, but there is a 180-degree difference in phase shift at a low-to-high index boundary, compared to a high-to-low index boundary, which means that these reflections are also in phase. In the case of a mirror at normal incidence, the layers have a thickness of a quarter wavelength.

Calculation of reflectance for a given material of dielectric coating can be performed using the Fresnel formulas for p and s polarization of the electromagnetic plane wave[89]:

$$\frac{E_p''}{E_p} \equiv r_{p_{12}} = -\frac{\tan(\theta_1 - \theta_2)}{\tan(\theta_1 + \theta_2)} = -\frac{n_2 \cos\theta_1 - n_1\sqrt{1 - [(n_1/n_2)\sin\theta_1]^2}}{n_2 \cos\theta_1 + n_1\sqrt{1 - [(n_1/n_2)\sin\theta_1]^2}} \qquad (3.1)$$

$$\frac{E_p'}{E_p} \equiv t_{p_{12}} = \frac{2\sin\theta_1 \cos\theta_2}{\sin(\theta_1 + \theta_2)} = \frac{2n_1 \cos\theta_1}{n_2 \cos\theta_1 + n_1\sqrt{1 - [(n_1/n_2)\sin\theta_1]^2}} \qquad (3.2)$$

$$\frac{E_s''}{E_s} \equiv r_{s_{12}} = -\frac{\sin(\theta_1 - \theta_2)}{\sin(\theta_1 + \theta_2)} = -\frac{n_1 \cos\theta_1 - n_2\sqrt{1 - [(n_1/n_2)\sin\theta_1]^2}}{n_2 \cos\theta_1 + n_1\sqrt{1 - [(n_1/n_2)\sin\theta_1]^2}} \qquad (3.3)$$
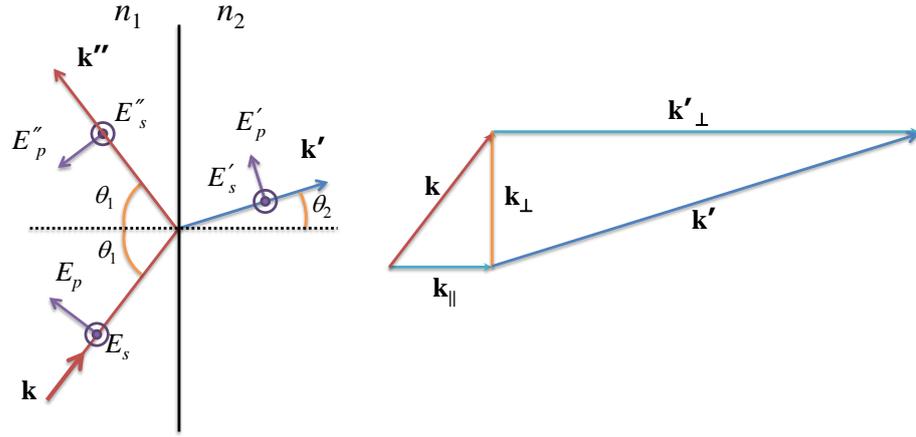
FIGURE 3.3: Refraction and reflection of a plane wave at a plane dielectric boundary.

$$\frac{E'_s}{E_s} \equiv t_{s12} = \frac{2\sin\theta_2\cos\theta_1}{\sin(\theta_1 + \theta_2)} = \frac{2n_1\cos\theta_1}{n_1\cos\theta_1 + n_2\sqrt{1 - [(n_1/n_2)\sin\theta_1]^2}} \tag{3.4}$$

where E''_p and E''_s are the p and s components of the reflected wave, E'_p and E'_s are the p and s components of the refracted wave, n_1 and n_2 are the refractive indexes of material media, θ_1 and θ_2 are the reflection and refraction angles, respectively (see Fig.3.3). The quantity r is known as the reflection coefficient and t as the transmission coefficient. Corresponding reflectance and transmittance will be given by:

$$R = |r|^2, T = \frac{n_2\cos\theta_2}{n_1\cos\theta_1}|t|^2 \tag{3.5}$$

The Fresnel coefficients have the symmetry properties according to the direction of wave propagation: if the wave going from n_1 to n_2 sees coefficients r_{12} and t_{12}, a wave coming in the opposite direction sees r_{21} and t_{21}, where

$$r_{p21} = -r_{p12}, \quad t_{p21} = \frac{n_1\cos\theta_1}{n_2\cos\theta_2}t_{p12}$$

$$\tag{3.6}$$

$$r_{s21} = -r_{s12}, \quad t_{s21} = \frac{n_2\cos\theta_2}{n_1\cos\theta_1}t_{s12}$$

A wave $e^{i\mathbf{k}\mathbf{x}-\omega t}$ delayed by propagating through a layer of index n_j and thickness d_j acquires a phase delay of $\exp(ik_{\|j}d_j)$, where $k_{\|j}$ is the absolute value of the wave vector $\mathbf{k}$ component parallel to the normal of the boundary between the media. The requirement for phase matching is the physical basis of geometrical optics. If there are m parallel planar interfaces, $\mathbf{k}_\perp$ is the same in all the layers, so since (in the jth layer) $k_j = n_jk_0$,

we can use the phase-matching condition to get $k_\parallel$ in the jth layer:

$$k_\parallel^2 = n_j^2 k_0^2 - k_\perp^2 \tag{3.7}$$

All the forward waves in the jth layer have this $k_\parallel$ value, and the reverse waves (i.e., those reflected an odd number of times) have $k'_{\parallel j} = -k_{\parallel j}$.

Hence, using the Fresnel formulas 3.1-3.4, one can calculate the reflectance of a given multylayer structure, knowing refractive indexes and thicknesses of every material, in order to match the phases of the light reflected by external and internal surface of the dielectric mirror and to get the maximum of reflectivity at the desired emission wavelength (see Fig.3.4(a)).

In Fig.3.4(b) the calculated Emission efficiency diagrams for different dielectric media
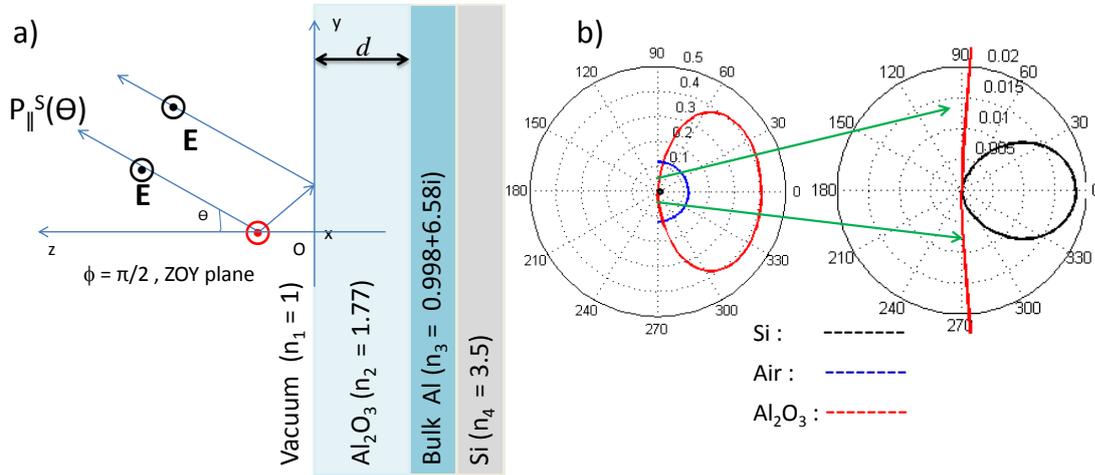

FIGURE 3.4: a) The scheme of the multylayer substrate. b) Emission efficiency diagrams for different dielectric media.

are shown. The strong enhancement of the emission at 540 nm is observed for Al_2O_3 of the thickness $d = 70$ nm. The multilayer substrates with compositions suitable for photoluminescence studies of ZnTe and CdTe/ZnTe nanowires have been produced by atomic layer deposition technique (ALD), which provides the precise control of deposited layer thickness.

3.2.3 Deposition of nanowires

The most commonly used method of nanowires deposition on the substrate is the ultra-sonic bath method. An as-grown sample is placed in a solvent (acetone, hexane, etc.) and agitated in an ultrasonic bath. The liquid containing nanowires is then transferred

with pipettes to a substrate, and upon evaporation of the solvent, the wires remain behind. This method, however, could affect the structural and therefore optical properties of nanowires because of the use of the solvent.

In our case, nanowires were mechanically deposited on the patterned silicon substrate.
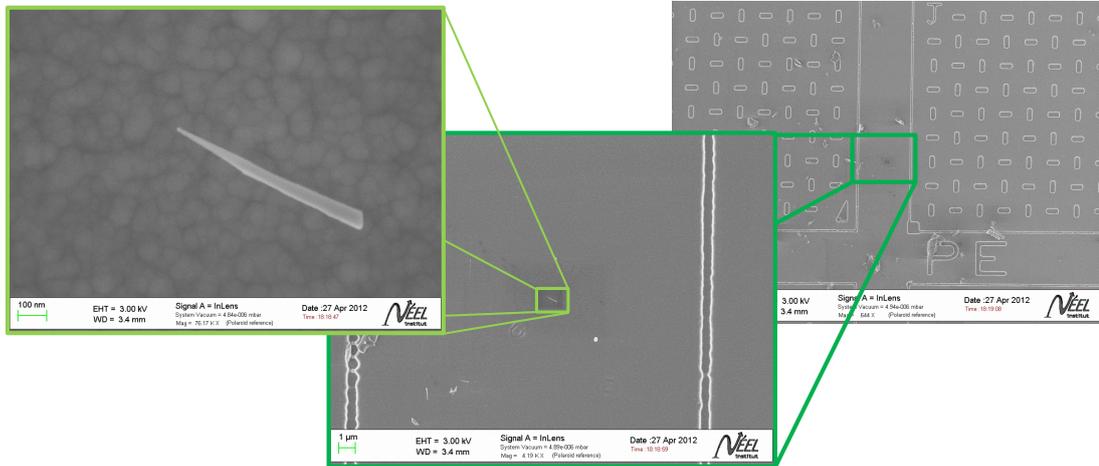
FIGURE 3.5: Localization of the nanowire on the patterned substrate with SEM

The as-grown sample is manually placed on the top of the patterned substrate in such a way, that the surface of the as-grown sample, containing the nanowires, is in contact with the patterned surface of the substrate. This method of deposition results in nanowires laid on the substrate. It means that excitation and detection are done from the side of the nanowire and not from its top. This method also results in some parts of buffer layer being deposited on the substrate.

The use of patterned substrate simplifies the position determination of isolated objects. By studying prepared samples with the scanning electron microscope we localize and note the positions of isolated wires (see Fig.3.5).

3.2.4   Micro-photoluminescence

The optical properties of single nanowires have been characterized by low temperature micro-photoluminescence (μPL) and cathodo-luminescence (CL). ZnTe nanowires are first deposited on a patterned silicon substrate. Isolated nanowires are first identified and precisely located on the substrate using a high resolution field effect scanning electron microscope (FESEM) (see Fig.3.6(c). Micro-photoluminescence spectra of single nanowires are recorded using a confocal micro-photoluminescence set-up depicted in

A 488 nm laser of typically 100 µW has been used for excitation. A laser spot of typically 4 µm^2 is focused on a single nanowire using a microscope objective and a piezoelectric scanner.
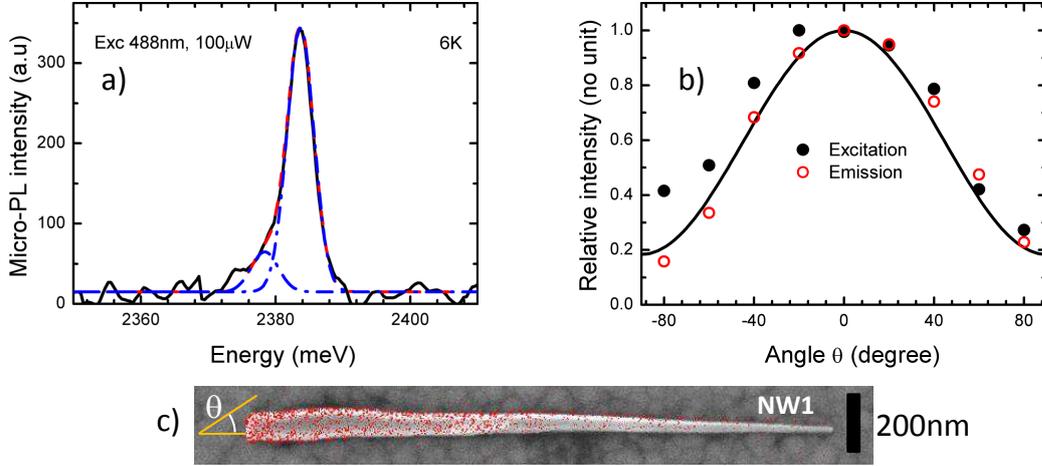

FIGURE 3.6: (a)µPL spectra of the NW shown in (c), recorded at 6 K using a 488 nm laser excitation at 25 µW/ µm^2. The dashed line is a Gaussian fit with a main peak at 2383.7 meV and a satellite line at 2378.4 meV. (b) Dependence of the PL intensity on the angle θ, shown in (c), between the NW axis and the direction of the linear polarization of the laser excitation (closed circles) or the emitted light (open circles). The solid line is the dependence expected from dielectric screening.

As shown in Fig.3.6(a), 5 K µPL spectra are dominated by a single emission peak close to the ZnTe exciton band edge (2381 meV [90, 91]). The spectra has been fitted using two gaussian lines having a full width at half maximum of 4 meV. The main peak located at 2383.7 meV is very close to the bulk exciton band edge and we will discuss it below as originating from a free or slightly localized exciton. The small satellite peak, observed 5 meV below the main emission peak is attributed to bound excitons [91]. In Fig.3.6(c), we plot the variation of the intensity of the band-edge emission peak when rotating the linear polarization of the laser excitation (solid symbols) or of the detection (open symbols) with respect to the NW axis (determined by SEM, using substrate marks). The maximum of the emission intensity is reached when the polarization is parallel to the NW axis (zero angle). Polarization rates of about 70% are observed for emission and detection, in agreement with the value reported with III-V standing NWs[92]. These effects result from the dielectric screening induced by the characteristic aspect ratio of the NWs[93].
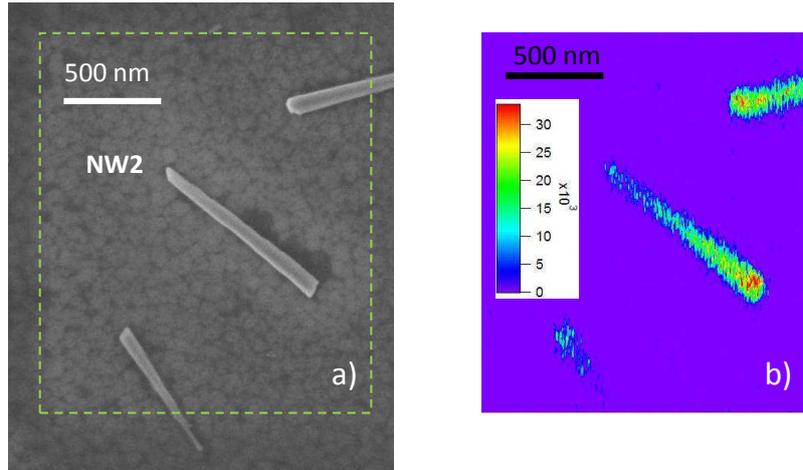
FIGURE 3.7: a) High resolution SEM image of 3 broken ZnTe NWs deposited on a silicon substrate. b) CL image of the NWs shown in (a) recorded at 5 K.

3.2.5 Cathodo-luminescence

Cathodo-luminescence (CL) images of isolated nanowires deposited on silicon substrates are recorded using the set-up depicted in Fig.1.13. Low temperature, polychromatic CL images were recorded in order to assess the homogeneity of the optical properties. CL emission was systematically observed from the NWs, as shown in Fig.3.7(b) for the three isolated, broken NWs of Fig.3.7(a). For thin cone-shaped NWs like the one labeled NW1 in Fig.3.6(c), and NW2 in Fig.3.7, the CL intensity decreases from the base to the tip. The local diameters D of NW1 and NW2, determined from the high resolution SEM images, are shown in Fig.3.8(a) as a function of the position along the NW. Both NWs display a similar cone shape with the same angle value. Fig.3.8(b)
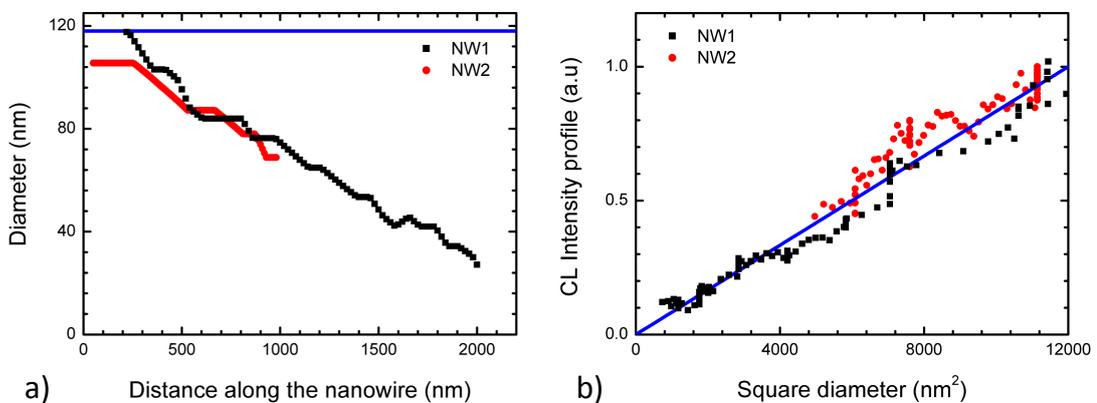

FIGURE 3.8: a) NW diameter as a function of the position along the NW axis for the two NWs shown in Fig.3.6 and Fig.3.7. b) CL intensity (integrated over a 12 nm × 120 nm window) as a function of the square of the NW diameter.

shows that the CL intensity integrated across the NW diameter at different positions along its axis is proportional to the square of the diameter. This suggests that the radiative efficiency remains constant along the NW, with a CL intensity determined by the excitation density which is proportional to D^2.

3.2.6 Influence of strain induced by the shell on optical properties

The results on position of the ZnTe NW emission line apparently contrast with previous studies performed with ZnTe/(Zn,Mg)Te core-shell NWs[80], where a band edge emission is observed at 2.31 eV. Such a line at lower energy might be ascribed to trapped excitons or complexes, but the position of the line in the present study, slightly above the exciton in bulk ZnTe, cannot be ascribed to the influence of lateral confinement, which remains negligible for a NW radius larger than 10nm. Indeed, such a difference in the exciton energy is expected from the high sensitivity of the band edge emission to the strain induced by the presence of a shell around the NW, formed during the growth process and observed by TEM studies.

Such an oxide-covered nanowire can be viewed as a cylindrical core/shell nanostructure, possessing a crystal lattice mismatch between the core and shell (Fig.3.9). In response to this mismatch, mechanical stresses induce deformation and, as a result, the mechanical, electrical and optoelectronic properties of the nanowire are affected [94, 95].

In the framework of isotropic elasticity, the core and surrounding shell can be charac-
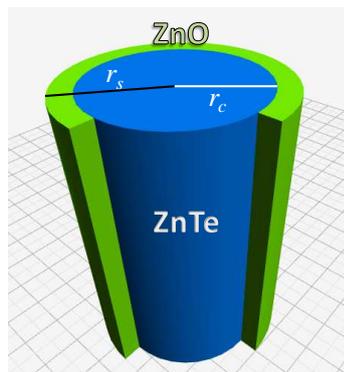
FIGURE 3.9: Scheme of core-shell nanowire structure

terized by the shear moduli μ and and Poissons ratio ν. The difference in the properties between the core and shell materials is also characterized by a misfit strain $f = \Delta a/a$,

where a is the crystal lattice parameter of the core and Δa is the mismatch in the crystal lattice parameters of the core and shell. In the absence of external loading, this mismatch gives rise to the displacements u_i, elastic strains ε_{ij} and corresponding mechanical stresses σ_{ij}.

In the case of an isotropic material and considering, that there is no difference in elastic constants for the core and the shell, the Hooke's law linking the stress and the strain can be written in the form:

$$\sigma_{ij} = 2\mu(\varepsilon_{ij} + \frac{\nu}{1 - 2\nu}\epsilon\delta_{ij}), \tag{3.8}$$

where the isotropic strain ϵ is expressed in form

$$\epsilon = \sum_i \varepsilon_{ii}, \delta_{ij} = \begin{cases} 1, i = j, \\ 0, i \neq j \end{cases} \tag{3.9}$$

$(i, j = r, \theta, z)$, and (r, θ, z) are the cylindrical coordinates. According to reference [96], the non-zero stress components for the stress in the core induced by a latticed mismatched shell covering an infinitely long cylindrical nanowire can be expressed by:

$$\sigma_{rr} = -\frac{\mu f(1 + \nu)}{(1 - \nu)} \times \begin{cases} 1 - t^2, 0 \leq r \leq r_c, \\ (\frac{r_c}{r})^2 - t^2, r_c \leq r \leq r_s \end{cases}; \tag{3.10}$$

$$\sigma_{\theta\theta} = -\frac{\mu f(1 + \nu)}{(1 - \nu)} \times \begin{cases} 1 - t^2, 0 \leq r \leq r_c, \\ (-\frac{r_c}{r})^2 - t^2, r_c \leq r \leq r_s \end{cases}; \tag{3.11}$$

$$\sigma_{zz} = -\frac{\mu f(1 + \nu)}{(1 - \nu)} \times \begin{cases} 2(1 - t^2), 0 \leq r \leq r_c, \\ -2t^2, r_c \leq r \leq r_s \end{cases}. \tag{3.12}$$

Here $t = D_c/D_s$ is the scale factor of the core-shell structure ($D_c = 2t_c$, $D_s = 2r_s$). Using the conversion formula $\nu = \frac{3K - 2\mu}{2(3K + \mu)}$, we can finally write:

$$\sigma_\parallel = 2 \times \sigma_\perp = \frac{18\mu K}{3K + 4\mu} f \left(1 - \frac{D_c^2}{D_s^2}\right), \tag{3.13}$$

where $\sigma_\parallel$ denotes the core stress component parallel to the nanowire, $\sigma_\perp$ denotes the core stress component perpendicular to the nanowires. K is the bulk modulus, D_c is the core diameter and D_s is the diameter of the core-shell structure.

For semiconductor nanowires, a more complete calculation [97] shows that previous expressions can be used for $\langle 111 \rangle$ oriented semiconductor nanowires using a bulk modulus $3K = c_{11} + 2c_{12}$ and a shear modulus $\overline{\mu} = \frac{1}{4}\frac{c_{11}-c_{12}}{2} + \frac{3}{4}c_{44}$ where c_{11}, c_{12} and c_{44} represent the stiffness coefficients of the semiconductor. This leads to an hydrostatic shift of the band edge emission Δ_{hyd} and a heavy hole-light hole splitting Δ_{HL} proportional to the lattice mismatch f reduced by the geometrical factor $(1 - \frac{D_c^2}{D_s^2})$, i.e., the ratio of the shell to the total cross section areas:

$$\Delta_{hyd} = -a\frac{12\overline{\mu}}{3K + 4\overline{\mu}}\left(1 - \frac{D_c^2}{D_s^2}\right)f, \tag{3.14}$$

$$\Delta_{HL} = -\frac{d}{\sqrt{3}}\frac{9K}{3K + 4\overline{\mu}}\left(1 - \frac{D_c^2}{D_s^2}\right)f, \tag{3.15}$$

where a is the hydrostatic deformation potential and d is the shear deformation potential. The energy of the excitonic emission is calculated with formula:

$$E_{NW}^X = E_{bulk}^X + \Delta_{hyd} \pm 0.5\Delta_{HL}. \tag{3.16}$$

For the deformation potentials in ZnTe, we take the values[90] a=5.3 eV and $\frac{d}{\sqrt{3}}$=2.5 eV; and for the stiffness coefficients [22] $c_{11} = 73.7$ GPa, $c_{12} = 42.3$ GPa, and $c_{44} = 32.1$ GPa. Then the excitonic emission of a $\langle 111 \rangle$ oriented cubic ZnTe NW is (in meV, with f in %):

$$E_{NW}^{hh} = 2381 - 88\left(1 - \frac{D_c^2}{D_s^2}\right)f \tag{3.17}$$

for the heavy hole, and

$$E_{NW}^{lh} = 2381 - 44\left(1 - \frac{D_c^2}{D_s^2}\right)f \tag{3.18}$$

for the light hole. The heavy hole is the ground state if $f < 0$, i.e., as noticed in work [80], if the core is under tensile strain. For the NWs studied in Ref.[80], with $D_c = 70$ nm, $D_s = 130$ nm, and $f = 1.04\%$ corresponding to the lattice mismatch between a ZnTe core and a $Zn_{0.8}Mg_{0.2}Te$ shell,[98] we obtain 2.31 eV for the heavy-hole exciton, in agreement with the observed PL line. One can note that in this core-shell geometry, the position of the band edge emission is more sensitive to the strain that in an epitaxial layer under compressive biaxial strain: the shifts of the heavy-hole state due to the hydrostatic and the shear strain add, while they partially compensate in the epitaxial layer. For the NWs studied in this work, we expect a compressive strain induced by
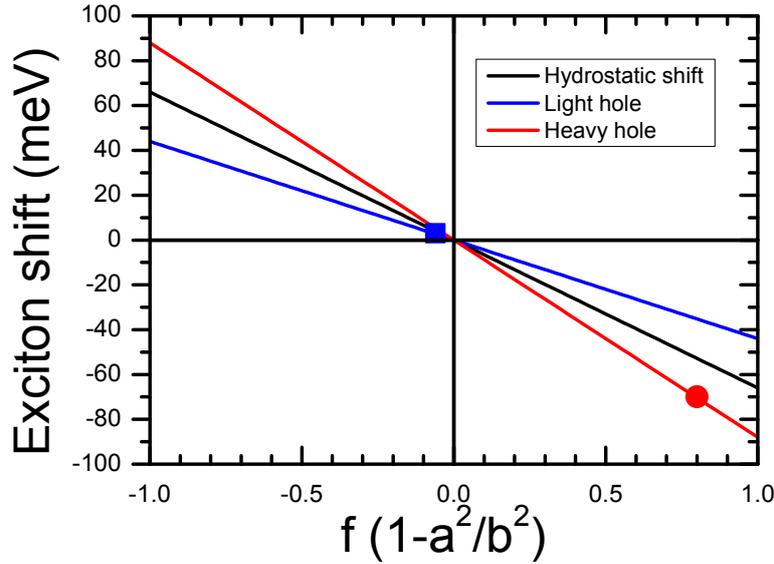
FIGURE 3.10: The heavy-hole (red curve) and the light hole (blue curve) exciton emission energy of a $\langle 111 \rangle$ oriented cubic ZnTe NW calculated using Eq.3.17 and Eq.3.18

the oxide layer around the NW. For instance, the Zn-Zn distance is 20% smaller in ZnO than in ZnTe. The shell thickness is small, 5 nm, resulting in a small geometrical factor, less than 0.2. Moreover, the shell is complex, amorphous and probably strongly relaxed. The band edge emission observed at 2383.7meV can be interpreted as the influence of a small residual compressive strain $f = -0.4\%$ on the light hole exciton. Hence, even if the nature of the lines observed in PL here and in Ref.[80] cannot be assessed without a complementary study such as PL excitation or photoconductivity, their position well agrees with the effect expected from the strain induced by the shells.

3.2.7   Summary on ZnTe nanowires

To conclude, ultra-low density ZnTe NWs have been grown by MBE at low temperature. Thus, a good control of their growth is a step toward the growth of Mn containing ZnTe NWs. These NWs feature a high crystalline quality that is reflected in their optical response. Low temperature CL of single ZnTe NWs deposited on Si substrates was obtained indicating an homogeneous radiative efficiency along the NWs. Near band edge PL emission was observed from single NWs. A small blue shift (2-3 meV) of the PL energy is attributed to the strain induced by the amorphous oxide layer surrounding

the NWs. This assumption is supported by a quantitative calculation of the excitonic shifts induced by strain in core-shell NWs.

3.3 Optical properties of CdTe/ZnTe nanowires

3.3.1 Introduction: CdTe insertion

First steps towards the study of photoluminescence of single CdTe/ZnTe nanowire were done by P. Wojnar in [83]. The micro-photoluminescence spectrum was shown and the 0D confinement of carriers inside the quantum dot was demonstrated by photon correlation measurements. The general purpose of this chapter is to confirm and extend these studies by considering the influence of the temperature and structural issues on exciton confinement. We will try to compare the optical properties of confined excitons in CdTe/ZnTe nanowires and in self-organized quantum dots of the same semiconductor heterostructure.

The growth of CdTe/ZnTe nanowire heterostructures performed by P.Rueda-Fonseca (INAC), E.Bellet-Amalric (INAC) and S.Tatarenko (NEEL). TEM characterization performed by M. Den Hertog (NEEL) and C. Bougerol (NEEL). CdTe/ZnTe nanowires are grown by gold assisted molecular beam epitaxy (MBE) using vapor-liquid-solid mechanism. Nanowire growth starts from a 500 nm-thick ZnTe(111)B buffer layer grown over a GaAs(111)B substrate.

A thin layer of gold has been deposited over the ZnTe epilayer followed by an annealing


a) b)
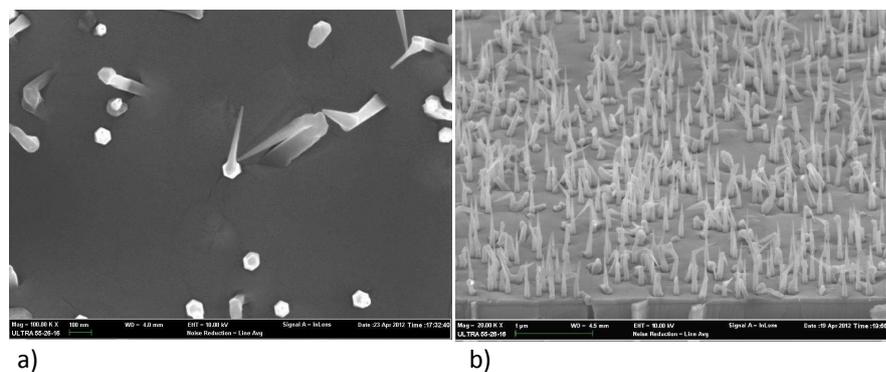
FIGURE 3.11: SEM image of an "as grown" CdTe/ZnTe NW sample. a) Top-view. b) 60 degrees view.

process at at 350 °C in order to form gold catalyst droplets. ZnTe/CdTe NWs are grown for 30 min with a Te rich flux. After 20 minutes of ZnTe NWs growth, a 3 minute CdTe insertion was grown and then it was followed by a 10 minute regrowth of ZnTe.

In Fig.3.11 we present a high-resolution field effect scanning electron microscope (FE-SEM) images of an "as grown" sample. Dozens of nanowires can be seen on the surface

with an average density of 11 wires per μm^2. The nanowires have a conical shape with a diameter at the base of about 70 nm and at the top (at the Au droplet) of about 10-15 nm. Their length varies from 430 to 530 nm. Many nanowires present a kink, a change of the grow direction at their upper part. The relationship between the formation of a kink and the presence of CdTe insertion is not yet clear.

Energy-dispersive X-Ray analysis were performed by P.Rueda-Fonseca (INAC) and E.Robin for single nanowires, revealing complex core-shell structure presented in Fig.3.12[86]. Each detected element is represented by a different color (red for Zn, green for Te, blue for Cd and magenta for O) and in Fig.3.12(b),(c) and (d), different couples of elements are chosen (Zn-Cd, Te-Cd, O-Cd) in order to illustrate the composition.

One can see from this figure, that the conditions used during the growth of CdTe
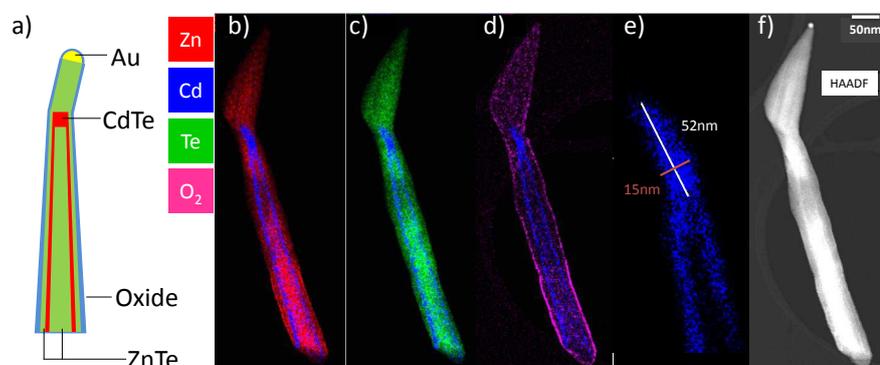
FIGURE 3.12: a) Sketch of the nanowire. b) to e) - EDX image, f) High-angle annular dark-field TEM image (HAADF)

insertion resulted in deposition of a thin CdTe shell around a ZnTe, which has been covered again by a ZnTe shell. One can see as well, that an oxidation layer is formed at the nanowire surface, similarly to the case of pure ZnTe nanowires. The size of the CdTe insertion in ZnTe nanowires studied with EDX ranges from 15 to 50 nm in height and ∼15 nm in width (see Fig.3.12(e)).

3.3.2 Macro-photoluminescence spectra

The photoluminescence spectrum of an ensemble of as grown nanowires is shown in Fig.3.13(b). It was recorded at $T = 5$ K with 405 nm, 200 μW CW laser excitation. Emission lines at 530 nm wavelength range are attributed to the emission of the ZnTe buffer layer, and a peak at 830 nm - to the emission of the GaAs substrate.

The dispersion of CdTe insertion sizes results in the set of sharp emission lines concen-
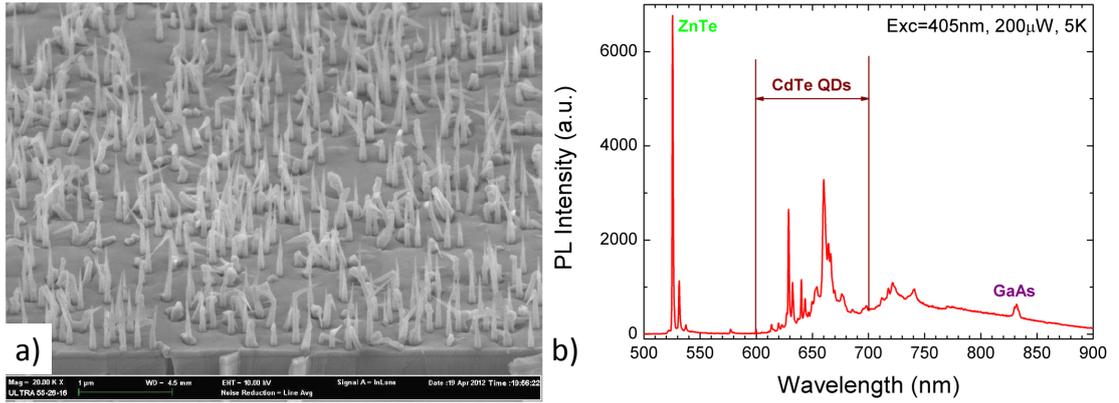
FIGURE 3.13:   a)High-resolution scanning electron microscope image.   b)Macro-photolumiscence spectra of CdTe/ZnTe nanowires

trated in the region of wavelengths between 600 and 700 nm. The origin of the broad luminescence emission between 700 and 800 nm is not known, but may possibly be attributed to the emission of CdTe 2D layer of 100 nm in thickness deposited on the buffer layer during the growth process.

3.3.3   Single nanowire micro-PL: statistics and polarization studies

Nanowires deposited on a patterned substrate (see Fig.3.14) have been studied under scanning electron microscope in order to select well isolated nanowires (Fig.3.14(b)) and to note their positions with respect to the pattern. After that the sample can be studied in micro-photoluminescence set-up. Using the microscope one can get a clear image of the sample surface with patterns and retrieve the position of the selected nanowire. In Fig.3.14(c) the image, obtained under simultaneous illumination of the sample with white light and laser, is shown. The field of view of the microscope is shown together with a white spot representing the image of the photoluminescence emitted by the nanowire and in Fig.3.14(d) the corresponding photoluminescence spectra is presented. This spectra was recorded at $T = 5$ K, with 532 nm CW excitation and 1 µW of excitation power. We attribute the single sharp line to the emission of the exciton confined in the nanowire quantum dot. Green arrow shows the wavelength of the bulk ZnTe exciton[90] and red arrow shows the wavelength of the bulk CdTe exciton [99]. In Fig.3.15 the normalized photoluminescence spectra of several nanowires is plotted. Each of these spectra has been recorded at low excitation power in order to observe a
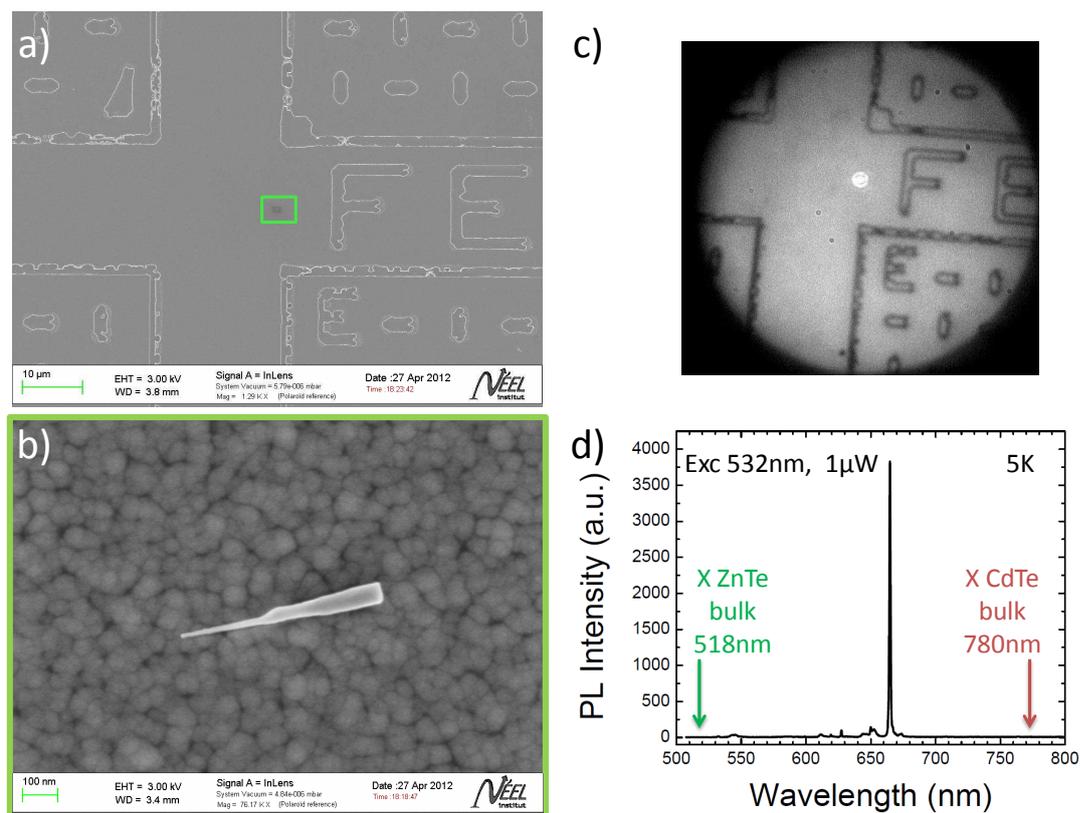
FIGURE 3.14: a) High-resolution SEM image of patterned silicon substrate. b) High-resolution SEM image of studied nanowire. c) Image obtained with optic microscope with superposed image of nanowire luminescence (white spot). d) Micro-photoluminescence spectra of the studied nanowire.
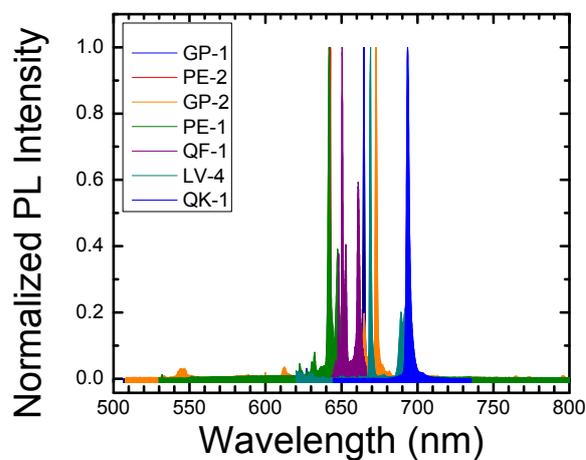

FIGURE 3.15: Spectra of different CdTe/ZnTe nanowires.

single line for each nanowire. The figure demonstrates that all emission lines are concentrated in the region of wavelengths around 600-700 nm corresponding to the emission of the ensemble of quantum dots of the as grown sample (see Fig.3.13(b)). In the Appendix B a detailed statistics on PL line energy position of different nanowires is presented.

In figure 3.16(a) we show the characteristic fine structure of the photoluminescence
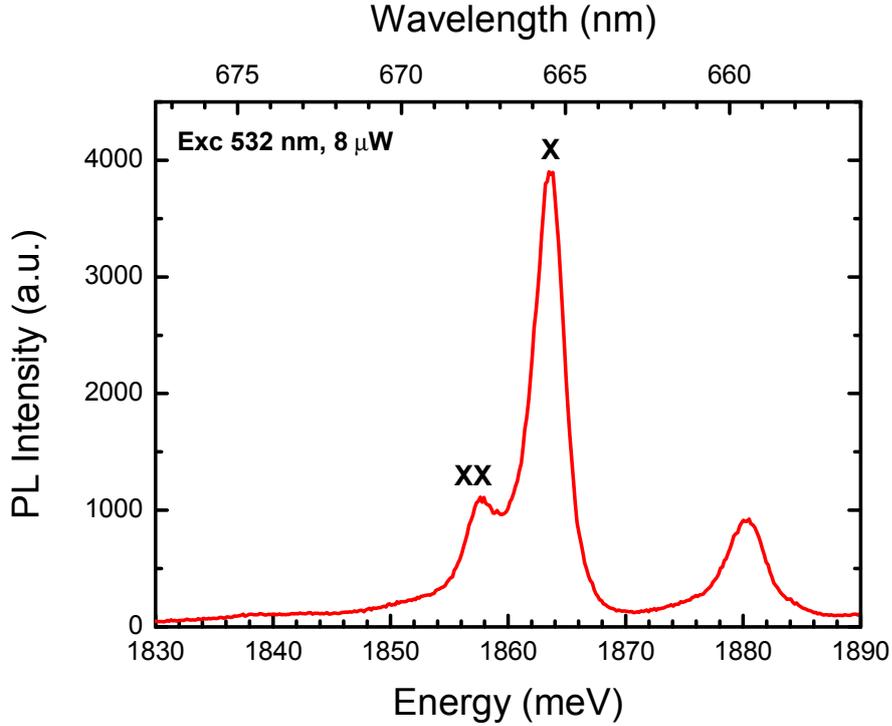
FIGURE 3.16: Characteristic micro-photoluminescence spectra of CdTe/ZnTe nanowire recorded with 532 nm laser excitation at 8 μW.

spectrum of a single CdTe/ZnTe nanowire (3.16(b)). This spectrum has been recorded using a 532 nm continuous laser excitation with an excitation power of 8 μW.

It consists of 3 lines, 2 of which will be identified as exciton and biexciton by photon correlation measurements described in section 3.4. The nature of the third line will be discussed later. The difference in energy between exciton and biexciton is about 7 meV (2.3 nm) which is twice smaller than the one of the self-organized quantum dots (binding energy: 13-14 meV) [64] and three times smaller than the one of CdSe/ZnSe nanowires (20 meV)[100]. This could be a sign of a weak confinement of carriers inside the nanowire quantum dot. The linewidth of the photoluminescence emission is about 2 meV which is larger than the resolution of the spectrometer. This results from spectral diffusion: Stark shift of the exciton line induced by surface charges [101]. Typical linewidth observed for self-organized quantum dots is about 10 to 50 μeV and its precise measurement is

limited by the resolution of the spectrometer. Self-assembled quantum dots are usually covered by the capping layer, the thickness of which keep the free charges far from the quantum dot surface, therefore, preventing the influence of spectral diffusion.

The characteristic feature of the photoluminescence emitted by 1D objects is the strong
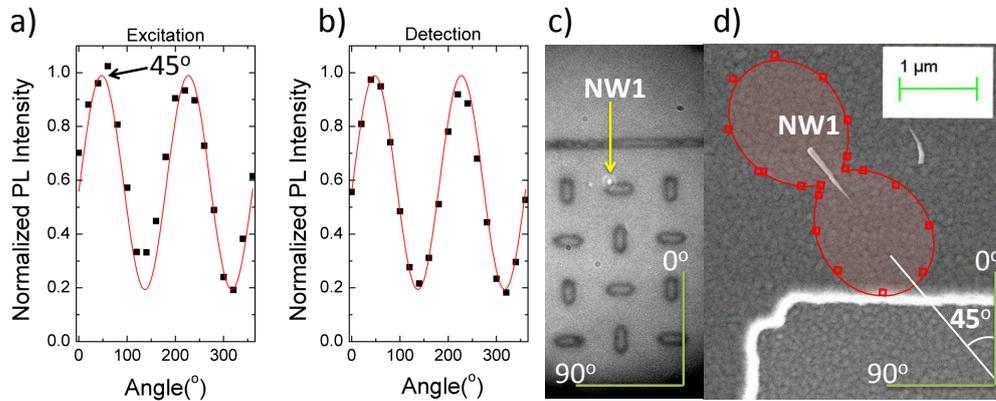
FIGURE 3.17: a) Normalized PL intensity as a function of the linear polarization angle of excitation (a) and linear polarization of emission (b). c) Optical image of patterned silicon substrate containing the studied nanowire. d) Superposition of the high-resolution SEM image of the studied nanowire and its photoluminescence emission polarization diagram.

linear polarization of the emission caused by the dielectric screening effect: the difference in refraction constants between nanowire material and surrounding vacuum. We can use this feature to prove that the photoluminescence recorded by CCD camera is related to a nanowire and to find the absolute orientation of the nanowire. The Fig.3.17 shows the normalized photoluminescence intensity of the exciton line as a function of the linear polarization angle of the excitation (a) and emission (b) recorded using the set-up depicted on the scheme 1.12. As expected, the maximal intensity of the photoluminescence is reached at the same linear polarization angles for the excitation and the detection, with a contrast between the maximal and minimal PL intensities of $\sim 80\%$. The maximal PL intensity is expected to occur at a linear polarization parallel to the nanowire axis. To confirm this point, one can use the optical image of the patterned silicon substrate (Fig.3.17(c)) and the high resolution SEM image of the studied nanowire. In Fig.3.17(d) the SEM image is superimposed with the emitted light polarization diagram showing a vivid demonstration of such approach.

In the case of self-assembled quantum dots there is no dependence of photoluminescence intensity on excitation polarization. Self-assembled quantum dots have the shape of a disk of about ten nanometers in diameter and several nanometers of thickness so the

luminescence is collected from the top of the disk. In case of the nanowire the luminescence is collected from its side without having any information about the size of the quantum dot respect to the length of the wire. The strong dependence of the intensity of the luminescence on different excitation laser polarization orientation is peculiar to the cylindric structure of the wire and was observed for different nanowires [93, 102].

3.3.4 Single nanowire cathodo-luminescence

Low temperature cathodo-luminescence (CL) images of isolated nanowires deposited on silicon substrates are recorded using the set-up described in Sec.1.4.2. The use of an avalanche photo diode (APD) as a detector allows us to study in details the localization of the emission inside the nanowire. In Fig.3.18(b) the polychromatic cathodolumines-
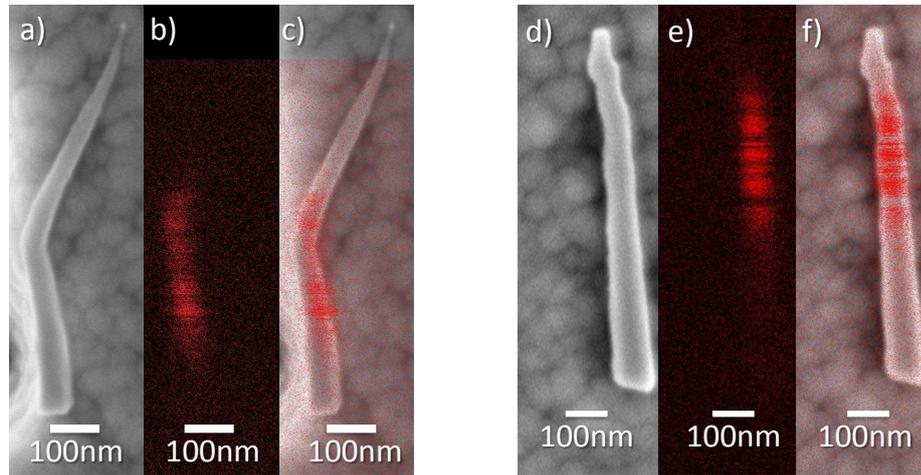

FIGURE 3.18: a)High-resolution SEM image of a CdTe/ZnTe nanowire. b) Cathodo-luminescence APD polychromatic image. c) Superposition of high-resolution image and APD image. e) to f): the same procedure for another nanowire

cence image recorded with 30 kV electron beam is presented. The superposition of this image with the high-resolution SEM image of the nanowire (Fig.3.18(a)) reveals a region in the middle of the nanowire where the luminescence emission is localized (Fig.3.18(c)). For a more precise spatial localization of the quantum dot emission the polychromatic light was dispersed by the grating (600 gr/mm). A wavelength corresponding to the emission of exciton was selected to be detected by the APD or by the CCD camera in order to record the cathodo-luminescence spectrum. In Fig.3.19(a) the photoluminescence (green line) and cathodo-luminescence (blue line) spectra of the same nanowire is presented. The single peak at 660 nm corresponds to the emission of the quantum dot. The larger width of the CL spectrum line is a result of the larger entrance slits of the
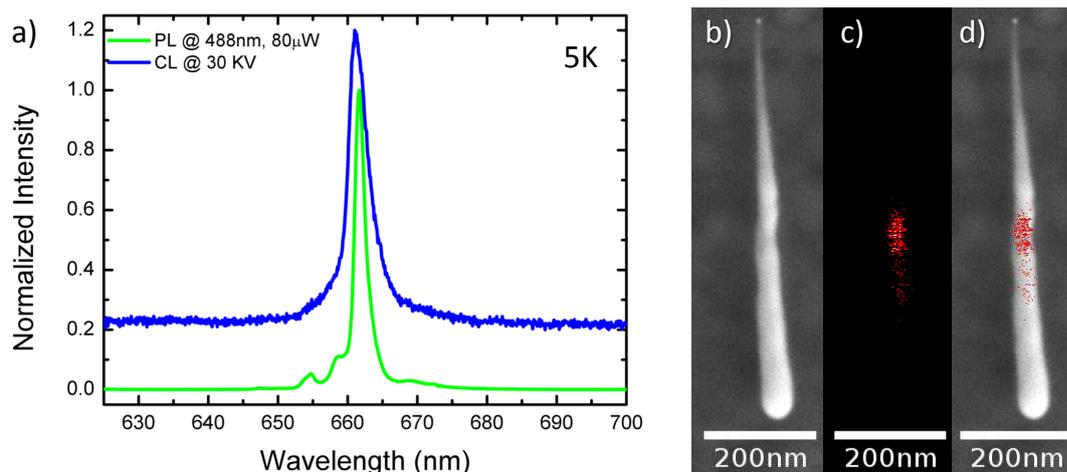
FIGURE 3.19: a)Low temperature cathodo-luminescence spectra (blue line) and photoluminescence spectra (green line) of studied nanowire. b)High-resolution SEM image of studied nanowire. c) Cathodo-luminescence APD monochromatic image. d) Superimposition of high-resolution image and APD image.

spectrometer used during the experiment. The monochromatic CL image is depicted in Fig.3.19(c). Its superimposition with the high-resolution SEM image of the studied nanowire (Fig.3.19(b)) results in Fig.3.19(d). It can be seen that the electron-hole pairs providing the photons in the studied energy range are created by an electron beam in an even more localized area in comparison with polychromatic images. The comparison between the monochromatic and the polychromatic CL images shows that the light is emitted not only by the QD. This light may as well be an origin of some emission lines observed in the photoluminescence spectra of some nanowires presented in the Appendix B. The comparison of CL images with an EDX image (see Fig.3.12) allows us to suggest that localized emission is originated from the CdTe insertion and non-localized emission could be originated from the CdTe shell deposited during the growth.

The analysis of emission spatial distribution can provide us an information about the diffusion length of an electron-hole pair and an approximate size of the CdTe insertion.

Cathodo-luminescence imaging and spectroscopy combined with micro-photoluminescence studies allow us to characterize the localization of emission. The next step is to determine the origin of emission lines present in photoluminescence spectra.

3.4 Identification of excitonic lines at low temperatures

In order to determine the nature of the luminescence of the quantum dot one should try to attribute each emission line (see Fig.1.5) to a certain excitonic transition and apply a theoretical model which will consistently describe all the experimentally observed dependencies.

By studying the behavior of the photoluminescence intensity as a function of laser excitation power one can have a first identification of different emission lines.

For a precise identification of the emission lines observed in the photoluminescence spectra one should prove that these lines originate from an exciton confined inside the quantum dot (0D confinement). The unique feature of such confinement is the single photon emission meaning that only one photon is generated after the recombination of the electron-hole pair from exciton level. Photon autocorrelation measurement is the powerful instrument for the verification of such behavior and dynamic studies inside this quantum system.

3.4.1 Power dependence of photoluminescence intensity

In Fig.3.20(a) we show the evolution of the photoluminescence spectra of a single nanowire under different excitation conditions. At low-power excitation, the spectra of the contains a single emission line at 665.45 nm with a linewidth of about 2 meV at 5 K. By increasing the laser power, the intensity of this line increases linearly with the laser power and we attribute this line to the emission of the exciton. With a further increase of the laser power, the intensity of this line saturates and the spectra becomes dominated by the emission of a line at 657.75 nm. We attribute this line to the emission from the biexciton level because its intensity increases quadratically with power as one biexciton formation requires the absorption of two electron-hole pairs (Fig.3.20).

One can note that the exciton and the biexciton photoluminescence intensity saturate approximately at the same value, and that the biexciton emission starts to dominate the exciton emission after the saturation of the latter. This behavior is quite different from the one observed with CdSe quantum dots inserted in ZnSe nanowires where a domination of the biexciton emission starts much before the saturation of the exciton emission[100]. The saturation of the biexciton emission intensity indicates the presence of a third energy level, which starts to be filled with excitons by increasing the laser
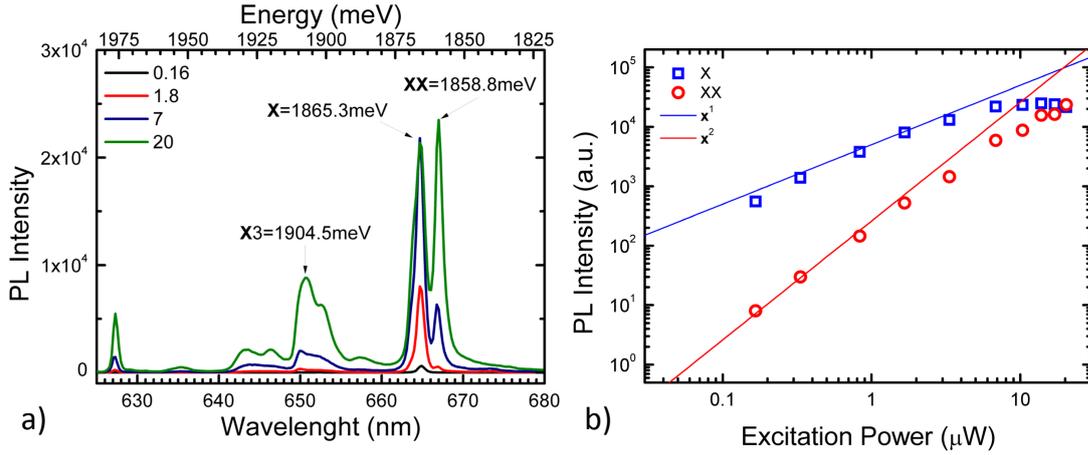
FIGURE 3.20: a) Power dependence of single wire photoluminescence. b) Photoluminescence intensity plotted as a function of excitation power.

power. Hence, the theoretical model which will be used to describe the photoluminescence intensity power dependence should contain at least three energy levels devoted to each exciton complex (exciton and biexciton). CdTe/ZnTe SK quantum dots show different values for the saturation level of the exciton and biexciton[64, 103] and the theoretical description for this case was limited to models, having the biexciton level as the highest in energy.

Under high-power excitation, PL-spectra reveals emission lines with energies higher than the energy of exciton. These lines could be attributed to the excited states of the exciton (p-shell), multi-exciton complexes (see Fig.1.5, Ch.1.) or any sort of the defects in the nanowire.

3.4.2 Theory of correlation measurements

Only in few cases, the CW micro-PL intensity is sufficient for a complete characterization of exciton lines. More accurate descriptions are possible in terms of an hierarchy of correlation functions as defined by optical coherence theory [104]. While this concept has been used with great success in atom quantum optics [105], correlations have recently also attracted significant attention from solid-state physicists addressing the light generation from nanostructures [106]. Of particular interest is the normalized intensity correlation function of second order, defined as

$$g^{(2)}(t,\tau) = \frac{\langle \hat{a}^\dagger(t)\hat{a}^\dagger(t+\tau)\hat{a}(t)\hat{a}(t+\tau)\rangle}{\langle \hat{a}^\dagger(t)\hat{a}(t)\rangle \langle \hat{a}^\dagger(t+\tau)\hat{a}(t+\tau)\rangle} \tag{3.19}$$

where $\hat{a}^\dagger$ and $\hat{a}$ are the photon creation and annihilation operators for the mode of interest evaluated at times t and $t + \tau$, respectively. This function quantifies, how the detection of one photon from a light source influences the probability to detect another one. The equal-time correlation function $g^{(2)}(t, 0)$ already allows one to distinguish between thermal ($g^{(2)}(t, 0) > 1$), coherent ($g^{(2)}(t, 0) = 1$) and quantum ($g^{(2)}(t, 0) < 1$) light emission. Only the correlation function of the second order can reveal the photon anti-bunching and prove the presence of a single photon source[107]. In addition this function allows us to study the dynamics of the system. For example one could evaluate the average time between the emission of consecutive photons and measure the time needed for the quantum dot to populate its different energy levels.

It can be shown [107] that the second order correlation function can be expressed as the ratio of the intensities of the incident light:

$$g^{(2)}(t, \tau) = \frac{\langle I(t + \tau)I(t) \rangle}{\langle I(t) \rangle^2} \tag{3.20}$$

Photon correlation measurement can be performed with a Hanbury-Brown and Twiss
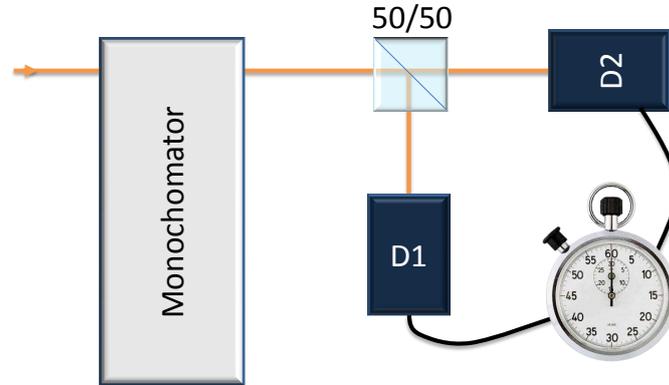
FIGURE 3.21: Scheme of Hanbury-Brown and Twiss set-up for photon autocorrelation measurement

set-up[108], schematically depicted in Fig.3.21. For spectrally resolved photon correlation measurement the beam splitter is placed after the monochromator. Each photon of the selected emission line can trigger the detector D1 or the detector D2 with the same probability. The idea of such experiment is the following: a detection of photon at D1 triggers the chronometer to start the time count ("START") and it will be stopped by the detection at D2 ("STOP"). Hence, we measure the time τ between 2 emitted photons by the quantum dot. By plotting the histogram of such events as a function of

the time between the two consequent photons one obtains the curve of the number of coincidences as a function of this delay time. This curve represents the probability to detect a photon at time τ knowing that a photon has been detected at time 0. Introducing the conditional probability $\wp(t + \tau|t)$ to detect a photon at the moment of time $t + \tau$ knowing that we have detected a photon at the moment t, we can write:

$$g^{(2)}(\tau) = \frac{\wp(t + \tau|t) \cdot \wp(t)}{\wp(t)^2} = \frac{\wp(t + \tau|t)}{\wp(t)}. \tag{3.21}$$

Normalization factor $\wp(t)$ is the probability to detect a photon at any time moment. Equation 3.21 shows, that by measuring (with set-up in Fig.3.22) the probability to detect a photon at the moment of time τ having detected one at 0, we measure directly the autocorrelation function of the second order.

Once the autocorrelation curve is obtained, it should be normalized in order to reconstruct the correlation function of the second order. The normalization factor is chosen as the average number of coincidences at the long delay time ($\tau \to \infty$).

The number of coincidences at a given time channel is influenced by background photons which could have the same wavelength as the selected ones, but which are not emitted by the studied exciton level of the quantum dot. To take these photons into account, and correct the correlation curve, we will consider that the number of photons ascertained by the detector n_i consists of the photons emitted by the quantum dot, n_i^s, and the photons of background n_i^{bg}, so $n_i = n_i^s + n_i^{bg}$ and correlation function $g^2(\tau)$ can be written in the form:

$$g^2(\tau) = \frac{< [n_1^s(t) + n_1^{bg}(t)][n_2^s(t + \tau) + n_2^{bg}(t + \tau)] >}{< n_1^s(t) + n_1^{bg}(t) >< n_2^s(t) + n_2^{bg}(t) >}. \tag{3.22}$$

Introducing the signal to signal+background ratio ρ:

$$\rho = \sqrt{\frac{< n_1^s(t) >< n_2^s(t) >}{< n_1^s(t) + n_1^{bg}(t) >< n_2^s(t) + n_2^{bg}(t) >}}, \tag{3.23}$$

one can deduce the corrected autocorrelation function $g_s^2(\tau)$ in the form:

$$g_c^2(\tau) = \frac{g^2(\tau) - (1 - \rho^2)}{\rho^2} = \frac{g^2(\tau) - 1}{\rho^2} + 1. \tag{3.24}$$

If the counting rate is identical for the two detectors then the expression for ρ will be simplified:

$$\rho = \frac{<n_s(t)>}{<n_s(t) + n_{bg}(t)>}.$$ (3.25)

Determining from the photoluminescence spectra the signal-to-background ratio, one can finally correct the correlation function of second order for the emitter under study.

### 3.4.3 Autocorrelation measurement
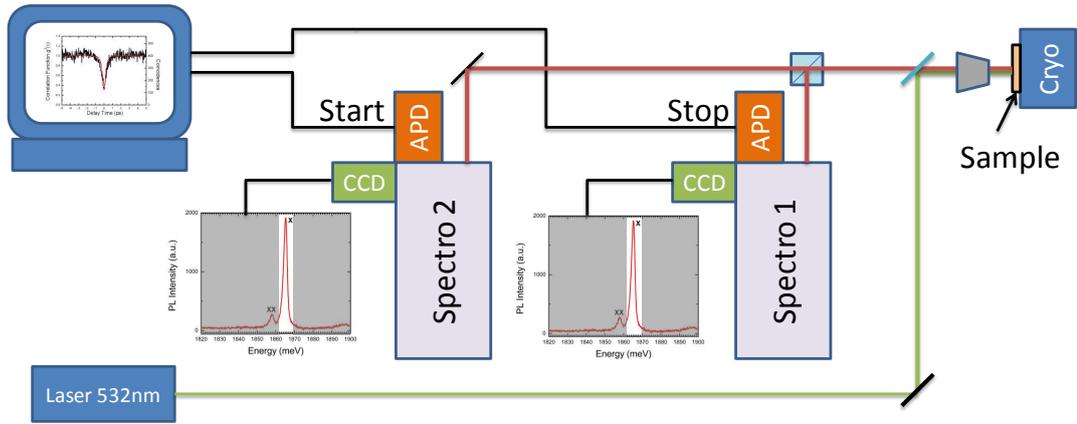
FIGURE 3.22: Scheme of autocorrelation set-up

The photon autocorrelation experimental set-up [109] is presented in Fig.3.22. Photoluminescence excited by the 532 nm Nd:YAG laser is collected by the microscope lens (50X/0.3 Olympus) and sent to two monocromators through the beam-splitter. Each monochromator with 150 gr/mm grating is connected to the CCD camera (Anchor Solid or Pixis 500) or to the APD detector. Photoluminescence spectra are recorded by each CCD camera in order to select the emission line, project it on the exit slits of monochromator and send it to APD. The temporal resolution of one APD is 45 ps and the use of 2 APDs results in a temporal resolution of the set-up of 90 ps. Both APDs are connected to an acquisition card which measures the delay time between START-STOP events. Thereby, the event of photon detection by an APD connected to the START input launches the time counter and an event at APD connected to the STOP input terminates the counter, thus providing a coincidence for the delay time τ. The number of coincidences plotted as a function of the delay time forms the experimental photon correlation curve. This curve represents the probability to detect a photon at the moment of time τ, knowing that one photon has been detected at the 0 moment of time.

For the photoluminescence line at 665.45 nm corresponding to the excitonic emission (Fig.3.23(a)) we obtain the curve of autocorrelation presented in figure 3.23(b). The curve was obtained for a 2.5 μW of excitation power at which the excitonic emission is not saturated. The left axis in this figure represents the number of coincidences inte-
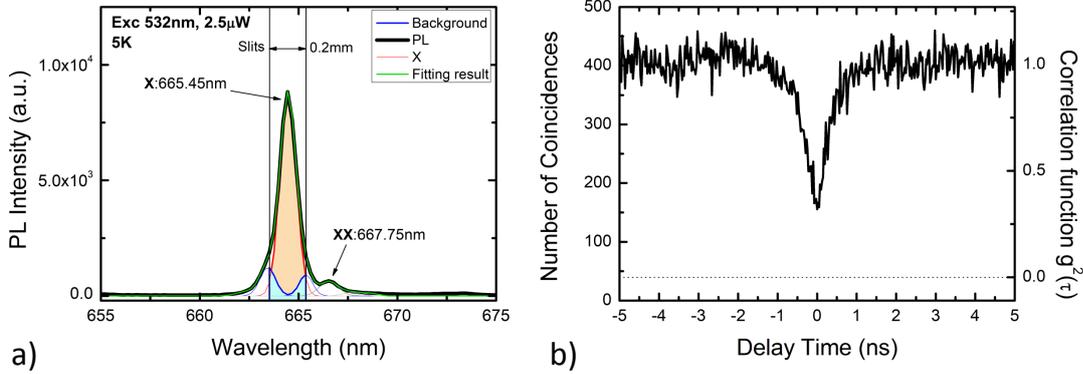

FIGURE 3.23: Autocorrelation of exciton photons. a) Photoluminescence spectra of CdTe quantum dot inserted in ZnTe nanowire recorded under continuous excitation of 532 nm with excitation power 2.5 μW. b) Exciton autocorrelation curve.

grated by the acquisition card, and the right axis represents the normalized data which has been corrected taking into account the noise level of APDs and the signal from the external sources apart from the quantum dot. The normalization factor is the number of coincidences at the steady state (400 in Fig.3.23(b)). The number of background counts entering in the spectrometer slits is estimated from fitting the photoluminescence spectra with Gaussian lines (Fig.3.23(a)) and the ratio between these counts and exciton counts define the correction factor according to Eq.3.25. The shape of the curve characteristic to the anti-bunching effect proves that the insertion of CdTe in ZnTe nanowire acts as a single photon emitter and that excitons are completely confined inside the quantum dot. The full width at half-minimum of the autocorrelation dip corresponds to the average time needed for quantum dot to absorb an exciton and reach its stationary state. We measured a width of 200 ps. The measured value of $g^{(2)}(0) = 0.35$ instead of 0 results from the temporal resolution of the APD.

3.4.4 Cross-correlation measurement

The scheme of the set-up for cross-correlation measurement is the same as the one for autocorrelation. Our goal here is to determine the correlation between two different energy states of the quantum dot, i.e. two different emission lines. Hence, we select with one spectrometer the emission line of the biexciton and direct its photons to the APD connected to the START input of the acquisition card. Photons of the exciton emission line are directed by the second spectrometer to the APD connected to the STOP input. For the photoluminescence spectrum (Fig.3.24(a)) measured under 532 nm continuous laser excitation of power 7.8 μW, we present the cross-correlation curve $g^{(2)}_{X-XX}(\tau)$ between the exciton (665.45 nm) and biexciton (667.75 nm)(Fig.3.24(b)) lines. This curve has an asymmetric shape for positive and negative delays. The peak of the curve at $\tau > 0$ shows a bunching effect meaning that two photons have been registered one right after another. This is a strong evidence of a cascade process of the quantum dot emission.

The correlation function is nothing else than evolution of level population from the
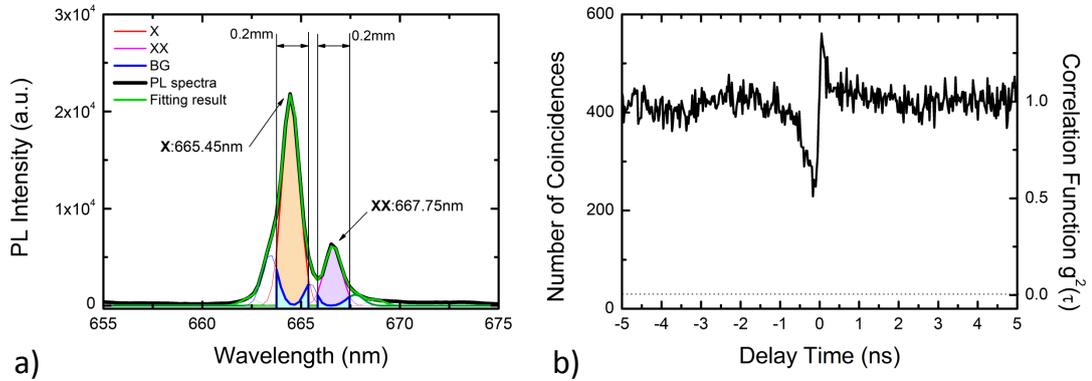
FIGURE 3.24: Cross-correlation of exciton and biexciton photons. a) Photoluminescence spectra of CdTe quantum dot inserted in ZnTe nanowire recorded under continuous excitation of 532 nm with excitation power 7.8 μW. b) Cross-correlation curve.

initial conditions determined by the experiment. So for $\tau > 0$ we measure the evolution of exciton population knowing that at $\tau = 0$ the probability of exciton level occupation is equal to 1. Moreover, we know that at the long delay time we measure the stationary population of the exciton level. All these considerations allow us to get some information about the photon bunching process. The height of the peak shows the probability of the exciton level occupation, $g^{(2)}_{X-XX}(0) = 1/n_X(\infty)$, where $n_X(\infty)$ is the population of the exciton level in a steady state. At long delay times we have always $g^{(2)}_{X-XX}(\infty) = 1$.

	This work	CdTe/ZnTe NW QDs[83]	CdTe/ZnTe SK QDs[110]
AC FWHM	200 ps	500 ps	400 ps
AC $g^2(0)$	0.35	0.2	0.3
CC peak FWHM	125 ps	300 ps	200 ps
CC peak height	1.5	9.5	3.5

TABLE 3.1: Comparison between the characteristic values of photon correlation measuremnts performed on different types of quantum dots of CdTe/ZnTe

The linewidth of the peak tells us the average time needed for exciton level to reach its stationary population.

We measure $g^{(2)}_{X-XX}(0) = 1.5$ and a full width at half-maximum of 120 ps. It is important to note that the curve is convoluted with the temporal resolution of the set-up, which is of order of 100 ps. Hence, the measured height of the bunching peak is an underestimated value.

The fact that the height of the peak at zero delay is just 1.5 times larger than the value of correlation at long delays shows that in stationary state and with the excitation power used for the experiment the probability of exciton level occupation is $n_X(\infty) \approx 0.67$.

We now consider the part of the curve $g^{(2)}_{X-XX}(\tau)$ at negative delay times ($\tau < 0$). Negative delay means that the first photon is registered by the APD-Stop and the second by the APD-Start. So the exciton is registered before the biexciton. The curve at negative delays has the characteristic shape of an anti-bunching process. At these delays we measure the probability to detect a photon emitted by biexciton at time τ knowing that we have already detected a photon emitted by exciton at time $\tau = 0$. From the scheme 3.28(a) one can conclude that the detection of the exciton at time 0 means that at this moment the system is in its ground state, i.e. the quantum dot is empty. One can see now why we cannot detect the biexciton at time 0 or at short delay: the quantum dot should capture 2 electron-hole pairs in order to emit the photon from the biexciton level. The width at half-maximum of the dip characterizes the time needed for quantum dot to capture these two excitons. On the curve we have measured a full width at half-maximum of 300 ps.

Correlation measurements performed with CdTe/ZnTe self-assembled quantum dots[110] allow us to compare their single-photon emitter properties with the ones of quantum dots inserted in nanowires. The Table.3.1 shows the comparison between the characteristic parameters of auto- and cross-correlation measurements. In general, the results obtained in the present work are in agreement with the ones of self-assembled CdTe/ZnTe quantum dots studied in [110]. The difference in nanowires growth conditions could

explain the large difference of these parameters in comparison with the work [83], where CdTe/ZnTe nanowires where grown at higher temperature (420°C) than the ones studied in present work (380°C see Sect.3.3.1).

3.4.5 Exciton lifetime measurements

Another important optical characterization of quantum dots is the determination of the decay times of the exciton lines. The characteristic exciton lifetime in II-VI self-assembled semiconductor quantum dots is between 200 to 300 ps both for CdSe/ZnSe[111, 112] and CdTe/ZnTe[68]. The biexciton lifetime is considered to be two times shorter than the one of the exciton, but one usually assumes that Coulomb interaction imposes a spatial separation between the holes present in the dot while electrons remain distributed homogeneously. Hence, the overlap of electron and hole wavefunctions decreases and the lifetime of the biexciton increases[112]. The values of exciton and biexciton lifetimes measured for CdSe/ZnSe quantum dots satisfy the ratio $\tau_{XX} = 0.7\tau_X$[110, 111].

A direct experimental study of the exciton lifetime is possible by measuring the transient
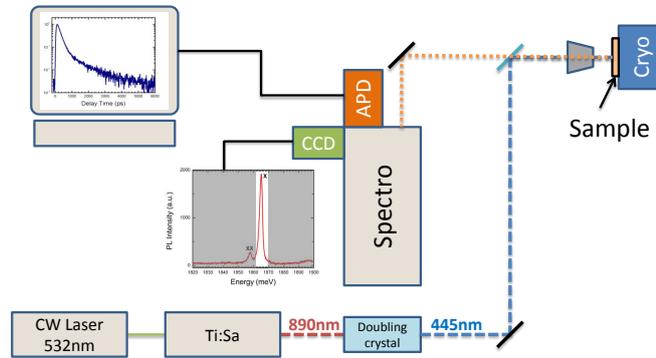

FIGURE 3.25: Decay measurements set-up

photoluminescence emission after a short laser pulse. The scheme of the experimental set-up [109] is presented in the Fig.3.25. For the excitation we used a Ti:Sa picosecond pulsed laser at 890 nm, the frequency of which had been doubled by a non-linear BBO crystal. The repetition frequency of pulses is 80 MHz.

The photoluminescence emission of quantum dot is dispersed spectrally and the photons are sent to a detector. We use for the detection a fast APD which has a temporal resolution (~ 50 ps) smaller than the expected lifetime. The statistics of the detection time is realized by using a counter hardware. On one side the standard fast photo-diode

detects the laser pulses and gives a start of counting. On the other side an APD which detects the photon arrival stops the time counter.

In Fig.3.26 the recorded curves of photoluminescence intensity decay for two levels,
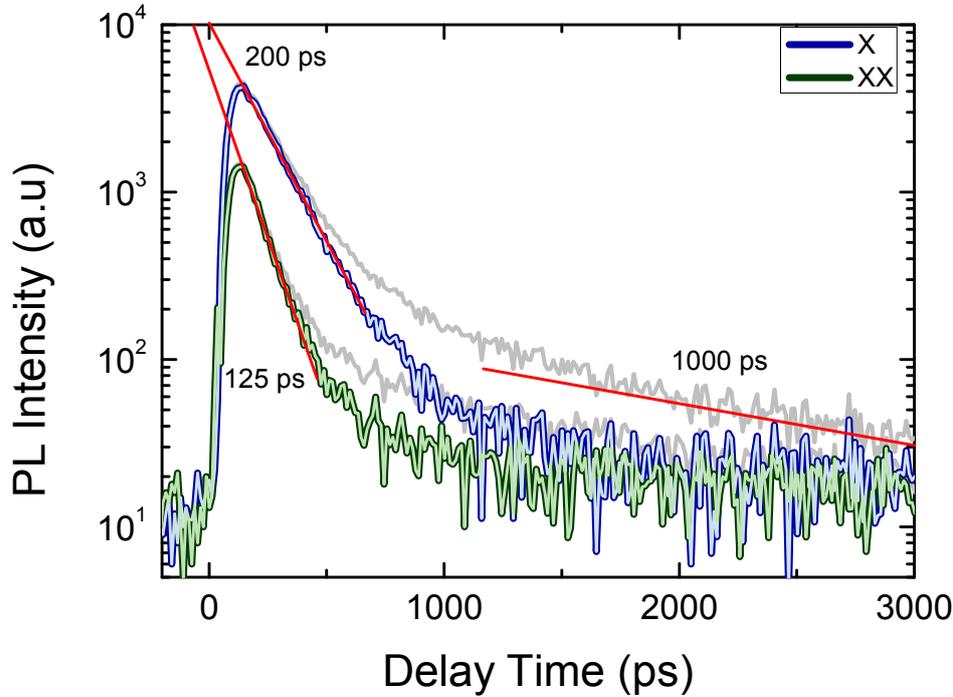
FIGURE 3.26: Decay of photoluminescence emission of exciton line (blue) and biexciton (green). The curves have been corrected by subtracting the long-time component induced by the "diffusion tail" of the APD. Grey curves correspond to the not corrected data.

exciton and biexciton, are presented. The photoluminescence intensities of the exciton and biexciton emission lines are proportional to the populations of the exciton ($n_X(\tau)$) and of the biexciton level ($n_{X2}(\tau)$), respectively. In our case the decay part of the curve can be fitted with the sum of two exponential decays: $\alpha \exp^{-\frac{t}{\tau_s}} + \beta \exp^{-\frac{t}{\tau_l}}$, where τ_s is the short-time decay corresponding to the exciton or biexciton lifetime and τ_l is the long-time component of decay originated from possible repopulation of the energy level. This is the typical situation for exciton which can recombine radiatively within its characteristic lifetime, or one of the charge carriers can invert its spin which transforms the exciton from the bright to the dark state: this effect was extensively studied in self-assembled quantum dots and in CdSe/ZnSe nanowires [100]. However, in our case the long-time component has the same time constant both for exciton and biexciton (grey curves in Fig.3.26) and it is attributed to the "diffusion tail" of the APD's Instrument

Response Function [113]. It is caused by carrier generation in the neutral layers below the avalanche region. The amplitude of the tail depends on the wavelength and can reach 10 to 20% of the IRF peak at wavelength ranged between 600 and 800 nm (see Fig.3.27). We can, therefore, subtract this long-time component from all experimental decay time curves ant fit only the short-time component.
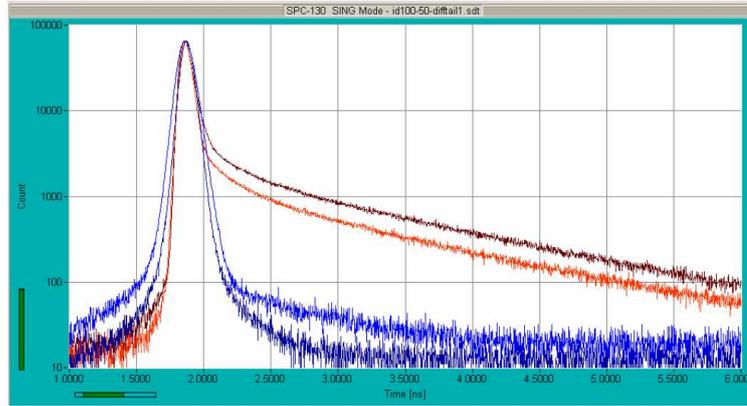

FIGURE 3.27: Diffusion tail in the IRF of the id-100-50. 785nm (dark red), 650 nm (red), 444 nm (light blue), 405 nm (dark blue). The amplitude of the tail is about 5% and 3% at 650 and 785 nm. At 444 nm the tail is at the limit of detection, at 405 nm it is not detectable. [113]

By fitting the decay curves we measure time of the fast decay which is equal to 200 ps for exciton and 125 ps for biexciton ($\tau_{XX} = 0.6\tau_X$). These values will be used later for a theoretical description of experimental data. They are in agreement with the ones obtained for the self-assembled quantum dots, where the shorter decay time of the biexciton that the exciton is observed [68].

3.4.6 Multi-exciton quantum cascade model and data fitting

a. Description of the model

Up to now we have measured the lifetime of exciton and biexciton (200 ps and 125 ps respectively), the depth of the dip and the full width at half-minimum of the autocorrelation curve ($g^{(2)}(0) = 0.35$, FWHM= 200 ps), the height (1.5) and the width (120 ps) of the peak of positive delay part of cross-correlation curve, the depth (0.45) and width (300 ps) of the dip at the negative delay part. We will try in this section to reproduce all the values measured in previous sections using a 3 level quantum cascade model.

For a system with several levels linked by a cascade process with certain exchange rates, first order rate equations are usually used. This is schematically represented in Fig.3.28(a). The value g is a generation rate meaning the number of electron-hole pairs created per time unit and it is the same for all levels. We assume that it is proportional to the laser excitation power. The depopulation rates for exciton(n_1), biexciton(n_2), and triexciton(n_3) levels are denoted as $\gamma_{X1} = 1/\tau_{X1}$, $\gamma_{X2} = 1/\tau_{X2}$ and $\gamma_{X3} = 1/\tau_{X3}$, respectively, where τ_{X1}, τ_{X2} and τ_{X3} are the radiative lifetimes of corresponding excitonic complexes. One can write a rate equation for each level and solve them using
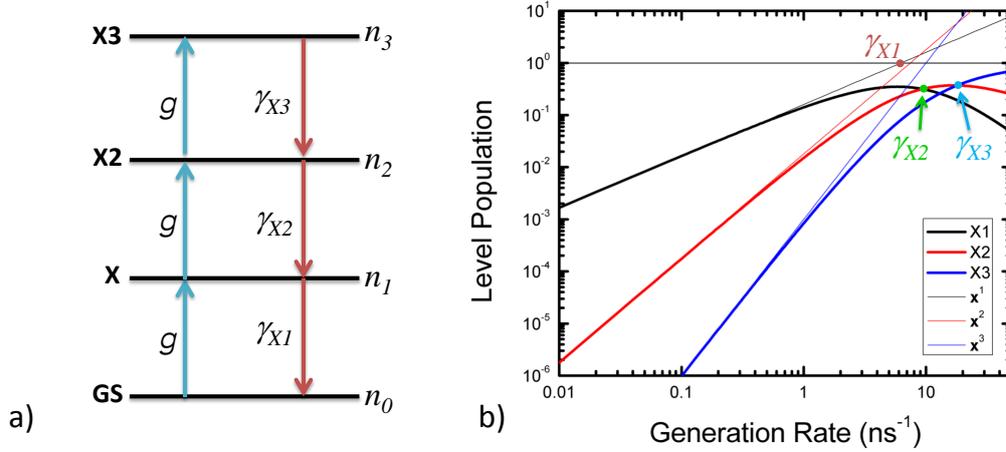

FIGURE 3.28: a) Scheme of 3 level model. b) Population of levels X1, X2 and X3 as a function of generation rate g plotted in log-log scale

the values of generation rate g and depopulation rates (γ_{X1}, γ_{X2} and γ_{X3}) as fitting parameters. A solution of this system describes the evolution of the population of the 3 excitonic levels after the laser pulse. Applying different initial conditions on the system, one obtains the population decay for CW measurements, photon correlation and decay time measurements. For a model with 3 exciton levels and a ground state the system of rate equations is written as follows:

$$\begin{cases} \dfrac{dn_3}{dt} = -\gamma_{X3}n_3 + gn_2 \\ \dfrac{dn_2}{dt} = \gamma_{X3}n_3 - (g + \gamma_{XX})n_2 + gn_1 \\ \dfrac{dn_1}{dt} = \gamma_{XX}n_2 - (g + \gamma_X)n_1 + gn_0 \\ \dfrac{dn_0}{dt} = \gamma_X n_1 - gn_0 \end{cases} \qquad (3.26)$$

$$n_3 + n_2 + n_3 + n_1 + n_0 = 1. \qquad (3.27)$$

b. Solution for cw experiment

The emission intensity is treated as proportional to the level occupation probability and its recombination rate. This is justified by the fact that the intensity of the emission reflects the oscillator strength of respective transition which is equal to the above mentioned product. Then, the respective expressions for the generation rate (excitation power) dependence of the emission intensity derived from the rate equations can be written as [114]

$$
\begin{cases}
I_{X1} = n_1(g)\gamma_{X1} = \dfrac{g\gamma_{X3}\gamma_{XX}\gamma_{X1}}{g^3 + \gamma_{X3}g^2 + \gamma_{X2}\gamma_{X3}g + \gamma_{X1}\gamma_{XX}\gamma_{X3}} \\[3mm]
I_{X2} = n_2(g)\gamma_{XX} = \dfrac{g^2\gamma_{X3}\gamma_{XX}}{g^3 + \gamma_{X3}g^2 + \gamma_{XX}\gamma_{X3}g + \gamma_{X1}\gamma_{XX}\gamma_{X3}} \\[3mm]
I_{X3} = n_3(g)\gamma_{X3} = \dfrac{g^3\gamma_{X3}}{g^3 + \gamma_{X3}g^2 + \gamma_{XX}\gamma_{X3}g + \gamma_{X1}\gamma_{XX}\gamma_{X3}}
\end{cases}
\tag{3.28}
$$

In Fig.3.28 (b) we plot the steady-state solution of the system (3.26) as a function of the increasing generation rate for three excitonic levels. At low values of g the population of a given level follows the power-law: $Int = g^p$, where p is the level's order. Being plotted in log-log scale, the graph demonstrates this behavior till certain value of the generation rate at which the level's population saturates. The value of the saturation depends only on the ratio of depopulation rates.
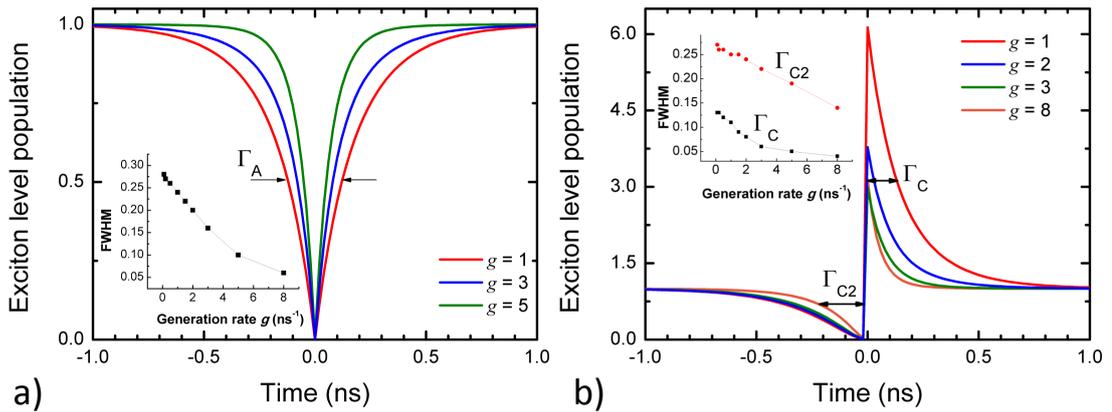

FIGURE 3.29: Modeling of correlation curves. a) Curve of exciton autocorrelation for three different values of generation rate g. Inset: FWHM as a function of the generation rate. b) Curve of cross-correlation for three different values of generation rate g. Inset: FWHM as a function of the generation rate.

The values of depopulation rates can be determined from the steady state solution if one considers the values of generation rate at which the curves intercept each other. For example, the population of level X2 is equal to the population of level X1 at $g = \gamma_{X2}$, the population of level X3 is equal to the population of level X2 at $g = \gamma_{X3}$. The value of γ_{X1} is determined by the value of the generation rate, at which the line characterizing the behavior of X1 level intercepts the value of level population $n_1 = 1$. Hence, by fitting the experimental power dependence of the exciton lines intensities with this steady-state solution, one determine the rates of depopulation for every excitonic level.

c. Solution for photon correlation measurements

By solving the set of rate equations and applying the initial conditions we obtain the time evolution of the level population and photon correlation curves. Fig.3.29(a) shows the evolution of the exciton population considering the initial condition

$$
\begin{cases}
n_0(t = 0) = 1, \\
n_1(t = 0) = 0, \\
n_2(t = 0) = 0, \\
n_3(t = 0) = 0.
\end{cases}
\tag{3.29}
$$

One sees in the inset graph that the full width at half-maximum of the dip depends on the generation rate so the time needed for the exciton level to reach its steady state is shorter for higher generation rate.

If now we apply the initial conditions corresponding to the dot in the exciton state

$$
\begin{cases}
n_0(t = 0) = 0, \\
n_1(t = 0) = 1, \\
n_2(t = 0) = 0, \\
n_3(t = 0) = 0.
\end{cases}
\tag{3.30}
$$

we calculate the cross-correlation function $g^{(2)}_{X-XX}(\tau)$ from the solution of rate equations as shown on Fig.3.29(b).The part of the curve corresponding to positive delays is the solution for exciton level showing the evolution of its population assuming that a biexciton has been detected at $\tau = 0^+$. The negative part corresponds to the evolution of the

biexciton level assuming that an exciton has been detected at $\tau = 0^-$. After a certain amount of time depending on the generation rate the population of biexciton reaches its stationary state having absorbed two electron-hole pairs.
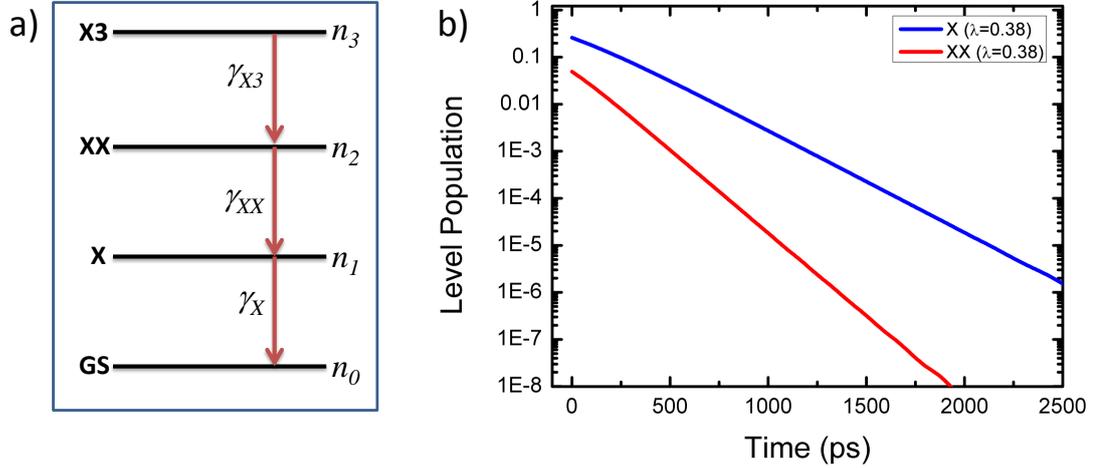

FIGURE 3.30: Modeling of population decay. a) Scheme of the population decay. b) Population of exciton and biexciton levels plotted as a function of time.

d. Solution for decay time measurements

In order to fit decay measurements and to model the decay of the level population in time one should describe the initial distribution of the electron-hole pairs created at each level after a short laser pulse and then solve the rate equations considering a generation rate $g = 0$ after the pulse. The scheme of decay process is presented in Fig.3.30(a). The laser pulse creates electron-hole pairs on each level according to the Poisson statistics:

$$n_k = \frac{\lambda^k}{k!} \exp^{-\lambda}, \ < n_k >= \sum_{k=0}^{\infty} n_k = \lambda, \tag{3.31}$$

where k is the order of the level and λ is the average number of the electron-hole pairs created in the dot by one laser pulse. It is proportional to the averaged lasedr power measured experimentally. The solution of rate equations with defined values of decay times is plotted on Fig.3.30(b) as a function of time for exciton (blue) and biexciton (red) level.

e. Fitting procedure

Now we use this theoretical approach to fit all our experimental data. The values of the fit parameters we have obtained are listed in the following table:

τ_{X1}	τ_{X2}	τ_{X3}	g_{AC}	g_{CC}	λ
200 ps	125 ps	67 ps	0.6	2	0.38

where τ_{X1} is the exciton lifetime, τ_{X2} - biexciton lifetime, τ_{X3} - triexciton lifetime, g_{AC} - generation rate for exciton autocorrelation measurement, g_{CC} - generation rate for exciton-biexciton cross-correlation measurement and λ is the pulsed generation rate. The difference in values for g_{AC} and g_{CC} comes from the difference of excitation powers used for autocorrelation and cross-correlation measurements (2.5 and 7.8 µW respectively).
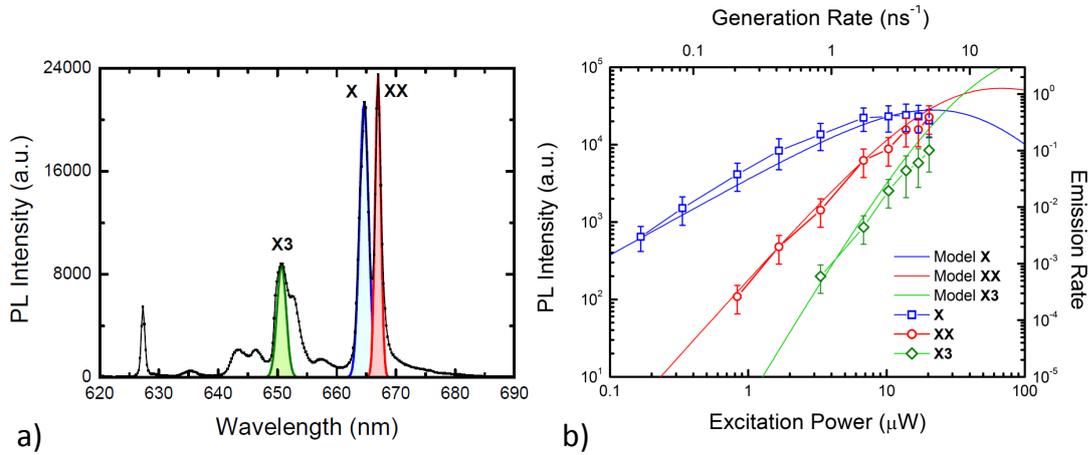

FIGURE 3.31: Power dependence fit. a) Indication of emission lines on photoluminescence spectra . b) Fit of photoluminescence intensity power dependence with 3 level model. Blue - exciton, Red - biexciton, Green - triexciton.

In the Fig.3.31(b) we show the result of the photoluminescence power dependence fit with previously defined parameters of the model. For the lines denoted as X(exciton) and XX(biexciton) in the Fig.3.31(a) the fit follows the measured values of PL intensities with linear and quadratic behavior respectively at low excitation power. As we have used the theoretical model considering triexciton level and we have calculated the behavior of its population with power, we have tried to identify the presence of the triexciton on the photoluminescence spectra. The intensity of the emission line at 650.8 nm follows the calculated power dependence for triexciton at high power excitation and it is hidden behind other emission lines at low power. The measured energy difference between triexciton and exciton is 40 meV. The behavior of photoluminescence power dependence of multi-exciton complexes has been studied in [115] for a single colloidal core-shell CdTe/CdSe quantum dot. It has been shown that multi-exciton complexes could have an energy larger than the one of the first excited state.
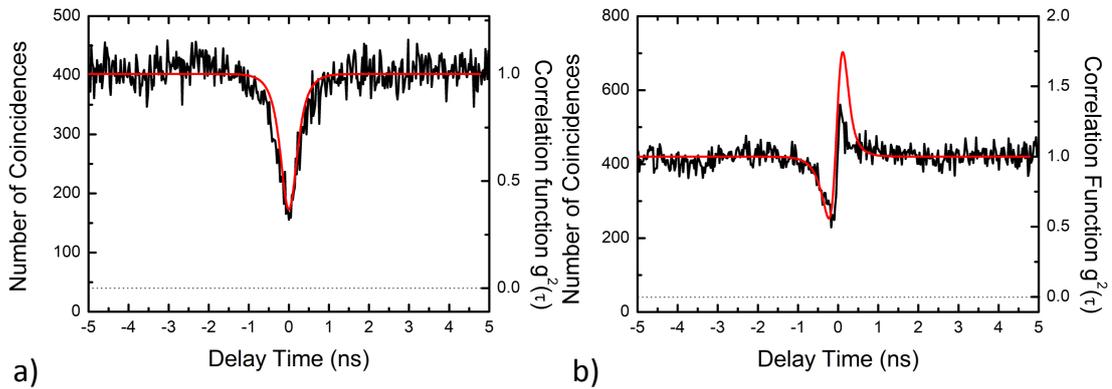
FIGURE 3.32: Fit of correlation measurements. a) Fit of autocorrelation of exciton. b) Fit of cross-correlation between exciton and biexciton

Further we use the same parameters to fit the measurements of photon correlation. The red curve in Fig.3.32 represents the result of a calculation according to the 3 level model described by equations 3.26 which fits our experimental data. The APD has a limited temporal resolution (~ 50 ps each) and in order to take this limitation into account the calculated result was convoluted to the resolution of the APD which we model as a Gaussian with a gaussian width $\sigma = 0.09$ns.
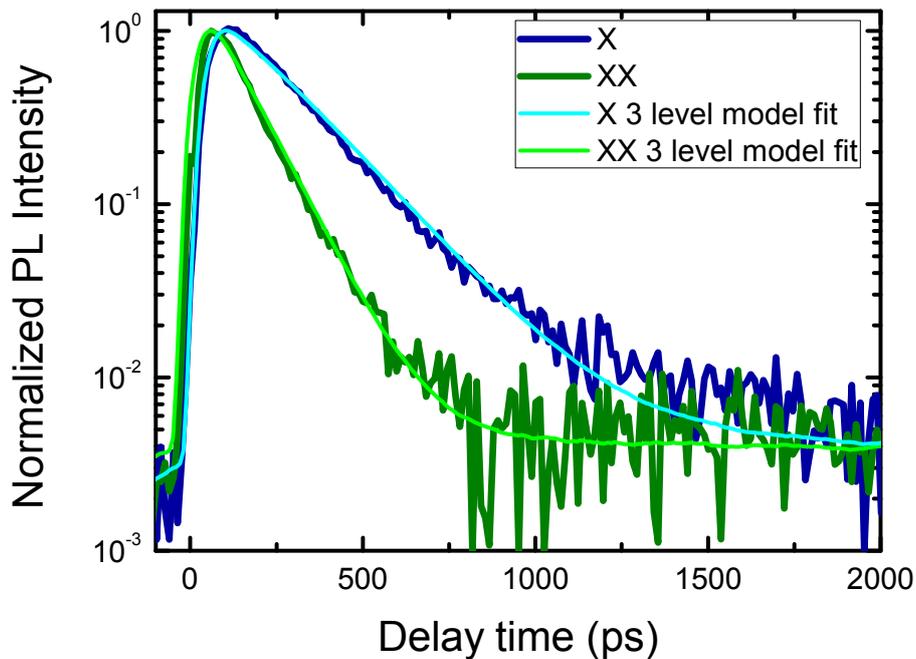

FIGURE 3.33: Decay time measurement fit.

Finally, we fit the decay time measurements. In Fig.3.33 we plot the normalized decay curves for exciton and biexciton and corresponding calculated dependencies of level population convoluted with the response function of the APD. The response function has been measured at the wavelength of the laser line.

The calculated curve fits well the experimental curve.

In order to use the model which includes these additional levels (for example like the one used in [100]) we need an information about the possible charged states occurring in the quantum dot (charged exciton and charged biexciton). We have not identified any charged states in the given quantum dot possibly because it is overlapped with the exciton line and cannot be resolved.

3.5 Influence of temperature on exciton confinement

In order to better characterize the 0D confinement properties one should investigate the evolution of the electron-hole pair dynamics in the QD as a function of temperature. An increase of the temperature activates nonradiative recombination processes which, as a result, influence the photoluminescence emission. In this section we will provide a detailed investigation of the photoluminescence properties of CdTe quantum dot inserted in a ZnTe nanowire as a function of temperature, and compare them with the ones of self-assembled QDs.

3.5.1 Photoluminescence temperature dependence
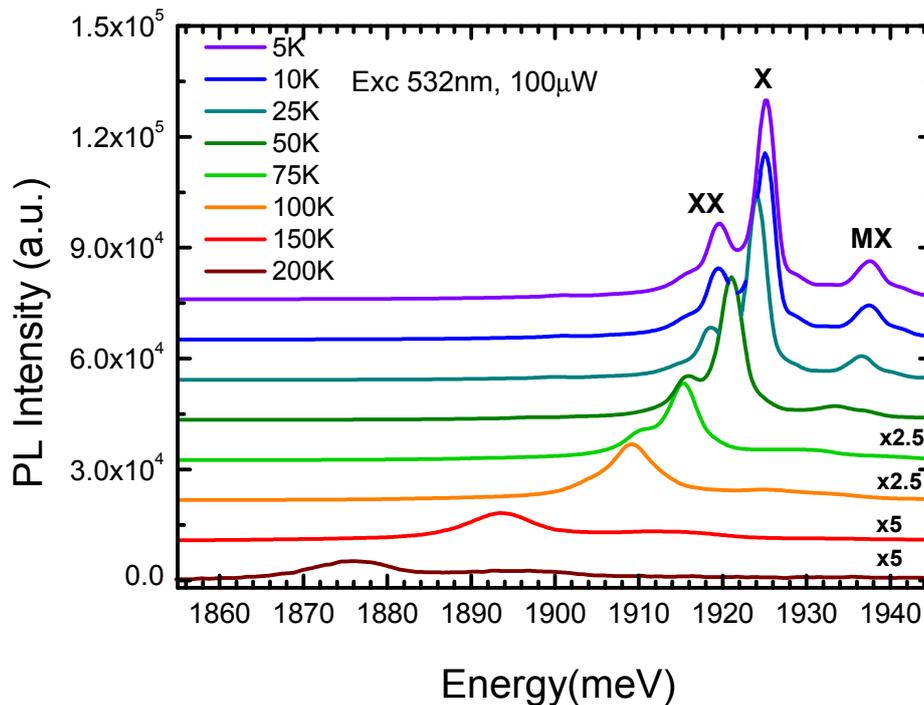
FIGURE 3.34: Photoluminescence temperature dependence. a) Photoluminescence spectra of the CdTe/ZnTe nanowire QD recorded at different temperatures with 532nm laser excitation at 100μW. b) Fit of the photoluminescence spectra recorded at 10K. Gaussian lines with equal width of 2.6meV give the best fitting result.

A set of photoluminescence spectra has been recorded at different temperatures for a single nanowire (Fig.3.34), using a set-up described in Sect.1.4.1. The low temperature spectra consists of emission lines of exciton, biexciton and multiexciton as well as the

emission of other QD energy states, acting as a background emission. As the sample temperature is increased, the PL intensity decreases, the emission energy redshifts, and the emission lines become broader. In order to trace the evolution of the emission lines as a function of temperature, the photoluminescence spectra were fitted with a set of Gaussian functions for each temperature. The example of such a fit is presented in Fig.3.35(b). The extracted parameters of these Gaussian functions (full width at half-maximum, area and center energy) are then used in the following studies.

The temperature dependence of the energy of exciton line is reported in Fig.3.35(a). This line exhibits a redshift of about 50 meV as the temperature increases from 5 K to 200 K. The experimental data have been fitted using the band gap variation introduced by Passler in [70]. It is based on a general assumption, that the band gap energy is influenced by the thermal expansion of the crystal along with the electron-phonon interaction. It is written in the form:

$$E(T) = E(0) - \frac{\alpha \Theta_p}{2} \left[\sqrt[p]{1 + \left(\frac{2T}{\Theta_p} \right)^p} - 1 \right], \tag{3.32}$$

where the parameter $\alpha \equiv S(\infty)$ represents the $T \to \infty$ limiting magnitude of the slope

$$S(T) \equiv -\frac{dE(T)}{dT}, \tag{3.33}$$

of the $E(T)$ curve under investigation, and Θ_p is approximately related to the average phonon energy, $\Theta_p \approx \Theta \equiv \frac{\bar{\varepsilon}}{k_B}$. The fractional exponent p is connected with the material-specific degree of phonon dispersion, $\Delta\varepsilon/\bar{\varepsilon}$, where $\bar{\varepsilon}$ and $\Delta\varepsilon$ are the first and the second moment of the phonon dispersion, by an approximate relation:

$$\frac{\Delta\varepsilon}{\bar{\varepsilon}} = \frac{1}{\sqrt{p^2 - 1}}, \tag{3.34}$$

i.e. conversely

$$p \approx \sqrt{1 + \left(\frac{\Delta\varepsilon}{\bar{\varepsilon}} \right)^{-2}} \tag{3.35}$$

Formula 3.32 provides a more accurate fitting result, comparing to the Varshni's empirical formula[116]

$$E(T) = E(0) - \frac{\alpha T^2}{T + \beta}, \tag{3.36}$$

where $E(0)$ is the energy gap at 0K and the value of β is close to the Debye temperature

	α (mev/K)	Θ_p (K)	p
CdTe/ZnTe NW QD	0.35	134	2.415
Bulk CdTe[70]	0.31	108	1.97
Bulk ZnTe[70]	0.454	145	2.71

TABLE 3.2: Parameters used for NW QD exciton energy temperature dependence fit in comparison with parameters for bulk CdTe in ZnTe obtained in [70]

θ_D of the material. The parameter α has the same meaning as for the Passler equation. Varshni's formula has been widely used for fitting the band gap temperature dependence of bulk semiconductor materials, but provokes misfits in the low-temperature region, due to its oversimplified nature [117]. Thus, we will use the Eq.3.32 for emission energy temperature dependence fitting.

The best-fit curve using parameters listed in Table.3.2, well reproduces the experimental data. These fitting parameters are in agreement with bulk ones and their values, situated in between of the CdTe and ZnTe bulk values, may represent a complex $Cd_xZn_{1-x}Te$ compound. As it can be seen from Fig.3.35(a) the temperature dependence of nanowire
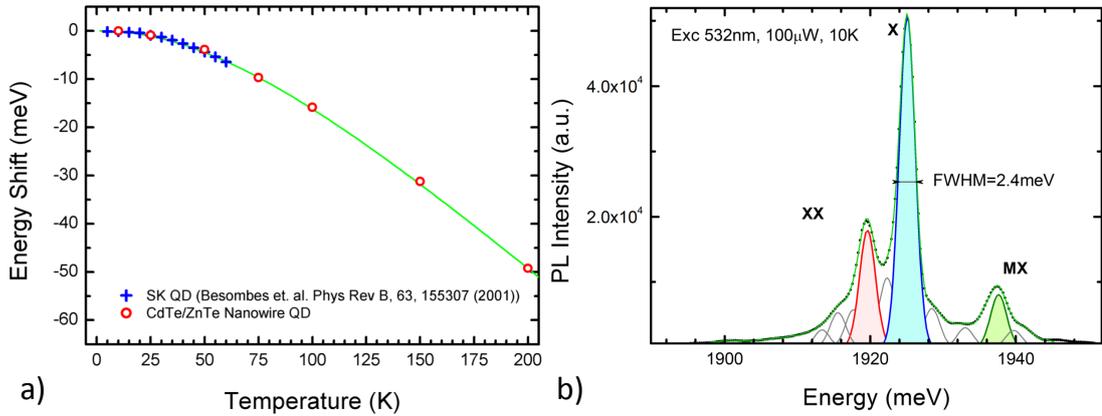

FIGURE 3.35: a) Energy shift of the photoluminescence as a function of temperature for the CdTe/ZnTe SK QD [118](blue crosses) and CdTe/ZnTe nanowire QD (red circles). Green line represents the fitting with formula 3.32. b) An example of photoluminescence spectra fit with gaussian functions.

quantum dot photoluminescence emission energy follows the same law as the one observed for self-assembled CdTe quantum dots[118].

It is interesting to compare the shape of emission lines for NW QD and self-assembled QD. For emission line at low (5K, Fig.3.36(a)) and high temperature ($\sim$ 50K, Fig.3.36(b)) one can see, that at 5K the width of the line is different ($\sim$ 2.3 meV for NW QD and 0.5 meV for self-assembled QD) but for high temperature the difference in the shape becomes also evident.

For CdTe self-assembled QDs, it was shown [118] that an elastic exciton-phonon inter-action in the low temperature range can not be described by a simple full width at half maximum (FWHM)[119, 120]. This is evidenced by the special temperature dependence behavior of the line shape of CdTe QDs emission: the zero phonon line (ZPL) and its acoustic phonon sidebands are distinctly observed due to a suited phonon coupling strength. These two components of the emission line are well described by a Huang-Rhys theoretical model [121] which considers the recombination from stationary eigenstates formed by mixing of discrete excitonic state with acoustic phonon modes. This non-perturbative coupling creates a discrete set of states which can recombine radiatively but with different probabilities depending on the phonon part of each exciton-acoustic phonon state. This elastic exciton-acoustic phonon interaction was confirmed by four-wave mixing experiments [122].

Such an approach is not an easy thing for the case of NW QD. An additional broadening of the zero phonon line occurs due to the spectral diffusion, i.e. ultrafast fluctuations caused by the vicinity of surface states[101].
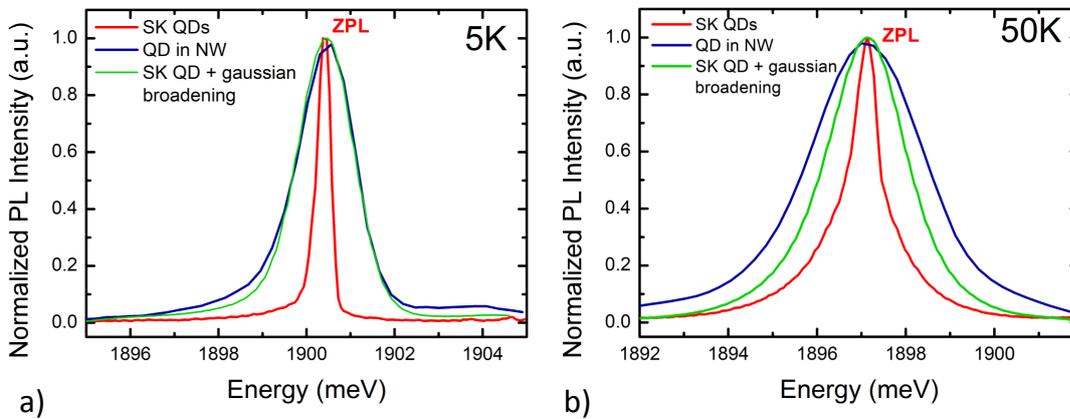

FIGURE 3.36: a) Photoluminescence spectra of the single CdTe/ZnTe self-assembled QD (red line) and NW QD (blue line) recorded at 5 K. The green line corresponds to the convolution of the PL spectra with Gaussian line. b) 50 K photoluminescence spectra of the same objects.

The fluctuations distribution of spectral diffusion has a Gaussian shape and is justified by the Kubo-Anderson theory, which describes the spectral diffusion as the result of fluctuations of a very large number of independent identical random variables, leading globally to a Gaussian distribution of the emitter energies [123–125]. For CdSe/ZnSe nanowires it was shown experimentally that the full width at half maximum of this distribution is few meV and it does not depend on temperature [126]. In Fig.3.36(a),

the green line corresponds to the spectrum of self-assembled QD (red curve) at 5 K convoluted with a Gaussian line of FWHM= 2.1 meV. We see, that it reproduces very well the spectrum of a NW QD (blue curve). The same procedure performed for QD spectrum at 50 K with Gaussian line of the same width results in the green line in Fig.3.36(b). As one can see, it does not reproduce anymore the spectrum of NW QD at this temperature. The broadening of the emission line caused by spectral diffusion describes only a part of NW QD spectrum. Additional broadening is attributed to the coupling of excitons with LO-phonons and is going to be discussed.

3.5.2 Exciton dynamics

The occupation of the exciton level is affected by the exciton-phonon interaction which becomes important at high temperature. It is, therefore, interesting to verify if our CdTe/ZnTe NW quantum dots will still exhibit single-photon source properties, whether it will be similar to the case of CdSe/ZnSe NW QDs for which the photon anti-bunching was demonstrated at room temperature [77].

Photon autocorrelation measurements of the exciton line have been performed, using the set-up depicted in scheme 3.22 in order to investigate the single photon emitter properties evolution with temperature. The sample was excited by a CW 532 nm wavelength laser of 20 μW. As it can be seen from the Fig.3.37, the full width at half-maximum of the autocorrelation histogram dip is continuously decreasing in the studied temperature range up to 100 K, above which the autocorrelation curve does not contain the anti-bunching anymore. This shrinkage of the width of the dip can not be explained by the influence of an increasing amount of photons originating from the increasing overlap with other emission lines and background emission, as an increasing amount of emitters provokes only a decrease of the minimum value of the dip and not of its width.

It can not be explained neither by the change of the exciton lifetime, because it stays constant up to 100 K, as it can be seen in Fig.3.38, where the decay time measurements of the exciton line at different temperatures are shown. These measurements have been performed using the set-up depicted in Fig.3.25 with a 445 nm pulsed laser excitation of 100 μW. The long-time decay component attributed previously to the "diffusion tail" of the APD's Instrument Response Function (see Fig.3.27) has been subtracted from the experimental curves. The value of the short-time decay stays constant in the
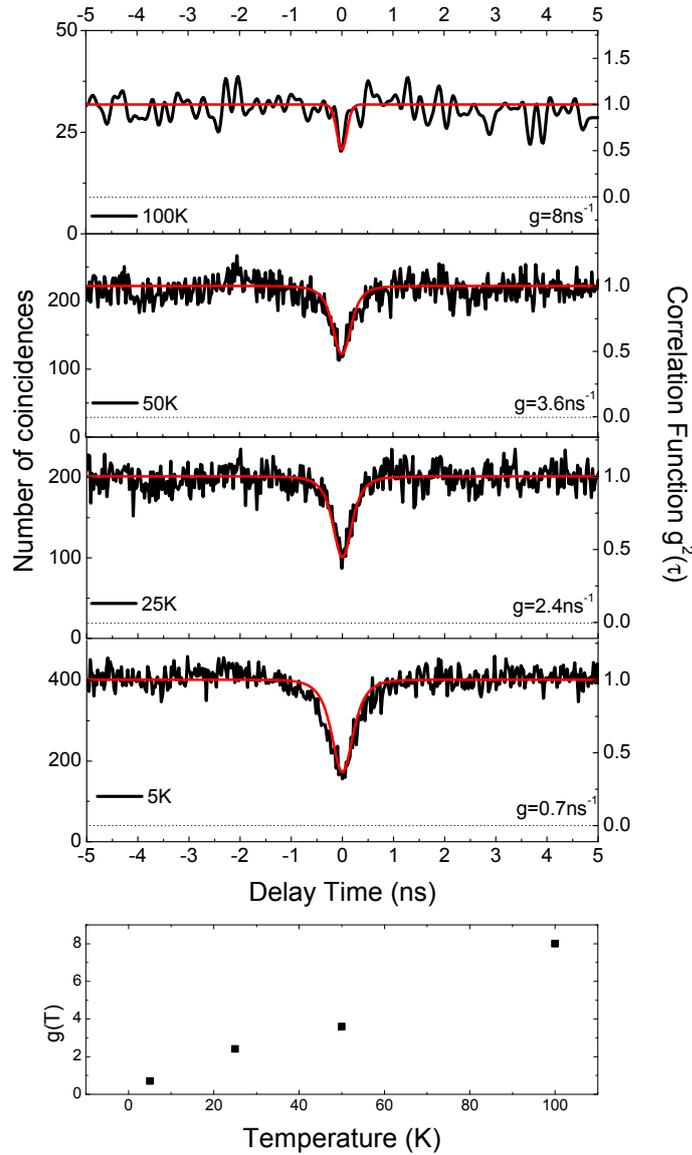
FIGURE 3.37: Temperature dependence of exciton autocorrelation.

studied temperature range. Hence, the only parameter which influences the width of the autocorrelation dip is the generation rate g (see Fig.3.29).

Even though the excitation power used for autocorrelation measurements was not changed, an increase of generation rate is still possible. In photon autocorrelation experiment we use the 532 nm excitation laser wavelength. It means that an electron-hole pair is created in the ZnTe barrier and, after relaxation of its energy by phonon emission, is captured by the quantum dot. At low temperature, the capture of excitons by the quantum dot takes
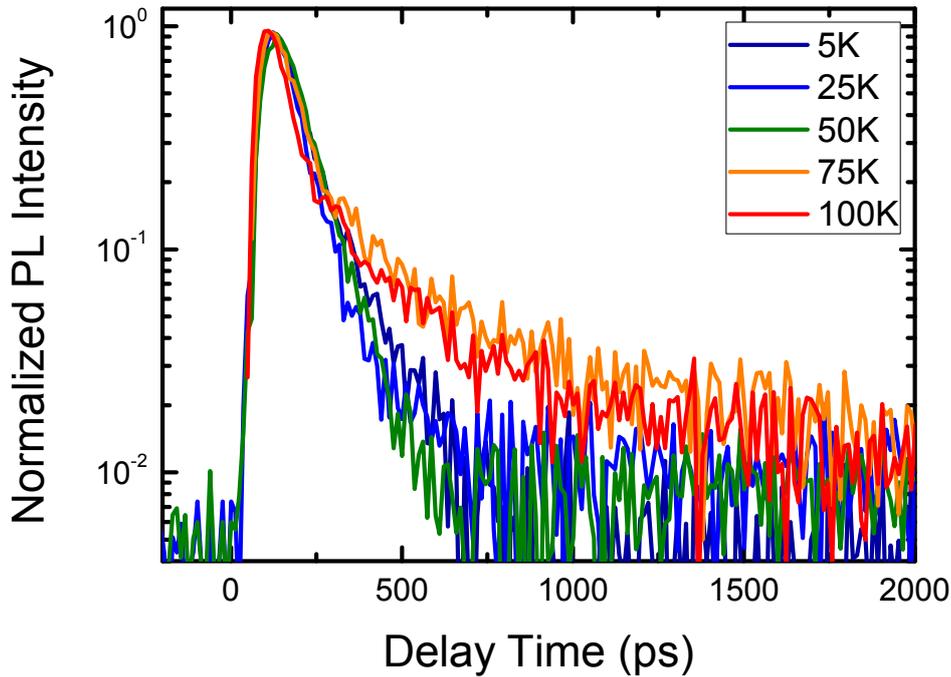
FIGURE 3.38: Temperature dependence of exciton decay time.

place only through spontaneous emission of phonons. At high temperature, the stimulated emission and absorption of phonons becomes important, leading to an increase in both capture and escape rates. An increase of the former influences the generation rate of excitons in the quantum dot and increasing of the latter goes faster which results in observed photoluminescence quenching. The increase of capture rate with an increasing temperature has been observed experimentaly for InAs/GaAs quantum dots [127, 128]. Hence, we can fit the measured second order correlation function by solving rate equations 3.26 with g being the only varying parameter. The resulting curve is plotted in Fig.3.37 as the red solid line demonstrating a good agreement with experimental curves.

Increasing generation rate with a constant exciton lifetime indicate that with an increasing temperature the exciton-phonon scattering process becomes of the major importance in our quantum dots. In order to quantitatively characterize the mechanism of the exciton-phonon interaction, we will study the dependence of the exciton emission linewidth and intensity as a function of temperature.

3.5.3   Coupling to phonons

The possible processes responsible for the exciton population decay in nanowire quantum dot are radiative relaxation, Auger non radiative scattering [129], thermal escape from the dot [130] and trapping in surface and/or defects states [131]. The influence of Auger processes should be investigated for nanowire quantum dots. Here, we will neglect this influence and consider the other two processes. The thermal escape and the exciton trapping are governed by the exciton scattering by phonons. They lead to the broadening of the emission linewidth, and are the ones responsible for the photoluminescence intensity quenching.

Let's consider the temperature dependence of the photoluminescence emission linewidth. As it can be seen from Fig.3.34 and Fig.3.39 the full width at half maximum Γ_h of the exciton emission line continuously increases with increasing sample temperature. In order to have a deeper insight into the carrier-phonon scattering processes involved in the increasing broadening, the experimental data have been fitted using the following relation, describing the temperature dependence of the excitonic line broadening observed in bulk semiconductors and which can be used for QDs [132–134]:

$$\Gamma_h(T) = \Gamma_0 + \sigma T + \Gamma_{LO}(e^{E_{LO}/k_B T} - 1)^{-1}. \tag{3.37}$$

Here, Γ_0 is the low temperature limit of Γ_h and, in the absence of exciton scattering on phonons, is attributed to the linewidth broadening due to the spectral diffusion; σ is the exciton-acoustic phonon coupling coefficient, Γ_{LO} represents the exciton-LO phonon coupling coefficient, E_{LO} is the LO-phonon energy, and k_B is the Boltzmann constant. The broadening of the emission line is, hence, defined by the exciton coupling to acoustic phonons in low-temperature range ($0 \leq T \leq 40$ K) and by exciton scattering on LO-phonons in high-temperature range ($T > 40$ K). A good agreement between the experimental data and the best-fit curve is obtained for $\Gamma_0 = 2.25 \pm 0.15$ meV, $\sigma = (8 \pm 3)$ μeV/K, $\Gamma_{LO} = (17 \pm 1)$ meV, and $E_{LO} = (20 \pm 1)$ meV. The best fit values of the carrier-LO phonons coupling coefficient Γ_{LO} are obtained in a temperature range where the emission is intrinsic. Γ_{LO} is smaller than the theoretical CdTe bulk value [132] ($\Gamma_{LO} = 24.5$ meV). This result can be ascribed to quantum confinement, and it is consistent with theoretical prediction and experimental observation[135, 136]. The

value of the LO-phonon energy is consistent with the bulk CdTe value: $E_{LO} = 21.1$ meV [137].
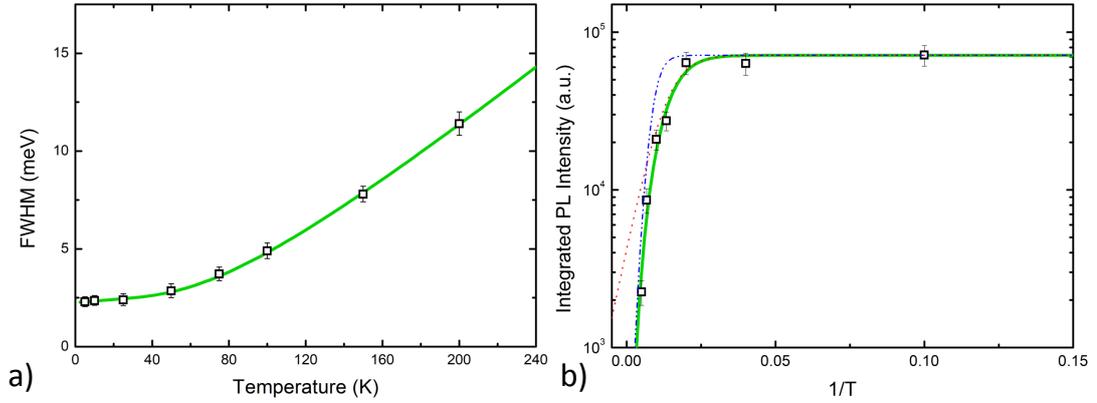

FIGURE 3.39: a) FWHM as a function of temperature. The solid green curve represents the best-fit curve calculated with Eq.3.37. b) Integrated PL intensity as a function of $1/T$. The green line corresponds to the fitting with Eq.3.43, which takes into account the thermal escape of the exciton and an interaction with LO-phonons. Red curve represents the situation when only thermal escape is accounted and blue curve accounts only the interaction with LO-phonons.

The extracted value of σ is higher than the value estimated for bulk CdTe by Rudin et.al.[132], which is around 0.74 μeV/K, and higher than the one obtained for CdTe quantum wells[133] ($\sim$3 μeV), but is smaller than the one obtained for colloidal CdTe/ZnS quantum dots[134], which is around 30 μeV/K. This indicates an increasing coupling with acoustic phonons, induced by the reduced dimensionality of the system[138].

In Fig.3.39(b) the PL intensity as a function of $1/T$ is shown. The photoluminescence intensity is almost constant up to about 30 K, while a first thermally activated PL decrease, followed by a stronger exponential decrease is visible in the range 40-200 K. This decrease of intensity is originated from the activation of non radiative processes with increasing temperature. In self-assembled quantum dots the main contribution to this non radiative process is an ejection of confined carriers to the non localized states of the CdTe wetting layer. Because of the small valence band offset between CdTe and ZnTe, the main contribution in the population decay is given by holes.

Quantitatively, the emission intensity can be described in terms of the rate equation model. For the carriers population n

$$\frac{dn}{dt} = g - \frac{n}{\tau_{rad}} - \frac{n}{\tau_{act}} - \frac{n}{\tau_{esc}}, \tag{3.38}$$

where g is the generation term, $1/\tau_{rad}$ is the radiative recombination rate, and $1/\tau_{esc}$ is the thermal escape rate given by

$$\frac{1}{\tau_{esc}} = \frac{1}{\tau_0} \left(\mathrm{e}^{E_{LO}/k_B T} - 1 \right)^{-m}, \tag{3.39}$$

where τ_0 is a fitting parameter acting as a weight for the probability of carrier-LO-phonon scattering, and m is the number of LO phonons involved in the process. The thermally activated process rate is given by

$$\frac{1}{\tau_{act}} = \frac{1}{\tau_a} \mathrm{e}^{-E_a/k_B T}, \tag{3.40}$$

where E_a is the activation energy and its value represents the energy needed for electron-hole pairs confined in the quantum dot to be transfered outside the confinement potential gap. Typical values of activation energy for self-assembled CdTe quantum dots are 13.2 meV[118] and 17 meV[139]. $1/\tau_a$ is a fitting parameter acting as a weight for the probability of this process. The intensity of the PL emitted per unit time is given by

$$I_{PL} \propto \frac{n_{eq}}{\tau_{rad}}, \tag{3.41}$$

where $n_{eq} = \tau g$ is the carrier population at equilibrium and τ is the temperature-dependent PL decay time given by

$$\frac{1}{\tau} = \frac{1}{\tau_{rad}} + \frac{1}{\tau_{act}} + \frac{1}{\tau_{esc}}, \tag{3.42}$$

The integrated PL intensity is instead given by

$$I_{PL}(T) \propto \frac{g}{1 + \tau_{rad}/\tau_{act} + \tau_{rad}/\tau_{esc}}. \tag{3.43}$$

The experimental data have been fitted to Eq.3.43 by fixing E_{LO} to 20.35 meV, as extracted from the temperature dependence of the emission linewidth. The best-fit curve is shown in Fig.3.39(b) by the green solid line. It describes well the experimental data for $\tau_a/\tau_{rad} = 0.058 \pm 0.008$, $E_a = 18 \pm 2$ meV, $\tau_0/\tau_{rad} = 0.013 \pm 0.005$ and $m = 2.4 \pm 0.4$. Blue and red dashed lines represent the Eq.3.43 with $\tau_a/\tau_{rad} = 0$ and $\tau_0/\tau_{rad} = 0$, respectively.

The obtained value for E_a suggests that the first thermally activated process is due to

carrier trapping in non localized states formed by the surface or by the shell of CdTe deposited during the growth. The main non radiative process, which limits the dots quantum efficiency at high temperature, is the thermal escape from the dot assisted by the scattering with LO phonons. This process, despite the higher activation energy, is characterized by a higher rate, as evidenced by the smaller value of τ_0 with respect to τ_a. The activation energy of this process is defined as an energy gained by scattering on m LO-phonons, which in our case gives $E_a^{LO} = 2.4 \times 20.3$ meV $= 48.7$ meV. This energy is comparable with the valence band offset between ZnTe barrier and CdTe QD (46 meV [110]).

The combination of all the experimental observations helps us to draw the full picture describing the exciton confinement in the CdTe quantum dot inserted in ZnTe nanowire. The good confinement of excitons is observed at 5 K: the strong exciton emission is accompanied by a photon anti-bunching which indicates that an exciton, indeed, recombines in the quantum dot radiatively and this scenario has a highest probability. The linewidth is governed by the spectral diffusion.

With an increasing temperature in the range between 5 K and 50 K, the scattering of the exciton by acoustic phonons leads to the activated migration of the exciton between the quantum dot state and the energy states localized in the CdTe shell (see Fig.3.12) or defects. The decrease of the anti-bunching dip width indicates the increased mobility of the excitons and the minor change of the photoluminescence intensity indicates that the majority of the excitons still recombines radiatively.

With further increase of the temperature above 50 K, thermal escape of the exciton from the quantum dot starts to dominate all other processes. The exciton which has interacted with two and more LO-phonons leaves the quantum dot and recombines non-radiatively. This is evidenced by the strong quenching of the photoluminescence emission. The linewidth of this emission is governed by the energy distribution of those few excitons, which have still succeed to recombine radiatively inside the quantum dot.

A consistent quantitative description of the observed experimental data will be provided in future works. A possible way for this is to write a system of rate equations describing the evolution of the QD exciton level population in interaction with traps (see the scheme depicted in Fig.3.40). This level is populated by excitons created by the laser pulse (with the same generation rate g) and by excitons which have been scattered by
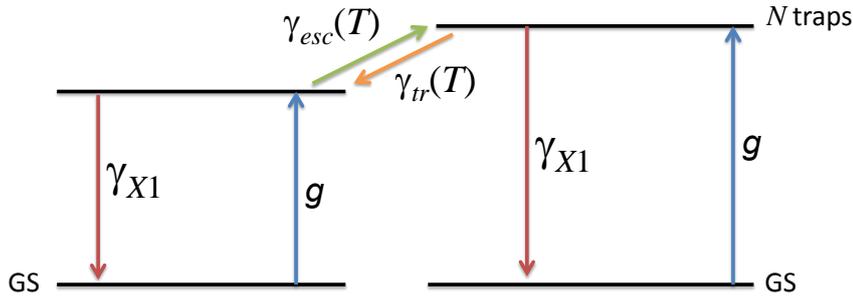
FIGURE 3.40: The scheme of exciton levels with an account of the level of traps.

phonons from the exciton level. The depopulation of this level is governed by exciton recombination (with the rate γ_{X1}). The processes of population and depopulation of each level should be described using the system of rate equations. If the solution of this system of equations provide a consistent description of the experimental data, it will clarify the influence of the traps states on the exciton confinement in the quantum dot. Otherwise, different mechanisms of the exciton level depopulation (for example Auger recombination) should be considered.

3.5.4 Summary on CdTe/ZnTe nanowires

In summary, the optical properties of ZnTe nanowires with CdTe insertion grown by MBE, have been investigated. The CdTe insertion results in the appearance of a photoluminescence band in 1.77 eV 2.06 eV energy range in the macro-PL spectra. We have shown that this broad band consists of several sharp lines coming from individual quantum dots inserted in the nanowire. The strong linear polarization of those lines has been observed and it proves that they originate from the nanowire heterostructure. Cathodoluminescence studies reveal the localized region of the nanowire in which the created electron-hole pairs recombine radiatively. This region corresponds to the localization volume of the quantum dot, which is confirmed by the EDX studies. The 0D confinement of excitons is confirmed by the presence of distinct antibunching in the photon correlation measurements, persisting up to 50 K. Moreover, several lines are attributed to multi-excitonic complexes of the same quantum dots. Emission lines from neutral exciton, biexciton, and triexciton are identified. A characteristic exciton lifetime of the order of 200 ps has been measured in photoluminescence decay time measurements. A

simple 3-level rate equations model allowed us to retrieve the characteristic parameters of exciton population evolution. Finally, the photoluminescence intensity evolution with temperature demonstrated the thermally activated processes of exciton escape from the quantum dot. The activation energy of the thermal escape process, which is responsible for the strong quenching of photoluminescence intensity, is comparable to the valence band offset between ZnTe barrier and CdTe quantum dot, which allows us to suggest that observed quenching of emission intensity is due to the holes detrapping.

Chapter 4

Conclusions

Exciton and charged exciton magnetic polaron in single DMS QDs

The formation of exciton magnetic polaron is a unique feature of diluted magnetic semi-conductors. In this work we have investigated the EMP formation in single CdMnTe self-assembled QDs. A set of samples with Mn concentration varied between 2% and 10% has been studied. The magnetic polaron formation was observed in the most concentrated sample and we have observed new features which were not described in previous studies.

First of all, we have shown, that charged excitons can be observed by simply changing the excitation laser wavelength. The sign of the charged exciton was determined performing micro-photoluminescence studies under gate voltage.

This finding allowed us to study the magnetic polaron formation process for both exciton complexes and to compare their parameters. The main results obtained are the following:

- **the magnetic polaron forms with the negatively charged exciton** along with the neutral exciton and, surprisingly, the MP formed with a charged exciton demonstrates **a higher polaron energy and a higher exchange field.**

  We have demonstrated, that the widely used in literature "exchange box" model is not able to consistently explain these experimental results. The reason of that is the oversimplified nature of this model, which does not take into account the Coulomb interactions between electron and hole in QD. Moreover, most of the

time the influence of an electron on the magnetic polaron formation is neglected due to the smaller exchange integral value [49, 51].

- In order to explain our experimental findings, we develop a **new theoretical approach**. This approach shows, that by taking into account the shape of electron and hole wave functions and assuming a linear response of Mn magnetic moments to the exchange field, it is possible to generalize the results obtained with the "exchange box" model and, to describe consistently the formation of MP in a QD containing a neutral or a charged exciton.

- We have confirmed the validity of the new approach by a numerical calculation of the magnetic polaron parameters for a neutral and a negatively charged exciton. A good agreement is found with experimental results. We have shown with this new approach that the main reason of the observation of higher magnetic polaron energy with negatively charged exciton is the increased overlap of the hole wave function with magnetic atoms. It is induced by the Coulomb interaction between the electrons and the hole. We have shown that a hole is mostly confined in the quantum dot by the attraction of well confined electrons. The potential barrier for a hole created by the valence band offset in the quantum dot with a high Mn concentration appears negligible.

Having identified negatively charged exciton in the photoluminescence spectra of DMS quantum dots, we have not found any biexciton emission lines. The reason should be found in future, especially if one wants to observe the so-called bipolaron, the existence of which has been predicted in some theoretical works [140, 141].

Nanowires optical properties

Some important results on the optical properties of ZnTe nanowires have been obtained in this work.

- First of all, **the near band-edge photoluminescence spectrum of pure ZnTe single nanowire has been demonstrated for the first time**. We have shown that the emission originates, indeed, from the nanowire by, first, investigating the photoluminescence intensity dependence on the excitation polarization and, second, by recording cathodo-luminescence images.

- We investigate theoretically the **influence of the strain** induced by the presence of an oxide shell. These findings will help to tune the emission energy of the nanowire by choosing the appropriate material for the shell.

The optical properties of CdTe quantum dots inserted in ZnTe nanowires have been studied in this work in order to characterize the exciton confinement.

- We have shown **monochromatic cathodo-luminescence image** of single nanowire, which allows us to correlate the spatial distribution of the emitted light with structural studies, such as EDX and TEM, and to verify that the exciton emission is, indeed, originating from the quantum dot.

- Using photon correlation measurements, we have demonstrated the **single-photon source properties** of this system, which are conserved up to 50 K. By developing a rate equations model we have fitted the experimental data and identified multi-exciton complexes such as biexciton and triexciton. Temperature dependence studies demonstrate the activation of the exciton thermal escape from the quantum dot towards trap levels.

Further studies will be related, first of all, with the observation of the magnetic polarons in DMS nanowires. The incorporation of Mn inside CdTe/ZnTe quantum dots is the next step of this investigation. For a better exciton confinement in such structures, an interesting perspective could be also the fabrication of core-shell structures or the incorporation of magnesium in the nanowire in order to increase the confinement potential of holes. A better hole confinement will result in a stronger exchange interactions with magnetic atoms and, as a consequence, in stronger magnetic polarons.

Appendix A

# Time-resolved photoluminescence measurements of single CdMnTe (10%Mn) quantum dots
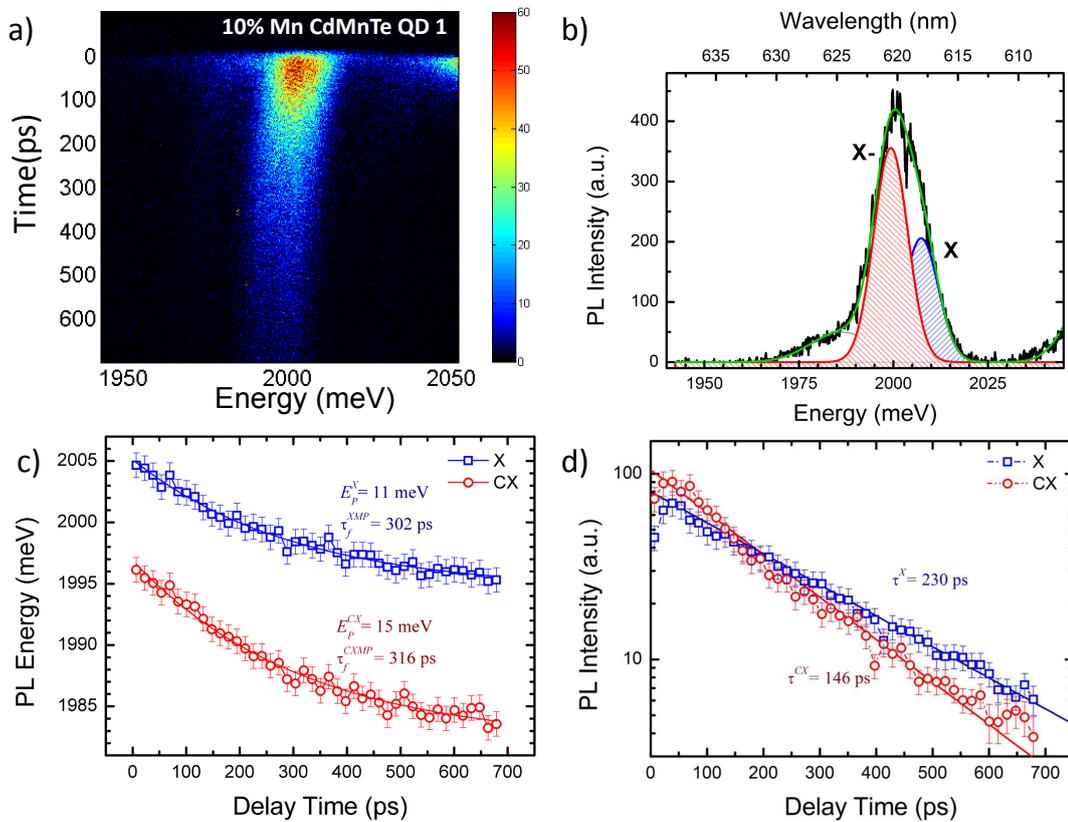

FIGURE A.1: CdMnTe single QD 1
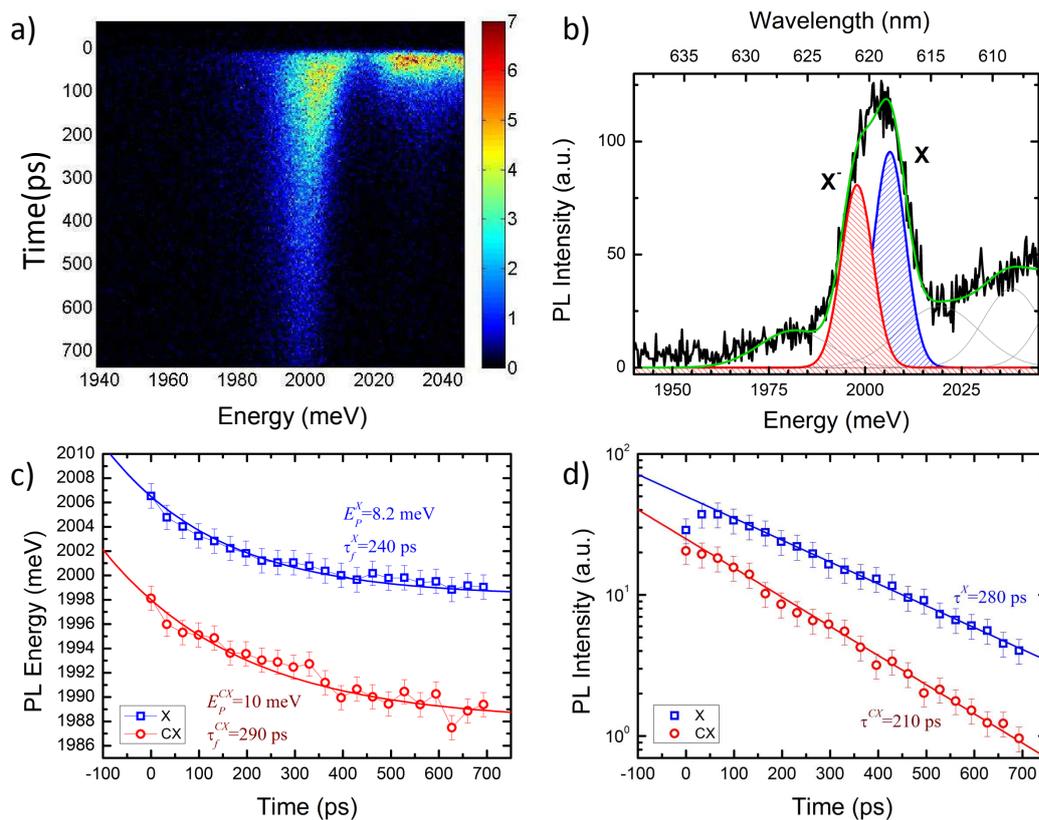
FIGURE A.2: CdMnTe single QD 2
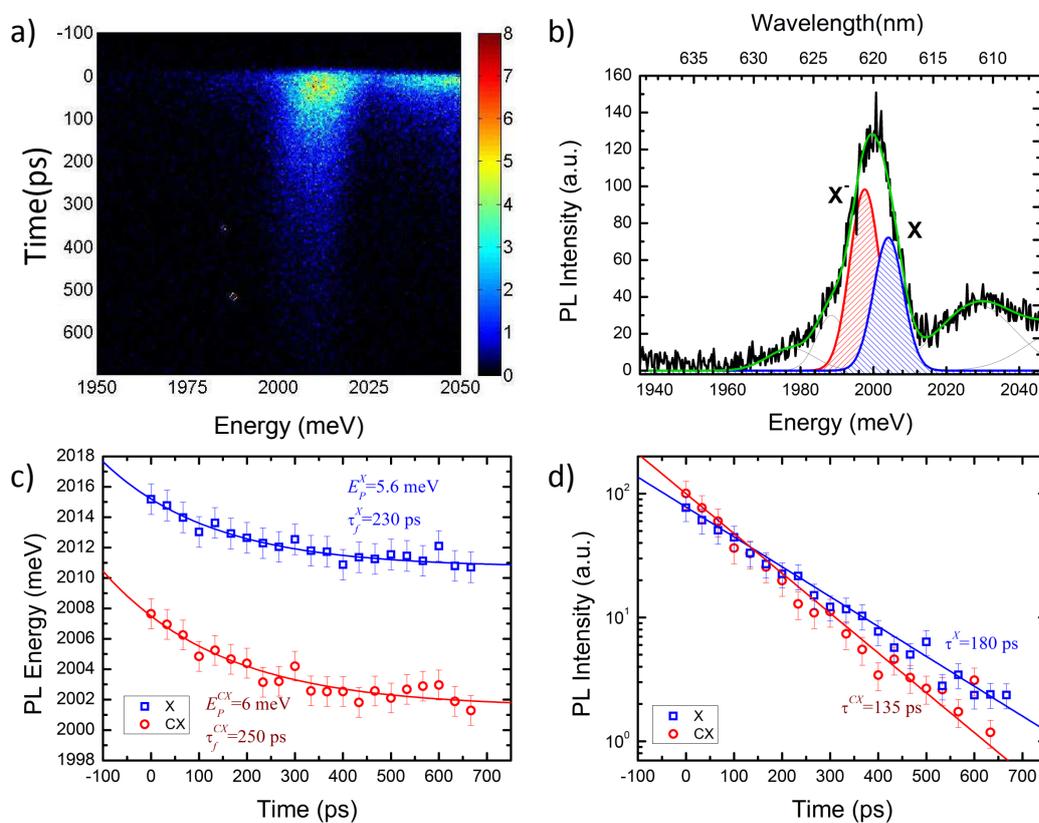
FIGURE A.3: CdMnTe single QD 3

Appendix B

CdTe/ZnTe nanowires
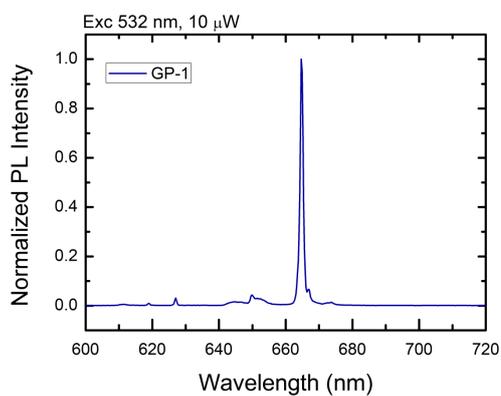
FIGURE B.1: CdTe/ZnTe NW GP-1
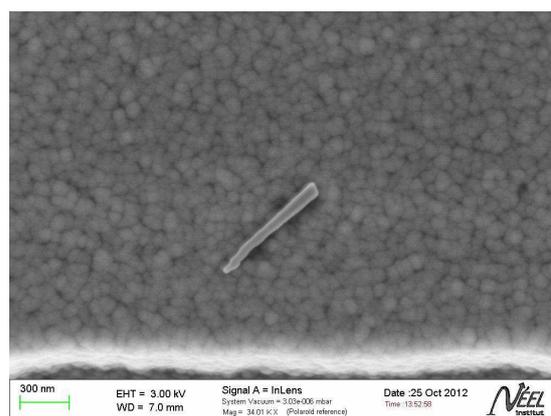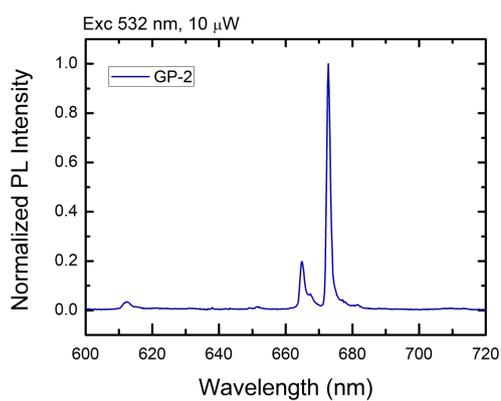
FIGURE B.2: CdTe/ZnTe NW GP-2
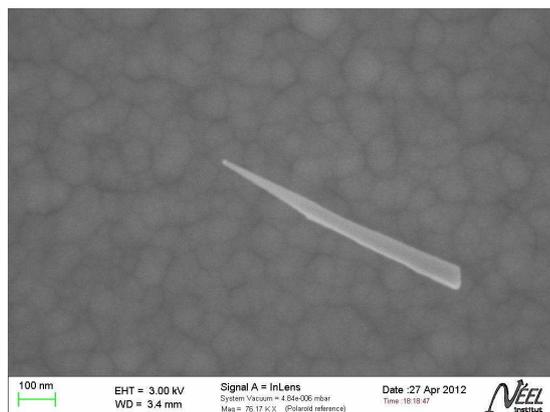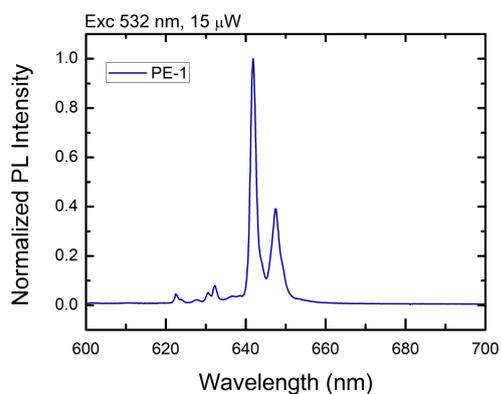
FIGURE B.3: CdTe/ZnTe NW PE-1
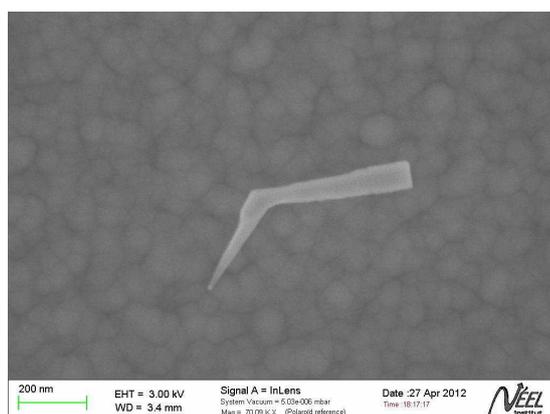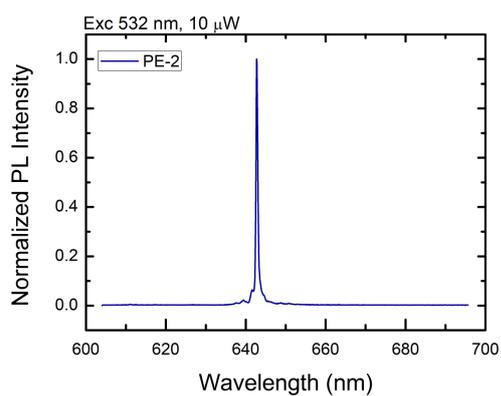

FIGURE B.4: CdTe/ZnTe NW PE-2
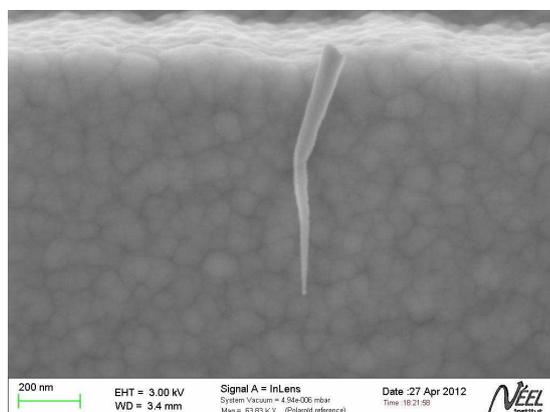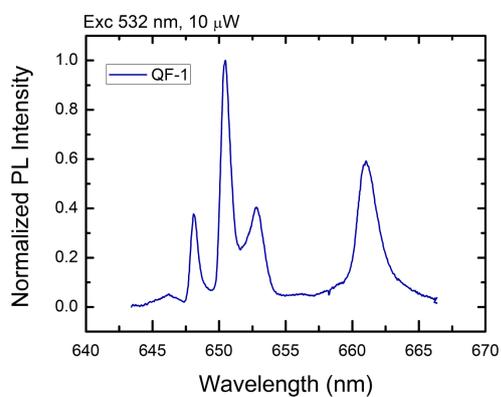

FIGURE B.5: CdTe/ZnTe NW QF-1
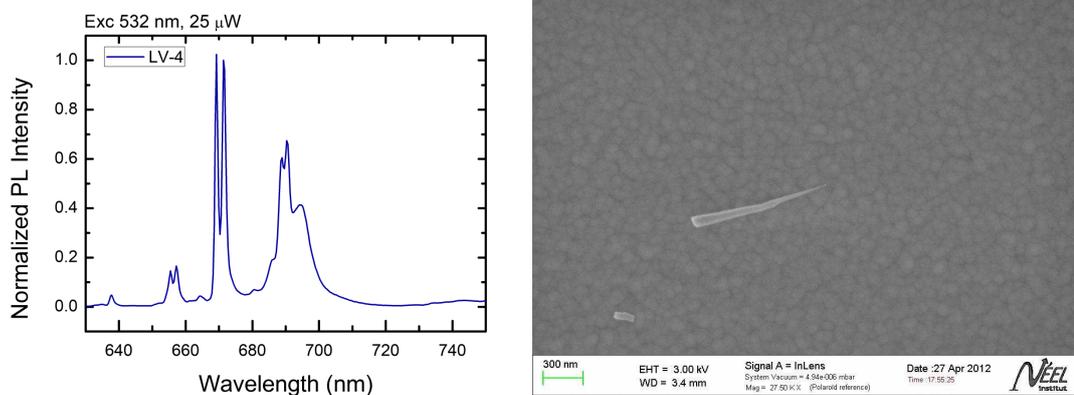
FIGURE B.6: CdTe/ZnTe NW LV-4
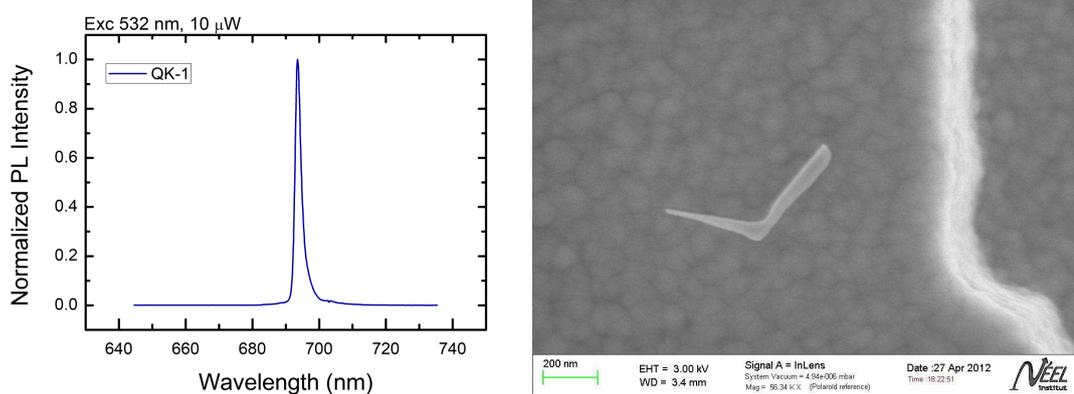
FIGURE B.7: CdTe/ZnTe NW QK-1

Bibliography

[1] M. N. Baibich, J. M. Broto, A. Fert, F. N. Van Dau, F. Petroff, P. Etienne, G. Creuzet, A. Friederich, and J. Chazelas, "Giant Magnetoresistance of (001)Fe/(001)Cr Magnetic Superlattices," *Phys. Rev. Lett.*, vol. 61, pp. 2472–2475, Nov 1988.

[2] S. Datta and B. Das, "Electronic analog of the electro-optic modulator," *Applied Physics Letters*, vol. 56, no. 7, pp. 665–667, 1990.

[3] H. Ohno, H. Munekata, T. Penney, S. von Molnár, and L. L. Chang, "Magneto-transport properties of p -type (In,Mn)As diluted magnetic III-V semiconductors," *Phys. Rev. Lett.*, vol. 68, pp. 2664–2667, Apr 1992.

[4] A. Haury, A. Wasiela, A. Arnoult, J. Cibert, S. Tatarenko, T. Dietl, and Y. Merle d'Aubigné, "Observation of a Ferromagnetic Transition Induced by Two-Dimensional Hole Gas in Modulation-Doped CdMnTe Quantum Wells," *Phys. Rev. Lett.*, vol. 79, pp. 511–514, Jul 1997.

[5] Jungwirth, T. and Horodyská, P. and Tesařová, N. and Němec, P. and Šubrt, J. and Malý, P. and Kužel, P. and Kadlec, C. and Mašek, J. and Němec, I. and Orlita, M. and Novak, V. and Olejnik, K. and Soban, Z. and Vašek, P. and Svoboda, P. and Sinova, Jairo, "Systematic Study of Mn-Doping Trends in Optical Properties of (Ga,Mn)As," *Phys. Rev. Lett.*, vol. 105, p. 227201, Nov 2010.

[6] L. Besombes, Y. Leger, L. Maingault, D. Ferrand, H. Mariette, and J. Cibert, "Probing the Spin State of a Single Magnetic Ion in an Individual Quantum Dot," *Phys. Rev. Lett.*, vol. 93, p. 207403, 2004.

[7] M. Goryca, T. Kazimierczuk, M. Nawrocki, A. Golnik, J. A. Gaj, P. Kossacki, P. Wojnar, and G. Karczewski, "Optical Manipulation of a Single Mn Spin in a CdTe-Based Quantum Dot," *Phys. Rev. Lett.*, vol. 103, p. 087401, Aug 2009.

[8] A. Kudelski, A. Lemaitre, A. Miard, P. Voisin, T. C. M. Graham, R. J. Warburton, and O. Krebs, "Optically Probing the Fine Structure of a Single Mn Atom in an InAs Quantum Dot," *Phys. Rev. Lett.*, vol. 99, p. 247209, Dec 2007.

[9] L. Besombes, Y. Leger, J. Bernos, H. Boukari, H. Mariette, J. P. Poizat, T. Clement, J. Fernández-Rossier, and R. Aguado, "Optical probing of spin fluctuations of a single paramagnetic mn atom in a semiconductor quantum dot," *Phys. Rev. B*, vol. 78, p. 125324, Sep 2008.

[10] C. Le Gall, L. Besombes, H. Boukari, R. Kolodka, J. Cibert, and H. Mariette, "Optical spin orientation of a single manganese atom in a semiconductor quantum dot using quasiresonant photoexcitation," *Phys. Rev. Lett.*, vol. 102, p. 127402, Mar 2009.

[11] C. Le Gall, R. S. Kolodka, C. L. Cao, H. Boukari, H. Mariette, J. Fernández-Rossier, and L. Besombes, "Optical initialization, readout, and dynamics of a Mn spin in a quantum dot," *Phys. Rev. B*, vol. 81, p. 245315, Jun 2010.

[12] R. Triboulet and P. Siffert, *CdTe and Related Compounds*. Elsevier, 2010.

[13] H. Boukari, P. Kossacki, M. Bertolini, D. Ferrand, J. Cibert, S. Tatarenko, A. Wasiela, J. A. Gaj, and T. Dietl, "Light and electric field control of ferromagnetism in magnetic quantum structures," *Phys. Rev. Lett.*, vol. 88, p. 207204, May 2002.

[14] A. A. Maksimov, G. Bacher, A. McDonald, V. D. Kulakovskii, A. Forchel, C. R. Becker, G. Landwehr, and L. W. Molenkamp, "Magnetic polarons in a single diluted magnetic semisemiconductor quantum dot," *Phys. Rev. B*, vol. 62, pp. R7767–R7770, 2000.

[15] L. Nirmal, Manoj; Brus, "Luminescence photophysics in semiconductor nanocrystals," *Accounts of Chemical Research*, vol. 32, pp. 407–414, 1999.

[16] J. K. Furdyna, "Diluted magnetic semiconductors," *J. Appl. Phys.*, vol. 64, p. R29, 1988.

[17] G. Fishman, *Energie et fonctions donde dans les semi-conducteurs*. Monographie de physique, 1988.

[18] L. S. Dang, G. Neu, and R. Romestain, "Optical detection of cyclotron resonance of electron and holes in CdTe," *Solid State Communications*, vol. 44, no. 8, pp. 1187 – 1190, 1982.

[19] A. Merad, M. Kanoun, J. Cibert, H. Aourag, and G. Merad, "Stress-dependence tight binding study of tellurium-based II-VI semiconductors," *Physics Letters A*, vol. 315, no. 12, pp. 143 – 149, 2003.

[20] H. J. McSkimin and D. G. Thomas, "Elastic Moduli of Cadmium Telluride," *J. Appl. Phys.*, vol. 33, p. 56, 1961.

[21] J. Allegre, B. Gil, J. Calatayud, and H. Mathieu, "Deformation potentials of CdTe epilayers from piezo and wavelength reflectivity spectra analysis," *Journal of Crystal Growth*, vol. 101, p. 603, 1990.

[22] D. Berlincourt, H. Jaffe, and L. R. Shiozawa, "Electroelastic Properties of the Sulfides, Selenides, and Tellurides of Zinc and Cadmium," *Phys. Rev.*, vol. 129, pp. 1009–1017, 1963.

[23] K. Kheng, R. T. Cox, M. Y. d' Aubigné, F. Bassani, K. Saminadayar, and S. Tatarenko, "Observation of negatively charged excitons X^- in semiconductor quantum wells," *Phys. Rev. Lett.*, vol. 71, pp. 1752–1755, Sep 1993.

[24] P. Kossacki, H. Boukari, M. Bertolini, D. Ferrand, J. Cibert, S. Tatarenko, J. A. Gaj, B. Deveaud, V. Ciulin, and M. Potemski, "Photoluminescence of p-doped quantum wells with strong spin splitting," *Phys. Rev. B*, vol. 70, p. 195337, Nov 2004.

[25] Y. Leger, *Détection de spins individuels dans les boites quantiques magnétiques*. PhD thesis, Université Joseph Fourier - Grenoble 1, 2007.

[26] J. Gaj, R. Planel, and G. Fishman, "Relation of magneto-optical properties of free excitons to spin alignment of Mn2+ ions in Cd(1-x)Mn(x)Te," *Solid State Communications*, vol. 29, no. 5, pp. 435 – 438, 1979.

[27] F. Donatini and L. S. Dang, "A single-step electron beam lithography of buried nanostructures using cathodoluminescence imaging and low temperature," *Nanotechnology*, vol. 21, p. 375303, 2010.

[28] B. Langen, H. Leiderer, W. Limmer, W. Gebhardt, M. Ruff, and U. Rassler, "Absolute absorption coefficients of znte single crystal layers: Experiment and theory," *Journal of Crystal Growth*, vol. 101, pp. 718 – 721, 1990.

[29] A. Golnik, J. A. Gaj, M. Nawrocki, R. Planel, and C. B. a la Guillaume *J. Phys. Soc. Japan, Suppl.*, vol. A49, p. 819, 1980.

[30] P. G. de Gennes, "Effects of double exchange in magnetic crystals," *Phys. Rev.*, vol. 118, pp. 141–154, Apr 1960.

[31] T. Kasuya and A. Yanase, "Anomalous Transport Phenomena in Eu-Chalcogenide Alloys," *Rev. Mod. Phys.*, vol. 40, pp. 684–696, Oct 1968.

[32] T. Kasuya, A. Yanase, and T. Takeda, "Stability condition for the paramagnetic polaron in a magnetic semiconductor," *Solid State Commun.*, vol. 8, p. 1543, 1970.

[33] S. M. Ryabchenko and Y. G. Semenov, "Spin-correlation effects for a large-radius electron center in a magnetically mixed semiconductor," *Sov. Phys. JETP*, vol. 57, p. 825, 1983.

[34] D. Yakovlev, W. Ossau, O. Landwehr, R. Bicknell-Tassius, and A. Waag, "First Observation And Experimental Proof Of Free Magnetic Polaron Formation In CdTe/(Cd,Mn)Te Quantum Wells," *Sold State Comm.*, vol. 76, pp. 325–329, 1990.

[35] M. Nawrocki, R. Planel, F. Mollot, and M. J. Kozielski, "Magnetization and Spin-Flip Raman Scattering in Cd(1-x)Mn(x)S," *Physica status solidi (b)*, vol. 123, pp. 99–103, 1984.

[36] A. Golnik, J. Ginter, and J. A. Gaj, "Magnetic polarons in exciton luminescence of Cd(1-x)Mn(x)Te," *J. Phys. C*, vol. 16, p. 6073, 1983.

[37] P. A. Wolff and J. Warnock, "Bound magnetic polarons in dilute magnetic semiconductors (invited)," *Journal of Applied Physics*, vol. 55, no. 6, pp. 2300–2304, 1984.

[38] J. Furdyna, J. Kossut, and P. A. Wolff, *Semiconductors and Semimetals.* 1988.

[39] D.Yakovlev, W. Ossau, J. Gaj, and J. Kossut, *Introduction to the Physics of Diluted Magnetic Semiconductors*, vol. 144, ch. 7, p. 222. Springer Series in Materials Science, 2010.

[40] T. Itoh and E. Komatsu, "Magnetic polaron formation of localized excitons in semimagnetic semiconductor alloys of Cd0.8Mn0.2Te," *Journal of Luminescence*, vol. 38, no. 16, pp. 266 – 268, 1987.

[41] V. F. Agekyan and A. Y. Serov *Sov. Phys. Solid State*, vol. 32, no. 1951, 1990.

[42] S. Takeyama, S. Adachi, Y. Takagi, and V. F. Aguekian, "Exciton localization by magnetic polarons and alloy fluctuations in the diluted magnetic semiconductor $Cd_{1-x}Mn_xTe$," *Phys. Rev. B*, vol. 51, pp. 4858–4864, Feb 1995.

[43] M. Umehara, "Effect of alloy potential fluctuations on the exciton magnetic polaron in the bulk diluted magnetic semiconductors $Cd_{1-x}Mn_xTe$," *Phys. Rev. B*, vol. 68, p. 193202, Nov 2003.

[44] J. Warnock, A. Petrou, R. N. Bicknell, N. C. Giles-Taylor, D. K. Blanks, and J. F. Schetzina, "Photoluminescence of $Cd_{1-x}Mn_xTe$-CdTe multiple-quantum-well structures and superlattices in a magnetic field," *Phys. Rev. B*, vol. 32, pp. 8116–8125, Dec 1985.

[45] T. Stirner, W. E. Hagston, P. Harrison, and J. P. Goodwin, "Exciton magnetic polarons in quantum wells," *Journal of Applied Physics*, vol. 75, no. 7, pp. 3466–3471, 1994.

[46] A. Kavokin and K. Kavokin, "Theory of two-dimensional magnetic polarons in an external magnetic field," *Semiconductor Science and Technology*, vol. 8, no. 2, p. 191, 1993.

[47] G. Mackh, W. Ossau, D. R. Yakovlev, A. Waag, G. Landwehr, R. Hellmann, and E. O. Göbel, "Localized exciton magnetic polarons in $Cd_{1-x}Mn_xTe$," *Phys. Rev. B*, vol. 49, pp. 10248–10258, Apr 1994.

[48] I. A. Merkulov, D. R. Yakovlev, K. V. Kavokin, G. Mackh, W. Ossau, A. Waag, and G. Landwehr, "Hierarchy of relaxation times in the formation of an excitonc magnetic polaron in (CdMn)Te," *JETP Lett.*, vol. 62, p. 335, 1995.

[49] K. V. Kavokin, I. A. Merkulov, D. R. Yakovlev, W. Ossau, and G. Landwehr, "Exciton localization in semimagnetic semiconductors probed by magnetic polarons," *Phys. Rev. B*, vol. 60, pp. 16499–16505, Dec 1999.

[50] M. Goryca, D. Ferrand, P. Kossacki, M. Nawrocki, W. Pacuski, W. Maślana, J. A. Gaj, S. Tatarenko, J. Cibert, T. Wojtowicz, and G. Karczewski, "Magnetization Dynamics Down to a Zero Field in Dilute (Cd,Mn)Te Quantum Wells," *Phys. Rev. Lett.*, vol. 102, p. 046408, Jan 2009.

[51] G. Bacher, A. A. Maksimov, H. Schmig, V. D. Kulakovskii, M. K. Welsch, A. Forchel, P. S. Dorozhkin, A. V. Chernenko, S. Lee, M. Dobrowolska, and J. K. Furdyna, "Monitoring statistical magnetic fluctuations on the nanometer scale," *Phys. Rev. Lett.*, vol. 89, p. 127201, 2002.

[52] T. Gurung, S. Mackowski, G. Karczewski, H. E. Jackson, and L. M. Smith, "Ultralong spin memory of optically excited single magnetic quantum dots," *Appl. Phys. Lett.*, vol. 93, p. 153114, 2008.

[53] L. Kłopotowski, L. Cywiński, P. Wojnar, V. Voliotis, K. Fronc, T. Kazimierczuk, A. Golnik, M. Ravaro, R. Grousson, G. Karczewski, and T. Wojtowicz, "Magnetic polaron formation and exciton spin relaxation in single $Cd_{1-x}Mn_xTe$ quantum dots," *Phys. Rev. B*, vol. 83, p. 081306, Feb 2011.

[54] R. Beaulac, L. Schneider, P. I. Archer, G. Bacher, and D. R. Gamelin, "Light-Induced Spontaneous Magnetization in Doped Colloidal Quantum Dots," *Science*, vol. 325, no. 5943, pp. 973–976, 2009.

[55] D. R. Yakovlev, G. Mackh, B. Kuhn-Heinrich, W. Ossau, A. Waag, G. Landwehr, R. Hellmann, and E. O. Göbel, "Exciton magnetic polarons in short-period $CdTe/Cd_{1-x}Mn_xTe$ superlattices," *Phys. Rev. B*, vol. 52, pp. 12033–12038, Oct 1995.

[56] P. Wojnar, J. Suffczyński, K. Kowalik, A. Golnik, G. Karczewski, and J. Kossut, "Microluminescence from Cd(1-x)Mn(x)Te magnetic quantum dots containing only a few Mn ions," *Phys. Rev. B*, vol. 75, p. 155301, Apr 2007.

[57] J. Kim, M. C. Gallagher, R. F. Willis, J. Fu, , and D. L. Miller, "Scanning tunneling microscope study of GaAs(001) surfaces grown by migration enhanced epitaxy," *J. Vac. Sci. Technol. B*, vol. 11, p. 1370, 1993.

[58] F. Tinjod, B. Gilles, S. Moehl, K. Kheng, and H. Mariette, "IIVI quantum dot formation induced by surface energy change of a strained layer," *Appl. Phys. Lett.*, vol. 82, p. 4340, 2003.

[59] L. Maingault, L. Besombes, Y. Léger, C. Bougerol, and H. Mariette, "Inserting one single Mn ion into a quantum dot," *Applied Physics Letters*, vol. 89, no. 19, p. 193109, 2006.

[60] Y. Terai, S. Kuroda, and K. Takita, "Self-organized formation and photoluminescence of Cd1-xMnxTe quantum dots grown on ZnTe by atomic layer epitaxy," *Appl. Phys. Lett.*, vol. 76, p. 2400, 2000.

[61] M. Strassburg, M. Dworzak, H. Born, R. Heitz, and A. Hoffmann, "Lateral redistribution of excitons in CdSe/ZnSe quantum dots," *Applied Physics Letters*, vol. 80, p. 473, 2002.

[62] A. Murayama, T. Furuta, K. Hyomi, I. Souma, Y. Oka, D. Dagnelund, I. A. Buyanova, and W. M. Chen, "Dynamics of exciton-spin injection, transfer, and relaxation in self-assembled quantum dots of CdSe coupled with a diluted magnetic semiconductor layer of Zn(0.80)Mn(0.20)Se," *Phys. Rev. B*, 2007.

[63] Y. Leger, L. Besombes, J. Fernndez-Rossier, L. Maingault, , and H. Mariette, "Electrical control of a single mn atom in a quantum dot," *Phys. Rev.Lett.*, vol. 97, p. 107401, 2006.

[64] L. Besombes, K. Kheng, L.Marsal, and H. Mariette, "Few-particle effects in single CdTe quantum dots," *Phys. Rev. B*, vol. 65, p. 121314, 2002.

[65] J. Seufert, M. Rambach, G. Bacher, A. Forchel, T. Passow, and D. Hommel, "Single-electron charging of a self-assembled IIVI quantum dot," *Appl. Phys. Lett.*, vol. 82, pp. 3946–3948, 2003.

[66] S. Bhunia and D. N. Bose, "Schottky barrier studies on single crystal ZnTe and determination of interface index," *Journal of Applied Physics*, vol. 87, pp. 2931–2935, 2000.

[67] W. Maslana, P. Kossacki, M. Bertolini, H. Boukari, D. Ferrand, S. Tatarenko, J. Cibert, and J. A. Gaj, "p-type doping of II-VI heterostructures from surface

states : Application to ferromagnetic Cd(1-x)Mn(x)Te quantum wells," *Applied Physics Letters*, vol. 82, pp. 1875–1877, 2003.

[68] L. Besombes, *Spectroscopie optique de boites quantiques uniques de semiconducteurs II-VI.* PhD thesis, Universite Joseph Fourier - Grenoble I, 2001.

[69] G. A. Narvaez, G. Bester, and A. Zunger, "Carrier relaxation mechanisms in self-assembled InGaAs/GaAs quantum dots: Efficient P→S Auger relaxation of electrons," *Phys. Rev. B*, vol. 74, p. 075403, Aug 2006.

[70] R. Passler, "Parameter sets due to fittings of the temperature dependencies of fundamental bandgaps in semiconductors," *Phys. Stat. Sol (b)*, vol. 216, p. 975, 1999.

[71] E. Kapon, G. Biasiol, D. Hwang, M. Walther, and E. Colas, "Self-ordering mechanism of quantum wires grown on nonplanar substrates," *Solid-State Electronics*, vol. 40, pp. 815 – 818, 1996.

[72] J. A. Gaj, W. Grieshaber, C. Bodin-Deshayes, J. Cibert, G. Feuillet, Y. Merle d'Aubigné, and A. Wasiela, "Magneto-optical study of interface mixing in the CdTe-(Cd,Mn)Te system," *Phys. Rev. B*, vol. 50, pp. 5512–5527, Aug 1994.

[73] T. Clement, *Etude par spectroscopie optique de la dynamique de spins dans les nanostructures CdMnTe.* PhD thesis, Thse de Doctorat de l'universit Joseph Fourier - Grenoble I, 2009.

[74] X. F. Duan, Y. Huang, Y. Cui, J. F. Wang, and C. M. Lieber, "Indium phosphide nanowires as building blocks for nanoscale electronic and optoelectronic devices," *Nature*, vol. 409, pp. 66–69, 2001.

[75] Z. Fan, D. J. Ruebusch, A. A. Rathore, R. Kapadia, O. Ergen, P. W.Leu, and A. Javey *Nano. Res.*, vol. 2, p. 829, 2009.

[76] Q. F. Meng, C. B. Jiang, and S. X. Mao, "Ohmic contacts and photoconductivity of individual ZnTe nanowires," *Appl. Phys. Lett.*, vol. 94, p. 043111, 2009.

[77] S. Bounouar, M. Elouneg-Jamroz, M. den Hertog, C. Morchutt, E. Bellet-Amalric, R. Andre, C. Bougerol, Y. Genuist, J.-P. Poizat, S. Tatarenko, and K.Kheng, "Ultrafast Room Temperature Single-Photon Source from Nanowire-Quantum Dots," *Nano. Lett.*, vol. 12, p. 2977, 2012.

[78] Z. Liu, G. Chen, B. Liang, G. Yu, H. Huang, D. Chen, and G. Shen, "Fabrication of high-quality ZnTe nanowires toward high-performance rigid/flexible visible-light photodetectors," *Opt. Express*, vol. 21, pp. 7799–7810, 2013.

[79] P. V. Radovanovic, C. J. Barrelet, S. Gradecak, F. Qian, and C. Lieber, "General Synthesis of Manganese-Doped II-VI and III-V Semiconductor Nanowires," *Nano. Lett.*, vol. 5, p. 1407, 2005.

[80] P. Wojnar, E. Janik, L. T. Baczewski, S. Kret, E. Dynowska, T.Wojciechowski, J. Suffczynski, J. Papierska, P. Kossacki, G.Karczewski, J. Kossut, and T. Wojtowicz, "Giant Spin Splitting in Optically Active ZnMnTe/ZnMgTe Core/Shell Nanowires," *Nano. Lett.*, vol. 12, pp. 3404–3409, 2012.

[81] A. Bouravleuv, G. Cirlin, V. Sapega, P. Werner, A. Savin, and H. Lipsanen, "Ferromagnetic (Ga,Mn)As nanowires grown by Mn-assisted molecular beam epitaxy," *J. Appl. Phys.*, vol. 113, p. 144303, 2013.

[82] D. Ferrand, J. Cibert, A. Wasiela, C. Bourgognon, S. Tatarenko, G. Fishman, T. Andrearczyk, J. Jaroszynski, S. Kolesnik, T.Dietl, B. Barbara, and D. Dufeu, "Carrier-induced ferromagnetism in p-Zn(1-x)Mn(x)Te," *Phys. Rev. B.*, vol. 63, p. 085201, 2001.

[83] P. Wojnar, E. Janik, L. T. Baczewski, S. Kret, G. Karczewski, T. Wojtowicz, M. Goryca, T. Kazimierczuk, and P.Kossacki, "Growth and optical properties of CdTe quantum dots in ZnTe nanowires," *Appl. Phys. Lett.*, vol. 99, p. 113109, 2011.

[84] Z. Zhong, F. Qian, D. Wang, and C. M. Lieber, "Synthesis of p-Type Gallium Nitride Nanowires for Electronic and Photonic Nanodevices," *Nanolett.*, vol. 3, p. 343, 2003.

[85] S. Li, Y. Jiang, D. Wu, B. Wang, Y. Zhang, J. Li, X. Liu, H. Zhong, L. Chen, and J. Jie, "Structure and electrical properties of p-type twin ZnTe nanowires," *Appl. Phys. A.*, vol. 102, p. 469, 2011.

[86] P. Rueda-Fonseca, "Unpublished," *Unknown Journal*, 2013.

[87] A. Ebina, K.Asano, and T. Takahashi, "Low-energy-electron loss spectroscopy of ZnTe (110) and (111) surfaces. II. Oxidation properties," *Phys. Rev. B*, vol. 18, p. 4341, 1978.

[88] K. Gas, E. Janik, W. Zaleszczyk, I. Pasternak, E. Dynowska, K. Fronc, V. Kolkovsky, S. Kret, J. Morhange, A. Reszka, M. Wiater, W. Caliebe, G. Karczewski, B. Kowalski, W. Szuszkiewicz, T. Wojtowicz, and T. Takahashi *Acta Phys. Pol. A*, vol. 119, p. 5, 2011.

[89] P. C. D. Hobbs, *Building Electro-Optical Systems: Making it All Work.* Wiley Series, 2009.

[90] L. S. Dang, J. Cibert, Y. Gobil, K. Saminadayar, and S. Tatarenko, "Optical study of residual strains in CdTe and ZnTe layers grown by molecular beam epitaxy on GaAs," *Appl. Phys. Lett.*, vol. 55, p. 235, 1989.

[91] J. Camacho, A. Cantarero, I. Hernndez-Caldern, and L. Gonzlez, "Raman spectroscopy and photoluminescence of ZnTe thin films grown on GaAs," *J. of Appl. Phys.*, vol. 92, p. 6014, 2002.

[92] M. H. M. van Weert; Nika Akopian; Freek Kelkensberg; Umberto Perinetti; Maarten P. van Kouwen; Jaime Gmez Rivas; Magnus T. Borgstrm; Rienk E. Algra; Marcel A. Verheijen; Erik P. A. M. Bakkers; Leo P. Kouwenhoven; Val Zwiller, "Orientation-dependent optical-polarization properties of single quantum dots in nanowires," *Small*, vol. 5, pp. 2134–2138, 2009.

[93] J. Wang, M. Gudiksen, X. Duan, Y. Cui, and C. Lieber, "Highly polarized photoluminescence and photodetection from single indium phosphide nanowires," *Science*, vol. 293, no. 5534, pp. 1455–1457, 2001.

[94] X. Chen, Y. Lou, A. C. Samia, and C. Burda, "Coherency strain effects on the optical response of core/shell heteronanostructures," *Nano Lett.*, vol. 3, p. 799, 2003.

[95] N. Usami, T. Ichitsubo, T. Ujihara, T. Takahashi, K. Fujiwara, G. Sazaki, and K. Nakajima, "Influence of the elastic strain on the band structure of ellipsoidal SiGe coherently embedded in the Si matrix," *J. Appl. Phys*, vol. 94, p. 916, 2003.

[96] K. E. Aifantis, A. L. Kolesnikova, and E. Romanov, "Nucleation of misfit dislocations and plastic deformation in core/shell nanowires," *Phil. Magazine*, vol. 87, p. 4731, 2007.

[97] J. Cibert and D. Ferrand, "Unpublished reslts," 2013.

[98] J. M. Hartmann, J. Cibert, F. Kany, H. Mariette, M. Charleux, P. Alleysson, R. Langer, and G. Feuillet, "CdTe/MgTe heterostructures: Growth by atomic layer epitaxy and determination of MgTe parameters," *J. Appl. Phys.*, vol. 80, p. 6257, 1996.

[99] N. Giles, K. Bowers, R. H. Jr., S. Hwang, and J. Schetzina, "Photoluminescence spectroscopy of CdTe grown by photoassisted MBE," *Journal of Crystal Growth*, vol. 101, pp. 67–72, 1990.

[100] G. Sallen and J. P. Poizat, "Exciton dynamics of a single quantum dot embedded in a nanowire," *Phys. Rev. B*, vol. 80, p. 085310, 2009.

[101] G. Sallen and et.al., "Subnanosecond spectral diffusion measurement using photon correlation," *Nature Photonics*, vol. 4, p. 696, 2010.

[102] V. Zwiller, L. Jarlskog, M. Pistol, C. Pryor, P. Castrillo, W. Seifert, and L. Samuelson, "Photoluminescence polarization of single InP quantum dots," *Phys. Rev. B*, p. 233301, 2001.

[103] J. Suffczynski, T. Kazimierczuk, M. Goryca, B. Piechal, A. Trajnerowicz, K. Kowalik, P. Kossacki, A. Golnik, K. P. Korona, M. Nawrocki, J. A. Gaj, and G. Karczewski, "Excitation mechanisms of individual CdTe/ZnTe quantum dots studied by photon correlation spectroscopy," *Phys. Rev. B.*, vol. 84, p. 085319, 2006.

[104] U. M. Titulaer and R. J. Glauber, "Correlation functions for coherent fields," *Phys. Rev.*, vol. 140, pp. B676–B682, Nov 1965.

[105] L. Mandel, "Sub-poissonian photon statistics in resonance fluorescence," *Opt. Lett.*, vol. 4, pp. 205–207, Jul 1979.

[106] J. Wiersig, C. Gies, F. Jahnke, M. A. zligmann, T. Berstermann, M. Bayer, C. Kistner, S. Reitzenstein, C. Schneider, S. Hfling, A. Forchel, C. Kruse,

J. Kalden, and D. Hommel, "Direct observation of correlations between individual photon emission events of a microcavity laser," *Nature*, vol. 460, pp. 245–249, 2009.

[107] C. Couteau, *Vers une source de Photons Uniques Indiscernables Produits par des Botes Quantiques Semiconducrices II-VI.* PhD thesis, L'universit Paris-Sud XI - Orsay, 2005.

[108] R. Hanbury-Brown and R. Twiss, "Correlation between photons in two coherent beams of light.," *Nature*, vol. 177, p. 27, 1956.

[109] G. Sallen, *Spectroscopie optique de boites quantiques de CdSe inserees dans des nanofils de ZnSe.* PhD thesis, 2009.

[110] S. Moehl, *Etude des proprits optiques de Botes Quantiques Semiconducrices II-VI pour leur application l'mission un photon haute temprature.* PhD thesis, Thse de Doctorat de l'universit Joseph Fourier - Grenoble I, 2005.

[111] B. Patton and et.al., "Trion, Biexciton, and Exciton dynamics in single self-assembled CdSe quantum dot," *Phys. Rev. B*, vol. 68, p. 125316, 2003.

[112] G. Bacher, R. Weigand, J. Seufert, V. D. Kulakovskii, N. A. Gippius, A. Forchel, K. Leonardi, and D. Hommel, "Biexciton versus Exciton Lifetime in a Single Semiconductor Quantum Dot," *Phys. Rev. Lett.*, vol. 83, pp. 4417–4420, Nov 1999.

[113] Becker and H. GmbH, *TCSPC Performance of the id100-50 Detector*, 2005.

[114] G. Sek, A. Musial, P. Podemski, and J. Misiewicz, "On the applicability of a few level rate equation model to the determination of exciton versus biexciton kinetics in quasi-zero-dimensional structures," *J. Appl. Phys.*, vol. 108, p. 033507, 2010.

[115] R. Osovsky, D. Cheskis, V. Kloper, A. Sashchiuk, M. Kroner, and E. Lifshitz, "Continuous-Wave Pumping of Multiexciton Bands in the Photoluminescence Spectrum of a Single CdTe-CdSe Core-Shell Colloidal Quantum Dot," *Phys. Rev. Lett.*, vol. 102, p. 197401, 2009.

[116] Y. P. Varshni, "Temperature dependence of the energy gap in semiconductors," *Physica*, vol. 34, p. 149, 1967.

[117] R. Passler, "Temperature dependence of exciton peak energies in multiple quantum wells," *J. Appl. Phys.*, vol. 83, p. 3356, 1998.

[118] L. Besombes, K. Kheng, L. Marsal, and H. Mariette, "Acoustic phonon broadening mechanism in single quantum dot emission," *Phys. Rev. B*, vol. 63, p. 155307, Mar 2001.

[119] X. Fan, T. Takagahara, J. Cunningham, and H. Wang, "Pure dephasing induced by excitonphonon interactions in narrow GaAs quantum wells," *Solid State Communications*, vol. 108, no. 11, pp. 857 – 861, 1998.

[120] F. Gindele, K. Hild, W. Langbein, and U. Woggon, "Phonon interaction of single excitons and biexcitons," *Phys. Rev. B*, vol. 60, pp. R2157–R2160, Jul 1999.

[121] C. B. Duke and G. D. Mahan, "Phonon-Broadened Impurity Spectra. I. Density of States," *Phys. Rev.*, vol. 139, pp. A1965–A1982, Sep 1965.

[122] P. Borri, W. Langbein, S. Schneider, U. Woggon, R. L. Sellin, D. Ouyang, and D. Bimberg, "Ultralong Dephasing Time in InGaAs Quantum Dots," *Phys. Rev. Lett.*, vol. 87, p. 157401, Sep 2001.

[123] R. Kubo, "Note on the Stochastic Theory of Resonance Absorption," *J. Phys. Soc. Jpn.*, vol. 9, p. 935, 1954.

[124] P. W. Anderson, "A Mathematical Model for the Narrowing of Spectral Lines by Exchange or Motion," *J. Phys. Soc. Jpn.*, vol. 9, p. 316, 1954.

[125] A. Berthelot, I. Favero, G. Cassabois, V. C., C. Delalande, P. Roussignol, R. Ferreira, and J. M. Gerard, "Unconventional motional narrowing in the optical spectrum of a semiconductor quantum dot," *Nat. Phys.*, vol. 2, p. 759, 2006.

[126] S. Bounouar, A. Trichet, M. Elouneg-Jamroz, R. André, E. Bellet-Amalric, C. Bougerol, M. Den Hertog, K. Kheng, S. Tatarenko, and J.-P. Poizat, "Extraction of the homogeneous linewidth of the spectrally diffusing line of a CdSe/ZnSe quantum dot embedded in a nanowire," *Phys. Rev. B*, vol. 86, p. 085325, Aug 2012.

[127] J. Feldmann, S. T. Cundiff, M. Arzberger, G. Bhm, and G. Abstreiter, "Carrier capture into InAs/GaAs quantum dots via multiple optical phonon emission," *J. Appl. Phys.*, vol. 89, p. 1180, 2001.

[128] S. Marcinkevičius and R. Leon, "Carrier capture and escape in In(x)Ga(1-x)As/GaAs quantum dots: Effects of intermixing," *Phys. Rev. B*, vol. 59, pp. 4630–4633, Feb 1999.

[129] V. I. Klimov and D. W. McBranch, "Auger-process-induced charge separation in semiconductor nanocrystals," *Phys. Rev. B*, vol. 55, pp. 13173–13179, May 1997.

[130] W. Yang, R. R. Lowe-Webb, H. Lee, and P. C. Sercel, "Effect of carrier emission and retrapping on luminescence time decays in InAs/GaAs quantum dots," *Phys. Rev. B*, vol. 56, pp. 13314–13320, Nov 1997.

[131] V. Klimov, P. H. Bolivar, and H. Kurz, "Ultrafast carrier dynamics in semiconductor quantum dots," *Phys. Rev. B*, vol. 53, pp. 1463–1467, Jan 1996.

[132] S. Rudin, T. L. Reinecke, and B. Segall, "Temperature-dependent exciton linewidths in semiconductors," *Phys. Rev. B*, vol. 42, p. 11218, 1990.

[133] E. Mayer, N. Pelekanos, J. Kuhl, N. Magnea, and H. Mariette, "Homogeneous linewidths of excitons in CdTe/(Cd,Zn)Te single quantum wells," *Phys. Rev. B*, vol. 51, p. 17263, 1995.

[134] G. Morello, M. D. Giorgi, S. Kudera, L. Manna, R. Cingolaniand, and M. Anni, "Temperature and Size Dependence of Nonradiative Relaxation and Exciton-Phonon Coupling in Colloidal CdTe Quantum Dots," *J. Phys. Chem. C*, vol. 111, p. 5846, 2007.

[135] F. Gindele, K. Hild, W. Langbein, and U. Woggon, "Temperature-dependent line widths of single excitons and biexcitons," *Journal of Luminescence*, vol. 8789, no. 0, pp. 381 – 383, 2000.

[136] S. Nomura and T. Kobayashi, "Exciton LO-phonon couplings in spherical semiconductor microcrystallites," *Phys. Rev. B*, vol. 45, pp. 1305–1316, Jan 1992.

[137] K. H. Hellwege, *Landolt-Bornstein Numerical Data and Functional Relationship in Science and Technology, Group II-VI*, vol. 17a. Springer-Verlag, Berlin, Germany, 1982.

[138] D. Valerini, A. Creti, M. Lomascolo, L. Manna, R. Cingolani, and M. Anni, "Temperature dependence of the photoluminescence properties of colloidal CdSe/ZnS

core/shell quantum dots embedded in a polystyrene matrix," *Phys. Rev. B*, vol. 71, p. 235409, 2005.

[139] H. S. Lee, K. H. Lee, J. C. Choi, H. L. Park, T. W. Kim, and D. C. Choo, "Enhancement of the activation energy in coupled CdTe/ZnTe quantum dots and quantum-well structures with a ZnTe thin separation barrier," *Apll. Phys. Lett.*, vol. 81, p. 3750, 2002.

[140] R. Oszwałdowski, I. Žutić, and A. G. Petukhov, "Magnetism in Closed-Shell Quantum Dots: Emergence of Magnetic Bipolarons," *Phys. Rev. Lett.*, vol. 106, p. 177201, Apr 2011.

[141] R. Oszwałdowski, P. Stano, A. G. Petukhov, and I. Žutić, "Spin ordering in magnetic quantum dots: From core-halo to Wigner molecules," *Phys. Rev. B*, vol. 86, p. 201408, Nov 2012.